Radiation Simulation for Air and Oxy-fuel Combustion using Computational Fluid Dynamics

Hung Ngoc Huynh

Submitted in accordance with the requirements for the degree of

Doctor of Philosophy

The University of Leeds

Centre for Integrated Energy Research

School Chemical and Process Engineering

July 2018

The candidate confirms that the work submitted is his own, except where work which has formed part of jointly authored publications has been included. The contribution of the candidate and the other authors to this work has been explicitly indicated below. The candidate confirms that appropriate credit has been given within the thesis where reference has been made to the work of others.

The work in Chapter 5 of this thesis has been submitted for publication: H. Huynh, A. G. Clements, J. Szuhánszki, W. F. Gale, L. Ma, D. B. Ingham, M. Pourkashanian "Investigation of particle radiation and its effect on NO prediction in a pilot-scale facility for both air and oxy-coal combustion" being submitted for the Fuel Journal.

In this publication the candidate was responsible for the CFD modelling and set-up of the cases for particle radiation, as well as the NOx pollution. Implementing the NGWSGG model, which was developed by Dr. A. G. Clements. The experimental data was performed by Dr. J. Szuhánszki.

This copy has been supplied on the understanding that it is copyright material and that no quotation from the thesis may be published without proper acknowledgement.

©2018 The University of Leeds and Hung Ngoc Huynh.

Acknowledgements

First and foremost, I would like to sincerely thank to my internal supervisor, Prof. Bill Gale, and external supervisors from the University of Sheffield, Prof. Mohamed Pourkashanian, Prof. Derek Ingham and Prof. Lin Ma for their guidance and support. A serious attitude on scientific research from them has brought to me a high standard in my work, and has encouraged me to overcome difficulties that I faced during my study period. I would also like to thank my talented colleagues at the Universities of Leeds and Sheffield, especially, Dr. Alastair and Dr. Janos, for their support during the past four years.

I would like to express special gratitude to my wife, Nhung, for her love, support, encouragement and understanding throughout my studies. Thanks to my daughter Nguyen and my son Khoi who have lived with me in the UK and have shared with me funny stories from their school every day.

Finally, I want to acknowledge the financial support from both the Vietnamese Government and the University of Leeds. I also would like to acknowledge the support from the UKCCSRC PACT Facilities, funded by the Department for Business, Energy & Industrial Strategy and the Engineering and Physical Sciences Research Council, for experimental/modelling work used in this study and support from the UKCCSRC Call2 project on radiation from large and small furnaces.

Abstract

Coal consumption is predicted to account for about 21% of the total global primary energy in 2040 and this continues to be a challenge for global warming and air pollution. Oxyfuel combustion is one of the leading options for carbon capture and storage (CCS) technologies to reduce the impact on the environment. Initially this technology has been studied successfully on small-scale facilities but it needs to be developed for large-scale applications. CFD has been demonstrated to be a key tool for the development and optimisation of pulverised coal combustion processes and it is still an important tool for new designs and retro-fitting of conventional power plants for oxyfuel combustion.

Radiation heat transfer plays an important role, influencing the overall combustion efficiency, pollutant formation and flame ignition and propagation. This thesis focuses on the radiation properties of the particles as well as gas property models on the overall influence of the prediction of the formation of NO_x pollutants in pulverised coal combustion. The radiative properties of the particles are investigated with a focus on the effect of the optical properties and approximate solutions to determine the radiative properties, with different experimental data for the optical properties and approximate solutions being employed. The effects of the radiative properties on the radiative heat transfer are investigated in three-dimensional enclosures for small and large-scale furnaces and implemented on a 250 kW pilot scale combustion for both air and oxyfuel conditions. The results from the study highlights the best selection for the particle properties for simulations in small and large-scale pulverised coal furnaces and employing radiation models for the gases and particles to improve the NO_x predictions in pulverised coal combustion under air and oxy-fired environments.

Contents

List of Figures

List of Tables

Nomenclature

Abbreviations

ADA	advanced differential approximation
ALBDF	absorption line blackbody distribution function
ANL	Argone National Laboratory
ASU	air separation unit
BET	Brunauer Emmett Teller
CAD	computer-aided design
CBK	carbon burnout kinetics
CCS	carbon capture and storage
CDSD	carbon dioxide spectroscopic databank
CFD	computational fluid dynamics
CK	Correlated-k
CPD	chemical percolation devolatilisation
CPU	compression and the purification unit
CTF	combustion test facility
d.a.f.	dry ash free
DNS	direct numerical simulation
DO	discrete ordinates
DTM	discrete transfer methods
DTRM	discrete transfer methods
EBU	eddy break-up
EDC	eddy dissipation concept
EDM	eddy dissipation model
ESP	electrostatic precipitator

EWBM exponential wide band model

FG-DVC functional group deployment vapourisation cross linking

FGD flue gas desulphurisation

FGR flue gas recirculation

GHG greenhouse gases

HITRAN high-resolution transmission molecular absorption database

HITEMP high-temperature spectroscopic absorption database

IDA improved differential approximation

IEA International Energy Agency

HWHM half-width at half maximum

LBL line by line

LES large eddy simulation

MDA modified differential approximation

NGWSGG non-grey weight sum of grey gas

PACT pilot-scale advanced capture technology

PDE partial differential equations

ppm parts per million

RANS Reynolds-averaged Navier-Stokes

RNG renormalisation group

RSM Reynolds stress model

RTE radiative transfer equation

SCR selective catalytic reduction

SLW spectral line-based weighted sum of grey gas

SNB statistical narrow band

SNBCK statistical narrow-band correct-k

SST shear stress transport

UKCCSRC United Kingdom Carbon Capture and Storage Research Centre

WSGG weighted sum of grey gas

UDFs user-defined functions

Greek Symbols

α_1, α_2	mass stoichiometric coefficients	-
c_0	speed of light in a vacuum medium	m/s
β	temperature exponential	-
$\beta_\eta(\vec{r})$	spectral extinction coefficient	-
δ	air pressure-induced line shift	-
$\bar{\delta}$	averaged line spacing over N lines in the spectral interval $\Delta\eta$	-
δ_{ij}	Kronecker-Delta operator	-
$\nabla.q_\eta$	radiative source term	W/m^3
ϵ	emissivity	1/m
ϵ_p	emissivity of particle	-
ε	the rate of dissipation of turbulent kinetic energy per unit mass	m^2/s^3
ω	the specific turbulence dissipation rate ($\omega = \varepsilon/k$)	1/s
ω_c	average velocity of flow	m/s
η	wavenumber	cm^{-1}
$\eta_{0,i}(p)$	line centre of the transition at pressure p	cm^{-1}
η_{vac}	vacuum wavenumber	cm^{-1}
$\bar{\gamma}$	average line Lorentz half-width	$cm^{-1}atm^{-1}$
$\gamma_{L,i}$	Lorentz half width at half maximum	$cm^{-1}atm^{-1}$
$\gamma_{D,i}$	Doppler line half-width	$cm^{-1}atm^{-1}$
$\gamma_{air,i}$	air-broadened half width at half maximum	$cm^{-1}atm^{-1}$
$\gamma_{self,i}$	self-broadened half width at half maximum	$cm^{-1}atm^{-1}$
κ	absorption coefficient	1/m
λ	wavelength	µm
μ	dynamic viscosity of the fluid	kg/m-s
μ_i	directional cosin i	-
ν	kinematic viscosity of the fluid	m^2/s
ϕ	scalar value	-

$\bar{\phi}$	mean scalar value	-
ϕ'	fluctuating scalar value	-
Φ	scattering phase function	-
Φ_{HG}	Henyey-Greentein phase function	-
ρ	density of a gas	kg/m^3
$\bar{\tau}$	narrow-band averaged transmissivity	-
σ	Stefan-Boltzmann constant	W/m^2-K^4
σ_p	scattering coefficient of particles	1/m
τ_{ij}	mean stress tensor	kg/m-s^2
$\bar{\tau_{ij}}$	stress tensor	kg/m-s^2
Ω'	solid angle	-

Roman Symbols

$\Im$	imaginary part	-
$\Re$	real part	-
$a_{g,i}$	emissivity weighting factor for the gas	-
$a_{pi,n}$	emissivity weighting factor for the n^{th} particle	-
A_p	projected surface area of the particle	m^2
A_{BET}	BET specific surface area of pulverised coal	m^2/kg
$c_{i,j}$	temperature dependent polynomial coefficients	-
c_2	second radiation constant ($c_2 = hc/k_B \approx 1.43877$)	cm K
c_s	concentration of the particles	kg/m^3
C_{abs}	absorption cross-section	-
C_{scat}	the scattering cross-section	-
C_{ext}	extinction cross-section	-
C_p	specific heat of particle	J/kg-K
C_j	absorption across the section	-
$\widetilde{C}_j$	supplemental absorption cross sections	-
$\widetilde{C}_j^{loc}$	local supplemental cross-sections	-
$\widetilde{C}_j$	supplemental absorption cross sections	-
d_p	particle diameter	m

D_M	median diameter	μm
D_{32}	the Sauter averaged diameter	μm
E_1, E_2	activation energy	J/kmol
$E_{p,i}$	equivalent emissivity of the particles corresponding to the i^{th} grey gas	-
f	forward scattering fraction	-
$f(\underline{\phi}, k)$	k-distribution function	-
f_c	correlation factor	-
$f_n(D)$	number density function	-
$f_m(D)$	mass distribution function	-
f_p	scattering factor of particle	-
$F_i(\eta)$	line shape function of the i^{th} transition line	-
g	asymmetry factor	-
g_i	gravity component in the i direction	m/s^2
G_η	incident radiation	W/m^2
h	heat transfer coefficient	$\text{W/(m}^2\text{-K)}$
$I_i(\vec{r}, \vec{s})$	radiation intensity of grey gas i^{th} at position $\vec{r}$ in direction $\vec{s}$	$\text{W/(m}^2\text{.sr)}$
$I_{b,g}(\vec{r})$	blackbody radiation intensity of grey gas at position $\vec{r}$	$\text{W/(m}^2\text{.sr)}$
$I_{bp,n}$	blackbody radiation intensity of grey particle	$\text{W/(m}^2\text{.sr)}$
k	turbulent kinetic energy	m^2/s^2
k_{fi}	forward rate of the reaction i	-
k_{ri}	reverse rate of the reaction i	-
k_1, k_2	devolatilisation rate constants	-
$k_{g,i}$	absorption coefficient of the i^{th} grey gas	m^{-1}
$k(\underline{\phi}, g)$	inverse function of $g(\underline{\phi}, k)$	-
κ_p	absorption coefficient of particles	m^{-1}
$K_{g,i}$	temperature dependent polynomial coefficients	-
m	complex index of refraction	-
m_c	mass of residual char	kg
m_p	mass of particle	kg
n	Rosin Rammler spread parameter	-

L	characteristic length	m
M	quadrature order	-
N	number of particles in volume V	-
N_c	number of polynomial coefficients	-
N_g	number of grey gases	-
N_s	number density of the molecular s	-
p	the static pressure	bar
P	total pressure of gas	bar
Pr	Prandtl numbers	-
q	heat flux	$\mathrm{W/m^2}$
P_N	spherical harmonics method	-
$Q(T)$	total internal partition sum at temperature T	-
Q_{abs}	absorption efficiency of particles	-
Q_{sca}	scattering efficiency of particles	-
Q^*_{sca}	effective scattering efficiency of particles	-
$\overline{Q}_{a\lambda}$	spectral average absorption efficiency for a cloud of particles	-
$\overline{Q}_{s\lambda}$	spectral average scattering efficiency for a cloud of particles	-
$\overline{Q}_p$	Planck mean properties of the particles	-
r	spherical particle radius	μm
R	universal gas constant	J/kmol-K
Re	Reynold number	-
$S_i\,(T)$	line intensity at temperature T	$\mathrm{cm^{-1}/(molecule\,cm^{-2})}$
S	source function	-
S_m	mass source terms from discrete phase	$\mathrm{kg/m^3\text{-}s}$
S^u_j	sources of momentum in j directions	-
$S_1(\Theta), S_2(\Theta)$	complex amplitude functions	-
s	pathlength	m
T_f	flame temperature	K
T_g	temperature of surroungding gas	K
T_p	temperature of particle	K

T_{ref}	reference temperature	K
t	time	s
u_i	component velocity in each the i directions	m^2/s
V_c	volume	m^3
V	mass fraction of volatiles released at time t	-
V_{inf}	mass fraction of volatiles released at time $t = \infty$	-
w_j	quadrature weights	-
x	particle size parameter	-
X	mass fraction of volatiles	-
X_c	fraction of unburnt char mass	-
$X_{v,c}$	fraction of unburnt combustibles	-
Y_D	cumulative mass fraction of particles	-
Y_{H_2O}	mole fraction of H_2O	-
Y_{CO_2}	mole fraction of CO_2	-

1 Introduction

From the BP Energy Outlook 2018 [1], the total primary energy in the world over the last 27 years (1990 to 2016) has increased by 63% and this is predicted to increase less quickly over the next 25 years, namely by 35% from 13,276 million tonnes in 2016 to 17,983 million tones in 2040, with the average increase in the rate being 1.3% per year lower than the average of the last 26 years, namely 1.9%. The global coal demand has grown by 2.0% per year between 1990 and 2016 and it is projected to flatten over the next 25 years. In 2016, coal consumption accounted for 28% of the total primary energy, the second largest fuel after oil (33%). Although coal consumption is predicted to decrease to 21% in 2040, it is still one of the most consumed fuel after oil and gas.

Global warming refers to the increase in the average temperature of the earth. The warming in the climate system is partly due to an increase in greenhouse gases (GHG) that are emitted from human activities [2]. Since the Industrial Revolution, human activity has increased the amount of greenhouse gases in the atmosphere, and this has led to increased radiative heating. CO_2 emissions have increased by an average rate of being 2.1% from 1995 to 2015, and the rate is projected to grow at 0.6% per year over the next 20 years [3]. From the World Energy Outlook 2016 [4], 42% of the CO_2 emissions come from the power sector, with about 13.5 Gt and for which coal power plants are responsible for about three-quarters [5]. Increasing the efficiency of coal fired plants and applying Carbon Capture storage has received significant attention over the past two decades by worldwide organisations in order to reduce the CO_2 emissions and to reduce the impact of global warming.

According to the report of the International Energy Agency (IEA) for 2015, the power sector is responsible for one-third of the global SO_2 emissions and 14% global NO_x emissions. The NO_x emissions mainly come from combustion activity, with 60% from burning oil, 15% from coal, natural gas and bioenergy account for 9% and 4%, respectively. Coal is the main fuel that is responsible for air pollutant in the power sector, with three-quarters of the sector's SO_2 emissions and 70% of its NO_x emissions [6]. The pollutant reducing technologies in the power sector can be classified into two types: primary combustion technologies, improving combustion technologies, using low-NO_x burner, and end-of-pipe technologies, removing NO_x from flue gas before releasing it to environment [6]. The introduction of higher emission standards for coal-fired power stations results in using coal that has a lower sulphur content and improving the pollutant technologies. This can be seen over the period from 2005 to 2015, where coal-fired power plants have increased 34%, while the emissions from the total power sector, such as SO_2 and NO_x have decreased by 55% and 34%, respectively [4]. The NO_x emission standards for existing and new power plants are different for different regions and countries, see Table 1.1.

1.1 Carbon capture technologies

Carbon capture and storage (CCS) is a key to its future role in the energy mix [7]. The CCS process consists of capturing CO_2 from the combustion product, transporting and storing the CO_2 deep underground [5, 8]. In recent years, the transport of CO_2 has been considerably developed [9], including pipeline networks, ship transport, etc. With CO_2 storage, deep saline formations have been identified as a great potential for the geological storage of CO_2[10]. Three main technologies have been proposed for the capture of the CO_2 emissions from coal-fired power plants: Post-combustion capture, Pre-combustion capture, Oxy-fuel combustion [5, 11–13] as follows:

(i) Post-combustion capture see Fig. 1.1: The CO_2 separation from the flue gas for the carbon capture occurs downstream of the furnace. In pulverised coal

Table 1.1: NOx emission limitations for currently operating power plants and new power plants in selected countries/regions (mg/m^3) [6].

Regions	Existing plants	New plants
China	200	100
European Union	200-450	150-400
United state	117-640	117
India	300-600	100
Indonesia	850	750
Japan	123-513	123-513
Mexico*	110-375	25-375
Philippines	1000-1500	500-1000
South Africa	1100	750
Korea	308	164
Thailand	400	200
Vietnam	1000	650-1000

Note: * for Mexico, NO_x are expressed in parts per million by volume (ppmv).

combustion plants, the combustion products consist mainly of nitrogen, CO_2 and water, with about 15% concentration of CO_2 by volume at pressures close to that of the atmosphere [5] and the volume flow rate of flue gas is very large. The separation of the CO_2 from the flue gas can be based on technologies, such as absorption [14], adsorption, cryogenics and membranes [15]. In these options, the amine-based solvents is the one that is most developed, that is often selected and developed for the post-combustion capture [9]. The post-combustion capture technology is the simplest way to be implemented and it is the most suitable for the retrofitting of the existing power plants because it requires the least modifications to the power plants [16]. The disadvantage of this technology is that a large amount of the energy is required to generate the solvent, about 80% of the total energy of process. This can result in a 10% energy efficiency penalty [17]. Another disadvantage of the post-combustion capture procedure is the low concentration of the CO_2 in the flue gas at low pressure requires a large size

equipment and a high capital cost [12].

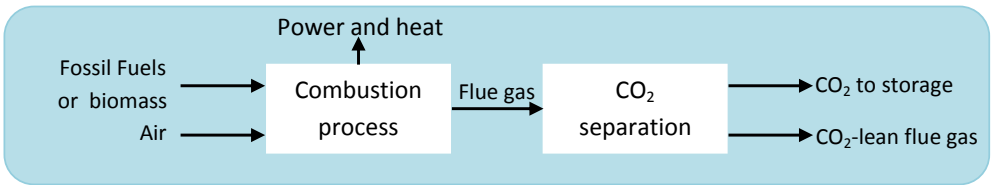

Figure 1.1: The post-combustion CO_2 capture procedure, adapted from [18].

(ii) Pre-combustion capture see Fig. 1.2: Fossil fuels and biomass are gasified to create a mixture known as synthesis gas or "syngas", consisting mainly of carbon monoxide (CO) and hydrogen (H_2). The CO in the syngas then reacts with the steam according to the exothermal water-shift reaction, Reaction (R1.1), to create the CO_2 and more H_2 as [5]:

$$CO + H_2O \rightleftharpoons CO_2 + H_2 + 41\,\mathrm{kJ/mol} \tag{R1.1}$$

The CO_2 is separated from the syngas for storage while the gas can then be used in the combustion process of the gas turbines or fuel cells. The CO_2 conditions in the pre-combustion process is different from that in the post-combustion process, having a concentration that ranges from 15% to 60% and it has a high total pressure of about 2 to 7 MPa [19]. The physical CO_2 absorption solutions to separate the CO_2 from the syngas, and therefore, will have a much lower energy consumption [13]. The disadvantage of the pre-combustion capture is the high investment costs required [12].

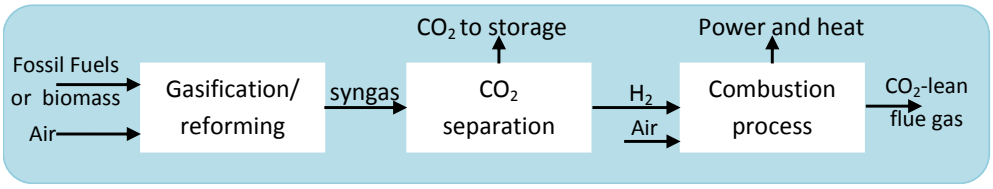

Figure 1.2: The pre-combustion CO_2 capture procedure, adapted from [18].

(iii) Oxyfuel combustion see Fig. 1.3: Instead of using air as the oxidizer in the combustion, a mixture of oxygen O_2, which is separated from the air, and recycled flue gas is used. The use of recycled flue gas is in order to maintain the

same operating temperature of the furnace. The main advantage of the oxyfuel combustion is that the gas products have a high CO_2 concentration and this is convenient for CCS. Under oxyfuel combustion conditions, the NOx emissions are also reduced. For more details on the oxyfuel combustion, see Section 1.2

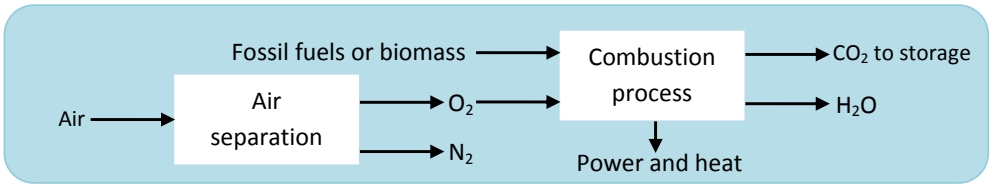

Figure 1.3: The oxy-combustion CO_2 capture procedure, adapted from [18].

1.2 Oxyfuel combustion

The idea of applying the oxyfuel combustion with flue gas recycle in coal-fired plants was first proposed in 1982 [20]. This process was investigated by the Argone National Laboratory (ANL) in the mid and late 1980s, focusing on the system and combustion characteristics [21]. Since the 1990s, this process has been studied widely and has become one of the three main approaches for carbon dioxide capture.

1.2.1 Oxyfuel combustion systems

The simplification of the coal-fired oxy combustion process is shown in Fig. 1.4, where, pure oxygen (95-99%) separated from the air by the Air Separation Unit (ASU) and it is mixed with the second flue gas recirculation (FGR) containing mainly CO_2 and supplied to boiler as an oxidant flow. The second flue gas can be recycled directly (wet recycle) or dried before returning to the boiler (wet recycle). The pulverised coal for the combustion is carried by the primary flue gas, which is pre-heated. The combustion products after the boiler are separated the NO_x, Ash and SO_2 by the Selective Catalytic Reduction Reactor (SCR), electrostatic precipitator (ESP) and the Flue Gas Desulphurization (FGD), respectively. A majority of the flue gas, about 70% to 72 Vol%, is recycled into the combustion

to regulate the combustion process with regards to the temperature [22]. The rest of the flue gas, mainly the CO_2 and some of the non-condensable gases, e.g. O_2, N_2, enter the CO_2 compression and the Purification Unit (CPU), where the non-condensable gases are separated in order to release to the environment and the CO_2 is compressed for transportation and storage.

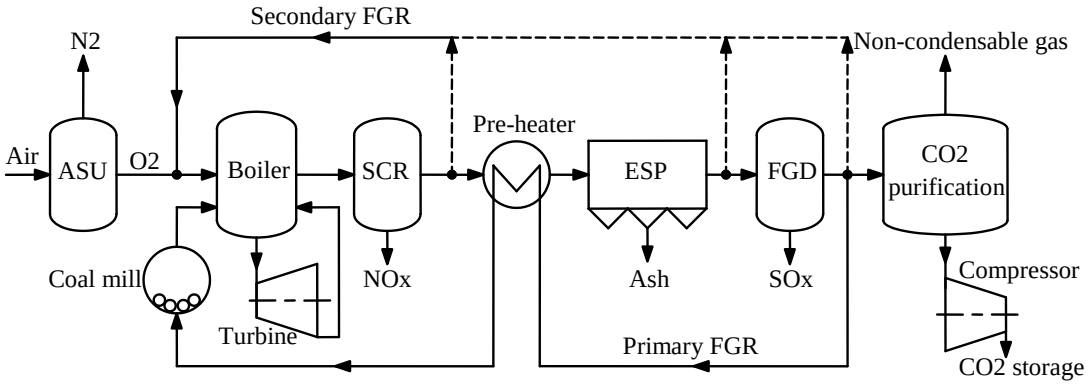

Figure 1.4: Schematic of the coal-fired oxy combustion process adapted from [23–25]. ASU: air separation unit, SCR: selective catalytic reduction reactor, ESP: electrostatic precipitator, FGD: flue gas desulphurization, FGR: flue gas recirculation. (dashed lines : optional recycle secondary FGR).

With the current state and size of power plants, the Air Separation Unit (ASU) using a cryogenic air separation technology is considered as the most appropriate technology for separating O_2 in the oxyfuel combustion technology [26]. While the ASU is a mature technology, the CPU is a relatively new technologies in the CCS [27]. Both of these technologies have a significant energy consumption, with the overall net efficiency being expected to be decreased by 8% to 12% [24]. Also this is a challenge for the oxyfuel combustion. Therefore, many studies have been focused on increasing the energy efficiency of the ASU and CPU [27–29].

1.2.2 Heat transfer under oxy-coal combustion

Under oxyfuel combustion, the concentration of carbon dioxide and water vapor are increased significantly because of the recycled flue gas and this also causes changes in the heat transfer from the flame. The higher specific heat of CO_2,

compared with that of nitrogen, changes the heat transfer (both convection and radiation) under oxyfuel combustion compared to that of air combustion [30, 31]. Experimental studies [32–34] have shown that, with the same oxygen concentration (21%Vol O_2), the flame temperature under the oxy combustion is lower than that for the air condition and therefore the ignition of the particles are delayed. Therefore, maintaining the same heat transfer characteristics needs to be considered when retrofitting conventional air-fired combustion to oxy-fired combustion. To obtain a stable flame, and similar adiabatic flame temperatures to that of air condition, some solutions to this issues have been proposed, such as changing the oxygen concentration, recycling the flue gas [35, 36], changing the burner [37, 38], etc. The range of oxygen concentration from 21- 45% has been examined for oxyfuel combustion in both experimental and numerical studies to find the optimal oxygen concentration that can match the heat transfer to that for the air condition. Some results for the oxygen volume concentration are presented in Table 1.2 which shown for the concentration of O_2 to be in the range 27-34% for a good match of the heat transfer for the air condition. However, all experimental studies were performed on pilot scale facilities, and therefore the studies on the large scale boilers need to be performed.

1.2.3 Pollutant emissions in oxy-coal combustion

Pulverised coal combustion results in some pollutants, such as NO_x, SO_x, mercury and particulate mater including soot and flyash. In the scope of this thesis, the formation and reduction of NO_x are mentioned under both air and oxyfuel conditions. NO_x pollutants from the flue gas in conventional pulverised coal combustion consists of more than 95% NO and the remainder is NO_2 [43]. Under oxyfuel combustion, many experimental and modelling studies have shown that the emissions per unit heat produced is significantly reduced compared to that of the air-fuel combustion [32, 33, 44–54]. It is clear that the thermal and prompt NO formation mechanisms under oxyfuel conditions are almost eliminated because of the replacing of the presence of nitrogen by CO_2. However, this is not the

Table 1.2: Experimental results for the oxyfuel combustion with different oxygen concentrations on the pilot scale facility.

Reference	Unit description	O_2Vol%	Comparison to air case
Liu et al. (2005) [32]	Experiment, 20kW facility	30	Matching gas temperature profile
Tan et al. (2006) [33]	Experiment, 0.3MWth facility	28, 35	28%: slightly lower heat flux and in-flame temperature, 35% slightly higher heat flux and temperature
Zhang et al. (2015) [39]	Experiment and modelling, 3MWth facility	27, 30	27% for dry coal(40% wt moisture), 30% wet coal(24% wt moisture)
Gou et al. (2017) [40]	Experiment and modelling, 35MWth boiler	28	Match average temperature and heat flux distribution
Hu et al. (2013) [41]	Numerical study, 300MW boiler	33	Match the highest flame temperature and total heat transferred through the side walls
Wu et al. (2016) [42]	Numerical study, 350MW boiler	26	The temperature is lower, heat absorbing capacity of waterwall less than 7-12%

main contribution to the reduction of NO because more than 80% NO is created from the Fuel-NO mechanism under the condition of pulverised coal combustion [55, 56], while the reduction of NO under oxyfuel condition reaches to an average of 65% of the emissions at air-fuel condition [47, 49–52, 57]. The reduction causes of NO under oxy condition have been shown for some other reasons, such as the higher NO concentration reducing the conversion of fuel-nitrogen to NO [32, 50, 58] and this also reduces the conversion of char-N to NO [59], reburning the NO recycled by reactions with the hydrocarbon radicals CH_i [33] and enhancing the

heterogeneous reburning because of the higher CO concentration [32], etc.

1.3 Combustion modelling

The development of computers over the last decade has brought powerful tools, such as CFD in to both the academia as well as in the industrial sectors. Computational modelling plays a very important role in the understanding, developing, operating and optimising the combustion process. The main advantage of CFD is that it can be a cheaper approach and less time consuming compared to experimental investigations. Under conventional combustion, CFD has been demonstrated to be a key tool for the development and optimisation of pulverised coal combustion processes. Under oxyfuel combustion, CFD is still an important tool for new designs and the current task is focused on retro-fitting of conventional power plants.

Currently, the modelling of oxyfuel combustion is based on the sub-models developed for air-fired conditions. Changes in the combustion environment under oxyfuel combustion requires some models to be developed and validated to make it applicable to the new combustion environment. The models recommended to be modified or can be used for both air and oxyfuel conditions can be found in the review of oxyfuel combustion by Yin and Yan [60]. In this review, the radiation of the gases, gas combustion, char reactions and NO emissions need to be modified when used for an oxy-fired environment while the turbulence, particle radiation, particle thermaldynamic and votalisation models can be applied for both air and oxyfuel combustions.

The characteristics of radiative heat transfer under oxyfuel combustion are different from those of air-fuel combustion. Therefore, this is considered to be a first priority for the study of retrofitting to keep the same heat transfer condition in the furnace to that of the oxy-fired condition as in the air-fired condition [25, 60]. The higher concentration of CO_2 and H_2O can result in higher partial pressures, absorptivity and emissivity of the gas phase. The spectral models for radiation of gases are believed to be applicable in oxyfuel combustion because

the absorption characteristics of each species are calculated over spectral bands. However, these models are computationally expensive so they are mainly used as a benchmark to evaluate other simplified models. The weighted sum of grey gas (WSGG) model correlated by Smith et al. [61], which assumes the non-grey gas as a number of grey gases having constant absorption coefficients independent of the wavelength, is the most popular model in CFD investigation, but it has parameters based on the air-fired condition and therefore this model is not appropriate for oxyfired combustion. Many efforts have been focused on correlations of the WSGG models for oxyfuel conditions can be found in the literatures [62–67]. The sub-models for particle radiation are considered to be similar for both the air and oxy-fired combustions.

The NO formation under pulverised coal combustion occurs from the mechanisms: Fuel-NO, Prompt-NO, thermal-NO, and N_2O mechanisms. The NO destruction by the reaction of NO with the hydrocarbons, named reburn, and the heterogeneous reaction of NO with the carbon atoms on the char surface. The formation and destruction of NO are often described in CFD by postprocesses. Apart from CO_2 capture purpose, oxyfuel combustion is considered as a an effective solution for the reduction the NO emissions because of the reburning NO from the recycled flue gas. Also replacing nitrogen by CO_2 under oxyfuel combustion almost eliminated the thermal-NO and prompt-NO mechanisms. Existing sub-models for prediction NO emission are developed for air combustion. Some studies have shown that the NO formation and reduction mechanisms in oxyfuel combustion are fundamentally similar to those in air condition [24, 68, 69]. Some other studies suggested that NO formation and reduction mechanisms under oxyfuel combustion have not yet been well understood and therefore further studies on NO need to be performed [58, 60, 70, 71].

1.4 Objectives

The objectives of this study are divided into 2 main parts: The first one is the evaluation of the gas and particle radiation in pulverised coal combustion under

air and oxyfuel conditions. The second part is the effect of the gas and particle models on the radiative heat transfer as well as NO pollutant in a pilot-scale facility.

The evaluation of the particle radiation is focused on the optical properties of the particles, and solutions to defining the particle properties. This is performed for both small and large-scale furnaces and for both air and oxy-fired conditions. In addition, the radiation solutions for the gas, both grey and non-grey models, are developed and those are coupled to the particle radiation. The study highlights the best selection of the particle properties for the simulation of small and large-scale pulverised coal furnaces under both air and oxy-fired environments.

Investigation on the effects of the gas and particle properties on the radiative heat transfer are implemented on the pilot-scale facility, the 250 kW pilot scale combustion test facility (CTF) of the Pilot-scale Advanced Capture Technology (PACT) facilities operated by the UK carbon capture and storage research centre (UKCCSRC). The simulation results are compared against experimental data for different operating conditions and the effect of gas and particle radiation on the NO emissions are also investigated.

1.5 Thesis outline

The contents of the study are presented in 6 chapters. Chapter 1 introduces the carbon capture technologies, oxyfuel combustion and the role of computational fluid dynamics in combustion. The objectives and contents of the study are also outlined in this chapter. Chapter 2 reviews combustion modelling, the radiation of the gas and particle phases and the NO_x emissions in pulverised coal combustion. In this chapter the mathematical models for the simulations performed in later chapters are discussed. Chapter 3 evaluates the effects of optical constants, and approximate radiative property models on radiative properties of particles. The validations of radiation models developed for gas and particle are also performed in this chapter. The investigation of the effects of the radiative properties of particles and the solutions to define the particle properties on the radiative heat

transfer in small and large scale furnaces are performed in Chapter 4. As an engineering application, Chapter 5 investigates the influence of the particles on the radiative heat transfer on the 250 kW pilot-scale facility. In this chapter, the effects of the radiation solutions on the NO emissions are also discussed. The final chapter, Chapter 6, consists of the conclusions of the study and suggests possible further studies in pulverised coal combustion.

2 CFD modelling for coal combustion

Computational fluid dynamic (CFD) modelling has become a powerful and effective tool for the design and optimisation of pulverised coal combustion. Combustion is one of the most complicated processes since it involves simultaneously physical and chemical processes, such as fluid dynamics, turbulence, heat transfer and chemical kinetics. Therefore, although combustion is a mature technology, it is still a challenge for mathematical modelling [72]. The combustion processes can be simulated by CFD based on solving simultaneously the conservative equations for mass, momentum, and heat transfer with some simplifications. Therefore the validation of the the sub-models need to be performed when they are applied for simulation [73]. Furthermore, in the available CFD codes, solving sub-processes in the pulverised coal combustion are supplied by simplified sub-models in order to save computational time and this can reduce the accuracy of prediction results [74]. A more exact solution for analysing the combustion process needs to apply a more accurate theory for a sub-process and this often requires more computational time. It is important to clearly identify and implement sub-models for modelling the combustion processes which can be described based on fundamental principles. Understanding combustion knowledge can help to enhance and develop sub-models for combustion of specific interest.

CFD codes have been demonstrated to be powerful tools in the air-fuel combustion. Under oxyfuel combustion, the air is replaced by a mixture of the flue gas and pure O_2, with a flue gas resulting in a high concentration of CO_2. This brings a new challenge for existing CFD codes since assumptions and approximations for sub-models may not be compatible with the CO_2-rich environment. Most of the current studies on oxyfuel combustion are mainly towards the retrofitting of

the convectional boilers [52]. However, further efforts still need to be done on the oxyfuel modelling in order to make it become a powerful tool in the oxyfuel combustion technology development as it has ben demonstrated in the air-fired combustion development [60]. In particular, significant challenges are expected in the combustion process, including the flame stability and pollutant emissions, burner aerodynamics and scaling, as well as determining the optimal operating conditions [25].

In this chapter, the underlying physics and chemistry sub-processes for CFD modelling of pulverised coal combustion will be reviewed, such as turbulence and particle combustion sub-processes are mentioned in Section 2.1. The radiation of gases and particles are presented in Section 2.2. In this section, different models for the gas and the particles are used for the studies in the thesis are reviewed. The pollution of NO_x is mentioned in Section 2.3.

2.1 Coal combustion modelling

Pulverised coal combustion is a complex process since it involves the simultaneous processes such as turbulence, chemical reaction and heat transfer [72]. Therefore, a confident results in the modelling needs to consider all the factors that effect the combustion process. This section reviews the fundamental principles for CFD modelling, turbulence models and particle combustion modelling. Further, the influence of the oxyfuel condition in the prediction of the results of the sub-models, which were originally developed for modelling the air condition, are also discussed.

2.1.1 Governing equations

- Conservation of mass: The change of mass density with time, $\partial\rho/\partial t$, is equal to the mass flow entering and leaving an infinitesimal control volume as expressed by the conservation of mass equation in Cartesian coordinates

$$\frac{\partial \rho}{\partial t} + \frac{\partial}{\partial x_i}\left(\rho u_i\right) = S_m \tag{2.1}$$

where ρ is the fluid density, u_i is the velocity components in each the x_i directions. The source terms S_m is the mass added to the control volume of the continuous phase from the discrete phase.

- Conservation of momentum: Conservation of momentum in j^{th} direction of an inertial reference frame is described by

$$\frac{\partial}{\partial t}\left(\rho u_j\right) + \frac{\partial}{\partial x_i}\left(\rho u_i u_j\right) = \frac{\partial \tau_{ij}}{\partial x_i} - \frac{\partial p}{\partial x_j} + \rho g_j + S_j^u \tag{2.2}$$

where p, τ_{ij} and g_j are the static pressure, stress tensor and gravimetric acceleration, respectively. S_j^u is the source of momentum in j^{th} direction added to the control volume. The stress tensor relating to the velocity components is given by

$$\tau_{ij} = \mu\left(\frac{\partial u_i}{\partial x_j} + \frac{\partial u_j}{\partial x_i} - \frac{2}{3}\frac{\partial u_k}{\partial x_k}\delta_{ij}\right) \tag{2.3}$$

where μ is the molecular viscosity, δ_{ij} is the Kronecker-Delta operator (δ_{ij}=1 if $i = j$ and δ_{ij}=0 if $i \neq j$).

- Conservation of energy: The balance of energy in a infinitesimal control volume can be written as

$$\frac{\partial\left(\rho E\right)}{\partial t} + \frac{\partial\left(\rho u_i E\right)}{\partial x_i} = \frac{\partial}{\partial x_i}\left(k_{eff}\frac{\partial T}{\partial x_i}\right) - \frac{\partial u_i p}{\partial x_i} + \frac{\partial}{\partial x_i}\left(\tau_{ij} u_j\right) - \rho g_i u_i + S_{rea} + S_{rad} \tag{2.4}$$

where k_{eff} is the effective conductivity defined by summation of conductivity of gas, k, and turbulent thermal conductivity k_t. The source terms for the change in reaction and radiation are S_{rea}, S_{rad}, respectively, and E is the total energy per unit mass.

The set of transport equations for the mass Equation (2.1), momentum Equation (2.2) and energy Equation (2.4) are sufficient to describe the turbulent fluid flow with no reaction. In pulverised coal combustion phenomenon, the species transport equation is involved. The discrete phase is often modelled in a Lagrangian frame by tracking a large number of particles. The change of mass, momentum and energy of the discrete phase are added to the continuous phase through the source terms.

2.1.2 Turbulence modelling

Turbulence is a common state in fluid flows and it plays an important role in most practical combustion processes. Characterisations of the gas flow can be described by the Reynolds number, $Re = \omega_c L/\nu$, which is a dimensionless quantity composed of the average velocity ω_c, characteristic length L, and kinematic viscosity ν of the fluid. Although the Navier-Stokes equations can resolve both laminar and turbulent flows, because of the computational limitations, the Direct Numerical Simulation (DNS) can only be applied to solve simple flows and at a small and moderate value of the Reynold number. Several turbulence models have been developed to deal with large Reynolds number flows and these are based on the Reynolds-averaged Navier-Stokes (RANS) or the Large Eddy Simulation (LES). Computational Fluid Dynamics (CFD) modelling of turbulent combustion is still largely based on RANS [25]. This is because it provides reasonably accurate flow solutions and also it is fast computationally, especially for the numerical computation of combustion flows.

2.1.2.1 Direct Numerical Simulation

DNS solves all scales of the reacting flow problems. The unsteady Navier-Stokes equations are solved with a sufficiently fine grid that fits the Kolmogorov length scales which are the smallest hydrodynamic scales in turbulent flows. Because of the need to employ such a small size mesh, this method requires very fast computational power and it is currently impractical for numerical predictions of complex flows in combustion flows. The DNS is used to validate other methods, such as RANS, LES [75] in single flow configurations. The DNS method has been applied for predicting the pulverised coal combustion by Luo et al. [76].

2.1.2.2 Reynolds-averaged Navier-Stokes

In the RANS approach, instantaneous variables of the Navier-Stokes equation are decomposed into the mean and fluctuating components:

$$\phi = \bar{\phi} + \phi' \tag{2.5}$$

where ϕ denotes a vector or a scalar such as energy or species concentration. Inserting the variable decompositions in Equation (2.5) for velocity into the conservation equation for mass Equation (2.1) and momentum Equation (2.2) we obtain equations for time-averaged variables for mass Equation (2.6) and momentum Equation (2.7) as follows:

$$\frac{\partial \bar{\rho}}{\partial t} + \frac{\partial}{\partial x_i}\left(\bar{\rho}\bar{u}_i\right) = S_m \tag{2.6}$$

$$\frac{\partial}{\partial t}\left(\bar{\rho}\bar{u}_j\right) + \frac{\partial}{\partial x_i}\left(\bar{\rho}\bar{u}_i\bar{u}_j\right) = -\frac{\partial \bar{p}}{\partial x_j} + \frac{\partial}{\partial x_i}\left(\bar{\tau_{ij}} - \bar{\rho}\overline{u_i' u_j'}\right) + S_j^u \tag{2.7}$$

where the mean stress tensor, $\bar{\tau_{ij}}$, is defined as:

$$\bar{\tau_{ij}} = \mu\left(\frac{\partial \bar{u}_i}{\partial x_j} + \frac{\partial \bar{u}_j}{\partial x_i} - \frac{2}{3}\frac{\partial \bar{u}_k}{\partial x_k}\delta_{ij}\right) \tag{2.8}$$

Equations (2.6) and (2.7) are called the Reynods-averaged Navier-Stockes (RANS) equations where the variables are presented as time-averaged values. However, in the RANS equation there appears a new term $-\bar{\rho}\overline{u_i' u_j'}$ called the Reynolds stress and this unknown term must be modelled in order to close Equation (2.7). The RANS models can be closed by (i) eddy viscosity models (via the Boussinesq hypothesis) or (ii) Reynolds-Stress Models (via transport equations for the Reynolds stresses).

(i) eddy viscosity models based on the Boussinesq hypothesis is where the relation between the Reynolds stress and the mean velocity are expressed as follows;

$$-\bar{\rho}\overline{u_i' u_j'} = \mu_t\left(\frac{\partial \bar{u}_i}{\partial x_j} + \frac{\partial \bar{u}_j}{\partial x_i}\right) - \frac{2}{3}\left(\bar{\rho}k + \mu_t\frac{\partial \bar{u}_k}{\partial x_k}\right)\delta_{ij} \tag{2.9}$$

where μ_t is the turbulent viscosity. The turbulent kinetic energy, k, is defined as

$$k = \frac{1}{2}\overline{u_i' u_i'} \tag{2.10}$$

Different models have been developed to calculate the turbulent viscosity μ_t and these models are normally classified by the number of partial differential equations employed for the calculation, such as zero-equation models, one-equation models

and two-equation models. The two-equations describe the turbulent viscosity as a function of k and the turbulent dissipation rate, ε, or k and the specific turbulent dissipation rate, ω, e.g. the standard $k-\varepsilon$ model [77], the standard $k-\omega$ model [78] and their variation of these models such as the RNG $k-\varepsilon$ [79], Realisable $k-\varepsilon$ [80] and SST $k-\omega$ models [81]. A limitation of the eddy viscosity models is that the Reynolds stress is assumed to be proportional to the mean flow strain rate and the turbulence viscosity is isotropic, and therefore it may not be represented correctly for the anisotropic phenomenon, such as in swirling flows that are typical in pulverised fuel combustion [82].

(ii) The Reynolds Stress Model (RSM) [83, 84] closes the RANS equation by solving additional transport equations for the Reynolds stresses plus an equation for the dissipation rate. In 3D flows seven additional transport equations must be solved that are 6 transport equations of Reynolds stresses corresponding to the six different Reynolds stresses ($\overline{u_1'u_1'}, \overline{u_2'u_2'}, \overline{u_3'u_3'}$ and $\overline{u_1'u_2'}, \overline{u_1'u_3'}, \overline{u_2'u_3'}$) and an equation for the dissipation rate. The advantage of this model is that it has great potential to give accurate predictions of complex flows. However, the effect of including additional resolving equations results in more computationally expensive time being required.

2.1.2.3 Large Eddy Simulation

The LES model resolves the large scales of the turbulent flows directly, while the small scales of the turbulence, which are assumed to be less dependent on the geometry, are modelled. The resolving of only these large eddies allows the use of much coarser meshes and larger time-step sizes in LES than in DNS. However, LES still requires substantially finer meshes than those typically used for RANS calculations. Therefore, LES falls between the DNS model and the RANS model in terms of computational cost.

Under Oxyfuel condition, the flue gas recycle flow and flue gas composition can change burner aerodynamics, the flame shape [34, 85]. However, there is no impact of the oxyfuel condition on the modelling capabilities of the turbulence

models [60]. The standard $k-\varepsilon$ model has been widely employed in oxyfuel modelling, followed by the Realisable $k-\varepsilon$ and the LES [25, 60].

2.1.3 Particle combustion modelling

Combustion process modelling of a particle can be defined by 4 main stages [86, 87] (i) Inert heating, (ii) Devolatilisation, (iii) Volatile combustion and (iv) Char combustion. Fig. 2.1 schematically illustrates the combustion process of a particle. Once the particle enters the furnace, the drying process occurs under the effect of the temperature of the furnace, the particle size, and the moisture content and porosity of the particle. As the particle is being heated, evaporation occurs. Following the heating process, the particle is further heated up to the devolatilisation (pyrolysis) temperature. As a result of the drying and heating, the particle may shrink, thus reducing its volume and pore sizes it starts to fragment [88]. The devolatilisation process produces volatile matter that is composed of tar (heavy hydrocarbon $C_xH_yO_z$), lighter gases (CH_4, C_2H_4, C_2H_6, CO, CO_2, H_2O, H_2, etc.) and char (the residual solid mainly carbon and ash) [88, 89]. In the volatile combustion process, the volatiles react with the oxygen in the air. This increases the temperature of the surrounding environment and produces CO_2 and H_2O. The char combustion is a heterogeneous gas-solid reaction that takes the most time in the total burning time of the particles [43, 90].

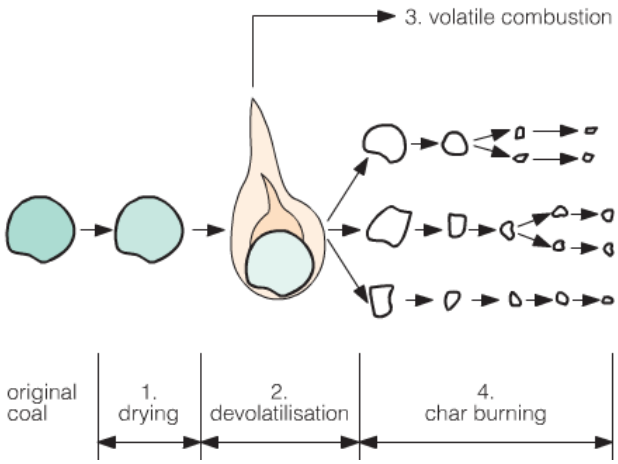

Figure 2.1: Schematic of the combustion process of coal particles [88].

A comprehensive knowledge of particle combustion processes has been outlined by Hutny et al. [91]. Further CFD-based particle combustion models have been introduced by Lu et al. [92] who studied the combustion behaviours: drying, pyrolysis, and reaction rate of single particles of solid biomass. Yang et al. [93] and Baum and Street [94] have performed experimental investigation and produced CFD models to study the combusting behaviour of particles

2.1.3.1 Heating of particle

The heating-up process of a coal particle is very fast when the particle enters the combustion furnace [87, 90]. This process includes the heating of the particle to the devolatilisation temperature and the moisture vaporisation from the particle. The heat transfer process in the heating particle includes the convective and the radiative heat transfer that occur from the surroundings to the surface of the particle and the heat conduction within the particle [95]. Under the oxyfuel combustion, the difference in the characteristics of the surrounding gases and temperature can results in a change in the heating and the evaporation of the particle and consequently this may influence the heating rate.

The heating rate, the rate of change of the particle temperature with time, depends on the initial particle temperature, particle size, temperature and combustion gases [96]. The heating rate of a coal particle in the pulverised coal combustion is quite fast, about 10^5 K/s, and can vary significantly between experimental studies [87]. The heating rate for a coal particle having a 100 µm diameter has been studied by [25] for both the air and oxy conditions. The results showed that the particle heating rate is more significantly influenced by the gas temperature than the gas compositions and with the same temperature, the particle heating rate under the oxyfuel condition is slightly higher than that in the air-fuel condition. This is due to the thermal conductivity of the CO_2 is slightly higher than that of the air condition. The heating rate of the coal particles in the gas steam can be calculated from the heat balance equation [25, 87, 97] as

$$m_p C_p \frac{dT_p(t)}{dt} = hA_p \left(T_g - T_p\right) + \epsilon_p \sigma A_p \left(T_f^4 - T_p^4\right) \tag{2.11}$$

where m_p, C_p are the mass and specific heat of the particle respectively, A_p is the particle surface area, ϵ_p is the emissivity of particle, σ is the Stefan-Boltzmann constant, and T_g, T_f, T_p are the local temperature of surrounding gas, flame temperature and particle temperature, respectively. The heat transfer coefficient, h, is calculated as [98]

$$Nu = \frac{hd_p}{k_\infty} = 2.0 + 0.6Re_d^{1/2}Pr^{1/3} \tag{2.12}$$

where d_p denotes the particle diameter, k_∞ is the thermal conductivity of the continuous phase, and Re and Pr are the Reynold number and Prandtl numbers, respectively.

In pulverised coal combustion models, the temperature within the particle is often considered to be uniform [93]. This may lead to the an inaccuracy in the combustion process modelling, especially when considering large particles, such as biomass. Gubba et al. [95] developed a model for the heat transfer within the large particles. This model takes into account of the effect of the particle size and shape distribution on the internal thermal gradients.

2.1.3.2 Devolatilisation

Devolatilisation is a complex process and it has a strong influence on the combustion of the pulverised coal combustion and the volatile yield. And therefore, ignition, stability of flame, char burnout and pollutant emissions are also affected [60]. Devolatilisation characteristics depend on the type of particle, particle size and operation conditions, e.g., the heating rate, temperature, environment gas compositions, pressure [91, 99–101].

Coal devolatilisation models can be classified into two groups [87, 88]: global kinetic models and network models. The global kinetic models are simplest models, such as single-step kinetics model [102], two-step kinetics models [103] and distributed activation energy models [104]. The network models, such as the Functional Group-depolymerization Vaporization Cross-linking (FG-DVC) model

[105], the FLASCHAIN model [106] and the Chemical Percolation Devolatilisation (CPD) model [107–109], have been considered as accurate models to describe devolatilisation processes, however, they are computational expensive.

In the case of the single rate model of devolatilisation, the devolatilisation is described by a simple reaction as [87]

$$\text{Coal} \xrightarrow{k_1} X\text{Volatiles} + (1-X)\text{Char} \tag{R2.1}$$

where X is the mass fraction of volatiles. The devolatilisation rate constant, k_1, is correlated with the particle temperature by an Arrhenius expression as

$$k_1 = A_1 \exp(-E_1/RT_p) \tag{2.13}$$

where A_1, E_1 is the pre-exponential factor, and activation energy, respectively, R is the universal gas constant and T_p is the particle temperature. The empirical parameters, A_1, E_1, can be correlated from experimental data or from more complex network models. The rate of of devolatilisation can be expressed as

$$\frac{\mathrm{d}V}{\mathrm{d}t} = k(V_{inf} - V) \tag{2.14}$$

where V_{inf} is the mass fraction of volatiles released at $t = \infty$. V is the fraction of volatiles released at time t.

The Competing Two Step Model approximates the devolatilisation by two single rate reactions as [103]

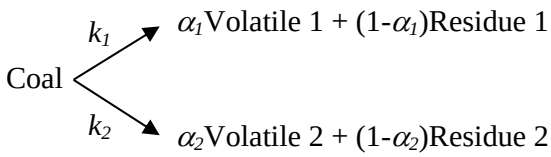

(R2.2)

where α_1 and α_2 are the mass stoichiometric coefficients referring to the reactions occurring at low and high temperatures, respectively. k_1, k_2 are the rate constants defined as follows:

$$k_1 = A_1 \exp(-E_1/RT_p) \tag{2.15}$$

$$k_2 = A_2 \exp(-E_2/RT_p) \tag{2.16}$$

The rate of devolatilisation can be expressed as

$$\frac{\mathrm{d}V}{\mathrm{d}t} = -m_c(\alpha_1 k_1 + \alpha_2 k_2)\exp\left(\int_0^t (k_1 + k_2)\,\mathrm{d}t\right) \tag{2.17}$$

where m_c is the mass of residual char.

From review of Yin and Yan [60], the single-step rate was the most popular and this was followed by the FG-DVG, and the CPD model in oxy-coal CFD simulations.

2.1.3.3 Volatile combustion

The combustion of volatiles plays important role in ignition, flame stability and pollutant emissions [60, 88, 110]. This is a complicated process because of a numerous intermediate species and reactions involved and therefore accounting all reactions will results in significantly computational consumption in combustion problem. For simplification in modelling, volatiles can be considered as a single hydrocarbon ($C_xH_yO_z$) or light hydrocarbon (C_xH_y). In case the coal consist of N_2 and S_2, the volatiles needs to contain nitrogen, sulphur species, $C_xH_yO_zN_mS_n$, to included the pollutant emissions of NO_x and SO_x. Also, instead of using detail kinetic mechanisms to describe the volatile combustion, simplified reaction mechanisms, such as global kinetic mechanism are selected as a solution for reducing computational cost.

The simplest reaction mechanism for the oxidation of hydrocarbon fuels is the global 1-step mechanism introduced by Westbrook and Dryer [111] with the assumption that the reaction products are CO_2 and H_2O. The global 1-step reaction mechanism overpredicts the total heat of reaction and this was because a large amount of CO and H_2 exist in the combustion products of the hydrocarbon fuels with CO_2 and H_2O [111]. The overall reaction for 1-step mechanism can be expressed as

$$\text{Volatiles} + O_2 \rightarrow CO_2 + H_2O \tag{R2.3}$$

The global 2-step reaction mechanism was introduced by Dryer [112] for methane oxidation in a turbulent flow reactor with the rate expressions that are derived

from the experiments. The common 2-steps reaction mechanism can be expressed as [87]

$$\text{Volatiles} + O_2 \rightarrow CO + H_2O \tag{R2.4}$$

$$CO + 1/2O_2 \rightarrow CO_2 \tag{R2.5}$$

The global 3-step mechanism was introduced by Hautman et al. [113] from the flow reactor experimental results. This mechanism combines the global and elementary kinetics. Jones and Linstedt [114] developed the global 4-step reaction mechanism. The mechanism consists of two irreversible reactions that describe the initial oxidation steps of a hydrocarbon and two reversible reactions which control the rate of reaction for CO and H_2.

The global combustion models have been applied frequently in CFD for air-fired combustion. Except for the 1-step reaction, which is considered having over prediction total heat [111], the global 2-step mechanisms and multi-steps mechanisms has been demonstrated adequately in describing the volatiles combustion. The four-step mechanism of Jones and Linstedt [114] was reported to be a good for both aspects of accuracy and computational efficiency [115].

Under the oxy-fired combustion, the high-concentration CO_2 has effects on the combustion of volatiles, such as slower volatile combustion rate, higher CO concentration comparing to the air-fired combustion. However, the detailed pathways or mechanisms for oxy-fired combustion are not yet well defined [60], therefore, using global mechanism developed for conventional combustion has been still applied in oxy-fired combustion. This can be found in some studies for the 2-step reaction mechanism [116], the 3-step mechanism [117, 118] and 4-step mechanism [100]. Some efforts on refining the global mechanism to make a better prediction the CO concentration under oxy-fired combustion. Anderson et al. [119] modified the 2-step mechanisms of [111] and the four-step mechanism of [114]. The models refined were compared against the detailed chemical kinetic mechanism of Glarborg and Bentzen [120]. The modified 2-step models showed an improving the temperature field and CO concentration prediction in the post flame while the

modified 4-step model show a little better the CO prediction in the flame zone. Yin et al. [121] implemented the modified models [119] on a lab-scale 0.8 MW oxy-natural gas flame furnace and a conventional 609 MW utility boiler which is assumed to be operating under the oxyfuel combustion condition. Results from this study demonstrates the advantage of both the modified 2-step and 4-step models for modelling of the oxy-fired combustion. Recently, Chen and Ghoniem [122] performed simulations of the quasi-global and 2-step global reaction mechanisms on a swirling diffusion flame under both air-fired and oxyfuel conditions using the eddy dissipation model and the eddy dissipation concept. The results show that the 2-step global mechanism underestimates the CO concentrations while quasi-global reaction mechanism showed an improved performance in both the air-fuel and oxyfuel flame CFD simulations.

2.1.3.4 Char combustion

After the release of the volatile matter, the remaining substances left are char and ash. The char combustion is an important process in the coal-combustion process, with the majority of the heat being released. The overall process of the char combustion includes the transport of oxygen and energy to the surface of the char particle, through the porous structures of the particles and then the reaction that occurs between the oxygen and the carbon at the internal and external surfaces of the char particles [123]. The char combustion is a complicated process that is influenced by a number of parameters, including the char particle size, pore size, density, surface area, available oxygen, etc. [88]. A comprehensive knowledge of the char combustion models can be found in the reviews by [43, 87].

The heterogeneous reactions of the char primarily occurs by the following reactions [124]:

$$\mathrm{C(s)} + 1/2\mathrm{O_2} \rightarrow \mathrm{CO} \tag{R2.6}$$

$$\mathrm{C(s)} + \mathrm{O_2} \rightarrow \mathrm{CO_2} \tag{R2.7}$$

$$C(s) + CO_2 \rightarrow 2\,CO \tag{R2.8}$$

$$C(s) + H_2O \rightarrow CO + H_2 \tag{R2.9}$$

Reaction (R2.7) is significant at low temperatures, such as ignition conditions. However, Reaction (R2.6) increases on increasing the temperature. Under the combustion conditions, Reaction (R2.6) is dominant and the Reaction (R2.7) can be ignored [88]. Many models have been developed to describe char combustion reactions, such as the diffusion limited model [94], the kinetic/diffusion limited [94, 125], the intrinsic mode [90], the carbon burnout kinetics (CBK) [126], etc.

2.1.4 Turbulence - chemistry interactions

For laminar flows, the interaction between the flow and the chemical reactions can be calculated using the laminar finite-rate model. However, in the turbulent flow cases, the turbulent and chemical interactions become important and it must be modelled [25]. The eddy dissipation model (EDM) [87] was based on the eddy break-up (EBU) model proposed by Spalding [127]. The finite rate/eddy dissipation model was proposed as an improvement to the eddy dissipation model, in which the net radiation rate is taken as the smaller of the Arrhenius rate and the eddy dissipation rate.

The drawback of the eddy dissipation model and the finite rate/eddy dissipation model is that they can not be applied to multi-step chemical reactions. The reason is that multi-step mechanisms are based on the reaction rates (Arrhenius rates) which differ for each reaction. Therefore, these models are only valid for one-step or two-step reaction mechanisms without reversible reactions. Another drawback of the EDM is that this model is not likely to be applicable in oxyfuel flames, which are under CO_2 decomposition at high temperatures [87].

The eddy dissipation concept (EDC) model [128] was developed as an extension of the eddy dissipation model. Andersen et al. [119] recommended the use of the EDC turbulence chemistry interaction model for modelling oxyfuel

flames after performing both the Eddy Dissipation Model (EDM) and the EDC model. The application of the EDC model can be found in some CFD models [115, 129, 130].

2.2 Radiative heat transfer in pulverised coal combustion

In combustion systems, radiative heat transfer is accounted for by solving the radiative heat transfer equation (RTE). Exact solutions for the RTE are very complicated and only possible for very simple cases, such as one-dimensional media without scattering [131, 132]. These models are not suitable for application in a real combustion model, which involves the simultaneous processes of multi-dimensional geometries of two-phase flows, turbulence, and chemical kinetics. Therefore, different approximations have been developed to solve the RTE, such as the discrete transfer, discrete ordinates, and spherical harmonics models.

The accuracy in the radiative properties of combustion products used in the calculations directly impacts on the accurate prediction of the radiative heat transfer in the combustion system [72]. In pulverised coal combustion, these products consist of the gas products, mainly CO_2, H_2O, and the particulate matter, such as soot, fly-ash, char and coal particles. The radiative properties of the combustion product can not be measured directly. The calculation of the radiative properties of the combustion products is not easy because of the wavelength dependence, size and shape of the particles and the particle distribution.

In this section, the radiative heat transfer in combustion systems are discussed. Sections 2.2.1 and 2.2.2 introduce the radiative heat transfer equations and techniques for solving these equations. Sections 2.2.3 and 2.2.4 discuss properties of the gas and particles, respectively. In these two sections, the solutions for the defining properties of the gas and particles are introduced.

2.2.1 Radiative heat transfer equations

The radiative transfer equation (RTE) for an absorbing, emitting, and scattering medium at a position $\vec{r}$ and the direction $\vec{s}$, is expressed in its steady form as [133]:

$$\frac{\mathrm{d}I_\eta\left(\vec{r},\vec{s}\right)}{\mathrm{d}s}=\kappa_\eta\left(\vec{r}\right)I_{b\eta}\left(\vec{r}\right)-\beta_\eta\left(\vec{r}\right)I_\eta\left(\vec{r},\vec{s}\right)+\frac{\sigma_\eta\left(\vec{r}\right)}{4\pi}\int_0^{4\pi}I_\eta\left(\vec{r},\vec{s'}\right)\Phi_\eta\left(\vec{r},\vec{s'},\vec{s}\right)\mathrm{d}\acute{\Omega} \tag{2.18}$$

where $I_\eta\left(\vec{r},\vec{s}\right)$ is the radiative intensity at location $\vec{r}$ travelling in the direction $\vec{s}$, $I_{b\eta}(\vec{r})$ is the black body emission calculated at the temperature at position $\vec{r}$, $\sigma_p(\vec{r})$ is the scattering coefficient of the particles, $\Phi_\eta\left(\vec{r},\vec{s'},\vec{s}\right)$ is the scattering phase function, Ω' denotes solid angle and $\beta_\eta\left(\vec{r}\right)$ is the total attenuation of the intensity of both absorption $\kappa_\eta\left(\vec{r}\right)$ and scattering $\sigma_\eta\left(\vec{r}\right)$ is known as the extinction coefficient, and is defined as follows:

$$\beta_\eta\left(\vec{r}\right)=\kappa_\eta\left(\vec{r}\right)+\sigma_\eta\left(\vec{r}\right) \tag{2.19}$$

The RTE is subjected to the boundary condition for a surface that emits and reflects diffusely is given as

$$I_\eta\left(\vec{r}_w,\vec{s}\right)=\epsilon\left(\vec{r}_w\right)I_{b,\eta}\left(\vec{r}_w\right)+\frac{1-\epsilon\left(\vec{r}_w\right)}{\pi}\int_{\vec{n}.\vec{s'}<0}I_\eta\left(\vec{r}_w,\vec{s'}\right)|\vec{n}.\vec{s'}|\mathrm{d}\Omega' \tag{2.20}$$

where $I_{b,\eta}\left(\vec{r}_w\right)$ is the blackbody intensity of the wall surface, $\vec{n}$ is the normal vector outward to the wall surface, $\epsilon\left(\vec{r}_w\right)$ is the emissivity of the wall at position $\vec{r}_w$, $\vec{s'}$ is the incoming direction, Ω' is the solid angle in the direction $\vec{s'}$, and $\vec{n}.\vec{s'}$ is the cosine of the angle between the incoming direction $\vec{s'}$ and the surface normal vector $\vec{n}$. In terms of black surface, $\epsilon\left(\vec{r}_w\right)=1$, Equation (2.20) reduces to:

$$I_\eta\left(\vec{r}_w,\vec{s}\right)=I_{b,\eta}\left(\vec{r}_w\right) \tag{2.21}$$

The total heat flux of the medium is obtained by integrating the spectral heat flux over the spectrum as follows:

$$q=\int_0^\infty q_\eta\mathrm{d}\eta=\int_0^\infty\int_0^{4\pi}I_\eta\left(\vec{s}\right)\vec{s}\mathrm{d}\Omega\mathrm{d}\eta \tag{2.22}$$

The radiative source term is defined as the divergence of the radiative heat flux per unit wavenumber at a certain spectral position, established by the energy balance on an infinitesimal volume by

$$\nabla . q_\eta = \kappa_\eta \left(4\pi I_{b\eta} - \int_0^{4\pi} I_\eta \mathrm{d}\Omega \right) = \kappa_\eta \left(4\pi I_{b\eta} - G_\eta \right) \tag{2.23}$$

where, $G_\eta = \int_0^{4\pi} I_\eta \mathrm{d}\Omega$ is the incident radiation.

2.2.2 Solutions for the radiative transfer equation

The RTE for the radiative heat transfer for an absorbing, emitting and scattering medium is an integro-differential equation. The intensity, $I_\eta \left(\vec{r}, \vec{s} \right)$, in Equation (2.18) for a complicated case is a function of six independent variables, three for the spatial and two for the angular directions, and one for the wavelength. This makes solving the RTE equation become very complicated and the exact solution for the RTE can only be obtained for simple cases that are based on some simplifications, such as the radiative properties being assumed wavelength independent and homogeneous, and the scattering being isotropic and one-dimensional [133–135]. The exact solutions are not practical and impossible for engineering applications which are multi-dimensional, have an inhomogeneous medium and have spectral properties [72]. Consequently, numerous approximate solutions have been developed that can be applied to practical applications. Different methods for solving the RTE in the combustion systems can be found in the reviews [72, 133]. In this study, only some approximate methods that are preferred in commercial software for the prediction of fluid flows, chemical reactions and heat transfer, especially for three-dimensional simulations, such as the Discrete Ray Tracing Method (DRTM), spherical harmonics and Discrete Ordinates (DO) methods, are discussed

2.2.2.1 Spherical harmonics method

The spherical harmonics (P_N) method converts the complicated RTE into a set of simple partial differential equations (PDE) which can be solved using a standard

PDE solution packages [136]. The radiative intensity, $I(\vec{r},\vec{s})$, in Equation (2.18) is expressed in terms of a two-dimensional generalized Fourier series as [133, 137]

$$I(\vec{r},\vec{s}) = \sum_{l=0}^{\infty} \sum_{m=-l}^{l} I_l^m(\vec{r})\, Y_l^m(\vec{s}) \tag{2.24}$$

where $I_l^m(\vec{r})$ are position-dependent coefficient functions that need to be determined, $Y_l^m(\vec{s})$ are angularly dependent normalized spherical harmonics given by

$$Y_l^m(\vec{s}) = (-1)^{(m+|m|)/2} \left[\frac{(l-|m|)!}{(l+|m|)!}\right]^{1/2} e^{im\psi} P_l^{|m|}(\cos\theta) \tag{2.25}$$

where $P_l^{|m|}$ is the associated Legendre polynomials, θ and ψ are the polar and azimuthal angles that describe to the direction $\vec{s}$, respectively.

The series in Equation (2.24) can be approximated by truncating to a limited number of terms N. By this way, the intensity $I_l^m(\vec{r})$, which are functions of space, are replaced by $(N+1)^2$ functions I_l^m, which are only functions of space. The limited number N is known as the order of the approximation, namely P_N. Reducing the the number of first-order partial different equations by the P_N approximations has been obtained by [136, 138], with a relatively small set, $N(N+1)$, of second-order elliptic partial differential equations. In practical applications, a finite value of N are employed, such as P_1 and P_3 [72]. The low-order approximations, for example the P_1 approximation, usually poorly describes media that have a strong nonisotropic intensity distribution, especially in an optically thin media within nonisothermal enclosures [139]. The P_3 approximation can yield accurate results for environments having optical thickness up to 0.5 and for anisotropic radiative media, but it is much more computational intensive. The two systems of boundary conditions, namely the Mark and Marshark boundary conditions, have been proposed to apply for the spherical harmonics method. The Mark boundary is preferred for the high order approximation (N>3), while the Marshark boundary gives better results for the lower order approximations, such as the P_1 and P_3 approximations [133].

The accuracy of the spherical harmonics method can be substantially improved when optimized values are employed in the boundary condition, and this

can be found in the studies [140, 141]. While other attempts have focused on enhancements or modifications to the differential approximations to make it reasonably accurate for a variety of conditions, such as the modified differential approximation (MDA) [142] and the improved differential approximation (IDA) [143], or the recent advanced differential approximation (ADA) [139].

The P_1 approximation is the simplest case of the general P_N method, and therefore is one of the most popular methods because of its simplicity and it requires much less computational effort [133]. Another advantage of the P_1 model is that it can take into account the scattering and the radiative exchange with particles in a relatively simple manner [144]. It can work reasonably well in combustion applications with a large optical thickness, but the P_1 tends to over-predict the radiative fluxes from local heat sources [97]. Because of the limitation of the P_1 model, namely the inaccuracy under an optically thin media, the application of this model is mainly found in large-scale furnace calculations [60]. Under the oxy-fired condition, the optical thickness is often higher compared to the air-fired condition for the same geometry so if the P_1 is selected for the air condition that satisfies the optical thickness it will be applicable for the oxy-fired condition. Some CFD studies have applied the P_1 approximation for small-scale furnaces under the oxy-fired conditions [145–147]. The results from these studies show the limitations of this model in the optically thin media.

2.2.2.2 Discrete transfer method

The discrete transfer method (DTM) was developed by Lockwood and Shah [148] based on a combination of the features and advantages of the zone, flux and Monte Carlo methods. This method involves representative rays travelling in specific directions from one surface to another within a finite difference control volumes, in which the temperatures and radiative properties are assumed to be uniform.

For a selected direction, the integration of the transport equation, Equation (2.18), for the thermal radiation along a ray across a control volume in which

the temperatures and radiative properties are assumed to be uniform, yields [148]:

$$I\left(\vec{r}_{n+1},\vec{s}\right)=I\left(\vec{r}_{n},\vec{s}\right)e^{-\beta.\delta s}+S\left(1-e^{-\beta.\delta s}\right) \tag{2.26}$$

where $I\left(\vec{r}_{n},\vec{s}\right)$, $I\left(\vec{r}_{n+1},\vec{s}\right)$ are the intensity entering and leaving the control volume, respectively, $\beta\left(=\kappa+\sigma\right)$ is the extinction coefficient, and δs is the distance the ray travels in the control volume. The source function, S, is assumed to be constant and equal to the average over δs and it is given as

$$S=\left(1-\omega\right)I_{b}+\frac{\omega}{4\pi}\int_{0}^{4\pi}I\left(\vec{s'}\right)\Phi\left(\vec{s},\vec{s'}\right)\mathrm{d}\acute{\Omega} \tag{2.27}$$

where $\omega\left(=\sigma/\beta\right)$ is the scattering albedo.

In the DTM, the intensities are traced from the origin point on the boundaries to the destination point. The change in intensity along a specific direction is calculated using Equation (2.26) with the original intensity calculated from the boundary point using Equation (2.20). This process is repeated until it reaches the destination point. The number of rays or directions depends on the angular quadrature scheme selected.

Applying the DTM method for the statistical narrow band model can be found in the studies [149, 150], with different implemented methods. The non-correlated narrow-band solution, which is employed to solve the radiative heat transfer equation for a one-dimensional non-grey gas case in Chapter 3, is mentioned. The discretisation form of the RTE is expressed as follows:

$$\overline{I}_{\eta,i,n+1}=\overline{\tau}_{\eta,i,n\rightarrow n+1}\overline{I}_{\eta,i,n}+(1-\overline{\tau}_{\eta,i,n\rightarrow n+1})\overline{I}_{b\eta,n+1/2} \tag{2.28}$$

where the subscripts η,i and n stand for the wavenumber, direction of angular discretisation and spatial discretisation, respectively, $\overline{I}_{\eta,i,n}$ is the radiative intensity at the nodal point n in the angular direction i, $\overline{\tau}_{\eta,i,n\rightarrow n+1}$ is the transmission over the path from the nodal point n to $n+1$ in the angular direction i, being evaluated as $\exp\left(-\beta\left(x_{n+1}-x_{n}\right)/|\mu_{i}|\right)$, where x_{n}, x_{n+1} are the positions of the nodal points n and $n+1$, respectively, and μ_{i} is the directional cosin i, and $\overline{I}_{b\eta,n+1/2}$ is the blackbody intensity evaluated at the centre point between the nodal point n and $n+1$.

Once the non-grey radiation intensity is obtained, the radiative heat flux at the nodal point is calculated as follows:

$$q_n = \sum_{\Delta\eta} \left(\sum_{i=1}^{N_i} w_i \mu_i \bar{I}_{\eta,i,n} \right) \Delta\eta \tag{2.29}$$

where μ_i, w_i are the directional cosine and weight function associated with the i^{th} direction, and N_i is the number of ordinates. The S_8 quadrature scheme is employed in this study.

The radiative source term is then calculated as

$$-\frac{dq}{dx} = -\frac{q_{n+1} - q_n}{x_{n+1} - x_n} \tag{2.30}$$

The DTM is quite simple and can increase the accuracy of the scheme by increasing the number of rays and it can be applied to a wide range of optical thicknesses. The limitation of the DTM is that it is difficult to include the method to anisotropic scattering media. Therefore, some development of the DTM, including the scattering media, can be found in simple assumptions about the scattering, such as the isotropic scattering phase function [151], linear anisotropic scattering phase function [152–155] or the Henyey-Greenstein scattering phase function in a one-dimensional media [156].

2.2.2.3 Discrete Ordinates method

In the Discrete Ordinate (DO) method, the radiative heat transfer, Equation (2.18), is approximated by solving a finite number of discrete angular directions taken from a given quadrature scheme and the integral in the RTE is also approximated by this quadrature scheme over the solid angle. For each direction $\vec{s}_i$ $(i = 1 \div n)$ the RTE may be expressed as follows [133]:

$$\vec{s}_i . \nabla I_\eta(\vec{r}, \vec{s}_i) = \kappa_\eta(\vec{r}) I_{b\eta}(\vec{r}) - \beta(\vec{r}) I_\eta(\vec{r}, \vec{s}_i) + \frac{\sigma_{s,\eta}}{4\pi} \sum_{j=1}^{n} w_j I_\eta(\vec{r}, \vec{s}_j) \Phi(\vec{r}, \vec{s}_i, \vec{s}_j) \tag{2.31}$$

where w_j is the weight corresponding to the direction $\vec{s}_i$. The unit direction vector $\vec{s}_i$ is expressed from the directional cosines, μ_i, ξ_i, η_i as follows:

$$\vec{s}_i = \mu_i \vec{i} + \xi_i \vec{j} + \eta_i \vec{k} \tag{2.32}$$

The boundary condition is applied for only one boundary condition when the beam emanates from the wall ($\vec{n}.\vec{s}_i > 0$) and it is given as

$$I_\eta\left(\vec{r}_w, \vec{s}\right) = \varepsilon\left(\vec{r}_w\right) I_{b,\eta}\left(\vec{r}_w\right) + \frac{1-\varepsilon\left(\vec{r}_w\right)}{\pi} \sum_{\vec{n}.\vec{s}_j<0} w_j I_\eta(\vec{r}_w, \vec{s}_j)|\vec{n}.\vec{s}_j| \tag{2.33}$$

The heat flux of the medium is obtained by integrating the spectral heat flux over all directions is determined by

$$q_\eta(\vec{r}, \vec{s}) = \int_0^{4\pi} I_\eta(\vec{r}, \vec{s})\vec{s}\mathrm{d}\Omega \simeq \sum_{i=1}^{n} w_i I_\eta(\vec{r}, \vec{s_i})\vec{s}_i \tag{2.34}$$

and the incident radiation is approximated by

$$G = \int_0^{4\pi} I_\eta(\vec{r}, \vec{s})\mathrm{d}\Omega \simeq \sum_{i=1}^{n} w_i I_\eta(\vec{r}, \vec{s_i}) \tag{2.35}$$

Different quadrature schemes have been proposed for the Discrete Ordinate model, such as the level symmetric or S_N quadratures developed by Lathrop and Carlson [157], Truelove [158] and Fiveland [159], the T_N quadratures developed by Thurgood et al. [160] and the Double Cyclic Triangles quadrature scheme developed by Koch et al. [161].

The DO solution suffers from some shortcomings, such as the ray effect and false scattering [162]. The ray effect occurs due to the approximation to a finite number of discrete angular directions, then producing a loss in the heat fluxes in some regions, while the false scattering occurs when using the spatial discretisation practice, thus producing smeared intensity fields. The ray effects can be reduced by increasing the angular discretisation, selecting an accurate quadrature scheme and the false scattering can be reduced by using a finer mesh for the control volumes, and selecting more accurate spatial discretisation scheme. The evaluation of the spatial discretisation schemes and quadrature schemes for the DO method can be found in the studies [163] and [164], respectively. Although the two errors caused by the two different origins, they tend to have interactions with each other and this means that reducing the errors due to this effect can result in an increasing error in the other effects [165].

2.2.2.4 Consider method for solving the RTE

The selection of the most appropriate methods for solving the RTE for certain conditions depend on some factors, such as the optical thickness, the effects of the discrete phase and the possibility of including other treatments such as scattering. Some popular models, such as the DO, P_1 and DTRM models are available in commercial CFD codes. The DTRM, however, in the commercial software, such as the CFD software ANSYS Fluent that is employed in this study, is only applicable for cases with a non-scattering medium and therefore not suitable for coal combustion environments [146]. The DO and the P_1 models are the the most selected models when modelling combustion systems. The selection of the RTE methods is less dependent on the air or oxy-fired conditions compared to that of the radiative properties models [43]. As mentioned in Section 2.2.2.1, the P_1 method may produce errors in the results if used when the optical thickness is low [166]. In this thesis, the DO model is selected for all cases investigated. In the oxyfuel CFD simulations, the DO method has been used dominantly in the predictions of the radiation as reviewed by [60].

2.2.3 Radiative properties of the combustion gases

There are a number of proximate models that can be used to calculate the radiative properties of gases. In general, these models can be classified into three groups (in order of decreasing accuracy and complexity): line-by-line model, spectral band models and global models. In this study, some models are employed to describe the radiative properties of the gas phase, the line-by-line model is used as a benchmark to evaluate other models in one-dimensional cases, the Statistical narrow band model is employed as a benchmark in 3D enclosures to evaluate the global models (the Weighted sum of grey gas, Spectral line-based WSGG models) of the gas phase. The correlated-k model is used as a benchmark to evaluate the global models in the environment having the presence of the gas and particles.

2.2.3.1 Line by line model

The line by line calculations using spectral databases can yield the highest accuracy results for calculating the radiative heat transfer but are significantly computational expensive [167]. The spectral absorption coefficient of specie s at frequency η, $\kappa_{\eta.s}$, contributes by all spectral lines over the entire spectrum and is given as [168]

$$\kappa_{\eta.s} = N_s \sum_i F_i(\eta) S_i(T) \tag{2.36}$$

where N_s is the number density of the molecular s of the participating gases (CO_2 or H_2O), $F_i(\eta)$ is the line shape function of the i^{th} transition line and $S_i(T)$ is the line intensity. The intensity S_i at temperature T is determined from the correlation as [169]

$$S_i(T) = S_i(T_0) \frac{Q(T_0)}{Q(T)} \frac{exp(-c_2 E_i/T)}{exp(-c_2 E_i/T_0)} \frac{1 - exp(-c_2 \eta_{0,i}/T)}{1 - exp(-c_2 \eta_{0,i}/T_0)} \tag{2.37}$$

where T_0 is the reference temperature (in the HITEMP-2010 database, T_0=296 K), $Q(T)$ is the total internal partition sum at temperature T, and c_2 is the second radiation constant ($c_2 = hc/k_B \approx 1.43877$ cm K). The line intensity $S_i(T_0)$ and the lower-state energy E_i are obtained from a spectral database. $\eta_{0,i}(p)$ is the line centre of the transition after adjustment for pressure from the vacuum wavenumber as [170]

$$\eta_{0,i} = \eta_{vac} + p\delta \tag{2.38}$$

where δ is the air pressure-induced line shift, and η_{vac} is the vacuum wavenumber found in the spectral database.

The spectral line shape profile, $F_i(\eta)$, can be calculated from the Lorentz, Dropper and Voigt line profiles. The Lorentz profile dominates at higher pressures (p >1 bar). A spectral line shape profile that follows the Lorentz profile can be expressed as [171]

$$F_i(\eta) = \frac{\gamma_{L,i}}{\pi \left[(\eta_{0,i} - \eta)^2 + \gamma_{L,i}^2 \right]} \tag{2.39}$$

where η_0 is the centre of the line intensity, and $\gamma_{L,i}$ is the Lorentz half width at half maximum. The $\gamma_{L,i}$ can be calculated from the spectral database as a function of the self-broadened half width at half maximum, $\gamma_{self,i}$, the air-broadened half width is at half maximum, $\gamma_{air,i}$, and the temperature exponent n is as given by [171]

$$\gamma_{L,i} = p\left(\frac{T_0}{T}\right)^n \left(\gamma_{self,i} + (1 - Y_s)\,\gamma_{air,i}\right) \tag{2.40}$$

where Y_s is the mole fraction of the participating species, p, T are the total pressure and temperature, respectively, and T_0 is the reference temperature.

The Doppler broadening is dominant at low pressure (p=0.1 bar) and at high temperatures, the profile of the Doppler broadening has a shorter wavelength and higher frequency compared to that of the Lorentz profile. The absorption coefficient, described by the Doppler broadening, can be expressed as [133]

$$F_i(\eta) = \frac{1}{\gamma_{D,i}}\sqrt{\frac{ln2}{\pi}}exp\left[-(ln2)\left(\frac{\eta - \eta_{0,i}}{\gamma_{D,i}}\right)^2\right] \tag{2.41}$$

where $\gamma_{D,i}$ is the Doppler line half-width, and it is given by

$$\gamma_{D,i} = \frac{\eta_0}{c_0}\sqrt{\frac{2kT}{m}ln2} \tag{2.42}$$

where c_0 is the speed of light in a vacuum medium, $c_0 \equiv 2.99792458 \times 10^{10}$ cm s^{-1}, and m is the mass of the molecule.

The combination effects of the Doppler and Lorentz profiles is described by the Voigt profile as [133]

$$F_i(\eta) = \frac{\gamma_{L,i}}{\pi^{3/2}}\int_{-\infty}^{+\infty}\frac{e^{-x^2}dx}{\left(\eta - \eta_{0,i} - \frac{x\gamma_{D,i}}{\sqrt{ln2}}\right)^2 + \gamma_{L,i}^2} \tag{2.43}$$

with

$$x = \nu\sqrt{\frac{m}{2kT}} \tag{2.44}$$

The spectral absorption coefficient of a mixture can be calculated as a summation of the absorption coefficients of the component gases [172]. Absorption of coal combustion products can be expressed as

$$\kappa_{\eta,mix} = \kappa_{\eta,CO_2} + \kappa_{\eta,H_2O} \tag{2.45}$$

where κ_{η,CO_2}, κ_{η,H_2O} are the absorption of CO_2 and H_2O, respectively.

Calculations using the line-by-line model have been performed in some studies [168, 173–175]. These calculations are based on a detailed knowledge of every single spectral line from the spectral database, and therefore, this method can be seen as the most accurate model when calculating the radiative heat transfer. However, the radiative problem is solved in each spectral interval, for several million wavenumbers over the spectrum and this results in the main reason for the impractical application of this model. The LBL model is often only used as the benchmark to evaluate and generate the accuracy of other approximation models.

In combustion modelling, the high-temperature databases called HITEMP, and CDSD are often used for the LBL calculations to create a benchmark to evaluate other approximate models. More recent versions of these spectral databases are HITEMP-2010 [169], and CDSD-4000 [176]. HITEMP contains information similar to HITRAN, but contains data for many more hot lines for high temperatures applications while the CDSD is a high-temperature spectral database for the radiative properties of CO_2. Validation of some of these database using LBL calculations compared to experimental data, can be found in some studies [177–181]. Alberti et al. [181] showed that the spectral database HITEMP-2010 is an excellent database for calculating the radiative properties of the CO_2 and H_2O molecules in the temperature range 500-1770 K. Comparison of the number of spectral lines are shown in Table 2.1 where the HITEMP-2010 database and CDSD-4000 are developed for higher temperature use so they contain significantly more spectral lines than HITRAN-2016 [182], which is assumed to be valid for temperatures up to 600 K [183].

In the LBL calculations, many factors that are used can affect the accuracy of the results, such as the spectral database, spectral resolution, spectral range used and cutoff schemes used in order to save computational time. Some studies have combined the two databases for LBL calculation, HITEMP was employed for water vapor, while CDSD was used for carbon dioxide, which is considered

Table 2.1: A comparison of the number of spectral lines for HITEM-2010, CDSD-4000, and HITRAN-2016.

Molecule	Number of spectral lines		
	HITEMP-2010	CDSD-4000	HITRAN-2016
H_2O	111,377,777		313,787
CO_2	11,167,618	628,324,454	559,874

more reliable [184, 185]. With the HITEMP database, the HITEM-2010 has been recommended for using for the LBL model to create a benchmark [186]. In the range of temperature and pressure in coal combustion, there is not much difference in the results obtained when using the Lorentz profile and the Voigt profile, and the Lorentz lineshape can be applied in the calculations [181, 184, 187]. The spectral absorption coefficient, calculated in the LBL from Equation (2.36), by contributions of all the spectral lines over the spectrum, significantly increases the computational time and therefore eliminating the spectra lines that do not effect the results of the LBL calculations that are required to be considered. Some cutoff schemes have been proposed for the LBL calculations, such as the intensity cutoff (eliminating lines having weak intensity) [167, 185], the line-wing cutoff or cut-off distance (neglecting the contribution of the spectral lines far away from the spectral location considered) [188].

2.2.3.2 Statistical narrow band model

The statistical narrow band (SNB) model provides narrow-band transmissivity instead of an absorption coefficient. This model shows very good agreement with the line-by-line calculations [186, 189].

The narrow-band averaged transmissivity $\bar{\tau}$ in a narrow band $\Delta\eta$ may be expressed as [133]

$$\bar{\tau}_{\Delta\eta} = \exp\left(-\frac{\bar{W}}{\bar{\delta}}\right) \tag{2.46}$$

where $\bar{\delta}$ is an averaged line spacing over N lines in the spectral interval $\Delta\eta$. The average equivalent line width $\bar{W}$ can be defined by a probability density function $P(S)$ by Goody [190] and Malkmus [191],

$$\bar{W} = \int_0^\infty P(S)\, W(S)\, \mathrm{d}S \tag{2.47}$$

The SNB model, based on the exponential-tail S^{-1} line intensity distribution function of Malkmus [191] consisting of the Lorentz line, was found to be in good agreement with the LBL calculations [179, 189, 192]. The average transmissivity over the spectral interval $\Delta\eta$ of a uniform path length ℓ, at a total pressure p of a specie having mole fraction x is given as [193]

$$\bar{\tau}_\ell = \exp\left[-2\frac{\bar{\gamma}}{\bar{\delta}}\left(\sqrt{1 + xp\ell\bar{k}\frac{\bar{\delta}}{\bar{\gamma}}} - 1\right)\right] \tag{2.48}$$

where $\bar{\gamma}$, $\bar{\delta}$ and $\bar{k}$ are the average line Lorentz half-width, the average line spacing and the average line intensity to space ratio, respectively. The parameters $\bar{\delta}$ and $\bar{k}$ are defined by the LBL calculations, or the EM2C SNB parameters [185, 193]. The transmissivity of a mixture of combusting product, CO_2 and H_2O, are calculated as

$$\bar{\tau}_{\ell,mixture} = \bar{\tau}_{\ell,\mathrm{CO_2}} \cdot \bar{\tau}_{\ell,\mathrm{H_2O}} \tag{2.49}$$

The SNB gives the spectral transmissivity averaged over a narrow band so it is difficult to couple the SNB model to the general solution method of the radiative transfer equation. Also the disadvantage of the SNB model is that it requires a large number of bands, and therefore it is very expensive for computation. The SNB model was found to be suitable to create a benchmark for a multi-dimensional gas problem to evaluate the accuracy of the other models, where the LBL calculations are not feasible due to being computational expensive [63, 185, 194, 195].

2.2.3.3 Correlated-k method

The correlated-k method (CK) is an extension of the k-distribution, which is used for non-homogeneous and non-isothermal cases in atmospheric problem [196, 197]. The CK model formulates the radiative properties in terms of the absorption coefficient and therefore it is applicable to the general radiative heat transfer equation. The CK method divides the spectrum into narrow bands and assumes that the Plank function is constant and then the radiative heat transfer in each band is solved. In each band, the absorption coefficient field is reordered into a smoothly increasing function in order to avoid repeating calculating the same value of the absorption coefficient as in the line-by-line model.

In the narrow band, the average transmissivity only depend on the absorption coefficient and can be written as

$$\bar{\tau}_\eta(L) = \frac{1}{\Delta\eta}\int_{\Delta\eta} e^{-\kappa_\eta(\eta,\underline{\phi})L}d\eta = \int_0^\infty e^{-\kappa_\eta(\eta,\underline{\phi})L} f(\underline{\phi},k)dk \tag{2.50}$$

where $\underline{\phi}$ is the local state variables that affects the absorption coefficient, such as the temperature, pressure and the mole fractions of the participating species, $f(\underline{\phi},k)$ is the k-distribution function, which can expressed as

$$f(\underline{\phi},k) = \frac{1}{\Delta\eta}\int_{\Delta\eta} \delta\left(k - k_\eta(\eta,\underline{\phi})\right)d\eta \tag{2.51}$$

where $\delta(k - k_\eta(\eta,\underline{\phi}))d\eta$ is the Dirac delta function. The k-distribution function can be determined from the inverse Laplace transform $\mathscr{L}^{-1}$ from Equation (2.50) as

$$f(\underline{\phi},k) = \mathscr{L}^{-1}\left\{\bar{\tau}_\eta(L)\right\} \tag{2.52}$$

The accumulative k-distribution $g(\underline{\phi},k)$ is given as

$$g(\underline{\phi},k) = \int_0^k f(\underline{\phi},k')dk' \tag{2.53}$$

The transmissivity in Equation (2.50) is rewritten as

$$\bar{\tau}_\eta(L) = \int_0^\infty e^{-\kappa_\eta(\eta,\underline{\phi})L} f(\underline{\phi},k)dk = \int_0^1 e^{-k(\underline{\phi},g)L}dg \tag{2.54}$$

where $k(\underline{\phi}, g)$ is the inverse function of $g(\underline{\phi}, k)$ which represents the fraction of the spectrum whose absorption coefficients are less than the value of k and, therefore, $0 \leq g(\underline{\phi}, k) \leq 1$. The reordered absorption coefficient, $k(\underline{\phi}, g)$, is smoothly increasing function of g, and it can be approximated using an efficient Gauss quadrature scheme as

$$\bar{I}_{\Delta\eta} = \int_0^1 I_g dg = \sum_{j=1}^{M} w_j I_{gj} \tag{2.55}$$

where M, w_j are quadrature order and quadrature weights, respectively. The intensity for each quadrature point, I_{gj}, is calculated from the radiative transfer equation (RTE) for an absorbing, emitting and scattering medium in a homogeneous medium over the g space and it can be expressed as [198]

$$\begin{aligned} \frac{\mathrm{d}I_{g_j}(\vec{r},\vec{s})}{\mathrm{d}s} &= k(\underline{\phi}, g_j)\left(I_{b,\Delta\eta} - I_{g_j}(\vec{r},\vec{s})\right) \\ -\sigma_{s,\Delta\eta}\left(I_{g_j}(\vec{r},\vec{s}) - \frac{1}{4\pi}\int_{4\pi} I_g(\vec{r},\vec{s}')\Phi_\eta(\vec{r},\vec{s},\vec{s}')\mathrm{d}\Omega'\right) \end{aligned} \tag{2.56}$$

where $I_{b,\Delta\eta}, \sigma_{s\Delta\eta}, \Phi_\eta$ are the blackbody intensity, scattering coefficient and scattering phase function assumed as constants over interval $\Delta\eta$, respectively, and k_{g_j} is the reorder absorption coefficient at quadrature point g_j. The total intensity over the spectrum is obtained obtained from

$$I = \sum_{i}^{N} \Delta\eta \sum_{j}^{M} w_j I_{gj} \tag{2.57}$$

where N is the number of spectral bands, and M is the number of quadrature points used to calculate the integral in Equation (2.55). The number of spectral bands proposed for the CK model can be found in the studies [185, 199]. The effect of the quadrature schemes on the accuracy of the CK model in one- and three-dimensional enclosure was investigated by [194]. The number of quadrature, from 6 to 16 quadrature points when using Gaussian or Gauss-Lobatto quadrature, are proposed for accurate calculation of the CK model [200]. In many studies, seven point quadratures are widely proposed for the CK model based on the considerations of accuracy and computer time [185, 193, 201–203].

The CK method requires significant computational resources to be applied to the CFD calculations, therefore, it is computationally prohibitive for many practical combustion applications. Implementations of the CK model in 1 dimension cases [197], 2D case [204] and 3D [205] have shown to be in good agreement with the most accurate LBL calculations. Most of calculations of the radiative heat transfer up to date using the CK model have employed the database of Taine et al. [193] which uses the correlated-k assumption. Recently, a new update of the parameters for H_2O and CO_2 has been developed to use for the CK model [185], which are generated from line by line calculations using new spectroscopic databases, the CDSD-4000 spectral database for CO_2 and the HITEMP-2010 database for H_2O, over a wide range of temperature and spectral ranges. A comparison of the two database sets, HITEMP-2010 and CDSD-4000 databases, for the CK model was performed in a 2D enclosure by [204] and he showed that the updated parameters [185] provide better accuracy than the old database [193].

2.2.3.4 Weighted sum of grey gas model

The Weight Sum of Grey Gas (WSGG) model is one of the non-grey gas treatments that has received the most attention in engineering applications, and it treats the non-grey gas as a finite number of grey gases N_g, having constant absorption coefficients κ_i and one transparent gas ($\kappa_0 = 0$). The total emissivity of an isothermal path length L is expressed as

$$\epsilon\left(T, L\right) = \sum_{i=0}^{N_g} a_i\left(T\right)\left(1 - e^{-\kappa_i P_a L}\right) \tag{2.58}$$

where a_i, κ_i are the emissivity weighting factors and absorption coefficient for the i^{th}grey gas, respectively. The a_i and κ_i can be obtained from correlations in which a_i depends on the mole fraction and temperature while the absorption coefficient κ_i depends only on the mole fraction. P_a is the sum of partial pressures of the absorbing gases, such as CO_2, H_2O, CO, etc. With the two most important combusting gases, CO_2 and H_2O, the total pressure P_a is calculated as

$$P_a = \left(Y_{CO_2} + Y_{H_2O}\right) P \tag{2.59}$$

where P is the total pressure of the combusting environment, and Y_{CO_2}, Y_{H_2O} are the molar fractions of CO_2 and H_2O, respectively.

The radiative transfer equation (RTE) for the i^{th} grey gas through a medium of a mixture of the non-grey gases and grey particles can be expressed as [206]

$$\frac{\mathrm{d}I_i\left(\vec{r},\vec{s}\right)}{\mathrm{d}s} = -\left(k_{g,i}+k_p+\sigma_p\right)I_i\left(\vec{r},\vec{s}\right)+a_{g,i}k_{g,i}I_{b,g}\left(\vec{r}\right)+a_{p,i}k_pI_{b,p}\left(\vec{r}\right) + \frac{\sigma_p}{4\pi}\int_{4\pi} I_i\left(\vec{r},\vec{s}\,'\right)\phi\left(\vec{s}.\vec{s}\,'\right)d\Omega' \tag{2.60}$$

where $k_{g,i}, k_p$ are the absorption coefficients of the i^{th} grey gas and grey particles, and $a_{g,i}, a_{p,i}$ are the emissivity weighting factors for the gas and particles, respectively. The boundary condition used for the non-grey WSGG with diffusely emitting and reflecting surfaces is gives as

$$I_{w,i}\left(\vec{r}_w,\vec{s}\right) = a_i\epsilon\left(\vec{r}_w\right)I_b\left(\vec{r}_w\right)+\frac{1-\epsilon\left(\vec{r}_w\right)}{\pi}\int_{\vec{n}\vec{s}'<0} I_j\left(\vec{r}_w,\vec{s}'\right)|\vec{n}.\vec{s}'|\mathrm{d}\Omega' \tag{2.61}$$

where $I_{w,j}$ is the radiation intensity for gas i leaving the boundary. The total radiation intensity is then found by adding the heat fluxes of the gray gases as [200]

$$I(L) = \sum_{i=1}^{N_g} I_i(L) \tag{2.62}$$

The simplest case of the WSGG model are often used in combustion modelling by assuming the medium is grey. In this case, the properties of gas are presented by the effective absorption coefficient and the number of the RTE reduced to one. The effective absorption coefficient of the grey gas is calculated from total the emittance, ϵ, and pathlength, s, as [207]

$$\kappa_g = -\frac{1}{s}\ln(1-\epsilon) \tag{2.63}$$

where ε is determined by Eq. (2.58) with the path length, s, being considered as a mean beam length of the domain. s is often determined from the volume of the domain, V, and the internal surface of the domain, A, as [208]

$$s = 3.6\frac{V}{A} \tag{2.64}$$

The RTE for the non-grey WSGG model, Equation (2.18), is rewritten for the grey gas WSGG model, with weighting factors for the gas and particle being unity, as

$$\frac{\mathrm{d}I\left(\vec{r},\vec{s}\right)}{\mathrm{d}s} = -\left(\kappa_g+\kappa_p+\sigma_p\right)I\left(\vec{r},\vec{s}\right)+\kappa_g I_{b,g}\left(\vec{r}\right)+\kappa_p I_{b,p}\left(\vec{r}\right) + \frac{\sigma_p}{4\pi}\int_{4\pi} I\left(\vec{r},\vec{s}\,'\right)\Phi\left(\vec{s}.\vec{s}\,'\right)\mathrm{d}\Omega' \tag{2.65}$$

The first WSGG model applied for a non grey participate media was proposed by Hotel and Sarofim [209] in the form of the zonal method and it has been demonstrated by Modest [210] for application as an arbitrary solution method. A set of fitted coefficients for the WSGG model, namely, absorption coefficients and weighting factors, for three grey gases and one transparent gas has been proposed by Smith et al. [61] through fitting the model to the total emissivity and absorptivity values obtained from the exponential wide-band mode (EWBM), with temperatures within the range 600 to 2400 K and partial pressure-path lengths from 0.001 to 10.0 atm-m. Recent refinements of this model for air-fuel combustion has been performed by Yin [211] for a wider temperature, pressure path length and mole fraction range and by Dorigon et al. [67] using the HITEMP 2010 data. However, these models were obtained at some specific mole fraction ratios of H_2O and CO_2, which limits its use for application in oxyfuel conditions.

Many investigations have been performed to improve the WSGG model for better application under oxyfuel conditions, such as Yin et al.[62] who extended the WSGG model for a wider range of discrete ratios and by Johansson et al. [63] for a variant wide range of CO_2 and H_2O ratios that present better radiative properties of the gas products for both air and oxyfuel combustion. Kangwanpongpan et al. [64] improved the WSGG model that is fitted from the HITEMP-2010 data for a wide range of CO_2 and H_2O ratios. Some recent developments of the WSGG model for oxyfuel combustion has been performed by Bordbar et al. [66] and Cassol et al. [212]. Table 2.2 shows the WSGG models that have been developed for air and oxy-fired conditions.

The improvement of the WSGG models for oxyfuel conditions based on the wide range of molar fraction ratios of H_2O to CO_2, spectral database and model

Table 2.2: Some representative comparisons of WSGG models that have been developed for air and oxyfuel conditions.

Models developed	Numbers grey gas	Model/ data fitting	Ranges af parameters	
			T(K), P(bar m)	mole ratio
Smith et al. [61] used for air	3+1	EWBM	T(600-2400) P(0.001-10)	1, 2
Yin et al. [62] used for air, oxy	4+1	EWBM	T(500-3000) P(0.001-60)	0.125, 0.25, 0.75, 1, 2, 4
Jonhanson et al. [63] used for air, oxy	4+1	SNB, EM2C 1997	T(500-2500) P(0.01-60)	(0.125 - 2)
Kangwanpongpan et al. [64] used for air, oxy	4+1	LBL, HITEMP 2010	T(400-2500) P(0.001-60)	(0.125 - 2)
Yin [211] used for air	4+1	EWBM	T(500-3000) P(0.001-60)	0.05, 1, 2
Borbar et al. [66] used for air, oxy	4+1	LBL, HITEMP 2010	T(300-2400) P(0.01-60)	(0.01 - 4)
Dorigon et al. [67] used for air	4 +1	LBL, HITEMP 2010	T(400-2500) P(0.001-10)	1, 2
Cassol et al. [212] used for air, oxy	(4 +1)× (4+1)	LBL, HITEMP 2010	T(400-2500) P(0.001-10)	(0.01 - 4)

selected for fitting. Evaluations of the WSGG models can be found in some studies reviewed by Kez et al. [213], see in Table 2.2. From this study, the WSGG model of Kangwanpongpan et al. [64] and Borbar et al. [66] are recommended for CFD simulations of practical oxyfuel applications with large pressure path-length and molar ratios of H_2O to CO_2 between 0.01 and 0.5.

2.2.3.5 Spectral line-based WSGG model

The SLW model calculates the radiative heat transfer based on the absorption coefficient which can be used with an arbitrary solution method for the radiative heat transfer equation (RTE). In this method, the absorption cross-section range is divided into n intervals by the supplemental absorption cross sections $\widetilde{C}_j$, $j = 0, 1, \ldots, n$, with each interval between $\widetilde{C}_{(j-1)}$ and $\widetilde{C}_j$ being presented for the j^{th} grey gas having absorption across the section $C_j = \sqrt{\widetilde{C}_{j-1}\widetilde{C}_j}$. The radiative transfer equation for the j^{th} grey gas in the SLW model may be written as [214]

$$\frac{\mathrm{d}I_j}{\mathrm{d}s} = -\kappa_j I_j + a_j \kappa_j I_{b,j}, \;\; j = 0, 1, 2, ..., n \tag{2.66}$$

where k_j, and a_j are the absorption coefficient and blackbody weights of grey gas j, respectively. These parameters are defined for a single absorbing gas and defined as [215]

$$\kappa_j = NYC_j \tag{2.67}$$

$$a_j = F\left(\widetilde{C}_j, T_g, T_b, p, Y\right) - F\left(\widetilde{C}_{j-1}, T_g, T_b, p, Y\right) \tag{2.68}$$

The weighting factor for the transparent gas is expressed as

$$a_0 = F\left(\widetilde{C}_{min}, T_g, T_b, p, Y\right) \tag{2.69}$$

where N, Y are the gas molar density and molar fraction of single gas , respectively. $F\left(\widetilde{C}_j, T_g, T_b, p, Y\right)$ is the absorption line blackbody distribution function (ALBDF) corresponding to $\widetilde{C}_j$ at the gas temperature T_g, blackbody temperature T_b, gas total pressure p, and the gas molar fraction Y. The supplement cross-section can be equally logarithmically spaced [216] as follows:

$$\widetilde{C}_j = C_{min}\left(C_{max}/C_{min}\right)^{j/n} \tag{2.70}$$

The primary basis in the SLW model is the absorption line blackbody distribution function $F\left(\widetilde{C}_j, T_g, T_b, p, Y\right)$ which is defined as the fraction of the blackbody radiation power that is emitted in the spectral regions where the spectral

absorption across-section, C_η is below the prescribed value C [217]

$$F(C, T_g, T_b, p, Y) = \frac{1}{\sigma T_b^4} \int_{\{\eta: C_\eta(T_g,p,Y)<C\}} E_{b\eta}(T_b) \mathrm{d}\eta \tag{2.71}$$

where T_b is the blackbody source temperature, T_g is the gas temperature, p is the total pressure, Y is the mole fraction of species of interest (H_2O, CO_2), and $E_{b\eta}$ is the spectral emissive power. The ALBDF is an increasing monotonic function of the variable C, varying between 0 and 1. It can be calculated directly using spectroscopic data or more convenient correlations for H_2O [217] and for CO_2 [218]. In this study, the ALBDF for H_2O, CO_2 [219] based on the HITEMP-2010 spectroscopic database, is valid for temperatures ranging from 400 K to 3000 K and the total pressures ranging from 0.1 atm to 50 atm is employed. In terms of a mixture, the ALBDF can be calculated based on different methods, such as the direct, convolution, superposition and the multiplication methods and the full details of these methods for the SLW can be found in [220]. The ALBDF for a mixture of coal combustion products, mainly H_2O and CO_2, can be calculated based on the multiplication approach [220]:

$$F_{mix}\left(\widetilde{C}_j, T_g, T_b, p, Y\right) = F_{\mathrm{CO_2}}\left(\frac{\widetilde{C}_j}{Y_{\mathrm{CO_2}}}, T_g, T_b, p, Y\right) F_{\mathrm{H_2O}}\left(\frac{\widetilde{C}_j}{Y_{\mathrm{H_2O}}}, T_g, T_b, p, Y\right) \tag{2.72}$$

where $Y_{\mathrm{CO_2}}$,$Y_{\mathrm{H_2O}}$ are the molar fraction of CO_2 and H_2O, respectively. The local weights for grey gas j are calculated as follows:

$$a_j = F_{mix}\left(\widetilde{C}_j, T_g = T_{ref}, T_b = T_{loc}, p, Y\right) - F_{mix}\left(\widetilde{C}_{j-1}, T_g = T_{ref}, T_b = T_{loc}, p, Y\right) \tag{2.73}$$

The local absorption coefficients in case using the multiplication methods is calculated as [220]

$$\kappa_j = N\sqrt{\widetilde{C}_{j-1}^{loc}\widetilde{C}_j^{loc}} \tag{2.74}$$

where N is the molar density of the mixture of gases, and $\widetilde{C}_j^{loc}$ are the local supplemental cross-sections found from the implicit relation as follows:

$$\begin{aligned} &F_{mix}\left(\widetilde{C}_j^{loc}, T_g = T_{loc}, T_b = T_{ref}, p_{loc}, Y_{loc}\right) = \\ &F_{mix}\left(\widetilde{C}_j, T_g = T_{ref}, T_b = T_{ref}, p_{ref}, Y_{ref}\right) \end{aligned} \tag{2.75}$$

In this study, the absorption cross-section range is selected for CO_2 and H_2O based on [219], with $C_{min} = 10^{-4}\text{m}^2/\text{mol}$, $C_{max} = 600\text{m}^2/\text{mol}$. The same number of intervals for the absorption cross-section of CO_2 and H_2O examined, corresponding the number of grey gas are 5, 10, and 15.

The SLW is considered to be the best choice, in comparison with the SNB, SNBCK, and WSGG models, for multi-dimensional radiation heat transfer calculations based on the considerations of computation time and accuracy [221]. Increasing the number of grey gases in the SLW can achieve higher accuracy, however, it will requires more computational time. Many implementations of the SLW model in the 1D and 2D cases [219, 220, 222–224] have shown that the number of grey gases from 10 to 25 can achieve a good accurate. In 3D cases, because of computationally spend required, from 10 to 15 grey gases are often selected [205, 225–227].

2.2.4 Radiative properties of particles

The presence of small particles, pulverised coal, char, fly ash and soot, in coal fired-furnaces have a significant impact on the radiative heat transfer compared to that of the gases [206, 228]. The radiative intensity of the electromagnetic wave through these suspended particles can change by absorption and scattering. The level of interaction between the wave and particles depend on the size, shape, particle size distribution and the change in status of these items during the combustion process. In pulverised coal combustion, it is reasonable to employ the Mie theory for calculating the radiative properties of a cloud particle with assuming that the particles are homogeneous and spherical [228]. In the Mie theory, the radiative properties of a spherical particle having radius r in the interaction with the electromagnetic wave having a wavelength λ can be defined using the complex index of refraction, m, and the particle size parameter, x, as follows:

$$m = n - ik \tag{2.76}$$

$$x = \frac{2\pi r}{\lambda} \tag{2.77}$$

In this section, the radiative properties of a particle, cloud of particles and solutions for radiative properties of particle are discussed.

2.2.4.1 The Mie theory for the radiative properties of a single particle

The interaction between the incident wave and a particle is expressed in terms of the absorption cross-section, C_{abs}, and the scattering cross-section, C_{scat}. The total absorption and scattering may be expressed in the extinction cross-section, C_{ext}, as

$$C_{ext} = C_{abs} + C_{sca} \tag{2.78}$$

The cross-sections are often expressed by dimensionless parameters, known as efficiency factors, by dividing the cross-section items with the projected surface area, πr^2, as follows:

$$Q_{ext} = Q_{abs} + Q_{sca} \tag{2.79}$$

According to the Mie theory, the scattering and extinction efficiencies are expressed in the following forms as [133]

$$Q_{sca} = \frac{2}{x^2} \sum_{n=1}^{\infty} (2n+1) \left(|a_n|^2 + |b_n|^2 \right) \tag{2.80}$$

$$Q_{ext} = \frac{2}{x^2} \sum_{n=1}^{\infty} (2n+1) \Re \left(a_n + b_n \right) \tag{2.81}$$

where a_n, b_n are the Mie scattering coefficients.

The scattering phase function, which describes the the fraction of the energy that is scattered into a given scattering angle, Θ, is expressed as

$$\Phi(\Theta) = 2 \frac{|S_1(\Theta)|^2 + |S_2(\Theta)|^2}{x^2 Q_{sca}} \tag{2.82}$$

where $S_1(\Theta), S_2(\Theta)$ are the complex amplitude functions expressed as

$$S_1(\Theta) = \sum_{n=1}^{\infty} \frac{2n+1}{n(n+1)} \left[a_n \pi_n(\cos\Theta) + b_n \tau_n(\cos\Theta) \right] \tag{2.83}$$

$$S_2(\Theta) = \sum_{n=1}^{\infty} \frac{2n+1}{n(n+1)} \left[b_n \pi_n (cos\Theta) + a_n \tau_n (\cos\Theta) \right] \tag{2.84}$$

The directional scattering behaviour can be expressed by simplifying the averaging cosine of the scattering angles, called the asymmetry factor, and defined as

$$g = \overline{\cos\Theta} = \frac{1}{4\pi} \int_{4\pi} \Phi(\Theta) \cos\Theta d\Omega \tag{2.85}$$

where g is the asymmetry factor, having a value in the range -1 to +1. A negative value of g shows backward scattering, a positive value shows forward scattering and g=0 has isotropic scattering (Φ=1). The asymmetry factor can be obtained directly from the Mie theory.

The scattering phase function from Equation (2.82) is complicated when applying in the radiative transport equation because of the complicated nature of Equations (2.83) and (2.84), and a large number of repeated calculation for every scattering angle, Θ. Therefore, many approximations for the scattering phase function has been introduced. The Henyey-Greentein phase function can be applied for the case with strong forward-scattering, and is given by [229]

$$\Phi_{HG}(\Theta) = \frac{1-g^2}{[1+g^2-2g\cos\Theta]^{3/4}} \tag{2.86}$$

where g is the asymmetry factor. The Henyey-Greenstein phase function is still complicated in many calculations [133]. One of the most popular approximation is the Dirac-delta function applied for highly forward-scattering [230]

$$\Phi(\Theta) = 2f\delta(1-\cos\Theta) + (1-f)\Phi^*(\cos\Theta) \tag{2.87}$$

where f is the forward scattering fraction, and Φ^* is the normalised phase function and it may be presented by a series of Legendre polynomials as [230]

$$\Phi^*(\Theta) = \sum_{n=0}^{M} A_n^* \Phi(\cos\Theta) \tag{2.88}$$

The coefficient A_n^* can be determined from the angular distribution coefficient A_n and the forward scatterign fraction f as

$$(1-f) A_n^* = A_n - (2n+1) f \tag{2.89}$$

The Dirac-delta function for the isotropic ($M = 0$) and linear-anisotropic ($M = 1$) cases are expressed as follows:

$$\Phi(\Theta) = 2f\delta(1 - \cos\Theta) + (1 - g) \tag{2.90}$$

$$\Phi(\Theta) = 2f\delta(1 - \cos\Theta) + (1 + 3g'\cos\Theta) \tag{2.91}$$

respectively, where g' is the asymmetry factor, determined as

$$g' = \frac{g - f}{1 - f} \tag{2.92}$$

A representative comparison between the Mie theory and other approximations, the Henyey-Greenstein phase function, the Dirac-delta function for the isotropic ($M = 0$) and linear-anisotropic ($M = 1$) for coal and ash particles are shown in Fig. 2.2 for coal particles having a complex index of refraction, $m = 2.1 - 1.12i$, size parameter x=20, and for an ash particle having $m = 1.5 - 0.2i$, x=5.

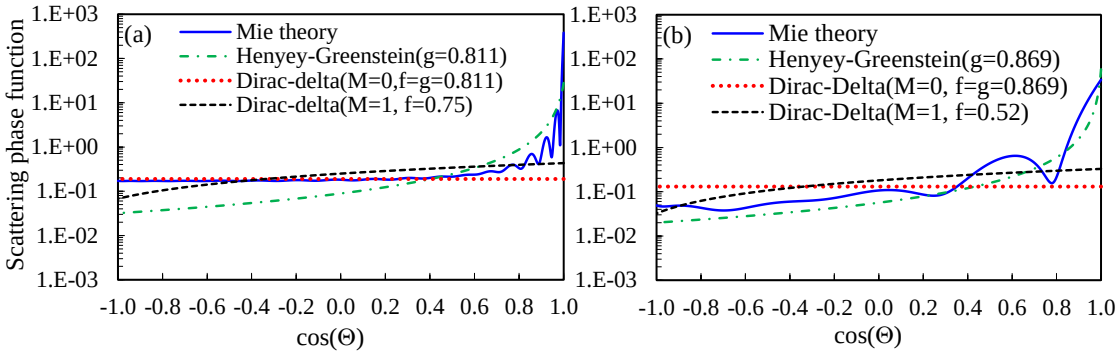

Figure 2.2: Scattering phase function for (a) coal, m=2.1-1.12i, x=20, and (b) ash, m=1.5-0.2i, x=5.

If the spherical particle is very small ($x = \frac{2\pi r}{\lambda} << 1$), for example soot particle having a size range 5nm to 80nm, the scattering and extinction efficiencies can defined through the Rayleigh theory as

$$Q_{sca} = \frac{8}{3}\left|\frac{m^2 - 1}{m^2 + 2}\right|^2 x^4 \tag{2.93}$$

$$Q_{ext} \approx \Im\left\{\frac{m^2-1}{m^2+2}\right\} x \approx Q_{abs} \tag{2.94}$$

where $\Im$ is the imaginary part. Due to $x << 1$, the scattering efficiency can be neglected in comparison to the absorption efficiency.

2.2.4.2 Radiative properties of a cloud of particles

Spectral radiative properties of a particle cloud, spectral absorption κ_λ, scattering coefficient σ_λ, can be calculated as [133]

$$\kappa_\lambda(m_\lambda, N_0) = \int_0^\infty Q_{a\lambda}(D, \lambda, m_\lambda)\frac{\pi D^2}{4} f_n(D) N_0 dD \tag{2.95}$$

$$\sigma_\lambda(m_\lambda, N_0) = \int_0^\infty Q_{s\lambda}(D, \lambda, m_\lambda)\frac{\pi D^2}{4} f_n(D) N_0 dD \tag{2.96}$$

where $Q_{a\lambda}(D, \lambda, m_\lambda)$, $Q_{s\lambda}(D, \lambda, m_\lambda)$ are absorption, scattering efficiencies of particle having diameter D, respectively. $f_n(D)$ is the number density function and $f_n(D)dD$ is the particle number fraction in the size range D to $D + \mathrm{d}D$ as

$$f_n(D)\mathrm{d}D = \frac{\mathrm{d}N}{N_0} \tag{2.97}$$

where $\mathrm{d}N$ is the number of particle in the diameter range of D to $D + \mathrm{d}D$, and N_0 is the total number of particles per unit volume.

In the combustion literature, some particle size distribution functions are used it to fit the experimental data, namely, modified gamma distribution, log-normal distribution and Rosin-Rammler distribution. The modified gamma distribution can be expressed as [231]

$$f_n(D) = aD^\alpha \exp\left(-bD^\gamma\right), 0 \leq D < \infty \tag{2.98}$$

where the four constants a, α, b and γ are positive and real, and α is chosen to be an integer. These constants depend on each other and they are related to quantities in the frequency distribution, which can be determined by experimental measurement. The modified gamma distribution distribution reduces to the Gamma distribution if $\gamma = 1$.

The log-normal distribution can be expressed as [232]

$$f_n(D) = \frac{1}{\sqrt{2\pi}\sigma_u D}\exp\left[-\frac{1}{2}\left(\frac{\ln D - \ln D_M}{\sigma_u}\right)^2\right] \tag{2.99}$$

where D_M is the median diameter, σ_u is the log of the ratio of the diameter for which the cumulative distribution curve has the value range 0.841 to the D_M.

In the Rosin-Rammler distribution, the cumulative mass fraction of the particles having a diameter smaller than D is given by [233]

$$Y_D = 1 - \exp\left(\frac{D}{D_m}\right)^n \tag{2.100}$$

where n is the constant describing a uniform distribution of particles, D_m is the characteristic particle diameter, defined as the diameter at which $Y_D = 1/e = 0.632$.

The Rosin-Rammler distribution can be expressed in terms of the mass fraction of particles having a diameter D as [234]

$$f_m(D) = \frac{n}{D_m}\left(\frac{D}{D_m}\right)^{n-1}\exp\left[-\left(\frac{D}{D_m}\right)^n\right] \tag{2.101}$$

where n is spread parameter, and D_m is the mean diameter of particles. The relation between the number density function and the mass distribution function may be expressed as

$$f_m(D) = \frac{N_0 m(D)}{M_0} f_n(D) \tag{2.102}$$

where N_0, M_0 are the total number of particles and the total mass of the particles per unit volume, respectively, and $m(D)$ is the mass of the particle having diameter D.

Fig. 2.3 shows the particle distribution obtained from laboratory measurements on flyash collected at a middle-field location of a power plant electrostatic precipitator as reported by Goodwin and Mitchner [235] and the distribution of the particles use the log-normal distribution with $\sigma_u = 0.747$, $\ln(D_M) = -0.214$, and the Rosin-Rammler distribution, with the mean diameter of the particles $D_m = 3.5$ μm, and the spread number $n = 1.65$.

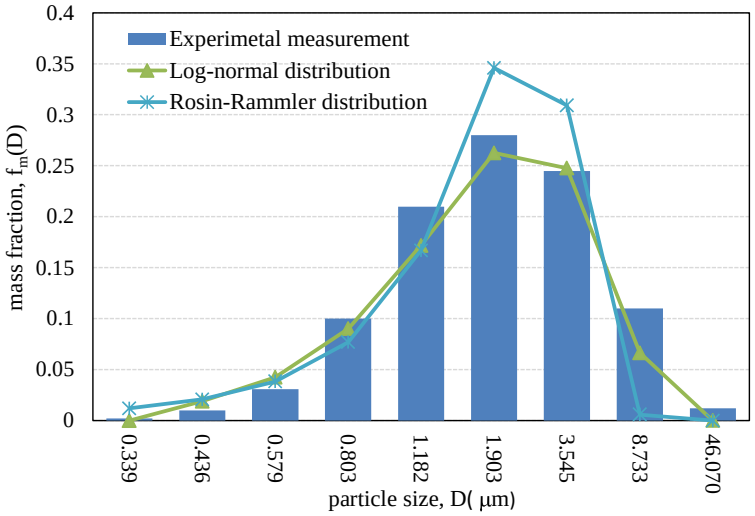

Figure 2.3: Representive comparison between a particle distribution obtained experimentally by [235], the log-normal distribution [235] with $\sigma_u = 0.747$, $\ln(D_M) = -0.214$, and the Rosin Rammler distribution with $D_m = 3.5$ μm, $n = 1.65$.

For a given particle size distribution, some average diameters of particles can be used in calculated properties of a cloud of particles. In a coal combustion process, the area averaged mean diameter D_{32}, or the Sauter averaged diameter, is often used as follows [232, 235, 236]:

$$D_{32} = \frac{\int_0^\infty D^3 f_n(D)\,\mathrm{d}D}{\int_0^\infty D^2 f_n(D)\,\mathrm{d}D} \tag{2.103}$$

The radiative properties, absorption and scattering coefficients (κ_λ), for a given size distribution (σ_λ), can be calculated from the averaged diameter by:

$$\kappa_\lambda = \frac{3}{2}\frac{V_p}{D_{32}}\overline{Q}_{a\lambda} \tag{2.104}$$

$$\sigma_\lambda = \frac{3}{2}\frac{V_p}{D_{32}}\overline{Q}_{s\lambda} \tag{2.105}$$

where V_p is the volume of the particles per unit volume, and $\overline{Q}_{a\lambda}, \overline{Q}_{s\lambda}$ are the spectral average absorption and scattering efficiencies for a cloud of particles, respectively, and these are given by

$$\overline{Q}_\lambda = \frac{\int_0^\infty Q_\lambda(D) D^2 f_n(D)\mathrm{d}D}{\int_0^\infty D^2 f_n(D)\mathrm{d}D} \tag{2.106}$$

The average scattering phase function is found from the relation

$$\overline{\Phi}_\lambda(\theta) = \frac{\int_0^\infty Q_{s\lambda}(D)D^2\Phi_\lambda(D,\theta)f(D)\mathrm{d}D}{\int_0^\infty Q_{s\lambda}(D)D^2 f(D)\mathrm{d}D} \tag{2.107}$$

The Planck mean properties of the particles are defined as

$$\overline{Q}_p = \frac{1}{\sigma T^4}\int_0^\infty \overline{Q}_\lambda(D)I_{\lambda b}\mathrm{d}\lambda \tag{2.108}$$

where $I_{\lambda b}$ is the spectral blackbody emissive power at the incident temperature T^4.

For a cloud of the soot particle, the absorption coefficient does not depend on the particle distribution and be calculated based on the volume fraction of soot, f_v, as [133]

$$\kappa_\lambda = -\Im\left\{\frac{m^2-1}{m^2+2}\right\}\frac{6\pi f_v}{\lambda} \tag{2.109}$$

2.2.4.3 Optical constants of the particles

The optical properties, spectral absorption ($Q_{a\lambda}$), scattering ($Q_{s\lambda}$) efficiencies and scattering phase function (Φ_λ) of a particle can be obtained by using the Mie theory, assuming that the particle is a homogeneous and isotropic sphere and requires the specification of the size parameter, x, and the complex refractive index, m, of the particle material. The complex refractive index, $m = n + ik$, of the particle material depends on the wavelength, composition and temperature of the particle [133, 235, 237]. The real part n of the complex refractive index is referred to as the refractive index and the imaginary part k is referred to as the absorption index. The optical constants n and k are the main differences between the particle types that can be measured for specific types of particles. In this section, different measurement data for the optical constants of the coal and fly-ash particles are discussed.

The characterisation of fly ash is complicated and varies from coal to coal and for a specific coal the properties fly ash particles are also different from particle to particle [238, 239]. Several measurement data for the optical constants of different types of coal fly ash have been obtained [240–245]. From these studies, similar

results for the real part n from 1.4 to 1.7 have been found. However, the imaginary parts showed considerable uncertainty between these studies with the range of the real part value being from 0.005 to 0.05. The uncertainty in the imaginary parts of the ashes has been explained by the differences in the ash material [238] and it can be due to the lack of reliable and sufficient experimental data [246]. Results have been obtained by Goodwin and Mitchner [247] from the measurement of three coal ash samples over the wavelength range 1 µm to 12 µm at room temperature. In this study, the effect of the ferrous iron on the absorption index in the wavelength range 1 µm to 5 µm is mentioned. The influence of the temperature on the absorption part, k, is also investigated, with the measurements being made for the temperatures up to 1200 K for the wavelength range 1-7.8 µm. The results showed that the absorption part increases with increasing temperature [235]. An extended study of the optical properties of slags to higher temperature and over a wide range of compositions has been performed in the study [237], with 8 slag samples measured at temperature 1600 K in the wavelength range 1 µm to 13 µm and a correlation formula for the optical constants for the fly ash being a function of the composition, wavelength and temperature are also performed.

The radiative properties of the fly ash and the effect of the fly ash on the radiative heat transfer have been investigated in some studies [235, 246, 248–251]. Most of these studies found that the use of wavelength-independent optical constants for fly ash can produce significant different results compared to that of the wavelength-dependent optical constants [235, 246, 249, 250] and the radiative properties calculated using the wavelength-independent optical constants, n=1.5 and k ranges from 0.005 to 0.05, can produce unacceptable results of Planck mean coefficients. The dependence of the optical properties of fly ash on temperature have been invested in studies [249, 252, 253] and these studies have found that the radiative properties of the fly ash are weak temperature dependence and the effect of temperature can be neglected.

The optical constants of the coal particle can be found in [245, 254–256] and these studies show that the real part varies between 1.6 to 2.1 for different coals

over a wavelength range 1 μm to 10 μm, while the imaginary part considerably differ between the studies in a range from 0.2 to 1.2. The wavelength independent refractive index of coals can be found in [257] and shown in Table 2.3 .

Table 2.3: Wavelength independent optical constants of coals [257]:

Coals	n	k
Carbon	2.20	1.12
Anthracite	2.05	0.54
Bituminous	1.85	0.22
Bituminous-K	1.85	0.04
Lignite	1.70	0.066

A recent study [236], using an FT-IR spectrometer to measure the optical properties of Blind Canyon and Kentucky no. 9 coals has been performed over the wavelength range 2 μm to 20 μm. It is observed that the results obtained, see in figure 3.7, are in good agreement with the single-wavelength data determined from in situ scattering experiments.

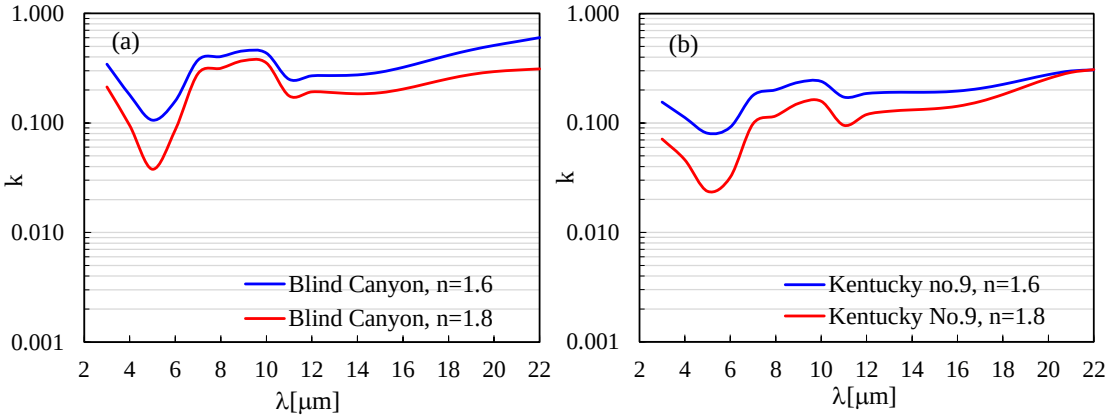

Figure 2.4: Absorption index as a function of the wavelength for a refractive index n is 1.6 and 1.8 for (a) Blind Canyon coal, and (b) Kentucky no. 9 coal [236].

2.2.4.4 Simplified approximations for the radiative properties of particles

Calculating exactly the radiative properties of particles in coal-fired combustion furnaces is a complicated process and significantly time consuming because of the different types of particles (coal, char and soot) and the dependence of the radiative properties of these particle on their shape, particle size distribution and the complex index of refraction [72]. On assuming that the particles are spherical and homogeneous, the Mie theory has been considered as an accurate and effective method to predict the radiative properties of the particles [133, 258]. Despite the power of the Mie theory in calculating the radiative properties of the particles, the application theory in combustion processes still has significant challenges computationally, especially the frequently changing properties of the particles that need to be calculated during the time that the particles are present in the furnace [257, 259]. Therefore, several approximations for the calculation of the radiative properties of the particles in pulverised coal combustion have been proposed.

(i) *Constant properties*: The most simple approach for the radiative properties of the particles are to assume that the properties are constants, with an emissivity value that varies from 1 for coal to 0.6 for the residual ash. Although this can introduce a large error in the calculation, currently it is still quite popular in engineering combustion modelling because it is extensively computationally time consuming. Some values of the radiative properties are showed in Table 2.4.

Table 2.4: Some radiative properties of the particles that are simplified as constant.

Radiative properties	value
Absorption coefficient	0.7[260], 0.85[261], 0.9[262–265]
Scattering factor	0.6[263, 265], 0.9[266]

(ii) *Linear properties*: Because of the change in the carbon content during the time that the coal particles in the furnace, Chui et al. [267] proposed that the

emissivity of the particle is a linear function of the unburnt char content in the particle, with the emissivity changing between 1 and 0.6, corresponding to the coal and ash as follows:

$$\epsilon_p = X_c + 0.6\,(1 - X_c) \tag{2.110}$$

where X_c is the fraction of unburnt char mass.

Yin [206] introduced a scattering factor, f_p, as a function of the fraction of the unburnt combustibles, with the values vary between 0.9 for coal to 0.6 for ash and is given by

$$f_p = 0.9X_{v,c} + 0.6\,(1 - X_{v,c}) \tag{2.111}$$

where X_v, c is the fraction of unburnt combustibles.

(iii) *Approximations for the radiative properties of ash* Bukius and Hwang [268] determined empirical equations for the extinction, absorption efficiencies and asymmetry factor based on a large number of calculations using the Mie theory for a single particle and three coals with different carbon content with wavelengths from 1 µm to 10 µm and different size distributions. They found that the dimensionless radiative properties do not depend on the particle size distributions and only depend on the mean diameter of the particle cloud and the index of refraction. The Planck and Rosseland mean coefficients were also defined as a function of the temperature and average diameter of the particles. The radiative properties are determined from Equation (2.112), with the parameters given in Table 2.5. This approximation was evaluated by Kim and Lior [259] for moderate size parameters ($1 \leqslant x \leqslant 60$) of coal and char. The extinction efficiency showed good agreement with the Mie theory with an error less than 5.9%. However, the scattering efficiency is only suitable for a more narrow range of size parameters with an error being larger than 10%. Recently, the Bukius and Hwang correlation has been used by [269, 270] for radiation of coal particle, however, the optical constants employed are independent of the wavelength.

$$\frac{1}{y^z} = \frac{1}{y_0^z} + \frac{1}{y_\infty^z} \tag{2.112}$$

Table 2.5: Emperical correlations for the calculation of the radiative properties.

y	y_0	y_∞	z
$\frac{\overline{Q}_{\lambda ext}}{x_{32}F}$	$24\left[1+\left(\frac{x_{32}F}{0.016}\right)^2\right]$	$\frac{2.25}{(x_{32}F)^{1.1}}$	1.2
$\frac{\overline{Q}_{\lambda abs}}{x_{32}F}$	$24\left[1+\left(\frac{x_{32}F}{0.0275}\right)^2\right]$	$\frac{1}{(x_{32}F)^{1.16}}$	1.6
$\frac{\overline{Q}_{Pext}}{r_{32}T}$	$0.0032\left[1+\left(\frac{r_{32}T}{355}\right)^{1.90}\right]$	$\frac{10.99}{(r_{32}T)^{1.02}}$	1.2
$\frac{\overline{Q}_{Pabs}}{r_{32}T}$	$0.0032\left[1+\left(\frac{r_{32}T}{725}\right)^{1.65}\right]$	$\frac{13.75}{(r_{32}T)^{1.13}}$	1.5

where x_{32} is the particle size parameter, F is the function of m, are defined as:

$$x_{32} = \frac{\pi D_{32}}{\lambda} \tag{2.113}$$

$$F\left(m\right) = \frac{1}{24}\Im\left(-4\frac{m^2-1}{m^2+2}\right) \tag{2.114}$$

An approximation for particles proposed by van de Hulst [271], called the anomalous diffraction limit being valid for $x \gg 1$ and $|m\text{-}1| \leq 1$, was recommended to be used for ash by Kim and Lior [259], with the extinction and absorption efficiencies being calculated as follows:

$$\begin{aligned} Q_{ext} &= 2 - 4\left(\frac{\cos\phi}{\rho}\right) \\ &\times \left(e^{-\rho\tan\phi}\left(\sin\left(\rho-\phi\right) - \left(\frac{\cos\phi}{\rho}\right)\cos\left(\rho-\phi\right)\right) + \left(\frac{\cos\phi}{\rho}\right)\cos 2\phi\right) \end{aligned} \tag{2.115}$$

$$Q_{abs} = 1 + \frac{e^{-4xk}}{2xk} + \frac{\left(e^{-4xk}-1\right)}{8x^2k^2} \tag{2.116}$$

where

$$\rho = 2x(n-1) \tag{2.117}$$

$$\phi = \tan^{-1}\left(\frac{k}{n-1}\right) \tag{2.118}$$

More recently, Johansson [272] proposed correlations for the calculation of the grey particle properties and the correlations have been fitted to the data calculated by the Mie theory and use the same relation, Equation (2.112), as Bukius and Hwang [268]. The correlations for ash particles are shown in Table 2.6, where r_p, T are the radius and temperature of the particle, respectively.

Table 2.6: Correlations for grey ash particle properties.

y	y_0	y_∞	z
$Q_{a,Ash1}$	$\left(\frac{r_p}{3.57-6.14e^{-0.0014T}}\right)^{1.09}$	$0.7+\frac{0.654}{r_p{}^{0.22}}$	1.1
$Q_{s,Ash1}$	$\left(\frac{r_p}{0.25-2.05e^{-0.0019T}}\right)^{4.0}$	$1.1+\frac{3.1}{r_p{}^{0.97}}$	0.42
$Q_{a,Ash2}$	$\left(\frac{r_p}{0.53T-32}\right)^{0.9}$	$0.7+\frac{1.16}{r_p}{}^{0.24}$	$0.31+2.8.10^{-4}$T
$Q_{s,Ash2}$	$\left(\frac{r_p}{0.22-1.87e^{-0.0015T}}\right)^{4.0}$	$1.1+\frac{2.06}{r_p{}^{0.4}}$	0.54

(iv) *Approximations for the radiative properties of coal*: Kim and Lior [259] recommended an approximation of van de Hulst [271], called the geometrical-limit approximation being valid for $x \gg 1$ and $|m| > 2$, for the calculation of the radiative properties of coal particles, with the size parameter $x > 60$, and the extinction and absorption efficiencies being calculated as follows:

$$Q_{ext} = 2 \tag{2.119}$$

$$Q_{abs} = \frac{1}{2}\left(f_1 + f_2\right) \tag{2.120}$$

where

$$f_i = \frac{8}{q_i^2}\left[q_i - \ln(1+q_i+\frac{1}{2}q_i^2)\right], \; i = 1, 2. \tag{2.121}$$

with

$$q_1 = (nk)^{1/2} \text{ and } q_2 = 2/q_1 \tag{2.122}$$

Recent approximation for the grey properties of coal particles were introduced by Johansson [272], having the same relation as that developed by Bukius and Hwang [268] , Equation (2.112). The correlation for coal particle are shown in Table 2.7, where x is the size parameter.

Table 2.7: Correlations for grey coal particle properties.

y	y_0	y_∞	z
$Q_{a,coal}$	$\left(\frac{x}{700}\right)^{1.1}$	$0.88+\frac{1680}{x}$	1.6
$Q_{s,coal}$	$\left(\frac{x}{570}\right)^{3.9}$	$1.2+\frac{2600}{x}^{1.2}$	0.65

2.3 NOx pollutant in pulverised coal combustion

Nitrogen oxides in the atmosphere consist of nitric oxide (NO), nitrogen dioxide (NO_2), nitrous oxide (N_2O) and some other oxides [273]. In fuel combustion, the NO_x emissions contain mostly NO, with a much lower amount of N_2O and NO_2 [274, 275]. Results of the measurements of N_2O concentration for fossil fuel fired power plants has been reviewed by Bowman [276] and show that the concentration of N_2O is very small compared to that of NO_x, less than 20 ppmv (at 3% O_2) and the ratio of the emissions N_2O/NO_x is less than 2%. However, the measurement results from this review for the coal-fired fluidized bed combustors, which operate at relatively low temperatures, show that the N_2O emission becomes more important. This study is based on pulverised coal combustion, and therefore, only the NO formation and destruction are investigated.

This section focuses on the discussion of the NO formation and the reduction in the pulverised coal combustion in the CFD model. The governing equations for NO transport are introduced in Section 2.3.1 and different NO formation mechanisms are discussed in Section 2.3.2. The reduction mechanisms are discussed in Section 2.3.3.

2.3.1 Governing equations for NO transport

The formation of the NO species does not significantly affect the fluid dynamics or the heat transfer of the combustion process, and so can be calculated as a post-processing step. Therefore, the accuracy in the predictions of the flame temperature, volatile released, char burnout and aerodynamics are the prerequisites in the NO_x formation predictions [277]. The post-processor is based on solving the transport equations for the NO and intermediate species, such as HCN, NH_3 and N_2O as follows:

$$\frac{\partial(\rho Y_{\mathrm{NO}})}{\partial t} + \nabla.(\rho \vec{v} Y_{\mathrm{NO}}) = \nabla.(\rho D \nabla Y_{\mathrm{NO}}) + S_{\mathrm{NO}} \tag{2.123}$$

$$\frac{\partial(\rho Y_{\mathrm{HCN}})}{\partial t} + \nabla.(\rho \vec{v} Y_{\mathrm{HCN}}) = \nabla.(\rho D \Delta Y_{\mathrm{HCN}}) + S_{\mathrm{HCN}} \tag{2.124}$$

$$\frac{\partial(\rho Y_{\mathrm{NH_3}})}{\partial t} + \nabla.\left(\rho \vec{v} Y_{\mathrm{NH_3}}\right) = \nabla.\left(\rho D \nabla Y_{\mathrm{NH_3}}\right) + S_{\mathrm{NH_3}} \tag{2.125}$$

$$\frac{\partial(\rho Y_{\mathrm{N_2O}})}{\partial t} + \nabla.\left(\rho \vec{v} Y_{\mathrm{N_2O}}\right) = \nabla.\left(\rho D \nabla Y_{\mathrm{N_2O}}\right) + S_{\mathrm{N_2O}} \tag{2.126}$$

where $Y_{\mathrm{NO}}, Y_{\mathrm{HCN}}, Y_{\mathrm{NH_3}}$ and $Y_{\mathrm{N_2O}}$ are the mass fraction of the species NO, HCN, NH_3 and N_2O, respectively, and D is the effective diffusion coefficient. The source terms $S_{\mathrm{NO}}, S_{\mathrm{HCN}}, S_{\mathrm{NH_3}}$ and $S_{\mathrm{N_2O}}$ are determined corresponding to the mechanism of the species.

2.3.2 Mechanisms of the NO formation

The NO formation can result from 4 mechanisms: fuel-NO, thermal-NO, prompt-NO and N_2O mechanisms. The fuel-NO mechanism is the dominant source of the NO formation in coal power plants, with more than 80% of the total NO formation [55, 56, 275] while the formation from the prompt-NO and N_2O mechanisms can be neglected since its contribution to the total NO is very small [278].

2.3.2.1 Thermal-NO

Thermal-NO is formed from the oxidation of atmospheric nitrogen in a relatively high-temperature environment and this mechanism is strongly temperature de-

pendent. The formation of NO under this mechanism is described by the Zeldovich mechanism. Themal-NO occurs in air-fired conditions with the presence of nitrogen in air and this mechanism is almost eliminated under the oxy-fired condition where nitrogen is replaced by CO_2. The set of reactions governing the formation of thermal-NO is known as the "extended Zeldovich" mechnism and this is expressed as follows [279]:

$$O + N_2 \rightleftharpoons N + NO \tag{R2.1}$$

$$N + O_2 \rightleftharpoons O + NO \tag{R2.2}$$

$$N + OH \rightleftharpoons H + NO \tag{R2.3}$$

Using the three reactions, Reactions (R2.1)-(R2.3), the net rate of thermal-NO formation is express as follows:

$$\begin{aligned}\frac{\mathrm{d}[\mathrm{NO}]}{\mathrm{d}t} = {} & k_{f1}[\mathrm{O}][\mathrm{N_2}] + k_{f2}[\mathrm{N}][\mathrm{O_2}] + k_{f3}[\mathrm{N}][\mathrm{OH}] \\ & -k_{r1}[\mathrm{NO}][\mathrm{N}] - k_{r2}[\mathrm{NO}][\mathrm{O}] - k_{r3}[\mathrm{NO}][\mathrm{H}]\end{aligned} \tag{2.127}$$

where k_{f1}, k_{f2}, k_{f3} are the rate constants for the forward reactions in the Reactions (R2.1)-(R2.3), respectively. The rate constants for the reserve reactions are k_{r1}, k_{r2}, k_{r3}. These rate constants have been reported in several studies [279, 280], a set of constants based on evaluation of Hanson and Salimian [280] that is widely accepted in the literature are shown in Table 2.8.

Table 2.8: Reaction rate coefficients in the form $k = A_r T^{\beta} \exp\left(-E_a/RT\right)$ [280].

Reaction constant	A_r (m^3/kmol-s)	β	E_a (J/kmol)
k_{f1}	1.80×10^{11}	0	3.19×10^{8}
k_{f2}	1.80×10^{7}	1	3.89×10^{7}
k_{f3}	7.10×10^{10}	0	3.74×10^{6}
k_{r1}	3.80×10^{10}	0	3.53×10^{6}
k_{r2}	3.80×10^{6}	1	1.73×10^{8}
k_{r3}	1.70×10^{11}	0	2.04×10^{8}

On assuming that the rate of consumption of free N atoms becomes equal to the rate of its formation, the overall rate for the three reversible reactions (R2.1)-(R2.3) can be expressed as [281]:

$$\frac{\mathrm{d[NO]}}{\mathrm{d}t} = 2[\mathrm{O}] \left(\frac{k_{f1}[\mathrm{N_2}] - \frac{k_{r1}k_{r2}[\mathrm{NO}]^2}{k_{f2}[\mathrm{O_2}]}}{1 + \frac{k_{r1}[\mathrm{NO}]}{k_{f2}[\mathrm{O_2}]+k_{f3}[\mathrm{OH}]}} \right) \tag{2.128}$$

The rate of thermal-NO formation, Equation (2.128), is a function of the local temperature and the local concentrations of O_2, N_2, O and OH. In addition to the temperature, the O and OH atoms strongly influence the thermal NO rate [277, 282]. The concentration of the O and OH atoms can be estimated using equilibrium and partial equilibrium assumptions.

(i) Equilibrium assumption: In the equilibrium assumption, the concentration of the O atom is determined as [274]:

$$[\mathrm{O}] = k_e^{1/2} \left[\mathrm{O_2}\right]^{1/2} \tag{2.129}$$

where k_e is the equilibrium constant. For the Reactions (R2.1) and (R2.2), the equilibrium is determined as follows:

$$k_e = \left(\frac{k_{f1}}{k_{r1}}\right)\left(\frac{k_{f2}}{k_{r2}}\right) \tag{2.130}$$

(ii) Partial equilibrium calculation: Different approximations for the partial approach used to estimate the concentration of the O atom can be found in the studies [278, 283]. One of those, which is appropriate in fuel rich regions, is based on the partial equilibrium assumption for the following reactions:

$$\mathrm{O + H \rightleftharpoons OH + O} \tag{R2.4}$$

$$\mathrm{CO + OH \rightleftharpoons CO_2 + H} \tag{R2.5}$$

The O atom concentration is determined as

$$[\mathrm{O}] = \left(\frac{k_{f4}}{k_{r5}}\right)\left(\frac{k_{f5}}{k_{r5}}\right)\frac{[\mathrm{O_2}][\mathrm{CO}]}{[\mathrm{CO_2}]} \tag{2.131}$$

where k_{f4}, k_{r4} and k_{f5}, k_{r5} are the rate constants for the forward and reserve reactions in Reactions (R2.4) and (R2.5), respectively.

The source term for the thermal-NO mechanism is calculated from the rate of thermal-NO in Equation (2.128) as

$$S_{\text{Thermal}-\text{NO}} = M_{\text{NO}} \frac{\text{d}[\text{NO}]}{\text{d}t} \tag{2.132}$$

where M_{NO} is the molecular weight of NO(kg/mol).

The thermal-NO concentration that is calculated using the equilibrium approach has been found to be much lower compared to that of the partial equilibrium approach in the flame region [283, 284], thus resulting in large errors in the NO formation calculations [278]. Therefore, in pulverised coal combustion modelling, the partial-equilibrium approach has been widely selected to determine the O atom in many studies [285–290].

Under the oxy-fired condition, nitrogen is replaced by CO_2, and the thermal-NO mechanism is therefore, mostly, eliminated. Results from the prediction of the 550 MW utility boiler and the 100-kW Chalmers laboratory-scale furnace under the air-fired and oxy-fired conditions show a remarkable decrease in the NO formation and this is because of the elimination of the thermal NO process under oxy-fired conditions [286, 291]. It should be noted that the thermal-NO mechanism was only employed for the air case in the study of Álvarez et al. [292] when modelling both air and oxyfuel conditions.

2.3.2.2 Prompt-NO

The prompt-NO mechanism describes the formation of NO by the reactions between N_2 with intermediate species from fuel fragmentation, such as CH, CH_2, C_2, C_2H, and this was first mentioned by Fenimore [293]. This mechanism occurs in fuel-rich regions where there are high concentrations of the hydrocarbon radicals in a low-temperature environment and for a short time because of the short-lived hydrocarbon radicals. From the experimental study, Blauwens et al. [294] found that CH and CH_2 have a major contribution on the NO formation due to the prompt mechanism. The prompt-NO mechanism is widely expressed

as a sequence of reactions as follows [277, 295]:

$$CH + N_2 \rightleftharpoons HCN + N \tag{R2.6}$$

$$CH_2 + N_2 \rightleftharpoons HCN + NH \tag{R2.7}$$

The product of the above reaction, HCN, has a further reaction to form NO or N_2as:

$$HCN + O_2 \longrightarrow NO + ... \tag{R2.8}$$

$$HCN + N \longrightarrow N_2 + ... \tag{R2.9}$$

The amount of NO formation by the prompt-NO mechanism depends on the number of carbons present in the molecule of the hydrocarbon fuels and the stoichiometry. Therefore, a global kinetic rate, which is correlated from experiments on different fuel types and different stoichiometric values, has been developed for the prediction of prompt NO as [97, 277]:

$$\frac{\mathrm{d[NO]}}{\mathrm{d}t} = f_c T^{\beta} k'_{pr} [O_2]^a [N_2][\mathrm{FUEL}] \exp(-E_a/RT) \tag{2.133}$$

where a and β are constants, f_c is the correlation factor which considers the effect of the fuel types and air-fuel ratio, and it is given as [277]:

$$f_c = 4.75 + 0.0819n - 23.2\phi + 32\phi^2 - 12.2\phi^3 \tag{2.134}$$

where n is the number of carbon atoms in the molecule of the fuel, and ϕ is the equivalence ratio. The factors k'_{pr} and E_a in Equation (2.133) are given as follows:

$$k'_{pr} = 6.4 \times 10^6 (RT/p)^{a+1} \tag{2.135}$$

$$E_a = 303 \mathrm{kJ/kmol} \tag{2.136}$$

The local mole fraction of oxygen, a, depends on the conditions in the flame as:

$$a = \begin{cases} 1.0 & \text{if } X_{O_2} \leq 4.1 \times 10^{-3} \\ -3.95 - 0.9 \ln X_{O_2} & \text{if } 4.1 \times 10^{-3} < X_{O_2} \leq 1.11 \times 10^{-2} \\ -0.35 - 0.1 \ln X_{O_2} & \text{if } 1.11 \times 10^{-2} < X_{O_2} < 0.03 \\ 0 & \text{if } X_{O_2} \leq 0.03 \end{cases} \tag{2.137}$$

The source term for the prompt-NO mechanism is calculated from the rate of the prompt-NO in Equation (2.133) as follows:

$$S_{\text{Prompt-NO}} = M_{\text{NO}} \frac{\text{d[NO]}}{\text{d}t} \tag{2.138}$$

where M_{NO} is the molecular weight (kg/mol).

In pulverised coal combustion, which usually operates under lean-fuel conditions, the contribution of the prompt NO to the total NO formed is small, and therefore this mechanism is usually assumed to be negligible in CFD modelling [278, 286, 290, 296]. However, in the burner region, which has a slightly fuel-rich, the prompt NO can increase [297, 298]. Under oxy-fired condition, where the N_2 is nearly eliminated, the prompt-NO mechanism, which is proportional to N_2, can be reduced compared to that in the air-fired condition.

2.3.2.3 Fuel-NO

The fuel-NO mechanism occurs from the oxidation of fuel-bound nitrogen which is released from fuel devolatilisation, called volatile-N, and the nitrogen remains in the char, called char-N. The volatile-N converts to intermediate nitrogen compounds, primarily HCN and NH_3 and then these species oxidise to form NO. The char-N converts directly to NO from the oxidised char-N atoms, or partly converts to intermediate nitrogen compounds which are then converted partially to NO. As a results, the formation from the char nitrogen is proportional to the carbon burnout. The volatile-N is dominant in the NO formation in regular pulverised coal combustion, with about 60-80% of the total NO being formed from the volatile-N [299, 300].

The split between the amount of the volatile-N and the char-N from the devolatilisation process of fuel-N is potentially important for the NO formation, which depends on fuel type, the temperature and and the residence time [301, 302]. The distribution of volatile-N and char-N for specific fuel can be determined by experiment or using network models, such as the FG-DVC, FLASCHAIN, CPD models. The distribution of volatile-N is dominant compared to that of char-N in fuel-N, with about 70-90% Volatile-N in the Fuel-N [297, 299].

The volatile-N is often assumed to be released mainly as HCN or NH_3 and the rate of HCN/NH_3 depends on fuel type, devolatilisation temperature and heating rate [301]. The high-ranking (bituminous) coal has been shown to produce mainly HCN, while the low-ranking (lignite) coal or biomass produces more NH_3 than HCN [303]. A low heating rate has shown to have a decreasing a HCN/NH_3 ratio for both coal and biomass because the dominant NH_3 released [304]. The HCN/NH_3 ratio increases at higher heating rates [305]. The source terms of the intermediate species, HCN, NH_3 and NO, created from volatile-N and char-N can be expressed by:

$$S_{vol,x} = \alpha_x \frac{S_{vol} Y_{\mathrm{N},vol} M_x}{M_{\mathrm{N}} V} \tag{2.139}$$

$$S_{char,x} = \beta_x \frac{S_{char} Y_{\mathrm{N},char} M_x}{M_{\mathrm{N}} V} \tag{2.140}$$

where x refers to HCN, NH_3, or NO, S_{vol}, S_{char} being the source of the volatile and char (kg/s), respectively, V is the volume of cell (m^3), $Y_{\mathrm{N},vol}, Y_{\mathrm{N},char}$ are the mass fraction of nitrogen in the volatile and char, respectively, M_x, M_{N} are the molecular weight of the intermediate specie x and nitrogen, respectively, and α_x, β_x are the mass fraction of nitrogen converted to species x from the volatile and char, respectively. The intermediate species can be oxidised to form NO and reduced back N_2 by the reactions

$$HCN/NH_3 + O_2 \longrightarrow NO + ... \tag{R2.10}$$

$$HCN/NH_3 + NO \longrightarrow N_2 + ... \tag{R2.11}$$

The mass consumption rates of HCN, NH_3 in Reactions (R2.10), (R2.11) are calculated as:

$$S_{\mathrm{HCN,NO}} = -R_1 \frac{M_{\mathrm{HCN}} p}{RT} \tag{2.141}$$

$$S_{\mathrm{HCN,N_2}} = -R_3 \frac{M_{\mathrm{HCN}} p}{RT} \tag{2.142}$$

$$S_{\mathrm{NH_3,NO}} = -R_2 \frac{M_{\mathrm{NH_3}} p}{RT} \tag{2.143}$$

$$S_{\mathrm{HCN,N_2}} = -R_4 \frac{M_{\mathrm{NH_3}} p}{RT} \tag{2.144}$$

where R_1, R_2 are the mass consumption rates according to the Reaction (R2.10) of HCN and NH_3, respectively, R_3, R_4 are the mass consumption rates according to the Reaction (R2.11) of HCN and NH_3, respectively, p, T are the pressure and temperature, respectively, and R is the universal constant.

The heterogeneous reactions of NO with char can result in the reduction of NO, and the reduction in NO can be expressed as:

$$\text{char} + \text{NO} \longrightarrow \text{N}_2 \tag{R 2.12}$$

The rate of NO consumption is calculated by

$$S_{\text{NO},char} = c_s A_{BET} M_{\text{NO}} R_{\text{NO},char} \tag{2.145}$$

where A_{BET} is the Brunauer Emmett Teller (BET) specific surface area of pulverised coal (m^2/kg), c_s is the concentration of the particles (kg/m^3), $R_{\text{NO},char}$ is the rate of heterogeneous reaction (2.150), being reported by several studies [306–309]. The rate of the heterogeneous NO reaction has been found to be significantly effected by the oxidise gases, particularly O_2, CO and H_2O. The enhancement of the NO-char reduction due to presence of CO in a high temperature media has been observed in several studies [310–313].

The overall source terms of NO, HCN and NH_3 are therefore given by

$$\begin{aligned} S_{\text{NO}} = {} & S_{vol,\text{NO}} + S_{char,\text{NO}} + S_{\text{HCN},\text{N}_2} + S_{\text{NH}_3,\text{N}_2} \\ & - S_{\text{HCN},\text{NO}} - S_{\text{NH}_3,\text{NO}} - S_{\text{NO},char} \end{aligned} \tag{2.146}$$

$$S_{\text{HCN}} = S_{vol,\text{HCN}} + S_{char,\text{HCN}} + S_{\text{HCN},\text{N}_2} + S_{\text{HCN},\text{NO}} \tag{2.147}$$

$$S_{\text{NH}_3} = S_{vol,\text{NH}_3} + S_{char,\text{NH}_3} + S_{\text{NH}_3,\text{N}_2} + S_{\text{NH}_3,\text{NO}} \tag{2.148}$$

The sensitivity of the NO emission in pulverised coal combustion to the fuel types, devolatilisation and heating rate have been performed using CFD modelling by several authors. Álvarez et al. [292] studied the NO emission from five coals by experiment and modelling. Regarding the intermediate species composition, the anthracite coals released mostly HCN with some NH_3, while the bituminous coals released NH_3 with some HCN. The HCN/NH_3 ratios for the

high ranking and low-ranking coals were found to increase with the higher temperatures and heating rates. The sensitivity of the intermediate species to the NO emission results show that the ratio HCN/NH_3, as determined from the FG-DVG model, shows better results for the NO emission compared to assuming the case having both volatile-N and char-N converting to HCN or the case with volatile-N converting to HCN and 20% of char-N converting to NO. Chui and Gao [314] studied five full-scale boilers, with a capacity range from 200 to 1000 MWe and burning different coal types: anthracites, bituminous and lignite coals. The study was performed with two ratios of volatile-N/char-N, one and three, and this shows that the NO emission is significantly effected by the distribution between volatile-N and char-N. The volatile-N/char-N =3 gives reasonable NO estimates for boilers burning the lower rank coals (bituminous and lignite). Also the study recommended that it is necessary to use the measured distribution in the NO model in order to obtain the best possible prediction results. A sensitivity study of the NO emissions with different parameters: different ratios of Volatile-N/char-N, HCN/NH_3 and conversion values was performed by [285] using Rhenish Lignite coal. The results for the NO concentrations at the boiler outlet show that the conversion values, which present the rate of volatile-N and char-N convert to intermediate species, has a large impact on the level of the NO emissions and therefore it needs to be considered when selecting these values in the simulation. The recent study on a pilot facility with bituminous coal by [290] shows the effect of the intermediates on the formation of NO, with the distribution of intermediate species: 52% HCN, 10% NH_3 and 38% NO, show very good agreement with the experimental data. A numerical investigation on a pilot scale test facility for an Australian sub-bituminous coal, performed by Cao et al. [58], shows that the NO emission behaviour is very sensitive to the volatile-N/char-N.

The higher concentration of CO under oxy-fired conditions has been found and there is a significant enhancement in the NO reduction by the heterogeneous reaction compared to that of the air-fired condition. An experimental study on a 20 kW down-fired combustor has been performed by [32] and it shows that the

higher concentration of CO in the combustion zone for the oxy case results in a larger reduction in NO compared to that of the air case. The heterogeneous reduction has been found to play an important role in the reduction of the NO from the flue gas recycled under the oxyfuel conditions [315].

2.3.2.4 N_2O-intermediate NO mechanism

The N_2O-intermediate mechanism was first proposed by Malte and Pratt [316]. This mechanism is important at low temperatures, lower than 1250 K, with the formation of the intermediate specie and subsequently by the formation of NO [317]:

$$N_2 + O + M \rightleftharpoons N_2O + M \tag{R2.13}$$

$$N_2O + O \rightleftharpoons 2NO \tag{R 2.14}$$

where M is the general third body. The concentration of N_2O is often assumed to be a quasi-steady state:

$$[N_2O] = \frac{k_{f1}[N_2][O][M] + k_{r2}[NO]^2}{k_{r1}[M] + k_{f2}[O]} \tag{2.149}$$

where k_{f1}, k_{r1} and k_{f2}, k_{r2} are the rate constants for the forward and reserve reactions in Reactions (R2.13) and (R 2.14), respectively. The rate of NO formation, via the N_2O intermediate mechanism, is calculated as follows:

$$\frac{\mathrm{d}[NO]}{\mathrm{d}t} = 2\left(k_{f2}[N_2O][O] - k_{r2}[NO]^2\right) \tag{2.150}$$

and the NO source term is therefore given as

$$S_{N_2O} = M_{NO}\frac{\mathrm{d}[NO]}{\mathrm{d}t} \tag{2.151}$$

2.3.3 Reburning NO mechanism

The reduction mechanism of NO, called reburn, occurs when the NO reactions with the hydrocarbon CH_i radicals, with the general reaction can be expressed as [318]:

$$CH_i + NO \rightarrow HCN + \text{products} \tag{R2.15}$$

where CH_i are the hydrocarbon species, i=1, 2, or 3, depending on the hydrocarbons used in the flame. Several pathways for reburning NO can be found in some studies [318–320]. A mechanism of the NO reburn, based the partial equilibrium approach, has been performed in the studies [320, 321] and this mechanism is also available in the CFD Fluent. The pathways of the NO reduction can be expressed by hydrocarbon radicals as follows:

$$NO + CH_2 \longrightarrow HCN + OH \tag{R2.16}$$

$$NO + CH \longrightarrow HCN + O \tag{R2.17}$$

$$NO + C \longrightarrow CN + O \tag{R2.18}$$

The hydrocarbon radicals in the Reactions (R2.16)- (R2.18) are determined from the reactions:

$$CH_4 + H \rightleftharpoons CH_3 + H_2 \tag{R2.19}$$

$$CH_3 + OH \rightleftharpoons CH_2 + H_2O \tag{R2.20}$$

$$CH_2 + H \rightleftharpoons CH + H_2 \tag{R2.21}$$

$$CH + H \rightleftharpoons C + H_2 \tag{R2.22}$$

In hydrocarbon diffusion flames, the concentration of the H radical has been observed to have the same order as H_2. The concentration of the OH radical can be estimated by reaction:

$$OH + H_2 \rightleftharpoons H_2O + H \tag{R2.23}$$

with

$$[OH] = \frac{k_{r8}}{k_{f8}}[H_2O] \tag{2.152}$$

where k_{f1} and k_{r1} are the forward and reverse rates of the Reaction (R2.23), respectively. The rates of the NO destruction and HCN formation from reburn, assuming CH_4 is the reburn gas, is given as:

$$\frac{d[NO]}{dt} = -\left(k_1\frac{k_{f4}k_{f5}}{k_{r4}k_{r5}} + k_2\frac{k_{f4}k_{f5}k_{f6}}{k_{r4}k_{r5}k_{r6}} + k_3\frac{k_{f5}k_{f6}k_{f7}k_{f8}}{k_{r5}k_{r6}k_{r7}k_{r8}}\right) y_2[NO][CH_4] \tag{2.153}$$

$$\frac{\mathrm{d[HCN]}}{\mathrm{d}t} = \left(k_1 \frac{k_{f4} k_{f5}}{k_{r4} k_{r5}} + k_2 \frac{k_{f4} k_{f5} k_{f6}}{k_{r4} k_{r5} k_{r6}} \right) y_2 [\mathrm{NO}][\mathrm{CH_4}] \tag{2.154}$$

where k_1, k_2 and k_3 are the rate of the Reactions (R2.16)-(R2.18) being taken form [322, 323], $k_{f4}, k_{f5}, k_{f6}, k_{f7}$ and $k_{r4}, k_{r5}, k_{r6}, k_{r7}$ are the forward and reverse reactions, Reactions (R2.19)-(R2.22), can be found in [324].

2.4 Summary

Oxyfuel combustion has brought a new challenge for existing CFD codes which has been demonstrated as a powerful tool in air-fuel combustion. From the review, many efforts have been made to develop and validate sub-models for the air-fuel condition to make them applicable to the new combustion environment. This is considered to be a first priority for the study of retrofitting in order to keep the same heat transfer condition in the furnace to that of the oxy-fired conditions as in the air-fired condition.

The gaseous radiation models, which need to be modified under the oxyfuel condition by the change of the gas combustion, has received a special attention, especially the global model which has been a preferred selection for complex combustion modelling, mostly due to its low computational expense. Several global models, WSGG, SLW models, and narrow band models, SNB and CK models being the benchmarks to evaluate the global models, has been reviewed in this chapter. The evaluation of global model used in this study will be performed in Chapters 3 and 4 under small and large-scale furnace conditions for both the air and oxyfuel conditions.

The Mie theory has been considered as an accurate and effective method to predict the radiative properties of the particles under pulverised coal combustion. Different measurement data for the optical constants used for the Mie theory calculation, including wavelength-independent and wavelength-dependent optical constants, of the coal and fly-ash particles have been reviewed. Also, several approximations have been used for the calculation of the radiative properties of particles, which is currently quite popular in engineering combustion modelling,

has been reviewed. The evaluation of the optical data and approximate solutions used for the calculation of the radiative properties of the coal and ash particles are investigated in Chapter 3 and the effects of the optical data and approximate solutions on the radiative heat transfer in 3D enclosures for different scales of the furnaces will be performed in Chapters 4 and 5.

The emission of nitrogen oxides from combustion systems is a significant pollutant source that is threatening the global environment. Mechanisms of NO_x formation and destruction processes in combustion systems have been reviewed in this chapter. The formation of NO is calculated as a post-processing step, and therefore the accuracy in the predictions of the flame temperature, volatile release, char burnout and aerodynamics are the prerequisites in the NO_x formation predictions. The sensitivity of the NO_x prediction to the choice of the radiation models on the 250 kW pilot scale combustion test facility (CTF) is performed in Chapter 5.

3 Evaluation studies on the radiative properties of gases and particles

This chapter focuses on the evaluation of the solutions developed for calculating the radiative properties of particles and gases. The radiation of the particles is investigated in Section 3.1. In this section, the validation of the Mie theory for calculating the radiative properties of a particle cloud is performed in Section 3.1.1. The relationship of the optical constants to the radiative properties of the particles is evaluated for both the wavelength-dependent and wavelength-independent optical constants and the evaluation of the approximate solutions used for the calculation of the particle properties are performed in Sections 3.1.2 and 3.1.3, respectively. Several models for calculating the radiative properties of gases are investigated in Section 3.2. The global models which are applied for the radiative heat transfer study in Chapters 4 and 5 are validated in one- and three-dimensional cases in Sections 3.2.1 and 3.2.2, respectively. The conclusions from these studies are summarised in Section 3.3.

3.1 Evaluation of the radiative properties of particles

The radiative properties of a particle cloud, absorption and scattering efficiencies, are investigated for both ash and coal particles, taking into account the effects of the optical constants and the solutions used to calculate the radiative properties of particles. The particle size distribution of a cloud of particles used in this study is described using the Rosin-Rammler function [233], see Equation (2.100). The

size and number density of the particles have a dominant effect on the radiative properties results of the coal and ash particles [235, 236, 325]. In the study of Goodwin and Mitchner [235], the Planck mean absorption efficiency and Planck mean asymmetry of the fly ash of a coarse particle size distribution is found to be higher than that of the fine one. However, it is clear that the radiative emission per unit of mass is not in proportion to the increase in the average diameter of a particle distribution because of the lower projected surface area being found for a coarser particle size distribution. The present study focuses on the effect of the optical constants and the approximate solutions used for the calculation of the particle properties and therefore this study is limited to only one particle size distribution. Selecting parameters for the particles distribution is based on the studies [326, 327]. Particularly, the mean diameter is 100 μm and 10 μm for the coal/char and the ash, respectively. The spread parameter $n = 1.2$ is assumed for both the coal/char and ash particles. For a specific range of wavelength, the absorption and scattering efficiencies can be defined as [235, 236]

$$\overline{Q}_\lambda = \frac{\sum_{i=1}^{n} Q_\lambda(D_i) D_i^2 f_n(D_i) \mathrm{d}D_i}{\sum_{i=1}^{n} D_i^2 f_n(D_i) \mathrm{d}D_i} \tag{3.1}$$

where $Q_\lambda(D_i)$ are the absorption and scattering efficiencies for the size distribution interval corresponding to particles with a diameter D_i. The Planck mean properties of particles can be performed numerically as follows:

$$\overline{Q}_p = \frac{\sum_{i=1}^{n} \overline{Q}_\lambda I_{b\lambda,i}(T) \Delta\lambda_i}{\sum_{i=1}^{n} I_{b\lambda,i}(T) \Delta\lambda_i} \tag{3.2}$$

3.1.1 Validation of the Mie theory code for calculated properties of a particle cloud

The Mie theory, as described by Bohren and Huffman [328], is employed to calculate the particle properties of a spherical particle, which is developed to calculate the properties of a particle cloud, and this code is validated against the results obtained by Goodwin and Mitchner [235] for ash particles. Two particle size distributions obtained from experimental measurements, a fine particle size

distribution reported by Goodwin [329] and a coarse particle size distribution reported by [253], are employed to calculate average absorption efficiencies. The two particle size distributions have mean diameters 3.25 μm and 15 μm for the fine and coarse particle size distributions, respectively. The log-normal function is used to describe the distribution of particles as [235]

$$f_n(D) = \frac{1}{\sqrt{2\pi}\sigma_u D}\exp\left[-\frac{1}{2}\left(\frac{\ln D - \overline{u}}{\sigma_u}\right)^2\right] \tag{3.3}$$

where $\overline{u}$ and σ_u are given in Table 3.1

Table 3.1: Parameters for log-normal particle size distributions.

Distribution	$\overline{u}$	σ_u
A	-0.214	0.747
B	0.35	0.971

The results for the average absorption efficiencies of the cloud of ash particles for two particle size distributions, Fig. 3.1, are in good agreement with the results obtained by Goodwin and Mitchner [235] with some differences. The differences can be explained by the optical properties calculated using data obtained by Liu and Swithenbank [250], which is fitted from the optical constants measured by Goodwin and Mitchner [235, 247].

3.1.2 Effect of optical constants on the radiative properties of particles

The sensitivity of the optical constants, wavelength-independent and wavelength-dependent values of the optical constants, to the radiative properties of particles are investigated in this section for both ash and coal. The radiative properties of particles calculated from wavelength-independent optical constants are compared against the reference case which is calculated from the Mie theory using data from Goodwin and Mitchner [235] for the ash and Manickavasagam and Mengüç [236] for the coal. In terms of wavelength-dependent optical constants, several optical

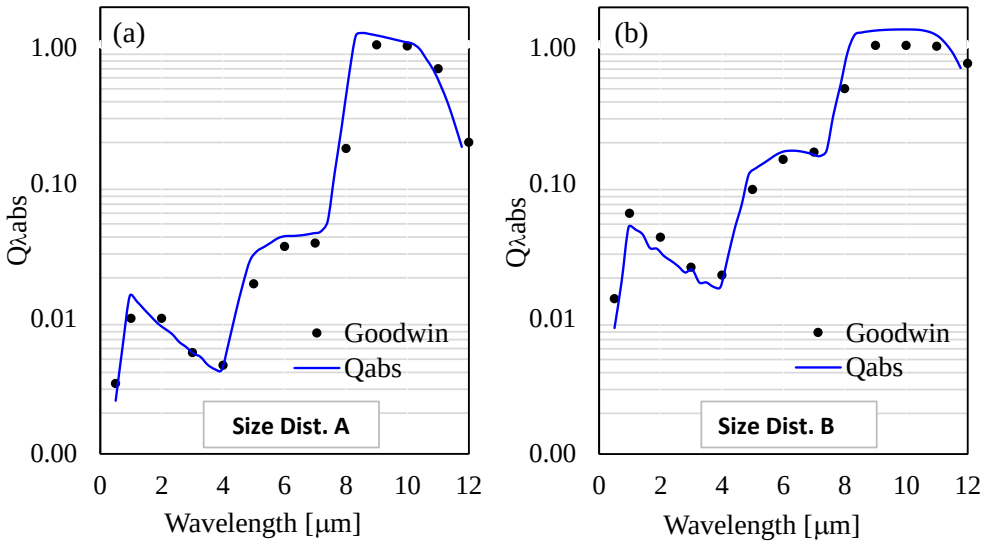

Figure 3.1: Average absorption efficency of fly ash calculated based on the fitting data performed by Liu and Swithenbank [250] compared to the results obtained by Goodwin and Mitchner [235], (a) fine particle size distribution A, and (b) coarse particle size distribution B.

databases for some specific ash types from the studies [235, 244, 245] and for some types of coal from [236, 245] are employed.

3.1.2.1 Wavelength-independent optical constants

As mentioned in Section 2.2.4.3, the real part n and the imaginary part k of the complex index of refraction of the fly ash found in different studies change in the range 1.4 to 1.7 and 0.005 to 0.05, respectively. For the coal, the values are reported to be between 1.6 to 2.1 for the real part and 0.2 to 1.2 for the imaginary part. In this section, the effect of n and k on the radiative properties of the particles are investigated based on Planck mean values which are calculated using the Mie theory.

Fig. 3.2 shows the sensitivity of the radiative properties of the fly ash to n and k which are coupled with k and n from [235], respectively. Results obtained are compared to the spectral radiative properties calculated using the experimental data of Goodwin and Mitchner [235]. The results show that the absorption efficiency is less sensitive to the real part, n, while the scattering efficiency is much

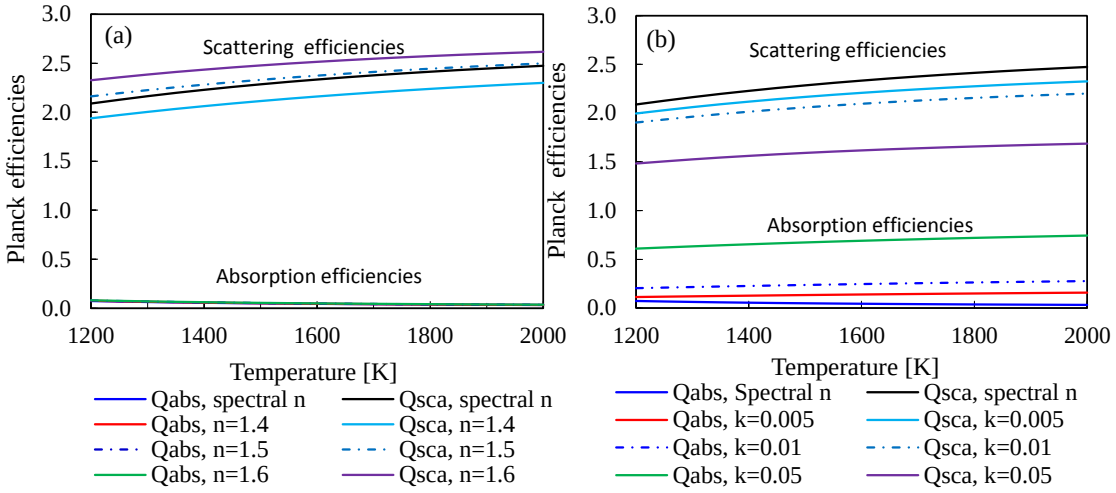

Figure 3.2: The effect of the optical constants on the radiative properties of ash, (a) effect of n (with k from [235]), and (b) effect of k (with n from [235]).

more sensitive to increasing values of n, Fig. 3.2 (a). Both absorption and scattering efficiencies strongly depend on the imaginary part, Fig. 3.2 (b). The values of the particle properties increase with increasing values of k and the maximum discrepancies in the particle properties are about 0.45 and 0.55 for the scattering and absorption efficiencies, respectively, for the range of values of k investigated. The radiative properties calculated from the range of wavelength-independent optical constants found from previous studies are significantly higher compared to those calculated from the experimental data of Goodwin and Mitchner [235]. The large difference is postulated to be due to the assumption of the optical constants being wavelength independent is far from realistic [235]. The discrepancies in the radiative properties calculated from the wavelength-independent optical constants vary in the range 0.1-0.65 for the absorption efficiency and 0.12-0.71 for the scattering efficiency. The wide range of discrepancies can be explained by the uncertainty in the imaginary parts, which are caused by the differences in the material of the ashes and the lack of reliable and sufficient experimental data as mentioned in Section 2.2.4.3.

The sensitivity of the radiative properties of the coal to the optical constants are shown in Fig. 3.3, for a wider ranges of values of n and k compared to those in the ash. The Planck mean properties of the coal show a weak dependence on the

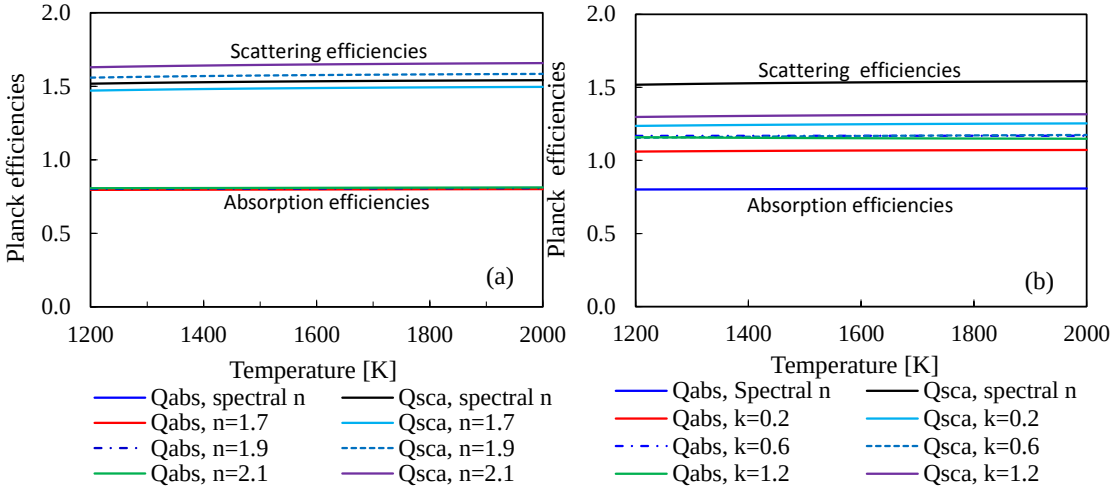

Figure 3.3: The effect of the optical constants on the radiative properties of coal, (a) effect of n (with k from [236]), and (b) effect of k (with n from [236]).

temperature range of interest, namely 1200 to 2000 K. The coal properties results are weakly dependent on the real part and the imaginary part in the ranges of values of k and n investigated compared to that of ash. The maximum difference in the absorption efficiencies is about 0.1 for the values of k investigated. However, the absorption efficiencies calculated from wavelength-independent optical constants are significantly higher compared to that of the spectral absorption coefficients of Manickavasagam and Mengüç [236] by up to 0.25 - 0.35. Further, the values of the spectral scattering efficiencies calculated from the wavelength-independent optical constants are higher than those obtained from the spectral optical constants being about 0.22 to 0.47.

3.1.2.2 Wavelength-dependent optical constants

Different databases for the wavelength-dependent optical constants of the ash [235, 244, 245, 330] and coal [236, 245] are used to calculate the radiative properties of these particles. The spectral average properties and the Planck mean properties for a particle cloud, presented in Equations (3.1) and (3.2), respectively, are employed in the calculation of the particle properties.

The compositions of the ashes used for the measurement of the optical constants are shown in Table 3.2 and the wavelength-dependent optical constants

Table 3.2: Composition of the ash used for measurement of the optical constants.

Ash	%SiO_2	%Al_2O_3	%CaO	%Fe_2O_3
Bl-5(BHVB)[245]	49.00	27.54	12.26	0.04
Br-1(SBC)[245]	30.00	11.00	42.00	9.00
Sub-bituminous[247]	52.05	26.80	15.68	5.47

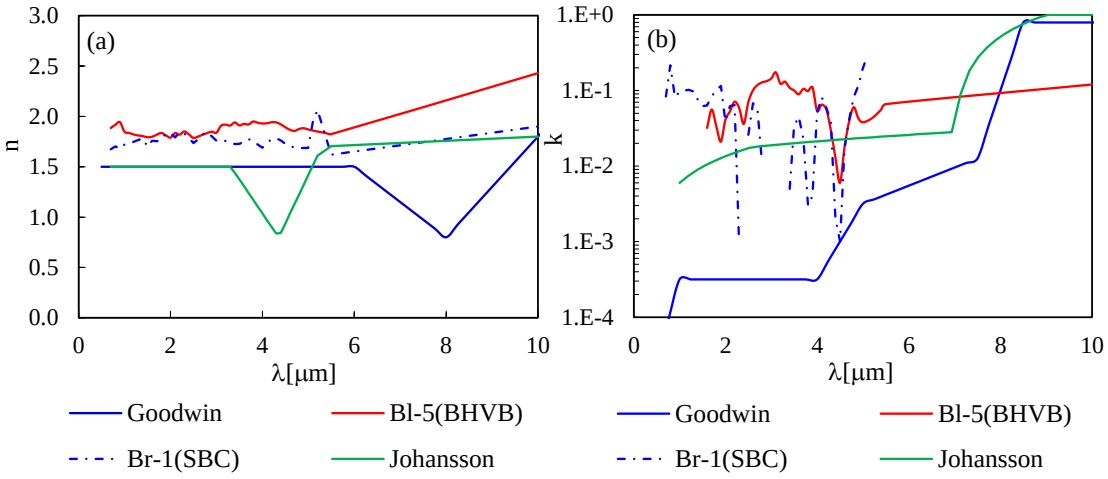

Figure 3.4: Optical constants for the different types of ash, (a) refractive index, and (b) absorptive index.

are presented in Fig. 3.4, where the optical constants measured by [235, 247] are based on the fitting performed by [250], and the combined data which is presented by [251] by combining the experimental data by [244, 330] and the data of [235]. The same wavelength range of 1 μm to 10 μm is used, which is a significant range for the radiative heat transfer at temperatures typical of coal combustion systems [247, 257]. Particularly, with the wavelength range selected, it produces 78.8% of the thermal emission by a black body at the temperature 1200 K, and 93.4 % at 2000 K. Measurement results for both the real and imaginary parts of the complex index of refraction, n and k, from the studies [244, 245] are much higher than the experimental measurements obtained by [247].

The spectral mean properties of 3 types of ash are shown in Table 3.2. The spectrum of the averaged absorption efficiencies as a function of wavelength shows

the same trend as their imaginary parts. For the short wavelengths, the values of the absorption efficiencies presented by Blokh [245] are significantly higher than those produced by Goodwin. Further, the values of absorption efficiencies of ashes show small in short wavelengths and large in longer wavelengths, while this trend is opposite for the scattering efficiencies. The Planck mean efficiencies are shown in Fig. 3.6 for the temperature range 1200 K to 2000 K. The maximum difference between the Planck mean efficiencies occur between the Bl-5(BHVA) ash from [245] and the sub-bituminous ash from [247], with about 0.7 and 0.35 for the absorption and scattering efficiencies, respectively.

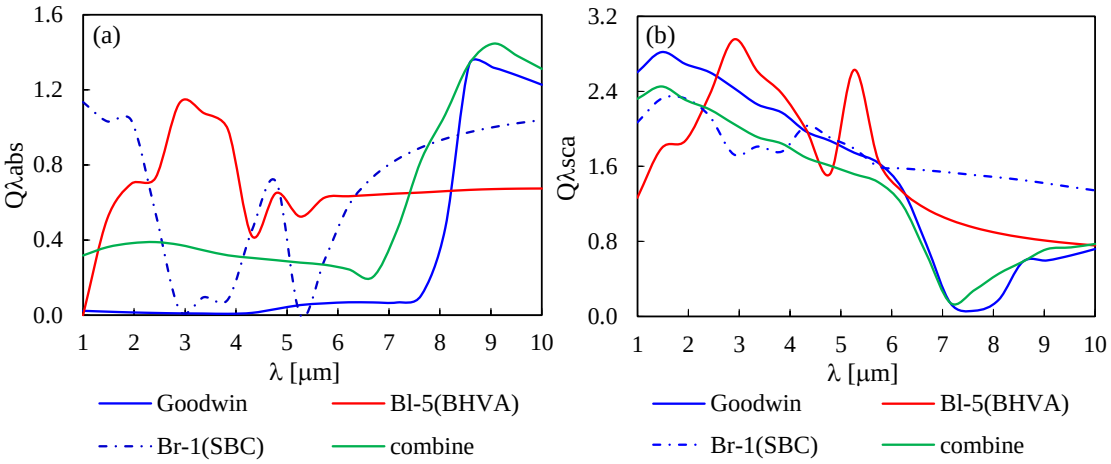

Figure 3.5: Radiative properties calculated from different spectral databases of ash, (a) absorption efficiency, and (b) scattering efficiency.

To date, there are not many spectral database measurements for ashes that have been published. Results from previous studies show significantly high spectral properties compared to the more recent studies of Goodwin. The properties of the ash calculated from the optical constants which are directly dependent on the composition of the ash, temperature and the accuracy of the measurement methods. The choice of data for the calculation of the radiative properties of the ash particle can result in a significant difference in the radiative heat transfer. The effect of the selection of the radiative properties of the ash on the radiative heat transfer are investigated in Chapter 4.

Six different types of coal have been considered, see Table 3.3, with the optical

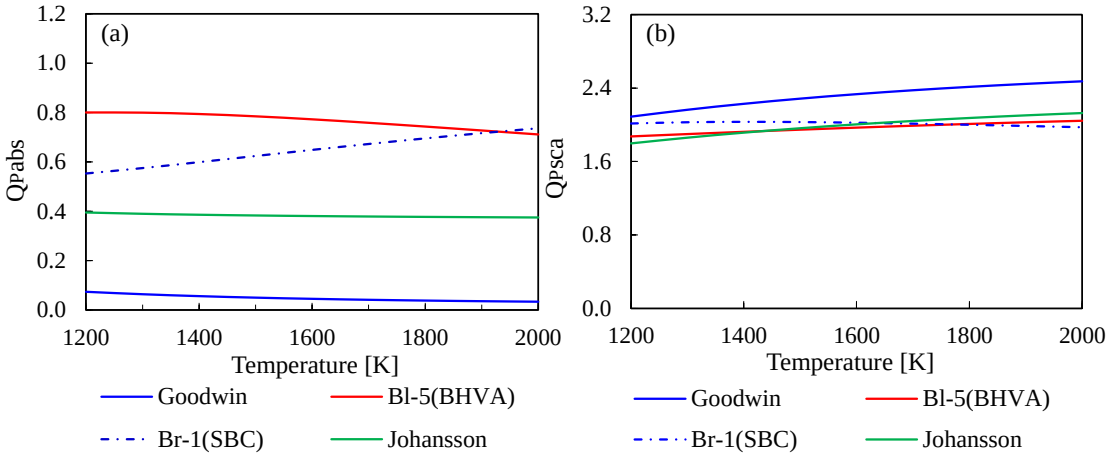

Figure 3.6: Planck mean optical constants for different types of ash, (a) absorption efficiency, and (b) scattering efficiency.

constants being measured within the wavelength ranges 0.8 μm to 5.53 μm and 3.0 μm to 22 μm, from [245] and [236], respectively. The refractive and absorptive indices are shown in Fig. 3.7, with the optical constants of the anthracite coal being significantly higher than that of other coals.

Table 3.3: Composition of coals used for the measurement of the optical constants.

Coals	%Carbon(C^{MAF})	%Volatile(V^{MAF})	Wavelength range
Anthracite[245]	93.00	2.50	0.8-5.53 μm
Bl-2(BHVA)[245]	88.10	21.10	0.8-5.53 μm
Bl-3(BMV)[245]	85.00	22.50	0.8-5.53 μm
Br-2(SBC)[245]	70.20	48.00	0.8-5.53 μm
Blind Cayon[236]	77.20	41.89	3.0-22.0 μm
Kentucky no.9[236]	66.40	34.90	3.0-22.0 μm

Results for the absorption and scattering efficiencies of the coals investigated are shown in Fig. 3.8. It is observed that the profiles of the absorption efficiencies are similar to those of the absorptive constants. In the same range of wavelength investigated, from 3 μm to 5.53 μm, the values of the absorption efficiencies for the coals investigated by [245] are much higher than those of [236]. Further, the Planck mean absorption and scattering coefficients of all the coals are almost

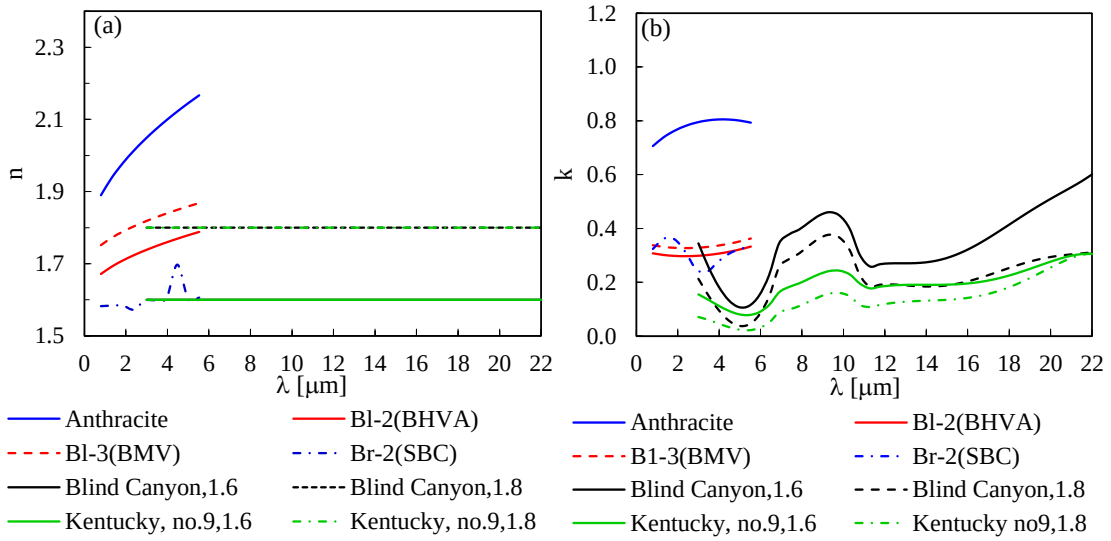

Figure 3.7: Optical constants for different types of coal, (a) refractive index, and (b) absorptive index.

independent of the temperature, Fig. 3.9, with the maximum difference between the coals can reach 0.3 for the absorption efficiencies and 0.4 for the scattering efficiencies. The Kentucky coal, which has a real part 1.8, has the lowest absorption efficiency and the highest scattering efficient compared to that of the other coals.

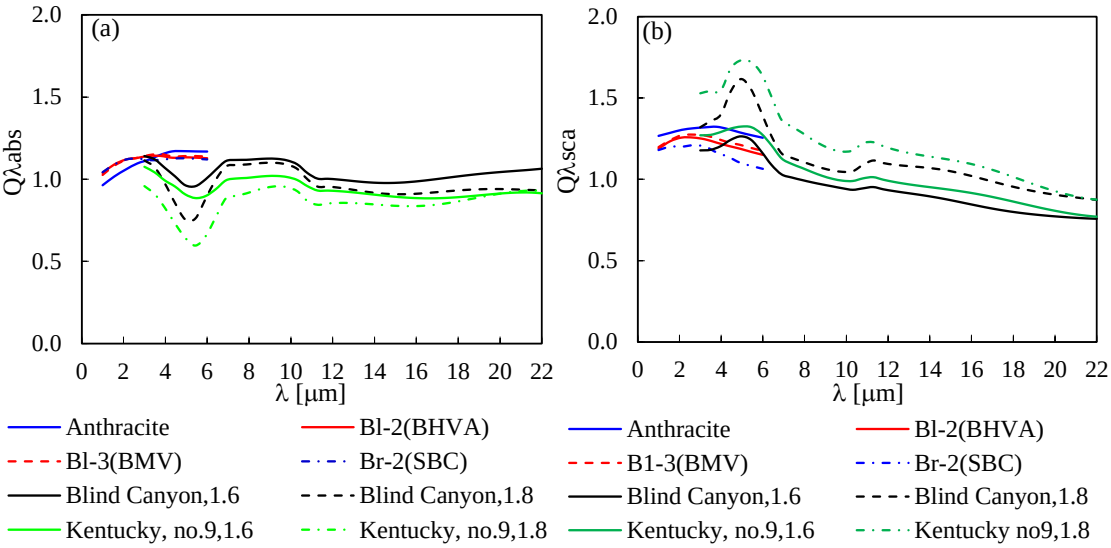

Figure 3.8: Radiative properties calculated from different spectral databases of coal, (a) absorption efficiency, and (b) scattering efficiency.

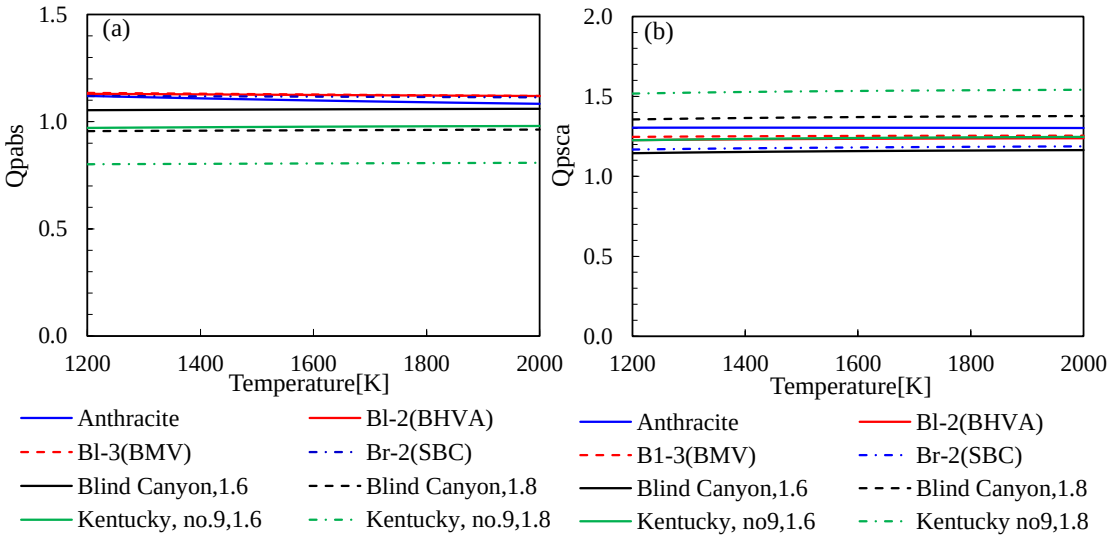

Figure 3.9: Planck mean radiative properties for different types of coal, (a) absorption efficiency, and (b) scattering efficiency.

3.1.3 Evaluation simplified approximations for the radiative properties of particles

The Mie theory is selected as a benchmark to evaluate approximate solutions developed for the simplification calculation of the radiative properties of the coal and ash particles. Approximations for calculations of the radiative properties of the ash [259, 272] and coal [259, 268, 272] are evaluated against the Mie theory which is validated in Section 3.1, using both wavelength-dependent and wavelength-independent optical constants. In the case of wavelength-dependent optical constants, the two recent experimental data are employed, namely the experimental measurement of Goodwin and Mitchner [247] for ash and data measurement of Manickavasagam and Mengüç [236] for Kentucky no.9 coal with n=1.8.

The validation of the Buckius and Hwang approximation [268] is shown in Fig. 3.10, with two values of the complex index of refraction being employed in the comparison with the Mie theory. The results are found to be in good agreement with the results obtained in the studies [133, 268].

Fig. 3.11 shows the radiative properties of the coal particle cloud calculated from two approximation solutions using the wavelength-independent and

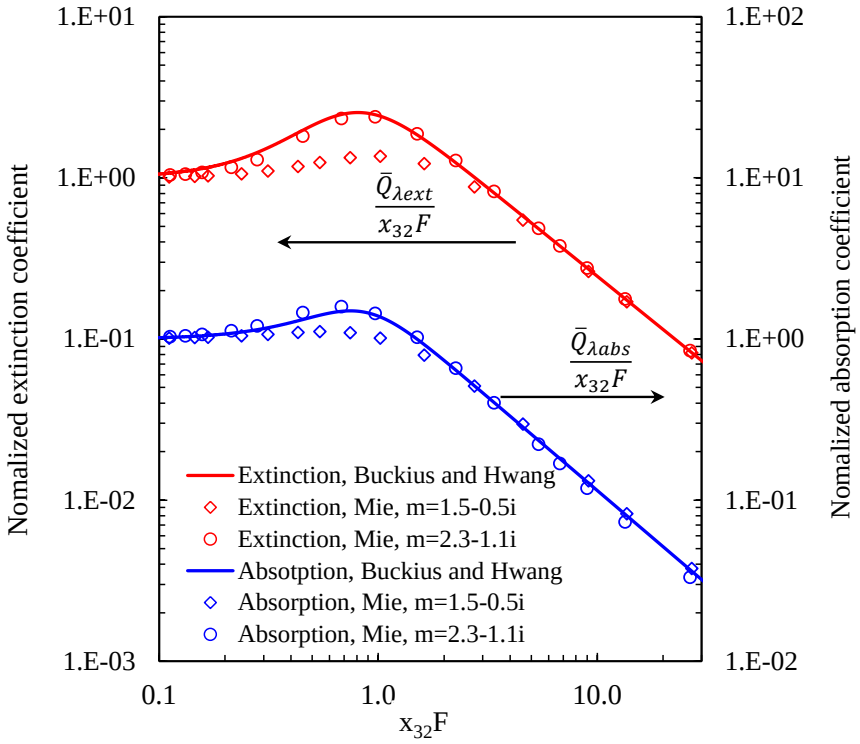

Figure 3.10: Extinction and absorption properties of coal calculated from the approximation of Buckius and Hwang [268].

wavelength-dependent optical constants. In terms of wavelength-independent optical constants, the approximation of Buckius and Hwang [268] shows better results compared to that of the approximation of Kim and Lior [259] and good agreement with the results calculated from the Mie theory, Fig. 3.11 (a), (b). However, significant errors occur when this approximation is applied using the wavelength-dependent optical constants, while the Kim and Lior [259] solution shows better results, Fig. 3.11 (c), (d).

The Planck mean properties of the coals using 2 approximate solutions are shown in Fig. 3.12. In this study, the approximation of Buckius and Hwang [268] is not mentioned because this approximation results in significant deviation compared to the Mie theory when it is used with the spectral data of Manickavasagam and Mengüç [236]. This is because the approximations of Buckius and Hwang do not depend on the optical properties of the coals. Therefore, this approximation has been considered as a crude approximation and not appropriate for

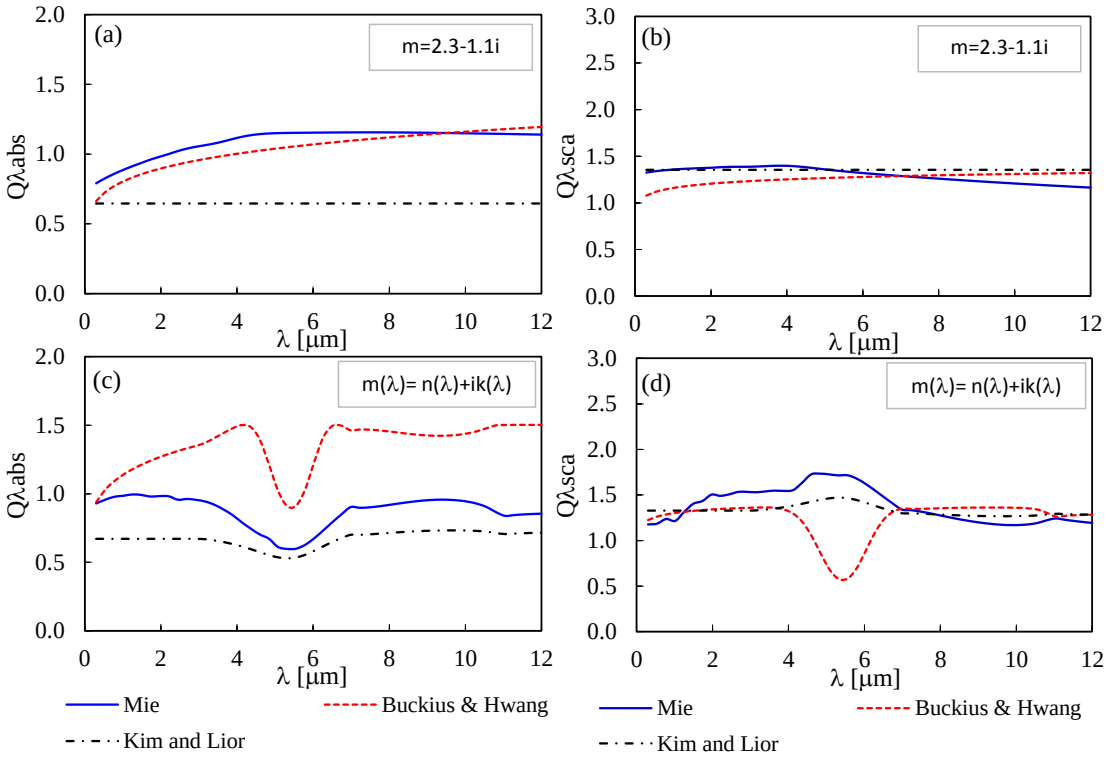

Figure 3.11: Comparison of the radiative properties of coal calculated from approximate solutions against the Mie theory, (a) absorption efficiency, and (b) scattering efficiency.

more accurate spectral data for different coals, having optical properties varying with wavelength, temperature, and particle size distributions [133]. Instead, a new correlation which has the same functional form as the correlations for the coal particles presented by Buckius and Hwang [268], and has been developed by Johansson [272], is used. The results show that the new correlation of Johansson [272] are in better agreement compared to that of Kim and Lior [259].

Three approximations for the radiative properties of ashes are mentioned in the present study, when using grey particle correlations. Two of those employed are from the study of Johansson [272], which is correlated based on two different sets of the complex index of refraction, namely ash1 and ash2. The third approximation, proposed by van de Hulst [271], and called the anomalous diffraction limit, was recommended to be used for ash by Kim and Lior [259]

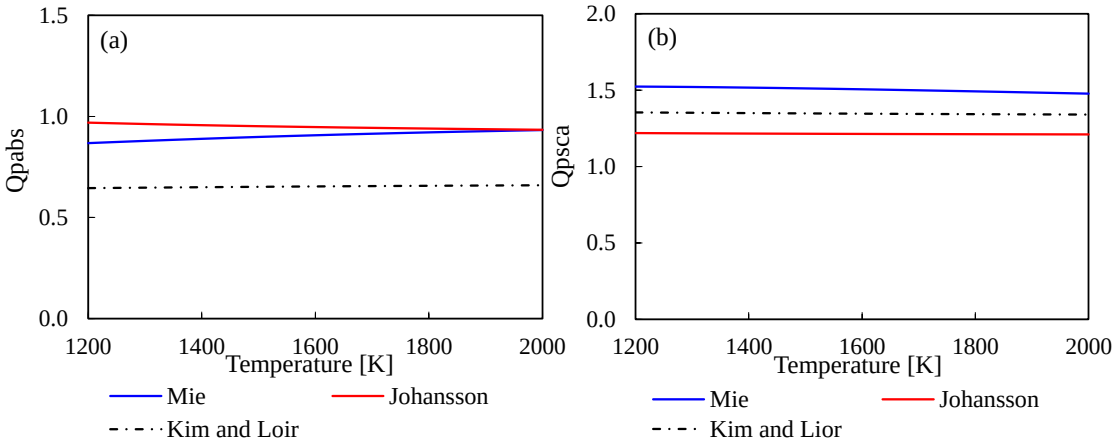

Figure 3.12: Planck mean radiative properties of coal calculated from different approximate solutions [259, 272] compared to the Mie theory, (a) absorption efficiency, and (b) scattering efficiency.

The results obtained for the Planck mean properties of the ashes are calculated from the three correlations and these are shown in Fig. 3.13. The anomalous diffraction limit and the ash1 show very good agreement with the Mie theory while the ash2 is much overpredicted. The large difference between the ash1 and ash2 can be explained by the two ashes being correlated based on two experimental databases which give significantly different absorption properties for the ash particles. The ash1 is correlated based on the experimental data of Goodwin and therefore the result is in very good agreement with the Mie theory. while the ash2 approximation was based on the data of [330], which has significant higher absorption properties compared to that of the Goodwin ash.

3.2 Evaluation of the radiation of the gas models

The LBL model is selected as a benchmark in order to evaluate the global models, NGWSGG and SLW, for the 1D case for both the air and oxyfuel conditions. In the 3D cases, the evaluation of the global models for the gas environment uses the SNB model as the benchmark. The radiative source term and the incident wall heat flux of the global models are compared against the benchmark with the

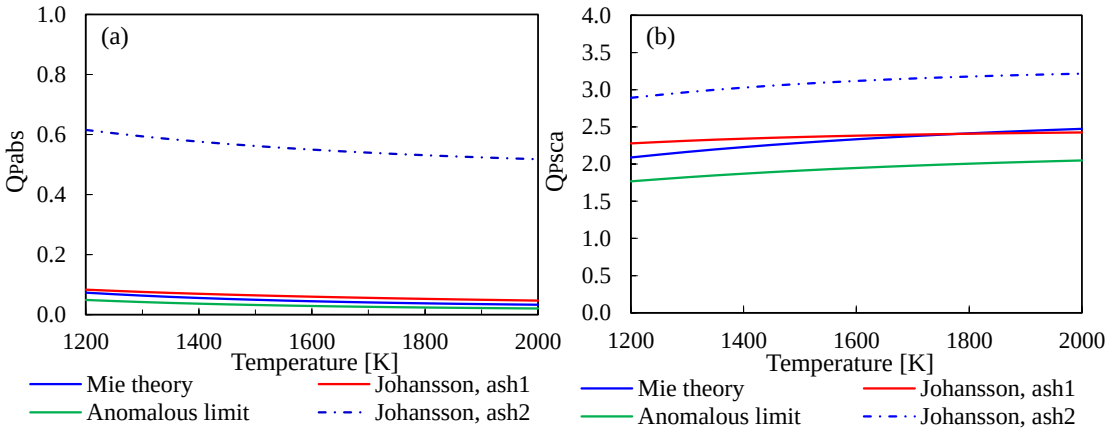

Figure 3.13: Planck mean radiative properties of ash calculated from the approximations [259, 272], (a) absorption efficiency, and (b) scattering efficiency.

relative error over the domains investigated being expressed as follows:

$$err = \frac{\int_N |\,(q_{b,i} - q_{gm,i})\,|}{\int_N |q_{b,i}|} \times 100 \tag{3.4}$$

where N is the number of elements in the domain investigated, and $q_{b,i}$, $q_{gm,i}$ are the source term and the incident wall heat flux of element i in the domain investigated for the benchmark and the global model, respectively.

3.2.1 1D-case evaluation

The non-correlated narrow-band solution developed by De Miranda and Sacadura [331], which was demonstrated to be in good agreement with the benchmark solution for different one-dimensional cases [149], is employed to solve the radiative heat transfer equation for a one-dimensional non-grey gas case.

3.2.1.1 Case description

The LBL model developed in this study, which is mentioned in Section 2.2.3.1, has been validated against the LBL model in the study of Chu at al. [186] for both the air and oxyfuel conditions. The medium is at a uniform pressure of 1 atm which is bounded by two parallel black plates which has a separation distance of 0.5 m which is divided into 20 equal elements with the temperature and species concentration, H_2O and CO_2, at each centre of the elements as shown in Fig. 3.14.

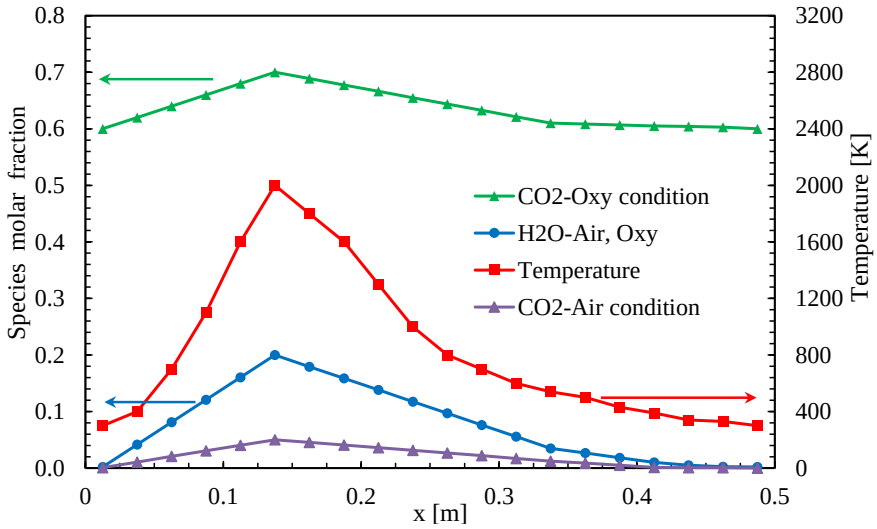

Figure 3.14: Temperature and CO_2 and H_2O molar fractions for both the air and oxyfuel conditions [186].

The concentration of the CO_2 under the oxy condition is higher than that in the air condition everywhere by about 0.6, while both conditions have the same H_2O concentration and temperature distribution. A similar set of parameters for the LBL model, using the HITEMP-2010 spectral database for both H_2O and CO_2, compared to that of [186] are selected, with a uniform spectral resolution of 0.02 cm^{-1} in a spectral range 150 cm^{-1} and 9300 cm^{-1} and a cut-off distance 20 half-width at half maximum (HWHM) being selected. Higher spectral resolutions, cut-off distances and wider spectrum were also examined. However, the influence of these parameters on the results is almost negligible for both the source term and the incident heat flux.

The radiative source term and heat flux results, see Figs. 3.15 and 3.16, show very good agreement with the LBL results of Chu et al. [186], except for the location of the peak temperature 1800 K, with the average differences in the source term and the heat flux for the air case being 7.4% and 6.6%, respectively. Larger differences are found for the oxy case, with approximately 7.6% and 9.7% for the source term and the heat flux, respectively. The differences can be due to the use of different solutions for the RTE and quadrature schemes in the two studies, with the DOM method and T3 quadrature schemes being employed in

the study of Chu et al. [186]. In this study, the same RTE solver is used for investigating the models in the 1D case. From the results evaluated, the LBL model developed can be used as the benchmark in order to evaluate the global models.

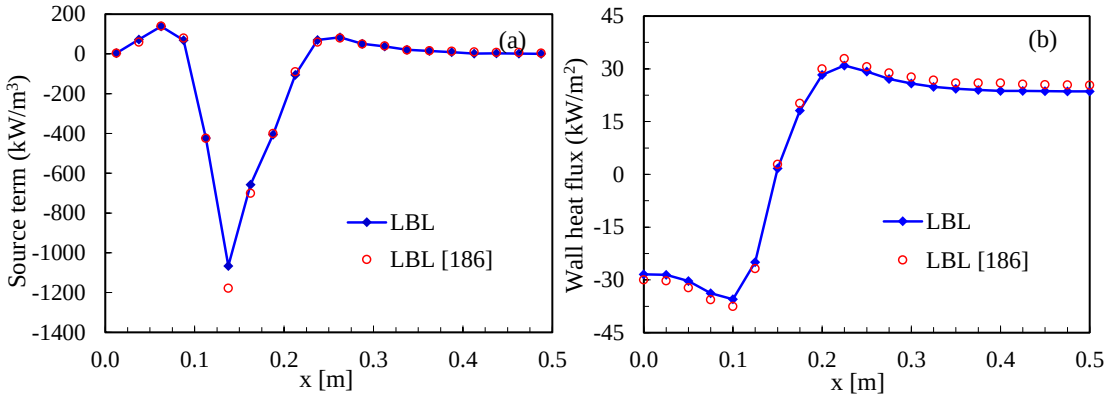

Figure 3.15: Validation of the LBL calculation for the air condition against the results of [186], (a) radiative source term, and (b) incident wall heat flux.

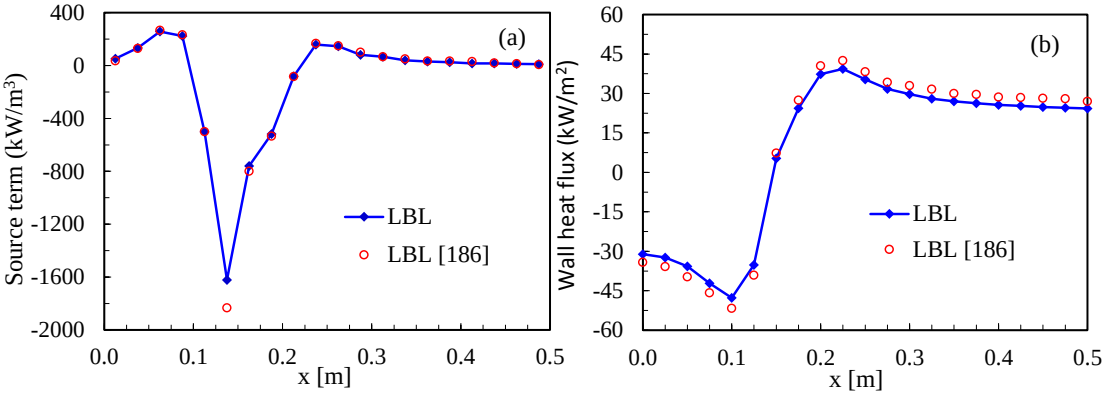

Figure 3.16: Validation of the LBL calculation for the oxyfuel condition against the results of [186], (a) source term, and (b) heat flux.

3.2.1.2 Validation of the global models in the 1D case

The validation of the global models in the 1D dimensional geometry are performed in two test cases. The first case, named C1, mentioned in Section 3.2.1.2, which is used to validation the LBL model for both the air and oxyfuel conditions. The second case, named C2, which was introduced in the study of Johansson et al.

[332] and it was used to validate the global model by Kangwanpongpan et al. [64], presents a non-isothermal and homogeneous oxyfuel environment, with the temperature profile along the path length between the two walls being expressed as

$$T = 1400 - 400\cos(2\pi x/L) \tag{3.5}$$

where x is the spatial coordinate, and L is the length of the one-dimensional environment. The boundary conditions on the 2 walls are assumed to be black and are at a temperature 700 K. The species concentration is assumed to be a dry flue gas recycling condition with the concentration of CO_2 being at 0.8 and the concentration of H_2O is given by

$$Y_{H_2O} = 0.12 + 0.04\cos(2\pi x/L) \tag{3.6}$$

The results of the case C1 for the radiative source term and the heat flux are shown in Figs. 3.17 and 3.18, respectively, for both the air and oxyfuel conditions. In this case, the results obtained for the global models show a much better agreement with the benchmark under the air condition compared to that of the oxyfuel condition. The NGWSGG model shows very good agreement with the benchmark for the air case (Fig. 3.17(a) and Fig. 3.18 (a)), with the relative deviations being about 4% and 10% for the heat flux and the source term, respectively, and these increase to about 22% and 16% under the oxyfuel condition. With the SLW model, increasing the number of gases beyond 10 does not affect the accuracy of the solution. The SLW model shows much better results compared to those of the NGWSGG model under the air condition, with about half the deviations being found for the heat flux and the source term. Under the oxyfuel condition, the SLW model produces a better result for the heat flux, however, a similar result has been found for the source term compared to that of the NGWSGG model. The significant deviation in the source term occurs at about the location x=0.14 m for both the models compared to the benchmark, where the temperature and species concentration reach maximum values.

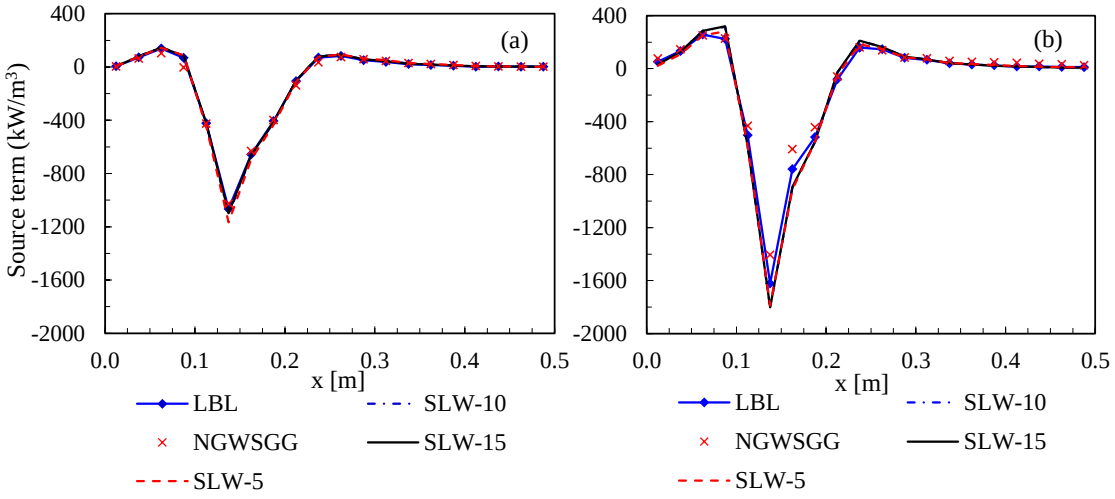

Figure 3.17: Radiative source term of the global models compared to the benchmark, (a) air condition, and (b) oxyfuel condition.

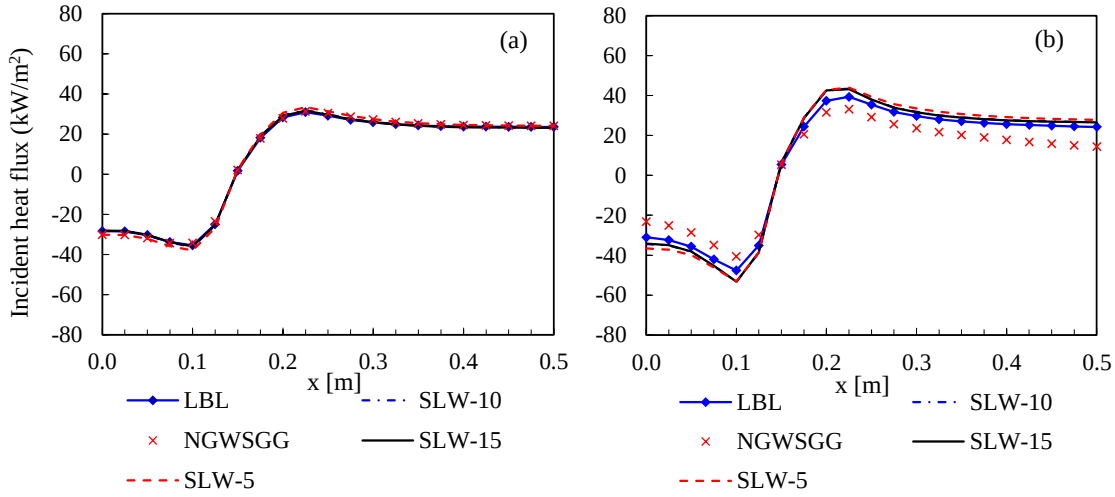

Figure 3.18: Incident wall heat flux of the global models compared to the benchmark, (a) air condition, and (b) oxyfuel condition.

Fig. 3.19 shows the results obtained for the radiative source term and the incident wall heat flux for case C2 under the oxyfuel condition, showing a very good agreement with the benchmark for both the NGWSGG and SLW models. The SLW model, with 10 grey gases, shows better results compared to those obtained in the NGWSGG model, with the discrepancies being about 7% and 4%, for the radiative source term and the heat flux, respectively, and about 11%

and 6%, respectively, for the NGWSGG model.

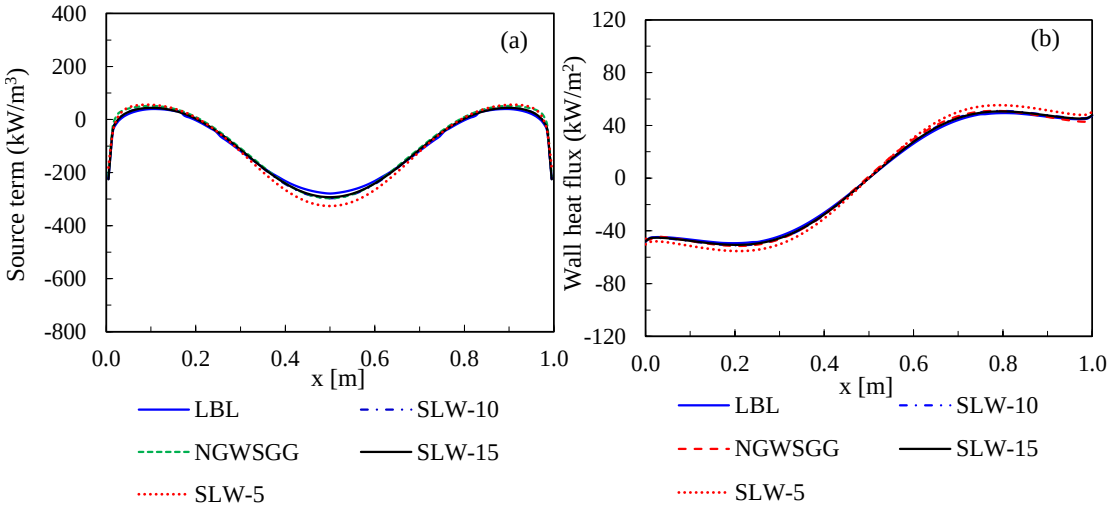

Figure 3.19: Comparation of the global models against the benchmark for, (a) radiative source term, and (b) incident wall heat flux.

3.2.2 3D-case evaluation

3.2.2.1 Case discription

The 3D cases used for the evaluation of the global models are based on the study of Liu [333]. And this geometry has been employed in many different publications [146, 334, 335]. The geometrical dimensions are 2 m × 2 m × 4 m with the black walls having a temperature 300 K. Both the air and oxyfuel conditions are investigated with the species concentrations shown in Table 3.4.

Table 3.4: Species concentrations for the air and oxyfuel conditions investigated.

Cases	CO_2(Vol%)	H_2O(Vol%)	N_2(Vol%)
Air case	10	20	70
Oxy case	85	10	5

The temperature profile for the two conditions are expressed as follows:

$$T = (T_c - T_e)\, f\left(\frac{r}{R}\right) + T_e \tag{3.7}$$

where T_c is the centreline temperature, T_e is the temperature at the end section, $z = 4$, and the function f is described as

$$f\left(\frac{r}{R}\right) = 1 - 3\left(\frac{r}{R}\right)^2 + 2\left(\frac{r}{R}\right)^3 \tag{3.8}$$

where r, R are the distance from the centreline and the half-width of the 3D enclosure, respectively. The temperature T_c is 400 K at $z = 0$ m and this value increases linearly to 1800 K at $z = 0.375$ m and then decreases linearly to 800 K at $z = 4$ m. The temperature profile is shown in Fig. 3.20 with the mesh size being $17 \times 17 \times 24$ elements which has been demonstrated to be grid independent and this mesh has also been employed in some later studies [146, 334]. The SNB results obtained from the study of Porter et al. [146], for both the air and oxyfuel conditions, are used as benchmarks to evaluate the global models for this study. The ANSYS FLUENT V17.0 CFD software was used, with the temperature, gas distributions and the gas global models, NGWSGG and the SLW models, are implemented by using UDFs. The DOM method was employed to solve the RTE with each octant of solid angle being divided into $N_\theta \times N_\phi = 3 \times 3$, but more refined solutions for $N_\theta \times N_\phi$ also were examined but the results obtained did not change significantly.

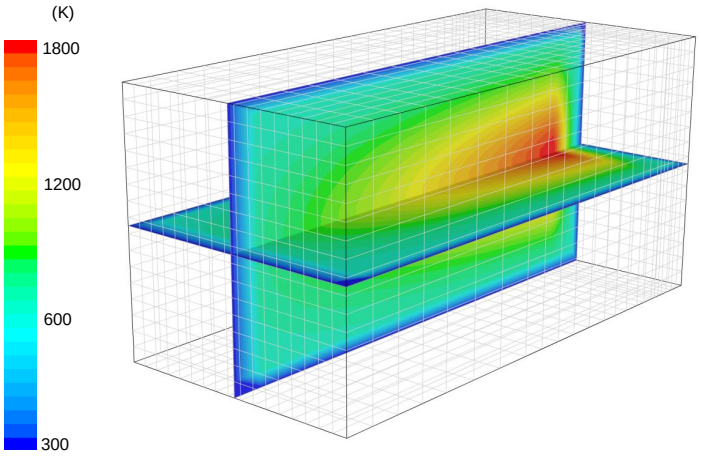

Figure 3.20: Temperature profile for the two centre planes for the 3D case investigated.

3.2.2.2 Results and discussion

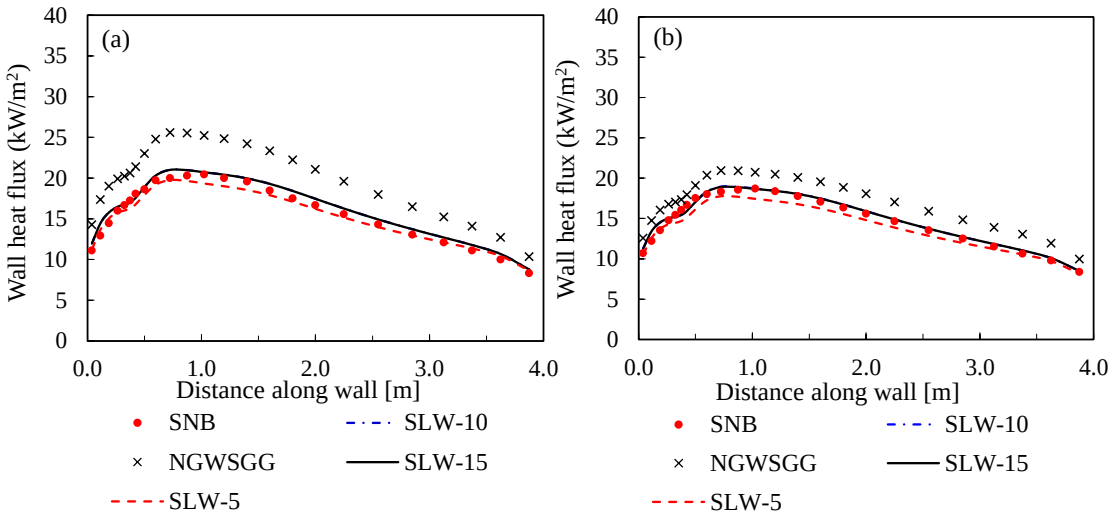

Figure 3.21: Incident wall heat flux results along wall centreline parallel the z-axis calculated from global models for the air and oxyfuel conditions compared against the SNB benchmark obtained by Porter et al. [146], (a) air condition, and (b) oxyfuel condition.

The results for the incident wall heat flux of the global models are shown in Fig. 3.21 for both the air and oxyfuel conditions. Both the NGWSGG and SLW models are in good agreement with the SNB benchmark, with much better results being obtained from the SLW model compared to those of the NGWSGG model for both the air and oxyfuel conditions. The NGWSGG model produces over-predicted results compared to those of the benchmark, with the errors being about 25% and 15% for the air and oxyfuel conditions, respectively. With the SLW model, the number of gases being about 10 can produce the accurate solutions and the results from the case having the number of gases being 10 show very good agreement with the benchmark, with the errors being less than 5% for both the air and oxyfuel conditions. It can be seen that the heat flux under the oxyfuel case is lower than that under the air case. This could be explained by the effect of the temperature profile and concentration of the participating gases. The higher concentration of CO_2 under the oxyfuel case can increase the emission of gases but this also increases the optical thickness which decreases the incident heat flux

to the wall. With the temperature profile in the investigated cases, the decrease in the incident heat flux is likely to increase the emissions under the oxyfuel condition, therefore, the incident heat flux under the oxyfuel condition is lower than that under the air condition.

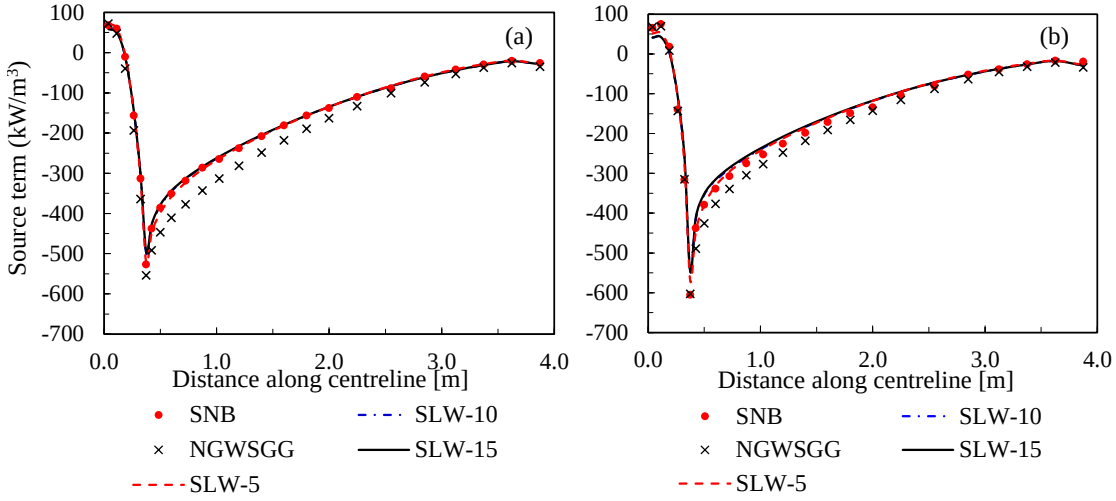

Figure 3.22: Radiative source term results along centreline (z axis) calculated from global models for the air and oxyfuel conditions compared against the SNB benchmark obtained by Porter et al. [146], (a) air condition, and (b) oxyfuel condition.

Fig. 3.22 shows the results obtained for the radiative source term of the global models compared to that of the benchmark. The NGWSGG model shows over-predicted results compared to those of the benchmark for both the air and oxyfuel conditions, with the errors being about 17% and 9% for the air and oxyfuel case, respectively. The SLW results are in very good agreement with the benchmark and the number of grey gas of 10 or higher shows much better results for the source term compared to those of the NGWSGG model. Conversely, this model requires much more computational time to run even for the case with number of grey gas being 5, see Table 3.5. It can be seen that the higher concentration of CO_2 results in a higher source term under the oxy case compared to that under the air case.

Table 3.5: Comparison of the computational time to reach a converged solution.

Models	NGWSGG	SLW-5	SLW-10	SLW-15
Ratio of computational time	1	40	48.57	62.86

3.3 Conclusions

This chapter has focussed on the evaluation of the radiation of gases and particles for the CFD modelling of pulverised coal combustion. In terms of the particle radiation, different experimental databases for the optical constants, wavelength-independent and wavelength-dependent optical constants, are evaluated using the Mie theory. The sensitivity of the particle properties to the spectral database has been investigated and different approximate solutions for calculating the radiative properties of the particle are also evaluated. In the case of the gas phases, the global models, NGWSGG and SLW models, are validated against the LBL and SNB models in 1D and 3D enclosures.

Different values of the wavelength-independent optical constants are obtained from previous studies for the ash and coal and these were employed to calculate radiative properties of a particle cloud in comparison to the results obtained from the wavelength-dependent optical constants. It is found that the radiative properties of the particles are more sensitive to the absorption part compared to that of the real part. The radiative properties of the particles are calculated assuming the wavelength-independent optical constants found in the previous studies for both the ash and coal are significantly different compared to those of the wavelength-dependent optical constants. Therefore, the more accurate data, which accounts for the non-grey properties of the particles, need to be considered when calculating the radiative properties of the particles.

Different spectral databases for the ashes and coals are used to calculate the radiative properties of a particle cloud. The results obtained show that there are large discrepancies between the results obtained for the radiative properties of the ash when different databases for the wavelength-dependent optical constants

are applied compared to that for coal. Because of the importance of ash on the radiative heat transfer in coal combustion systems, developing a spectral database for a wide range of ashes based on confident measurements are necessary and the choice of the database for the calculation of the radiative properties of the ash needs to consider carefully the effect of the composition of the ash, temperature and the accuracy of the measurement method.

Approximate solutions for calculating the radiative properties of the particles, coal and ash, can produce significant errors compared to the Mie theory. The correlation of Buckius and Hwang [268], for the calculation of the radiative properties of the ash and coal particles, are not appropriate for the more accurate spectral database developed later, such as the experimental data of Manickavasagam and Mengüç [236] for coal and Goodwin and Mitchner [247] for ash. Recent approximate solutions for the grey properties of particles of Johansson [272] was developed based on the spectral databases of coal and ash, and therefore they can give good agreement with the grey properties calculated from the Mie theory. In terms of the spectral properties of particles, the non-grey approximations introduced by Kim and Loir [259] for the coal and the anomalous approximation [271] for the ash show a good agreement with the Mie theory. However, using these solutions needs to be validated against the conditions of the particle size parameter and the complex refractive index.

The two non-grey global models for calculating the radiative properties of a gas, NGWSGG and the SLW models, are evaluated for both the 1D and 3D cases against the benchmark results for both the air and oxyfuel conditions. Both models show good agreement with the benchmark, with much better results being obtained when using the SLW model. However, the number of gases required for this model to reach an accurate solution of the SLW model, about 10, results in a significant computational cost in comparison to the use of the non-grey WSGG model, and the implementation of the SLW model is also more complex compared to that of the NGWSGG model.

4 Investigation of the radiation of the gases and particles in small and large scale furnaces

In this chapter, the effects of the gases and particles on the radiative heat transfer are investigated in small and large-scale boilers for both air and oxyfuel conditions. Three-dimensional enclosures are defined based on the parameters from the opposed wall-fired boiler with different scales, including the effect of the optical pathlength. In terms of the gases, two non-grey models, namely the NGWSGG and the SLW models, are evaluated under the air and oxyfuel conditions. The results for the radiation energy source term and heat flux are compared against the narrow-band CK model which has been found to be adequate for most practical applications [336]. In terms of the effect of the particles, the sensitivity of the radiative heat transfer to the spectral databases and approximations, which were mentioned in Chapter 3 for calculating the radiative properties of a non-uniform particle size distribution of coal/char and fly ash, are investigated. In addition, different particle radiation models, which are often employed for modelling the radiative heat transfer, are investigated in small and large-scale boilers. In these models, the NGWSGG model [64] has been employed to calculate the radiation of the gas phase coupled with the radiation interaction from the particulate phase, and the Mie theory, as well as the constant models, have been employed to describe the particle radiative properties. The results obtained have been compared against the benchmark created by the CK model for the gas and the narrow band spectral Mie theory for the particles.

In the cases used in this study, the temperature, particle profiles and gas distributions for air and oxyfuel conditions are defined in Section 4.1. The effect of the non-grey gas models on the radiative heat transfer are investigated in Section 4.2. Section 4.3 studies the effects of the particles on the radiative heat transfer, with the sensitivity parameters, temperature and concentration of the particles, being investigated in Section 4.3.1, the sensitivity of the spectral databases, approximations being investigated in Sections 4.3.2 and 4.3.3, respectively, and the evaluation of the radiation models for the particles is discussed in Section 4.3.4.

4.1 Case studies

The test cases used in this study are based on an opposed wall-fired boiler, namely the 1200 MW_{th} large-scale furnace [38] with the schematic of the furnace being shown in Fig. 4.1. The geometry of the boiler is simplified as a 3D enclosure, for a large-scale furnace. A small scale boiler is also investigated in this study, and this is scaled from the large-scale furnace with the scaled ratio being 1:10. The dimension of the two scales of the furnaces, are shown in Table 4.1.

Table 4.1: Dimentions of the small and large-scale furnaces used in this study.

Furnace	Thermal input [MW]	Dimension of furnace (m) Width x Depth x Height
Small-scale furnace		0.685 x 0.865 x 4.7
Large-scale furnace	1200	6.85 x 8.65 x 47

The concentrations of the gases under the air condition are uniform with 14% CO_2, 7% H_2O and 79% N_2 by volume. For the oxy-fired condition, the gas mixture contains 80% CO_2, 10% H_2O and 10% N_2 by volume.

The temperature distribution for the large-scale furnace are assumed such that the average heat flux to the waterwalls of the furnace are about 290-300 kW/m^2 [245]. The centreline temperature (T_0) is piecewise linear that increases

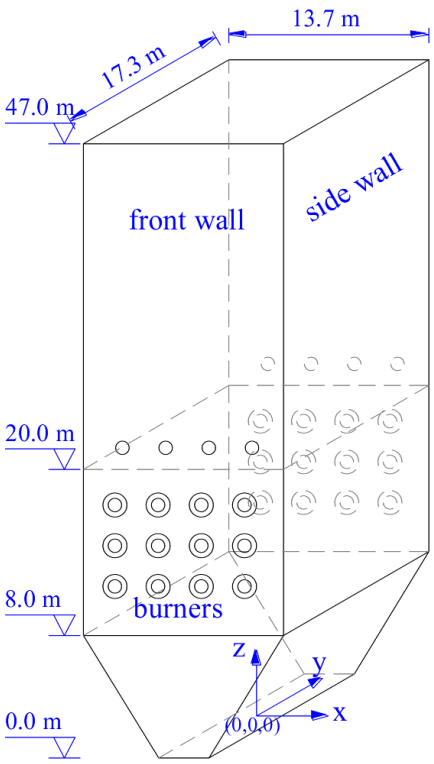

Figure 4.1: Schematic of the furnace geomertry of the 1200 MW_{th} opposed wall-fired boiler.

from 1300 K at the bottom of the furnace (z=0) to 2000 K at the burner region. The temperature remains constant at 2000 K in the burner region (0.8 m $\leq z \leq$ 2.0 m for the small-scale furnace and 8.0 m $\leq z \leq$ 20.0 m for the large-scale furnace) and then decreases to 1500 K at the exit point (at z = 4.7 m and 47 m for the small and large-scale furnaces, respectively). The temperature distribution on a cross section are adapted from [326], with the temperature of a cell i on the cross section at the location z_i of the centreline being given as follows:

$$T_{ci} = T_{min} + \frac{1}{2}\left(T_{xi} - T_{min}\right)\left[1 + \cos\left(\pi \frac{y_i}{1.4 * y_{max}}\right)\right] \tag{4.1}$$

where $T_{min} = T_{wall} + 850$ K, y_i is the component coordinate of the cell i , and T_{xi} is the temperature of the cells on the axis x along the burner wall, is defined as

follows:

$$T_{xi} = T_{min} + \frac{1}{2}\left(T_{zi} - T_{min}\right)\left[1 + \cos\left(\pi \frac{x_i}{1.1 * x_{max}}\right)^3\right] \tag{4.2}$$

where T_{zi} is the temperature on the centreline line at the location z_i along the furnace, and x_{max}, y_{max} are the distance from the centreline to the side and front walls of the furnace, respectively. The temperature profile in the furnaces are shown in Figs. 4.2 and 4.3.

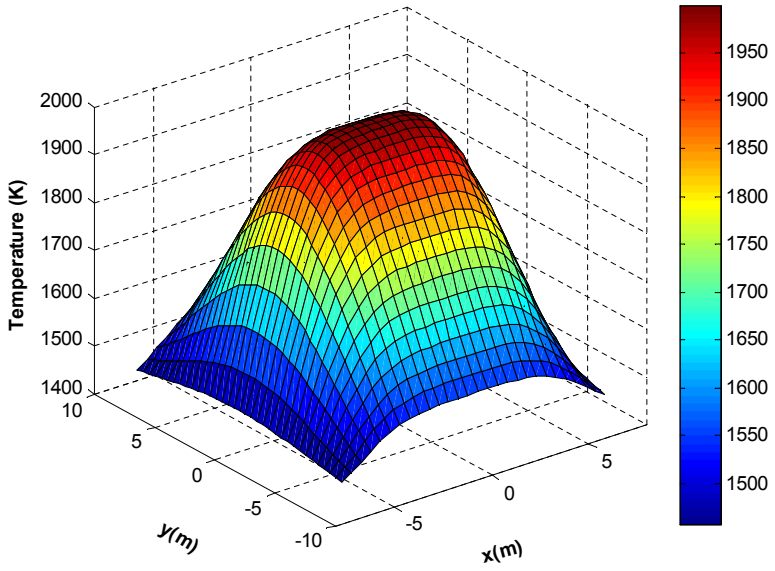

Figure 4.2: The temperature profile at cross section in the burner region of the large-scale furnace.

The concentration of the coal/char and the ash are expressed as a projected surface area per unit volume. The maximum concentration of the coal/char is 1.5 m^2/m^3, which is obtained in the centre of the flame region by modelling the 250 kW facility, and a similar value has been reported in [327] from a 100 kW facility. The maximum concentration of the fly ash is 0.25 m^2/m^3 [327]. The concentration of the particles of a cell i on the cross section at z_i on the centreline is based on [326, 327] and is adapted along the furnace as follows:

$$f_{ci} = \frac{1}{2} f_{cx}\left[1 + \cos\pi\left(\frac{y_i}{y_{max}}\right)^4\right] \tag{4.3}$$

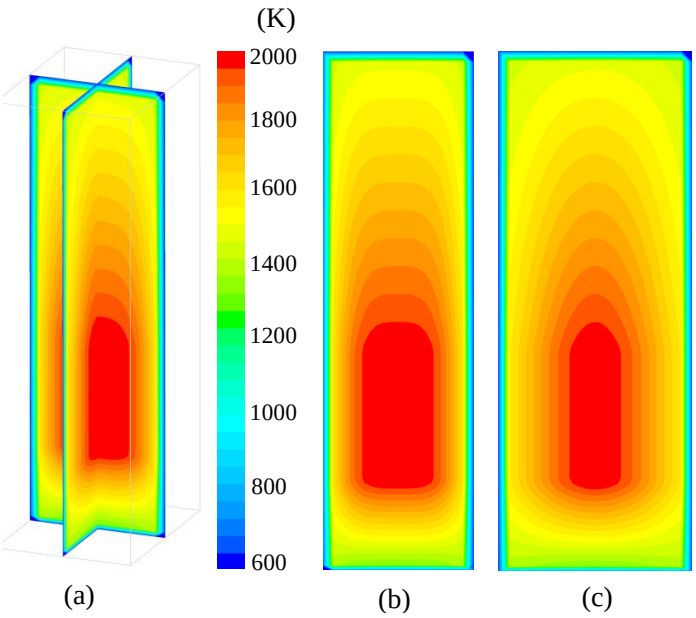

Figure 4.3: Temperature profile of the small and large-scale furnaces used in this study at, (a) the centre at cross-sections, (b) central cross-section along the front wall and (c) central cross-section along the side wall.

$$f_{ai} = 0.25 - \frac{1}{2} f_{ax} \left[1 + \cos \pi \left(\frac{y_i}{y_{max}} \right)^4 \right] \tag{4.4}$$

where f_{ci}, f_{ai} are the concentrations of the coal/char and the ash at the cell i, respectively, y_i is the component coordinate of the cell i, and f_{cx}, f_{ax} are the concentrations of the coal/char and the ash of the cell on the x axis corresponding to the cell i, respectively, which are defined as follows:

$$f_{cx} = \frac{1}{2} f_{cz} \left[1 + \cos \pi \left(\frac{x_i}{x_{max}} \right)^4 \right] \tag{4.5}$$

$$f_{ax} = \frac{1}{2} f_{az} \left[1 + \cos \pi \left(\frac{x_i}{x_{max}} \right)^4 \right] \tag{4.6}$$

where x_i is the component coordinate of the cell i, and f_{cz}, f_{az} are the maximum concentrations of the coal/char and the fly ash at the cross section z, respectively. f_{cz}, f_{az} increase linearly from the values 0 at z=0 to 1.5 and 0.25 at the burner region for the coal/char and the fly ash, respectively. Also these values are kept

constant in the burner region and then decrease to zero at the exit point of the furnace. Figs. 4.4 and 4.5 show the distributions of the coal/char and ash at a cross section in the burner region, respectively. UDFs are used to implement the temperature, gas and particle distributions in the CFD Fluent software.

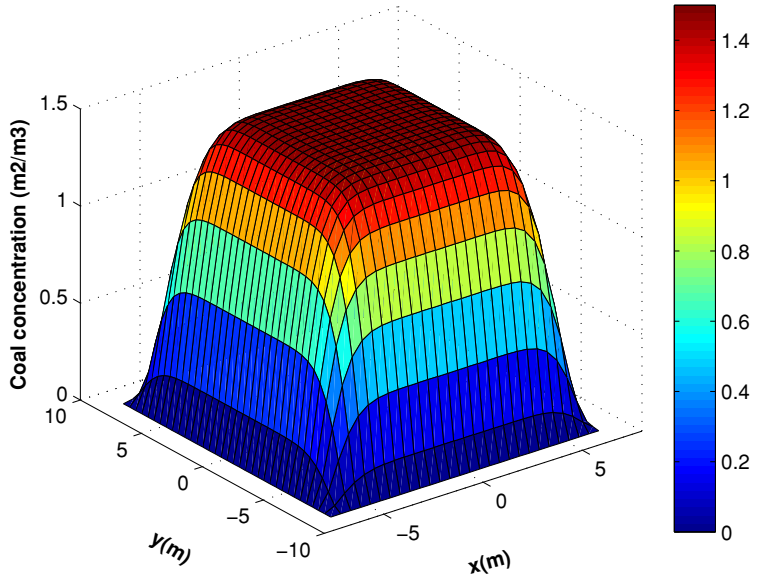

Figure 4.4: The distribution of the coal concentration in the burner region.

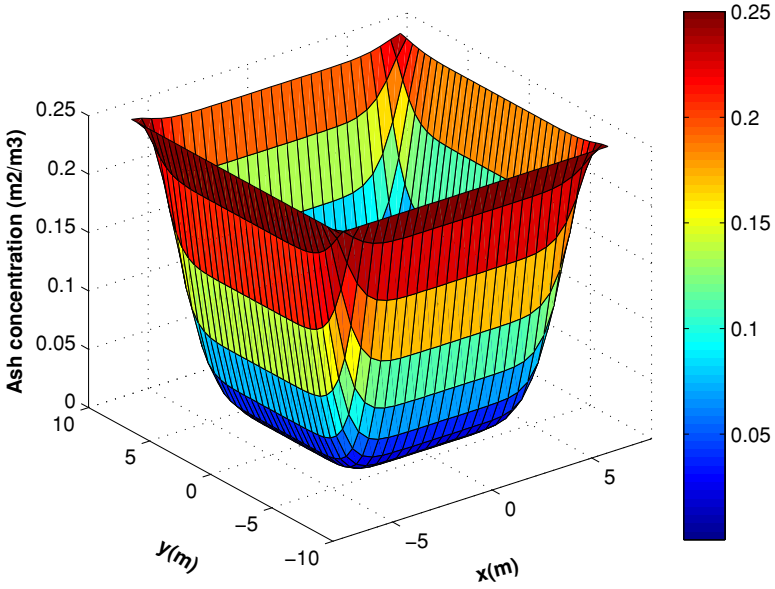

Figure 4.5: The distribution of the ash concentration in the burner region.

4.2 Investigation of the radiation of the gases

In this section, two global models for the radiative properties of the gases, the NGWSGG and SLW models are evaluated for the small and large-scale furnaces without the presence of particles under both the air and oxyfuel conditions. The radiation results, the total heat flux and the radiative source term, are compared against the results obtained from the CK model. The number of grey gases used in the SLW model is 10, and this was validated in Chapter 3 as being an optimal value for the SLW model.

The results obtained for the total heat flux transfer through the side wall of the furnace and the radiative source term along the centerline of the small-scale furnace for both the air and oxyfuel conditions are shown in Figs. 4.6 and 4.7, respectively. The results for both global models show a good agreement with the benchmark. A slight difference results between the SLW and NGWSGG models under the air condition and both the global models show very good agreement with the benchmark for both the heat flux and the source term, with the errors being less than 5% for heat fluxes and 3% for the source terms. However, much larger errors have been found for the oxyfuel condition, especially, for the NG-WSGG model. It has been found that the NGWSGG model produces about 15% and 13% errors for the heat flux and source term, respectively. While the SLW model shows much better results, with about 3% and 6% errors for the heat flux and source term, respectively. It can be seen that the heat flux and the source term under the oxyfuel condition are much higher compared to those under the air condition for all the cases and the largest difference being found for the NG-WSGG model, being about 33% and 30% higher for the heat flux and the source term, respectively. The higher heat flux and radiative source term under the oxy-fuel condition could be due to the increase in the gas absorption coefficient when there is a high presence of the CO_2 concentration under the oxyfuel condition, which increases the heat emission from the gases. The higher concentration of CO_2 can increase the optical thickness but this increase can be eliminated by the effect of the temperature profile, with a high temperature in the wall region. In

addition, it can be seen that, along the furnace, the heat flux and the source term obtain their highest value at the flame region for all cases. The high value of the heat flux and source term in the flame region are due to the high temperature in this region and this results in a high heat emission from the gas. Also, there are some sharp changes in the values of the source term at the bottom, top and the furnace. This is can be explained by the sharp changes in the gradient of the temperature in these regions along the furnace and this changes the local incident radiation.

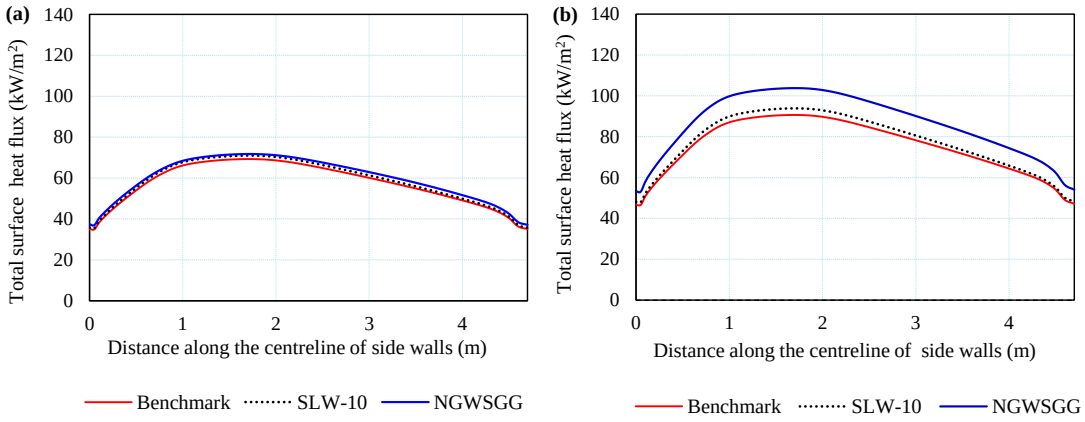

Figure 4.6: Surface heat flux in the side wall along the small-scale furnace for gas radiation only, (a) air-fired condition, and (b) oxy-fired condition.

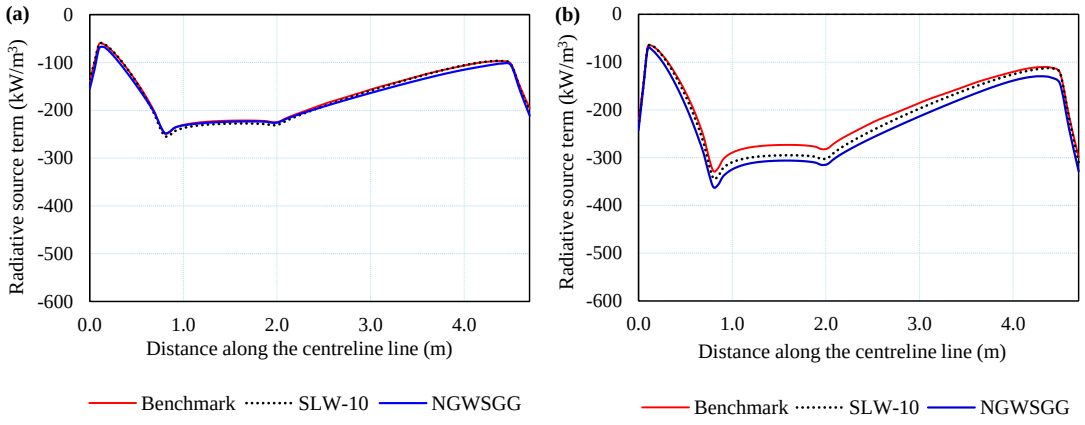

Figure 4.7: Radiative source term along the centreline of the small-scale furnace for gas radiation only, (a) air-fired condition, and (b) oxy-fired condition.

The results for the large-scale furnace are shown in Figs. 4.8 and 4.9 for both the air and oxyfuel conditions. Similar to the small scale, the heat flux and the source term under the oxyfuel condition are higher compared to those under the air condition. However, the average heat flux obtained from the large-scale furnace is much higher than that from the small-scale furnace for both the air and oxyfuel conditions, with about 130 kW/m^2 and 160 kW/m^2 of the large-scale furnace in comparison to about 60 kW/m^2 and 80 kW/m^2 of the small-scale furnace for air and oxyfuel combustion, respectively, while the source terms are much lower. The higher wall heat flux can be explained by the increase in the furnace size and this results in a wider isothermal region which has a high temperature and this increases the incident heat flux to the wall of the furnace although the high optical pathlength can decrease the the emission of the incident radiation from the centreline region. Correspondingly, there is an enhancement of the the isothermal flame region under the large-scale furnace and this decreases the local incident radiation in this region and this results in the lower of radiative source term. The average total heat flux through the walls for different scales of the boiler furnaces are shown in Fig. 4.10. It can be observed that the heat flux increases with the increasing of the furnace size for all the investigated cases. However, the errors between global models compared to the benchmark appears to be less sensitive to the scales of the furnace.

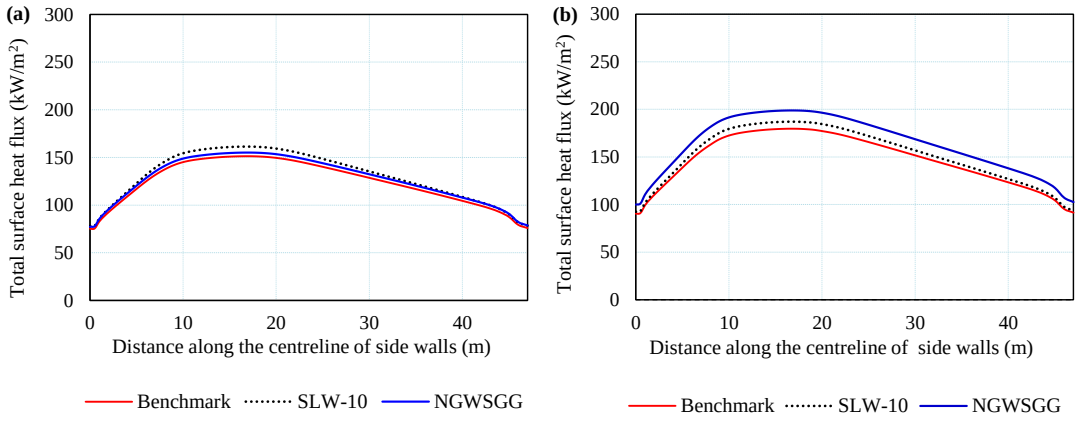

Figure 4.8: Surface heat flux on the side wall along the large-scale furnace for gas radiation only, (a) air-fired condition, and (b) oxy-fired condition.

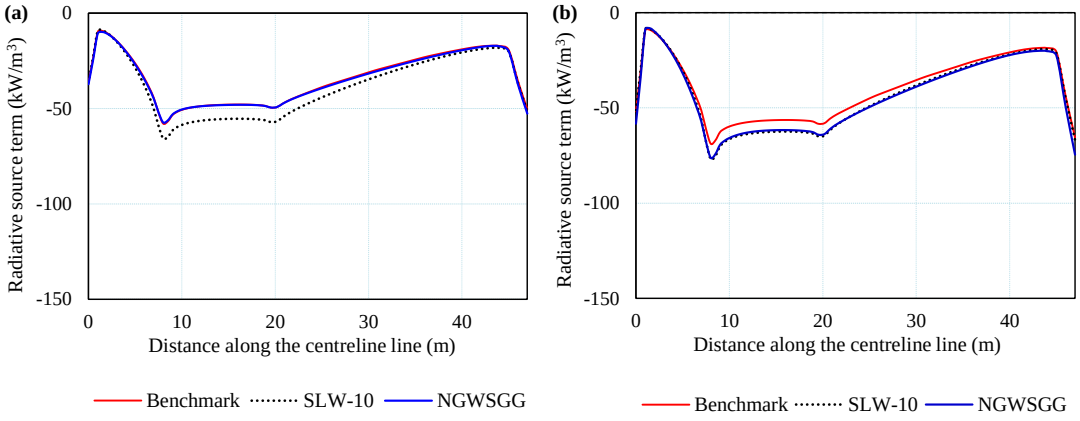

Figure 4.9: Radiative source term along the centreline of the large-scale furnace for gas radiation only, (a) air-fired condition, and (b) oxy-fired condition.

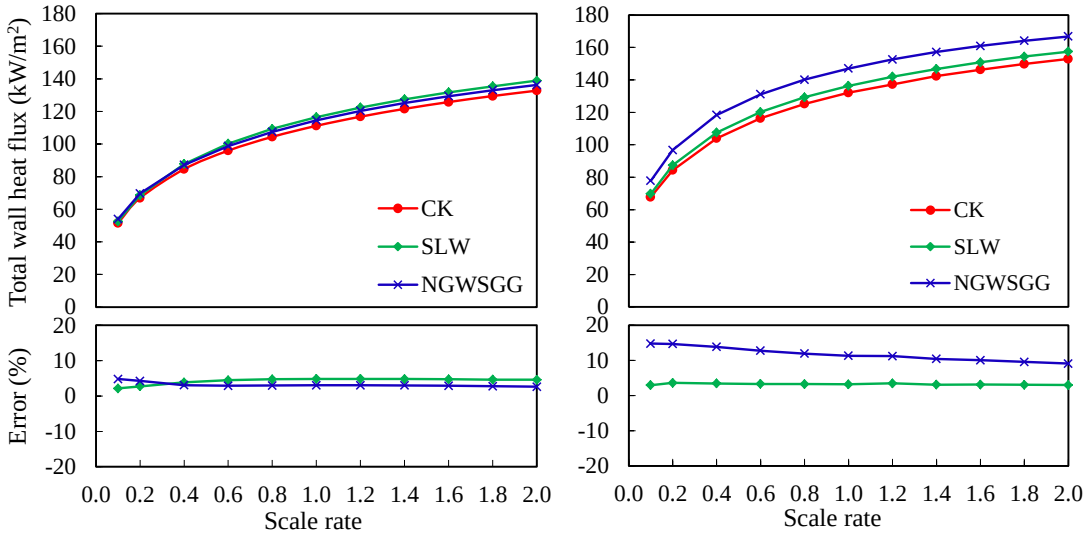

Figure 4.10: Average total surface heat flux for different scales of the boiler furnaces for both the air and oxyfuel conditions for gas radiation only, (a) air condition, and (b) oxyfuel condition.

4.3 Investigation of the radiation of the particles

The particle distribution selected is non-uniform and is described by the Rosin-Rammler distribution [233], see Equation (2.100) and the parameters for the particle size distribution are mentioned in Section 3.1. The averaged spectral

absorption and scattering efficiencies of a particle cloud are calculated by an integration over the particle diameter range of the number particle size distribution function, $f_n(D)$, as given by [235], namely

$$\overline{Q}_\lambda = \frac{\int_0^\infty Q_\lambda(D) D^2 f_n(D) \mathrm{d}D}{\int_0^\infty D^2 f_n(D) \mathrm{d}D} \tag{4.7}$$

where $Q_\lambda(D)$ is the spectral absorption or scattering efficiency of a particle having a diameter D at a wavelength λ, and $\overline{Q}_\lambda$ is the average spectral absorption or scattering efficiency of a particle cloud. The Planck mean properties of a particle cloud are defined as follows:

$$Q_p = \frac{\int_0^\infty \overline{Q}_\lambda I_{\lambda b} \mathrm{d}\lambda}{\int_0^\infty I_{\lambda b} \mathrm{d}\lambda} \tag{4.8}$$

where $I_{\lambda b}$ is the spectral blackbody emissive at the temperature T.

The spectral absorption or scattering efficiency of a particle, $Q_\lambda(D)$, is calculated from the Mie theory [337]. The particle effects are accounted for as described in Equation (2.60) with the equivalent absorption coefficient κ_p, and scattering coefficient σ_p being defined as follows:

$$\kappa_p = Q_{p,abs}.A_p \tag{4.9}$$

$$\sigma_p = Q_{p,sca}.A_p \tag{4.10}$$

where $A_{p,n}$ is the projected surface area of the particle in the volume, and $Q_{p,abs}$, $Q_{p,sca}$ are the Planck mean absorption and scattering efficiencies of a particle cloud.

4.3.1 Sensitivity study of the parameters of the particles

The concentration and temperature profiles of particles, which are presented in Section 4.1, are assumed based on experimental measurements and CFD studies. These parameters can be different depending on the type of furnace, fuels and operating conditions. In this section, the sensitivity of the radiative heat transfer

to the temperature and concentration of the coal and fly ash are investigated for different scales of the furnace.

Fig. 4.11 shows the total wall heat flux results calculated from the different temperature values of the coal for both the air and oxyfuel conditions. It can be observed that the total wall heat flux is significantly sensitive to the temperature of the coal, increasing with an increase in the temperature of the coal. In comparison to the case of having the temperature of the coal assumed in Section 4.1, the average heat flux decreases approximately 20% when the temperature of the coal decreases by 100 K. Under the oxyfuel condition, the behaviour of the wall heat flux is different compared to that of the air condition, depending on the temperature of the coal. In particular, the heat flux under the oxyfuel condition is slight higher than that under the air condition when the temperature of the coal is equal to that of the gas and this is in contrast to the cases with the temperature of the coal increasing by 100 K or 200 K. The higher optical pathlength under the oxyfuel condition can reduce the emission of the coal particles to the wall. Therefore, when the effect of the coal is dominant by a high temperature being assumed for the coal, the heat flux under the oxyfuel condition can be lower than that under the air condition although the heat flux under the oxyfuel condition is higher in the case when only gas is considered. In general, when having the presence of particles, the difference between the heat flux under the air and oxyfuel conditions becomes much less than that in the case when having only the gas being considered.

The effect of the concentration of the coal and ash particles to the total wall heat flux are shown in Fig. 4.12 for the air condition. In terms of the coal, it can be seen that the wall heat flux increases with an increase in the value of coal concentration and the heat flux is much more sensitive under the thin optical pathlength compared to the large optical pathlength. The large sensitivity in the small scale furnaces can be explained by the effect of the optical thickness to the reducing of the incident radiation from the coal being almost ignored. For the large-scale furnaces, it is clear that the increase in the concentration of the

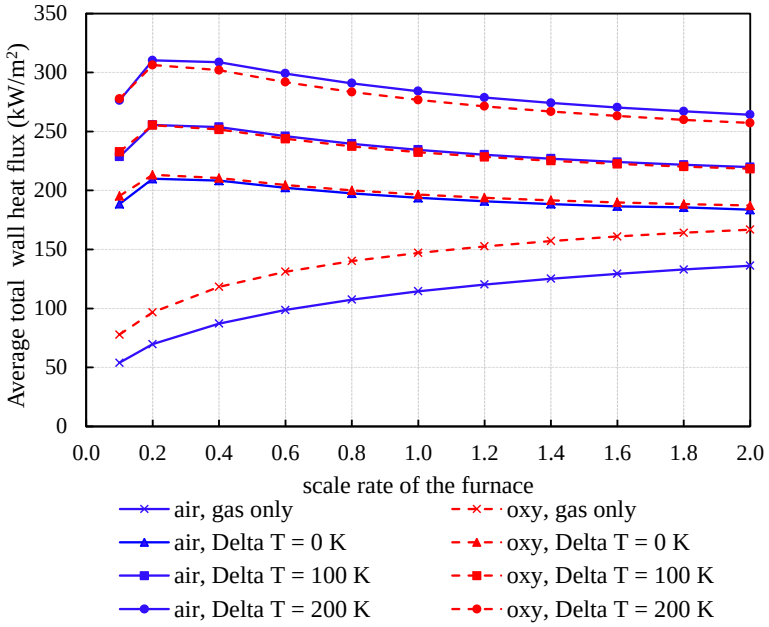

Figure 4.11: Sensitivity of the temperature of the coal to the radiative heat transfer for the different scales of the furnace under both the air and oxyfuel conditions.

coal, one side, increases the emissions from the particles, on the the other side it causes an increase in the optical thickness, which reduces the incident radiation. In terms of the ash, the increase of the ash concentration results in an increase in the heat flux but the effect of the ash in the investigated cases appears to be very small to the average heat flux through the walls of the furnace for both the small and large-scale furnaces. The smaller effect of the ash can be explained by its low temperature and concentration in the flame region, where the contribution of the coal is significant to the wall heat flux. The high sensitivity of the heat flux to the concentration of the ash occurs in the burnout region but the contribution to the average heat flux is low because of the lack of presence of the coal and the low temperature gradient.

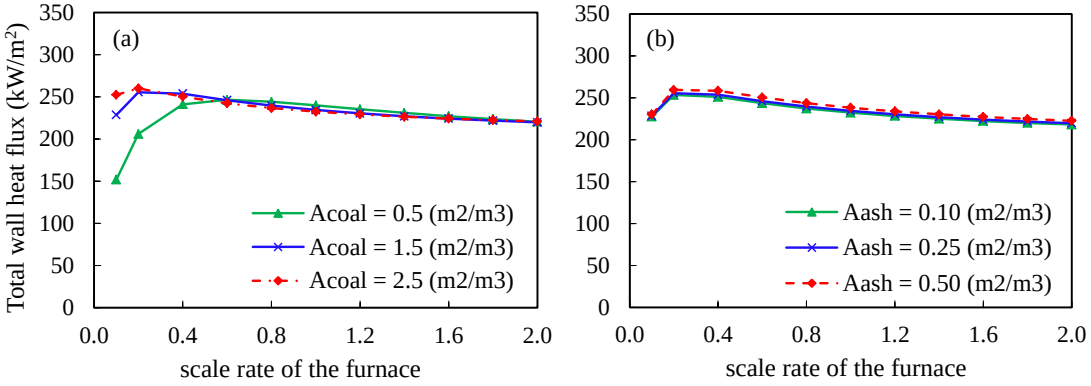

Figure 4.12: Sensitivity of the concentration of particles to the radiative heat transfer under different scales of the furnace for the air condition (a) effect of the concentration of the coal , and (b) effect of the concentration of the ash.

4.3.2 Effects of the optical properties on the radiative heat transfer

The sensitivity of the radiative heat transfer to the spectral databases for both the coal and ash are investigated in this section, by employing 8 databases for coal and 4 databases for ash. The NGWSGG model is employed to calculate the properties of the gas and the properties of the particles are described using the Planck mean coefficients. Using these models to describe the radiative properties of the gas and particles is appropriate because using the spectral models for both the gas and particles for the 3D case requires a significant computational time. Further, a similar model has been performed in the 1D case [272] and this produce a relative small error of about 2% in comparison to the case when using the SNB model for the gas and the spectral Mie for the particles.

Figs. 4.13 and 4.14 show the sensitivity of the radiative heat transfer to the spectral databases employed to calculate the radiative properties of the particles for both the small and large scale furnaces. The total surface heat flux and the radiative source term are calculated from the spectral databases of 8 coal types under the air condition. For the small-scale furnace, Fig. 4.13 shows that the relative difference between the maximum result from the minimum result is ap-

proximately 10% for both the total surface heat flux and the radiative source term, with the lowest results being from the Kentucky, no.9 coal which has $n = 1.8$. The radiative heat transfer appears to be less sensitive to the coal database selected for the large-scale furnace. The selection of the spectral coal database can vary by about 2% and 6% for the total surface heat flux and radiative source term, respectively. This can be explained by the higher absorption properties of the coal increasing the emissions but, on the other hand, it can decrease the transmission of this emission by the increase in the optical thickness in large-scale furnaces. Also, the source term in the large-scale furnace is significantly lower than that in the small-scale furnace. This is because the wider isothermal region in the large-scale furnace increases the local incident radiation to the elements on the centreline and this decreases the radiative source term. Also the sensitivity study has examined for the oxyfuel condition. However, there is not much difference in the effect of the spectral databases of the coal to the radiative heat transfer under the oxyfuel condition compared to that under the air condition.

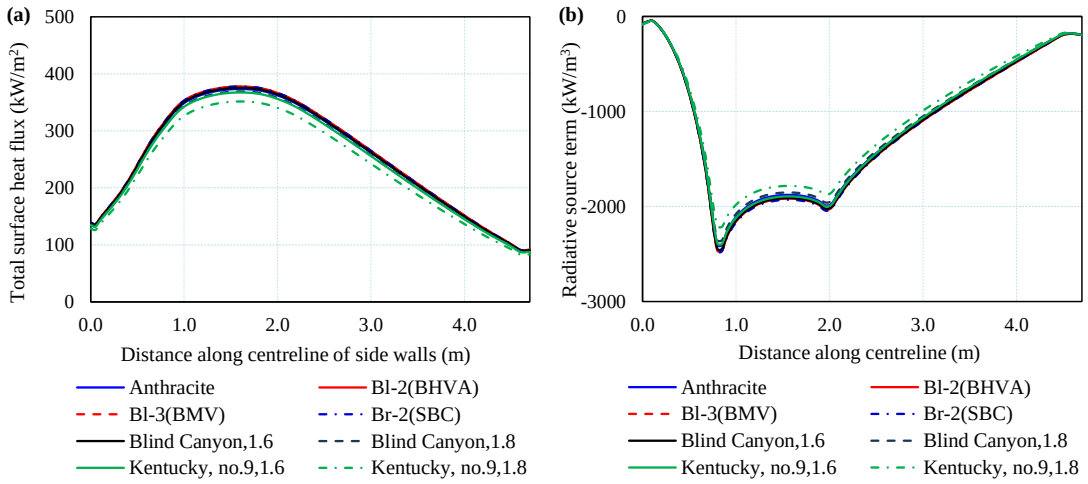

Figure 4.13: Effect of the optical properties of the coals on the radiative heat transfer under the small-scale furnace of the air case through the size wall for (a) total surface heat flux, and (b) radiative source term.

Figs. 4.15 and 4.16 show the total surface heat flux and the radiative source term with different spectral databases for the fly ash that is being employed. The

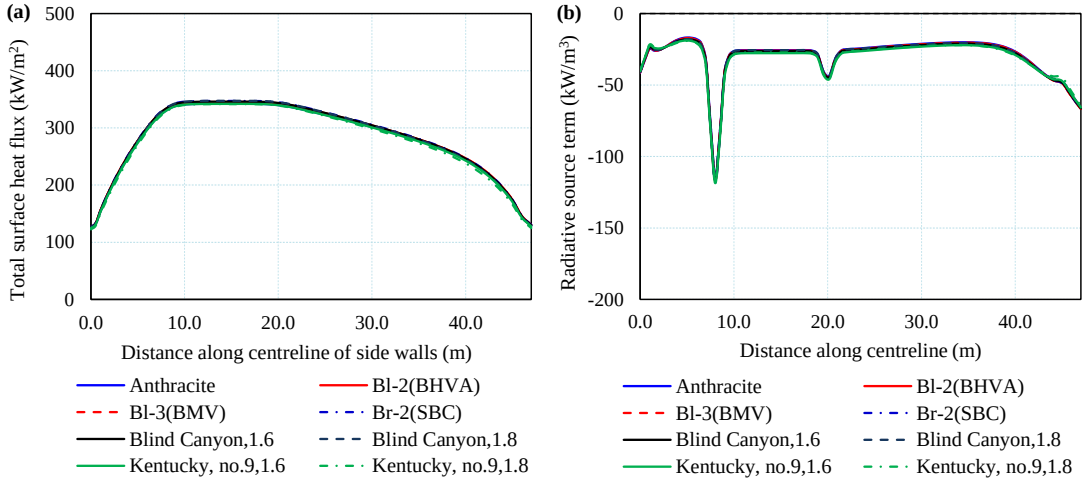

Figure 4.14: Effect of optical properties of the coals on the radiative heat transfer under the large-scale furnace of the air case through the side wall for (a) total surface heat flux, and (b) radiative source term.

results show that the radiative heat transfer of the small-scale furnace appears to be less sensitivity to the spectral databases of the fly ash, with the maximum difference being less than 1%. However, a large sensitivity occurs in the exit region of the furnace where a high concentration of the ash exists. In the burnout region, the heat flux increases with an increase in the absorption property of the ash particles. In particular, the heat flux calculated from the spectral database of Goodwin and Mitchner [235] is lower than that from the Bl-5(BHVB) of Blokh [245]. In terms of the large-scale furnace, a significant effect of the fly ash on the total surface heat flux was found, see Fig. 4.16. There is about 7% and 4% average difference between the databases of Goodwin and Mitchner [235] and the Bl-5(BHVB) [245] for the total wall heat flux and source term, respectively. The presence of the ash in the large-scale furnace increases significantly the optical pathlength and this is the main cause for a significant reduction in the incident emissions of the coal. Therefore, a spectral database that has higher absorption can result in a higher reduction in the heat flux that occurs in the flame region where there is the dominant effect of the coal. In the exit region of the furnace, where there is only the presence of the ash and the temperature is almost isother-

mal in the inner region, the heat transfer mainly occurs in the boundary layer. Therefore, a spectral database with a higher absorption property will produce a higher heat flux.

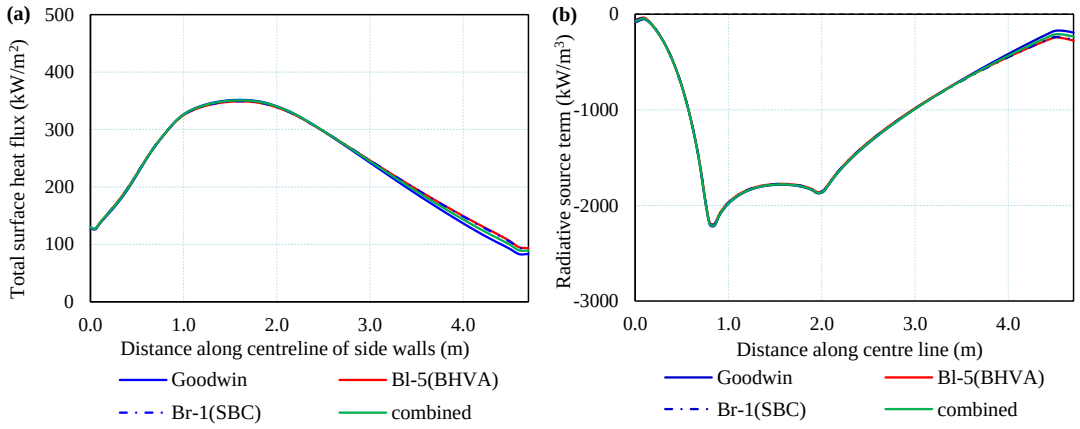

Figure 4.15: Effect of the optical properties of the ashes on the radiative heat transfer under the small-scale furnace of the air case through the side wall for (a) total surface heat flux, and (b) radiative source term.

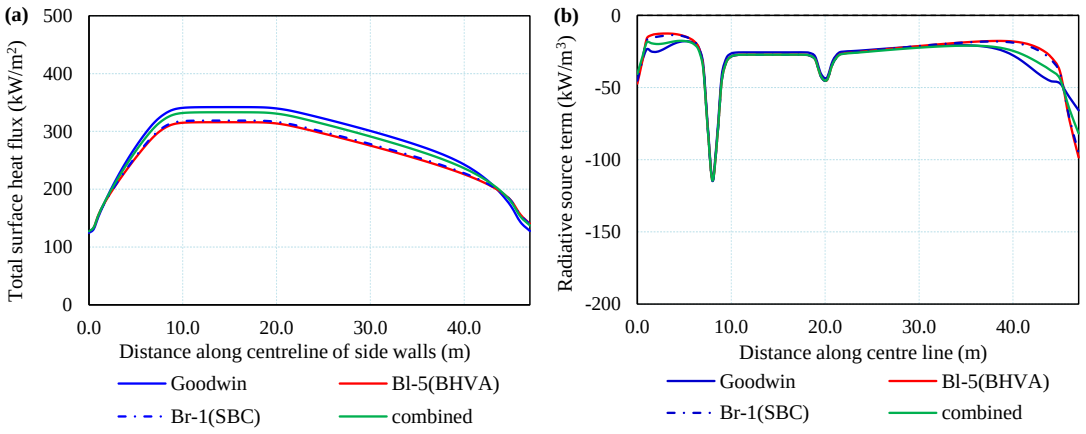

Figure 4.16: Effect of the optical properties of the ashes on the radiative heat transfer under the large-scale furnace of the air case through the side wall for (a) total surface heat flux, and (b) radiative source term.

4.3.3 Effects of the approximate solutions

Different approximate solutions are employed to calculate the radiative properties of the coal and ash particles and these data are applied to calculate the radiative heat transfer in comparison to that of the Mie theory for both the small and large-scale furnaces. For each type of particle, coal and fly ash, two spectral databases are employed, which are for particles that have small and high absorption properties. The spectral database of the Kentucky no.9 [236] and the anthracite [245] coals are used, presenting the low and high absorption properties, respectively. For the ash, the data measured for the sub-bituminous [247] ash, which shows low absorption properties, and the the Bl-5(BHVB) [245] which shows high absorption efficiency. The NGWSGG model and the Planck mean approximation are employed to describe the radiative properties of the gas and the particles.

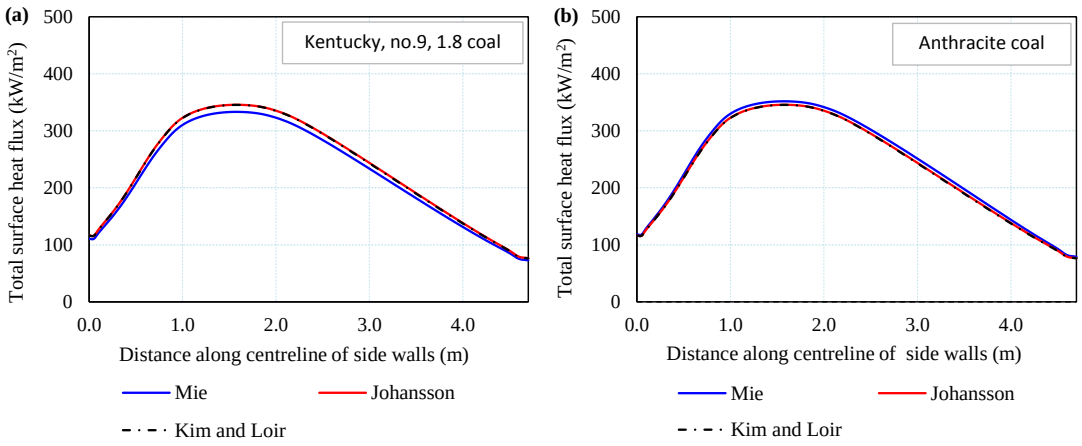

Figure 4.17: Effect of the approximate solutions employed on the total surface heat flux thought the side wall of the small-scale furnace under the air condition for (a) the Kentucky, no.9 coal, and (b) anthracite coal.

Figs. 4.17 to 4.20 show the radiative heat transfer results for the small and large-scale furnaces under the air condition, with the radiative properties of the coal being calculated using the approximations of Johansson [272] and Kim and Loir [259] in comparison to the Mie theory results. Both the approximations show, in general, the same results for both furnace scales and higher errors compared to the Mie theory have been found for the small-scale furnace than for

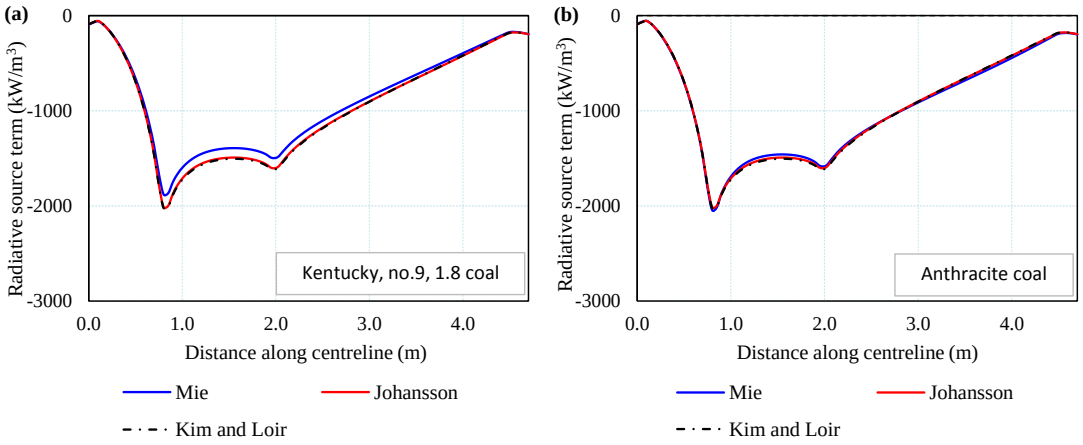

Figure 4.18: Effect of approximate solutions employed on the radiative source term of the small-scale furnace under the air condition for (a) the Kentucky, no.9 coal, and (b) anthracite coal.

the large-scale furnace. The effect of the approximate solutions also depend on the spectral database of the coal employed in the calculation. In particular, the approximations produce better results when they are applied to the calculation the anthracite coal [245], which has high absorption properties, with the average errors for both the radiative heat flux and source term being less than 2%. However, it should be noted the condition for applying these approximations, the complex index of refraction $|m| \geq 2$. In this study, both spectral databases employed are checked and do not satisfy this condition, with the value of $|m|$ being about 1.1 and 1.5 for the Kentucky, no.9 and anthracite coals over the range of wavelengths investigated, respectively. It should be noted that it is difficult to satisfy these conditions when using wavelength-dependent optical constants. However, in the large-scale furnace, the sensitivity of the radiative heat transfer to the approximations for coal is small so these approximations can be applied to reduce effect of the computational time.

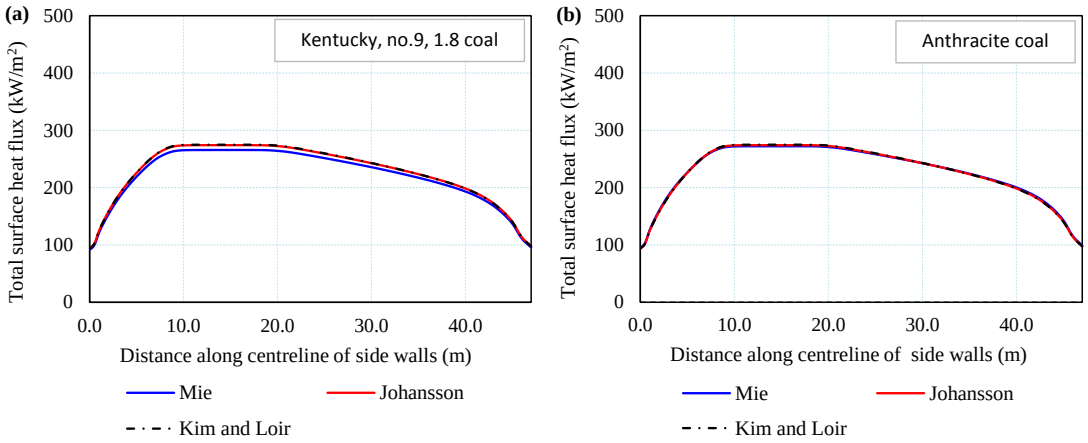

Figure 4.19: Effect of the approximate solutions employed on the total surface heat flux throught the side wall of the large-scale furnace under the air condition for (a) the Kentucky, no.9 coal, and (b) anthracite coal.

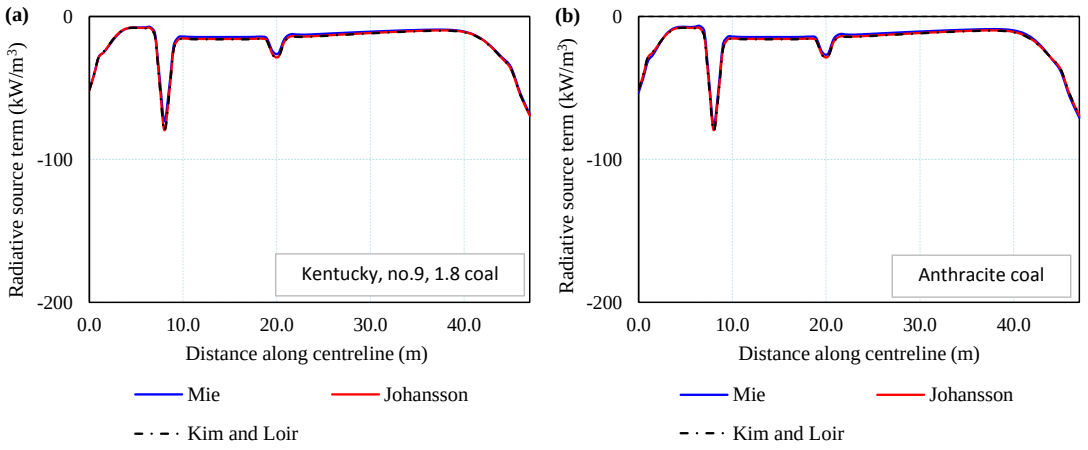

Figure 4.20: Effect of the approximate solutions employed on the radiative source term of the large-scale furnace under the air condition for (a) the Kentucky, no.9 coal, and (b) anthracite coal.

The sensitivity of the radiative heat transfer to the methods applied to calculate the radiative properties of the ash particles are shown in Figs. 4.21 to 4.24. The radiative heat transfer results appear to be less sensitive to the approximate solutions under the small scale furnace, with the largest difference, in comparison to the Mie theory, being less than 2% for both the total surface heat flux and the source term. However, significant differences in the results between approximate solutions has been found for the large-scale furnace in the burnout region.

The behaviours of the solutions are different when the two spectral databases are employed in the calculation. The anomalous limit approximation is in good agreement with the Mie theory for the database of Goodwin and Mitchner [235], however, it produces an overpredicted result when the Bl-5(BHAV) ash is employed. This can be explained by the complex index of refraction in the case of using the data of Goodwin which has been found to satisfy the condition $|m\text{-}1| \leq 1$. However, this condition is not satisfied for the Bl-5(BHAV) ash, with the value of $|m\text{-}1|$ being found to be in the range 1.2 to 1.4 over the investigated wavelength range. In terms of the correlations of Johansson [272], it can be seen that the first correlation, namely ash1, which has been correlated based on the ash properties [244, 330] having a high absorption property, shows only appropriate when applying the Bl-5(BHAV) ash and the second correlation, namely ash2 which is based on the spectral database of Goodwin and Mitchner [235] having low absorption properties. Therefore, this approximate solution is appropriate for ash that has low absorption properties. From the results investigated, applying an approximations for calculating the radiative properties of the fly ash for specific combustion environments, especially for calculating the radiative heat transfer for a large-scale furnace, needs to be considered the effect of the spectral database employed.

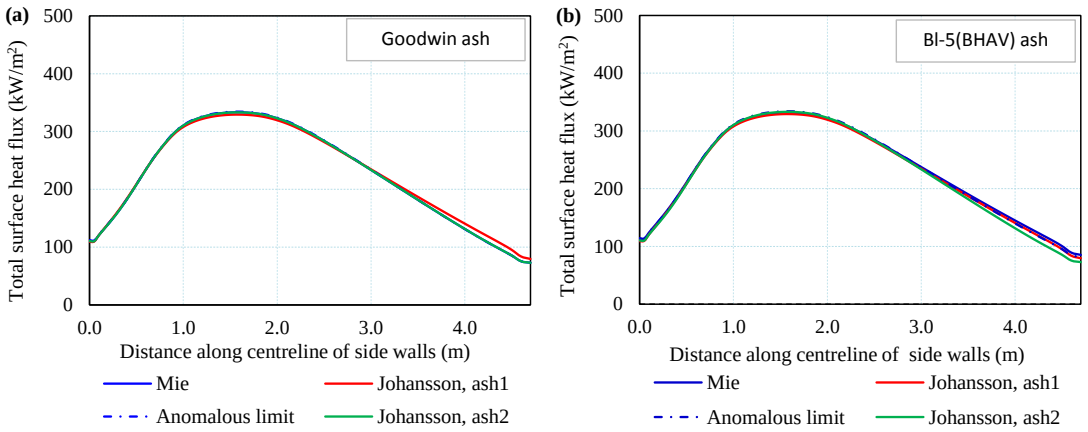

Figure 4.21: Effect of the approximate solutions for the ash employed on the total surface heat flux throught the side wall of the large-scale furnace under the air condition for (a) the Goodwin ash, and (b) the Bl-5(BHAV) ash.

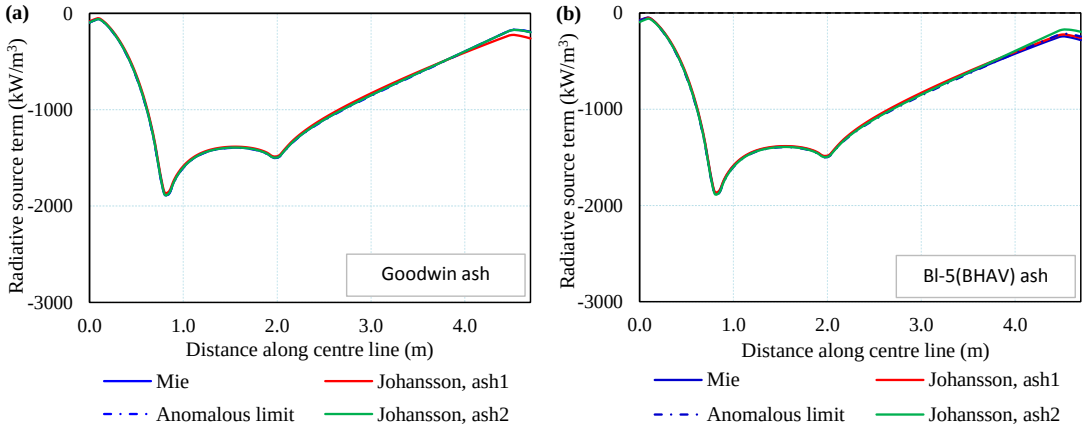

Figure 4.22: Effect of the approximate solutions for the ash employed on the radiative source term of the large-scale furnace under the air condition for (a) the Goodwin ash, and (b) the Bl-5(BHAV) ash.

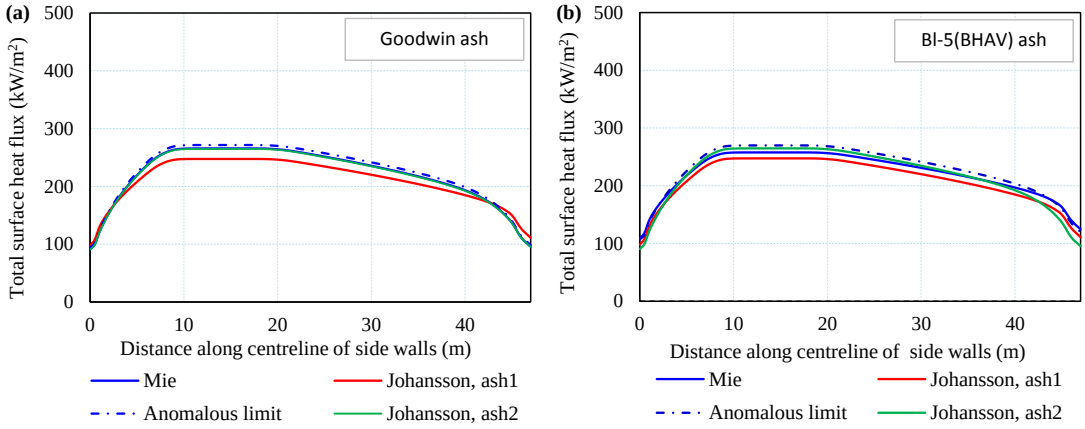

Figure 4.23: Effect of the approximate solutions for the ash employed on the total surface heat flux throught the side wall of the large-scale furnace under the air condition for (a) the Goodwin ash, and (b) the Bl-5(BHAV) ash.

4.3.4 Evaluation of the particle models

In this section, the Planck mean and constant models for the particle radiation, which are widely employed for modelling in pulverised coal combustion, are evaluated for the small and large-scale furnaces under both the air and oxyfuel conditions, with the NGWSGG model being employed to calculate the properties of the gas. For the constant models, the constant values for radiative properties

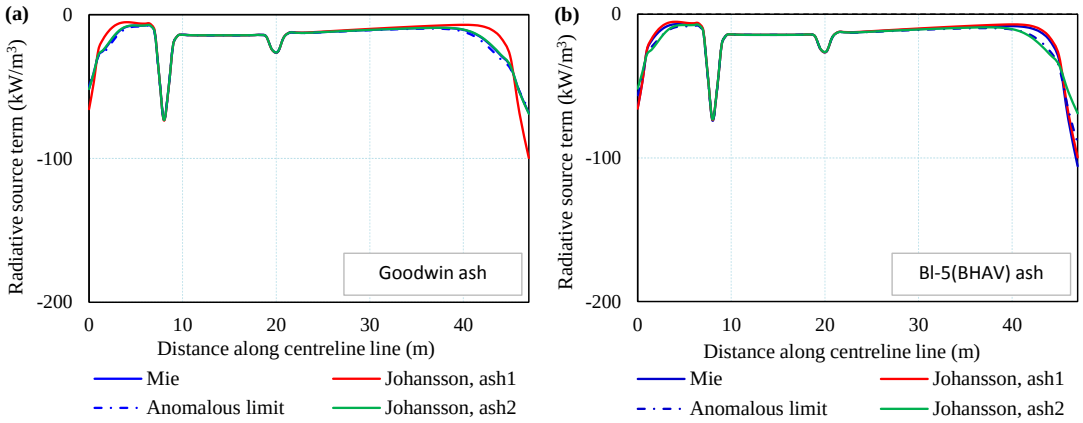

Figure 4.24: Effect of the approximate solutions for the ash employed on the radiative source term of the large-scale furnace under the air condition for (a) the Goodwin ash, and (b) the Bl-5(BHAV) ash.

of the particles, with particle emissivity ranging from 0.6 to 0.9, are employed and the scattering efficiency of the particles being chosen as the default value in ANSYS Fluent, $Q_{p,sca} = 0.01$. The results obtained are compared against the benchmark calculated using the CK model for the gas and the Mie theory for the spectral radiative properties of the particles. The CK model is implemented using the updated parameters by Rivière and Soufiani [185], with the spectrum being divided into 51 narrow bands and using the seven-point quadrature. Particle properties are calculated for each corresponding band of the narrow-band CK model, which covers the spectral range 37.5 - 11262.5 cm^{-1}. The anisotropic scattering phase function is simplified to be isotropic, with the effective scattering efficiency [208, 338] being used. The optical constants used in the calculation of the refractive index of the coal particles are taken from the experimental measurements for the Kentucky No. 9 coal, with the real part n=1.8 [236]. For the fly-ash particles, the wavelength-dependent optical constants measured by Goodwin and Mitchner [247], as parameterised by Liu and Swithenbank [250], are used. Other solutions for the particle properties that are also compared in this study include the Planck mean properties without using the effective scattering efficiency being coupled with the NGWSGG model, and the Planck mean properties of particle being coupled with the CK model.

Figs. 4.25 and 4.26 show the results obtained for the small furnace, the total surface heat flux and the radiative source term, of the mixture of the gas and the particle under the air and oxyfuel conditions compared to the benchmark. In terms of the benchmark, there is no virtually difference between the case using the Planck mean properties for the particles, namely CK-PL, and the case of having the spectral properties of the particles, namely CK-SP. For the cases evaluated, the radiative heat flux results show under prediction in comparison to the the benchmark, with the largest error being about 22% for the NGWSGG-0.6 case. However, with scaling the scattering efficiency, the radiative source term is in good agreement with the benchmark, with the largest errors being about 8% and 5% for the air and oxyfuel cases, respectively. It can be seen that using the Planck mean coefficient without scaling the scattering efficiency, in the NGWSGG-PL0 case, can result in a significantly lower radiative source term in comparison to the scaled case, NGWSGG-PL, with about 18% decrease for both the air and oxyfuel cases, while the radiative heat flux results are better, with about 8% and 5% decrease for the air and oxyfuel cases, respectively. For the constant properties of the particles, the heat flux increases with increasing of the absorption efficiency for both the air and oxy cases and the NGWSGG-0.9 case is in good agreement with the NGWSGG-PL case compared to the NGWSGG-0.6 case. This is due to the higher emission of the case having higher absorption, while the effect of the optical pathlength appears to be not significant in the small-scale furnace. In addition, the effect of the composition of the gas under the air and oxyfuel condition appears to disappear when having the presence of the particles for all the cases investigated.

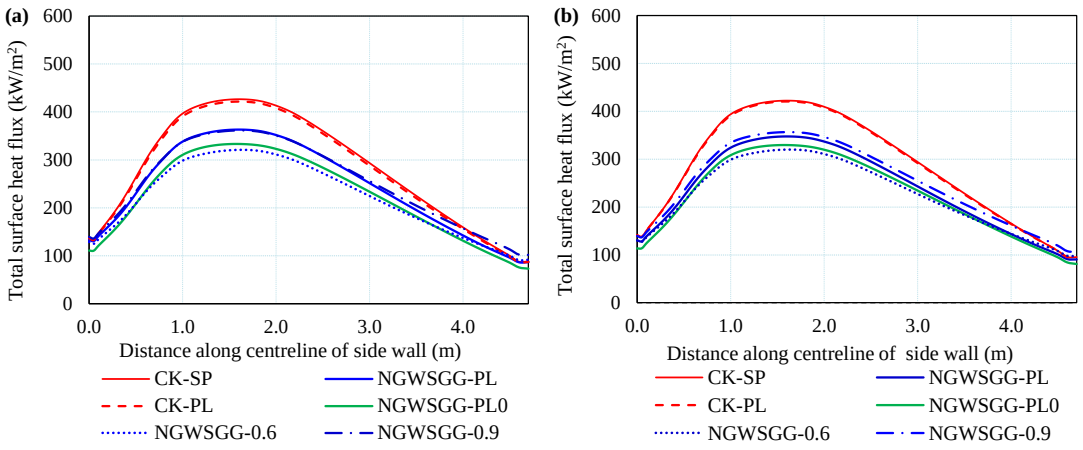

Figure 4.25: Total surface heat flux at the side wall along the small-scale furnace for both the gas and the particle radiation, (a) air-fired condition, and (b) oxy-fired condition.

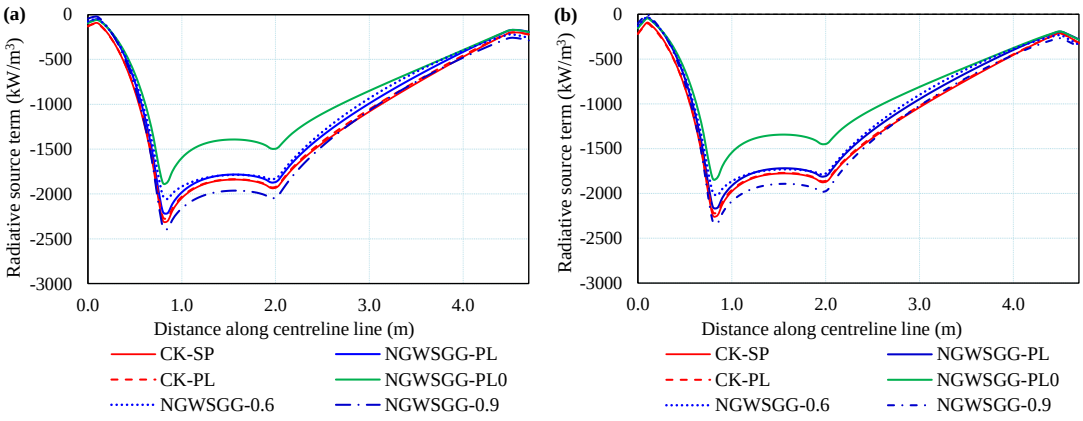

Figure 4.26: Radiative source term along the centreline of the small-scale furnace for both the gas and particle radiation, (a) air-fired condition, and (b) oxy-fired condition.

The evaluation of the radiative heat transfer for a mixture of gases and particles under the large-scale furnace are shown in Figs. 4.27 and 4.28. Similar to the small scale furnace, in the CK-PL case, there is very good agreement with the CK-SP case. However, the behaviour of the different cases evaluated are quite different. In particular, the radiative heat flux results are in very good agreement with the benchmark, with the largest error being found in the NGWSGG-0.6 case being 12% and for the other cases being less than 5%. While significant

errors have been found for the radiative source term, being about 30% and 90% for the NGWSGG-0.9 and NGWSGG-0.6, respectively. The NGWSGG-PL produces very good results in comparison to the benchmark for both the heat flux and source term, with about less than 1% error for the radiative heat flux and 6% for the source term. The NGWSGG-PL produces significantly higher results in comparison to the NGWSGG-PL0 case, being 20% and 40% higher for the radiative heat flux and source term, respectively. This demonstrates the significant effect of the scattering to the heat flux under the high optical thickness in contract to the thin optical environment. In contrast to the small-scale furnace, the heat flux and source term under the large-scale furnace decreases with the increase in the absorption efficiency. This can be explained by the increase in the absorption coefficient increasing the emission of the particles but the higher absorption properties also increase the optical thickness, which, in contrast, reduces the incident heat flux to the wall. The NGWSGG-0.9 case produces very good results for the heat flux and source term when compared to the NGWSGG-PL and the benchmark.

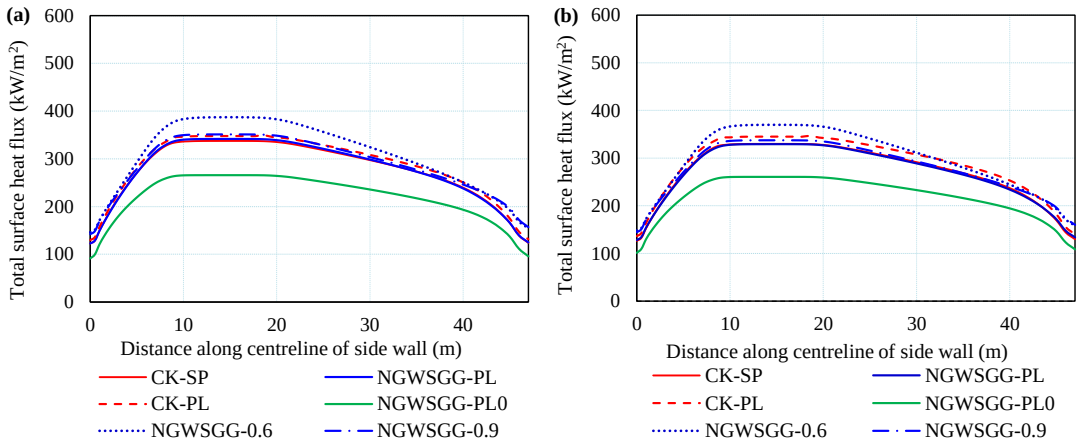

Figure 4.27: Total surface heat flux through the side wall along the large-scale furnace for both the gas and particle radiation, (a) air-fired condition, and (b) oxy-fired condition.

Fig. 4.29 shows the total of the heat flux through the walls of the small and large-scale furnaces for both the air and oxyfuel conditions. It can be seen that

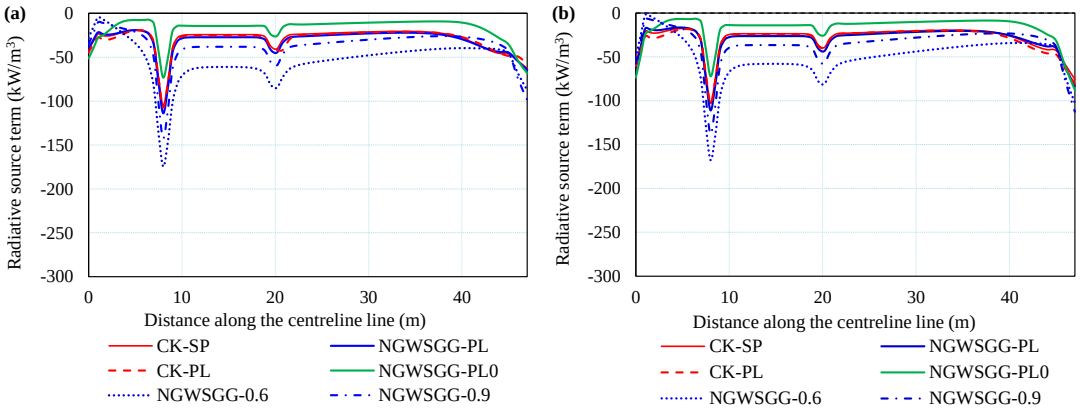

Figure 4.28: Radiative source term along the centreline of the small-scale furnace for both the gas and particle radiation, (a) air-fired condition, and (b) oxyfuel condition.

the selection of the solutions for calculating the absorption efficiency has a larger effect on the wall heat flux result of the small-scale furnace compared to that of the large-scale furnaces. The effect of the gas phase to the heat flux can be neglected for both the small and large-scale furnaces in the presence of particles. The effect of the coal and fly ash in the cases investigated on the heat flux are shown in Fig. 4.30. In terms of the coal, it can be seen that the coal has a dominant effect on the total wall heat flux for both scales of the furnaces and its effect is different between the small and the large-scale furnaces, and this is different from the effect of the ash. Also, the effect of the coal to the heat flux in comparison to that of the gas under the small scale furnace has a much higher effect for the large-scale furnace. This can be explained by the effect of the optical thickness under the large-scale furnace, especially when having the presence of the coal, which has a high absorptive property. It should be noted that the effect of the coal can be different and it depends on the gas temperature profile, and the temperature of the coal particles. For the effect of the ash, a similar effect of ash on the heat flux for both the small and large-scale furnaces, the heat flux increases with an increase in the absorption efficiency of the ash when the mixture of the ash and gas are considered. However, the presence of the ash appears to decrease the total heat flux in the presence of coal, producing about 8% reduction for the

NGWSGG-PL case under the large-scale furnace in comparison to less than 1% for the small-scale furnace.

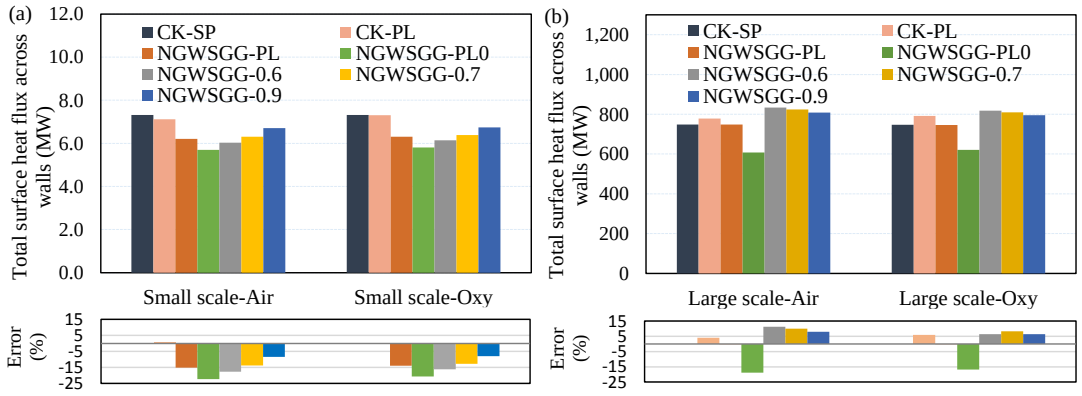

Figure 4.29: Total surface heat flux throught the walls of the furnaces for both the air and oxy-fired conditions, (a) small-scale furnace, and (b) large-scale furnace.

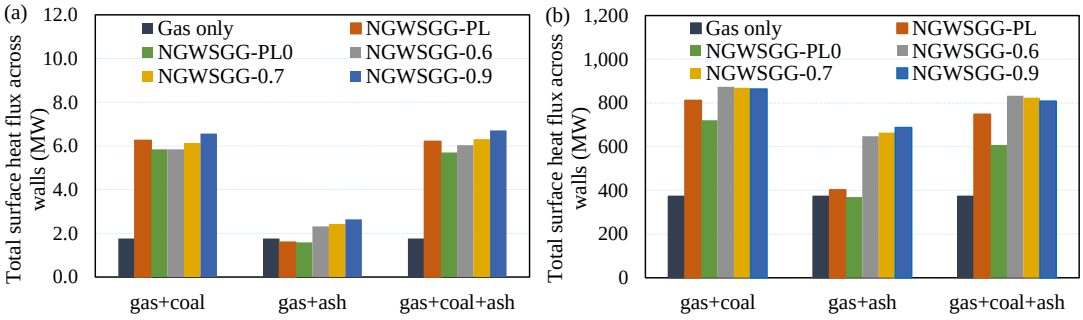

Figure 4.30: Total surface heat flux throught the walls of the furnaces for the air condition with the presence of only the coal, the ash and both the coal and ash, (a) small-scale furnace, and (b) large-scale furnace.

4.4 Summary and Conclusions

This section has focused on the radiation of the gas and particles under the air and oxyfuel conditions for both the small and large-scale furnaces. For the radiation of the gas, some global models have been evaluated for both the small and large-scale furnaces under the air and oxyfuel conditions. In terms of the particles, the sensitivity of the radiative heat transfer to the spectral databases

and approximations in the calculation of the radiative properties of the coal/char and fly ash has been investigated. Also, the evaluation of the models used for the particle radiation has been performed. Some conclusions are highlighted from this section as follows:

The effect of the gas phase on the radiative heat transfer have been investigated for both the small and large-scale furnaces under the air and oxyfuel conditions using global models and the results obtained are compared to the benchmark. It has been found that the total surface heat flux and the radiative source term in the cases investigated under the oxyfuel condition are higher than those under the air condition for both the small and large-scale furnaces. Further, the wall heat flux result is different from the results found from the Chapter 3. This demonstrates that the high concentration of CO_2 under the oxyfuel condition can increase or decrease the wall heat flux depending on the the temperature profile. Also, the results show that the increase in the results obtained under the oxyfuel condition depends on the model employed for the calculation of the radiative properties of the gas and the scale of the furnaces. Among the global models investigated, the NGWSGG model produces the highest differences, with the average surface heat flux and the source term under the oxyfuel condition being higher than those under the air condition by about 45% and 28%, respectively. In addition, the difference in the radiative heat transfer between the oxyfuel and air conditions of the large-scale furnace is less than that of the small-scale furnace. This can be explained by the effect of the optical pathlength.

The sensitivity of the total wall heat flux to the temperature of the coal/char particle and the concentration of the coal/char and fly ash particles has been investigated for different scales of furnace. For the thin optical thickness, it is demonstrated that the heat flux is significantly sensitive to the changes in the temperature and the concentration of the coal. The increase in the temperature and concentration of the coal results in an increase in the wall heat flux. Also, the heat flux sharply increases with an increase in the path length. In terms of the large optical thickness, the heat flux is likely to be significantly sensitive to

the temperature of the coal/char and steadily decrease with an increase in the path-length. Both the small and large-scale furnaces show less sensitivity to the range of the ash concentrations investigated.

Different spectral databases for coal and ash have been employed in the calculation of the radiative heat transfer for both the small and large-scale boilers furnace. The results show that the heat transfer in small-scale boiler are much more sensitive to the spectral database of coal compared to that of ash, and the relative difference between the database to the wall heat flux can be about 10% for small-scale boilers. It has been found that the selection of the ash databases results in more sensitivity in the radiative heat transfer in the large-scale boiler furnace compared to that in the small-scale furnace, namely about 7% and 1%, respectively. However, the results can be different for different types of boilers. Also it demonstrated that the effect of the ash selected in the large-scale furnace are different between the regions of the furnace. A spectral database that has a higher absorption can result in a lower heat flux in the flame region where there is the dominant effect of the coal. In the burnout region of the furnace, a spectral database with a higher absorption property will produce a higher heat flux.

Different approximate solutions are employed to calculate the radiative heat transfer in comparison to that of the Mie theory for the small and large-scale furnaces. In terms of the spectral approximations, the Kim and Loir approximation [259] for the coal and the anomalous approximation [271] for the ash show good agreement with the Mie theory. However, these solutions can give considerable errors when compared to the Mie theory depending on the scale of the furnace, such as the small-scale for the coal and large-scale for the ash. Furthermore, It should be noted that it is difficult to satisfy the condition of these approximations when using wavelength-dependent optical constants. For grey-properties approximations, the recent approximations of Johansson [272] are developed using a specified spectral database so they can give a large error when they are applied to different spectral databases compared to that of the Mie theory.

Different models for calculating the radiative heat transfer of the particles

have been evaluated for both the small and large-scale furnaces and for both the air and oxyfuel condition. It has been found that the difference between the air and oxyfuel conditions on the radiative heat transfer appears to disappear in the presence of particles. This demonstrates the dominance of the particles to the total radiative heat transfer compared to that of the gas. The effect of the particles to the radiative heat transfer is different and depends on the optical pathlength of the furnace, with a higher sensitivity of the radiative heat transfer to the particle radiation model selected under the small-scale furnace being found. Employing the NGWSGG model and the Planck mean coefficient to describe the radiative properties of the gases and the particles, respectively, can produce good results in comparison to the the benchmark under the large-scale furnace, with errors being less than about 1%. However, a significant error occurs when this method is applied to a small-scale furnace, with about 15% error for both the air and oxyfuel conditions. In terms of the constant properties of the particles, the total surface heat flux increases on increasing the absorption coefficient of the particles in the small-scale furnace, while it decreases in the large-scale furnace. An absorption coefficient of about 0.9 has been found to be in good agreement compared to the benchmark for both the small and large-scale furnaces, with about 8% error compared to the benchmark. The Planck mean properties coupled with the CK model gives very similar results in comparison to the spectral properties coupled with the CK model, meaning that spectrally resolving the particle properties is not important.

5 Investigation of the radiation of particles in a 250 kW pulverised coal combustion facility

This chapter focuses on an investigation of the radiative heat transfer in a pulverised coal combustion facility, using the 250 kW pilot scale combustion test facility (CTF), and focusing on the particle radiation and how this affects the NOx predictions. The modelling results are compared against the experimental measurements, which were obtained under air-fired and oxy-fired conditions, for both surface radiative heat flux and in-flame NO concentrations.

The combustion facility and numerical cases are introduced in Sections 5.1 and 5.2, respectively. In Section 5.3, the effects of the particles on the radiative heat transfer are investigated and the effect of the radiative properties on the NO emissions are investigated in Section 5.4

5.1 Experimental facility description

The combustion test facility used for this study is the 250 kW down-fired furnace of the Pilot-scale Advanced Capture Technology (PACT) facilities operated by the UKCCSRC. The cylindrical furnace has an internal diameter of 0.9 m and is 4 m high and constructed of 8 sections, Fig. 5.1, with each section being 0.5 m high. The furnace is lined with a 0.1 m thick refractory and the first six sections are water cooled. The furnace was designed with detailed measurement and characterisation capabilities. The experimental data obtained from the measurements

for air-fired condition and different cases of oxy-fired conditions, such as Oxy-27, Oxy-30, were used to evaluate the CFD study results.

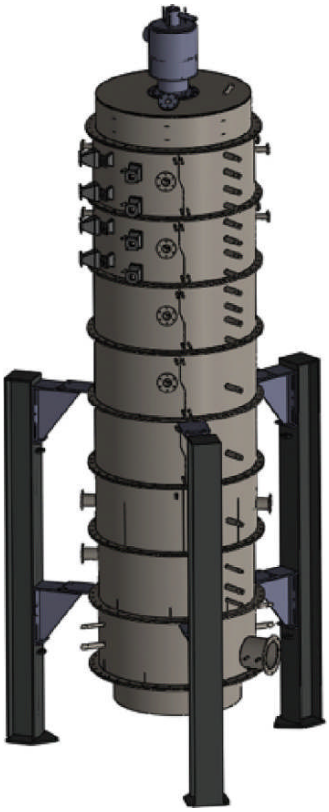

Figure 5.1: A CAD image of the combustion test facility [116].

The burner is a commercial low-NO burner which has been scaled to the 250 kW_{th} and provided by Doosan Babcock. The primary stream and coal are supplied through a primary annulus, and the two other streams, secondary and tertiary streams, supply the majority of the swirled oxidiser. A CAD image and a schematic of the burner are shown in Figs. 5.2 and 5.3, respectively.

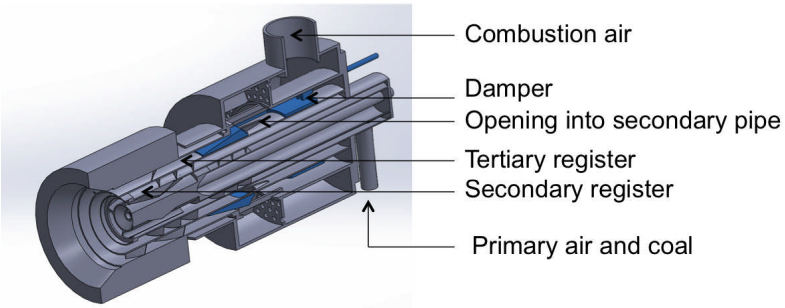

Figure 5.2: A CAD image of the 250kW Doosan Babcock burner [339].

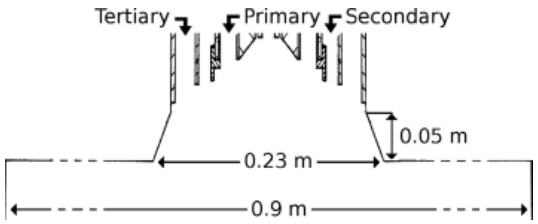

Figure 5.3: A schematic of the 250kW Doosan Babcock burner [116].

The concentration of NO was measured in different regions within the furnace and at the exit section of the furnace using a Signal 4000VMA chemiluminescence analyser which is based on the chemiluminescent gas phase reaction between ozone and nitric oxide to produce nitrogen dioxide and oxygen. Approximately 10% of the NO_2 produced emissions of a photons, varying in wavelength between 0.6 and 0.3 micrometres. The intensity of this emission is proportional to the mass flow rate of NO and is measured by a photomultiplier tube.

The radiative heat flux was measured using an ellipsoidal radiometer, which consists of a gold-lined ellipsoidal cavity that focuses most of the radiative flux coming into the cavity from the orifice at the probe tip upon a thermopile sensor, which is held behind a special glass window, where a nitrogen purge is used to prevent contamination from the combustion environment.

5.2 Case description

Three combustion conditions have been considered in this study, a baseline air-fired combustion and two oxyfuel regimes. The El-Cerrejon coal were used, with the properties of the coal being shown in Table 5.1 and the operating conditions for both the air- and oxy-fired environments are listed in Table 5.2. Both cases were set up with a thermal load of 200 kW. User defined functions (UDFs) were used to customise the radiative property models of the gas and particle phases.

Table 5.1: Properties of the El-Cerrejon coal*.

Proximate analysis (AR, wt.%)				Ultimate analysis (DAF, wt.%)				
Fixed carbon	Volatiles	Ash	Moisture	C	H	N	S	O**
53.98	35.50	2.9	7.63	80.92	5.12	1.65	0.52	11.79
Calorific value (AR) (MJ/kg): 29.61								

* AR, as received; DAF, dry ash-free.

** Calculated by difference.

Table 5.2: Inlet flow parameters used in the CFD calculations.

	Air	Oxy-27	Oxy-30
Mass flow rate (kg/h)			
Coal	25.71	25.71	25.71
Primary	63.6	60.90	54.85
Secondary	92.2	87.77	78.00
Tertiary	158.4	150.73	133.96
Inlet gas temperature (K)			
Primary	297.15	294.95	294.95
Secondary	524.65	525.15	525.15
Tertiary	524.65	525.15	525.15
Oxygen concentration (mass%)			
Primary	23.15	16.20	16.20
Secondary	23.15	22.50	25.71
Tertiary	23.15	22.50	25.71

The particles distribution is fitted to the Rosin-Rammler size distribution in the range of particle diameter from 1 to 600 µm, having an average diameter of 120 µm and the spread number 1.1, as shown in Table 5.3. The CTF was modelled using one quarter of the full geometry, thus exploiting the rotational symmetry of the furnace, and this results in a structured mesh containing about 1.4 million hexahedral cells, see Fig. 5.4. The mesh is refined with a high density of cells inside the quarl and the region close to the quarl in order to meet the mixing between the primary and secondary flows and the high behaviour of the

flame in these regions, respectively.

Table 5.3: Parameters for the Rosin-Rammler particle size distribution.

Parameter	value
Minimum diameter (µm)	1
Maximum diameter (µm)	600
Mean diameter $\overline{d}$ (µm)	120
Spread number n	1.1

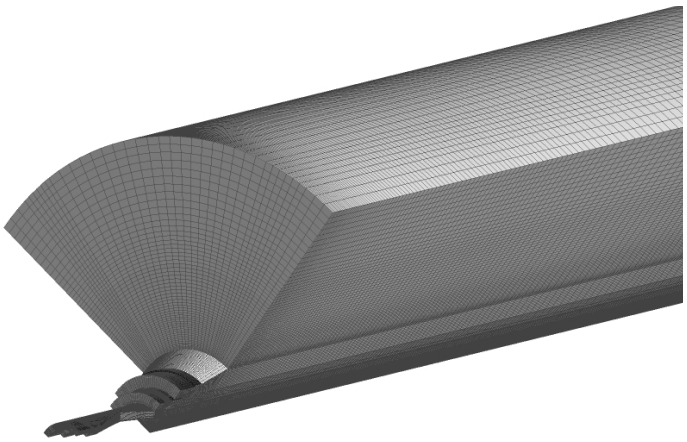

Figure 5.4: A quarter mesh of the 250 kW furnace employed in the CFD calculations.

All of the cases presented in this study were calculated using a RANS approach, using the Reynolds stress model of Launder et al. [84] to model the unclosed terms. The Reynolds stress model has been found to produce better prediction results for the temperature and oxygen concentration in the recirculation zone [340] and better predictions of NO_x [341] than those obtained when using the k-ε model. The single kinetic rate [102] was used to describe the devolatilisation of the coal particles, with the pre-exponential factor of 14,841 s^{-1} and an activation energy of 35.3 kJ/mol. A two-step global reaction mechanism was employed for the homogeneous combustion of an empirically defined volatile species, reactions (R5.1) and (R5.2), and the eddy dissipation model was used

for the turbulence-chemistry interaction:

$$\begin{aligned} &C_{1.733}H_{2.448}O_{0.354}N_{0.0568}S_{0.0077} + 1.309O_2 \\ &\longrightarrow 1.733CO + 1.224H_2O + 0.0284N_2 + 0.0077SO_2 \end{aligned} \tag{R5.1}$$

$$CO + \frac{1}{2}O_2 \longrightarrow CO_2 \tag{R5.2}$$

The surface char combustion reaction is described by the Smith intrinsic model [90], with the kinetic parameters from [342]: a pre-exponential factor of 4×10^{-4} kg/(m^2.s.Pa) and an activation energy of 66 kJ/mol. Some of the main model settings for the cases investigated in this section are presented in Table 5.4.

Table 5.4: General model setting used in modelling the 250 kW combustion test facility.

Submodel	Models employed and parameters
Turbulence model	Reynolds stress model [77]
Gas combustion	Eddy dissipation model with two step reaction
Particle combustion	Intrinsic model [90], with parameters from [342]:
	$A_i = 4 \times 10^{-4}$ kg/(m^2.s.Pa)
	E_i= 66 kJ/mol
Devolatilisation model	single kinetic rate [102]
	A_r = 14,841 s^{-1}
	E_a = 35.3 kJ/mol
Radiation model	Discrete ordinates
	$N_\Theta \times N_\phi = 3 \times 3$
Particle size distribution	Rosin-Rammler

The non-grey WSGG model [64] is applied with 4 grey gases and 1 transparent gas ($\kappa_{g,0} = 0$). Therefore, 5 RTEs, as shown in Equation (2.60), have been solved, with the weighting factors and the absorption coefficients for the gas as follows:

$$a_{g,i}(\vec{r}) = \sum_{j=1}^{N_c} c_{ij} \left(\frac{T_g(\vec{r})}{T_{ref}} \right)^{j-1}, i = 1, 2, \ldots, N_g, \quad a_{g,0} = 1 - \sum_{i=1}^{N_g} a_{g,i}(\vec{r}) \tag{5.1}$$

The particle effects are accounted for in Equations (2.60) and (2.65) with equivalent absorption coefficient κ_p, scattering coefficient σ_p and the equivalent emissivity $E_{p,i}$ being defined as follows:

$$\kappa_p = \lim_{V \to 0} \sum_{n=1}^{N} Q_{abs,n} \frac{A_{p,n}}{V_c} \tag{5.2}$$

$$\sigma_p = \lim_{V \to 0} \sum_{n=1}^{N} Q_{sca,n} \frac{A_{p,n}}{V_c} \tag{5.3}$$

$$E_{p,i} = \lim_{V \to 0} \sum_{n=1}^{N} a_{pi,n} I_{bp,n} Q_{abs,n} \frac{A_{p,n}}{V_c} \tag{5.4}$$

where N is the total number of particles within the volume V_c, $a_{pi,n}$ is the weighting factor for the i^{th} grey gas, being determined from Equation (5.1) with replacing T_g by the temperature of the n^{th} particle $T_{p,n}$, $I_{bp,n}$ is the blackbody emissivity at the temperature of the particle n, and $A_{p,n}$ is the projected area of the n^{th} particle. The absorption efficiency $Q_{abs,n}$ and the scattering efficiency $Q_{sca,n}$ are calculated from the Mie theory [337] using the Planck mean values. In this study, a simplification of the scattering phase function, namely an isotropic scattering phase function, is applied and the effective scattering efficiency, $Q^*_{sca,n}$, is used, which is obtained from scaling the scattering efficiency, $Q_{sca,n}$, by the asymmetry factor, g, as [208, 338], $Q^*_{sca,n} = (1-g)Q_{sca,n}$. The optical constants used for the calculation of the refractive index of the coal particles were taken from experimental measurements for the Kentucky No. 9 coal, with the real part n=1.8 and the wavelength-dependent k determined within the spectral range 2-20 μm [236]. For the fly-ash particles, the wavelength-dependent optical constants measured by Goodwin and Mitchner [247], as parameterised by Liu and Swithenbank [250], were used. The Planck mean coefficients were pre-calculated for a range of diameters and temperatures of the particles. For each calculation of the coal and fly ash particles, the $Q_{abs,n}$ and $Q_{sca,n}$ values were obtained by employing linear interpolation. The radiative properties of the burning particles are also linearly

interpolated between the coal and fly ash values based on the current mass of the char in the burning particles.

Two other approaches for the particle radiative properties were also investigated and compared to the Planck mean coefficients, namely the constant and the linear-function values. In terms of constant values, a particle absorption efficiency value of 0.9 [262–265] and a particle scattering factor 0.6 [263, 265] for both air-fired and oxy-fired conditions are employed. The particle scattering efficiency is calculated from the scattering factor, f_p, as $Q_{sca} = (1 - f_p)(1 - Q_{abs})$, thus resulting in a constant scattering efficiency of 0.04. For the linear-function value, the radiative properties of particles vary as linear functions of the mass fraction of char and volatiles in the particles. The linear emissivity function [267], as shown in Equation (5.5), and the linear function scattering factor [206], as shown in Equation (5.6), are used as follows:

$$\epsilon_p = X_c + 0.6\,(1 - X_c) \tag{5.5}$$

$$f_p = 0.9X_{v,c} + 0.6\,(1 - X_{v,c}) \tag{5.6}$$

where X_c is the fraction of unburnt char mass, and $X_{v,c}$ is the fraction of unburnt combustibles.

5.3 Investigation of the particle radiation

5.3.1 Sensitivity of the particle concentration

Although the inlet particle size distribution in this study was fitted to a Rosin-Rammler distribution function, with two parameters: the mean diameter and the spread number being identified in Table 5.3, the sensitivity to particle size resolution needs to be investigated. Because of the computational cost, most of the studies have assumed that the number of diameter intervals 6 to 10 are adequate for practical modelling [206, 261, 343, 344]. In a more recent study, the sensitivity of the radiative heat transfer to the number of diameter intervals has

been investigated by Krishnamoorthy [345] with three values of the number of particle diameters being employed, namely 8, 40 and 80. The study shows that the number of particle diameters employed has a large impact on the incident radiative flux predictions, however, they have minimal impact on the temperature. In this section, the sensitivity to the number of diameter intervals is investigated for both constant and Mie theory solutions for the particle properties in order to select an appropriate value to eliminate the sensitivity of the radiative heat transfer to the particle size distribution.

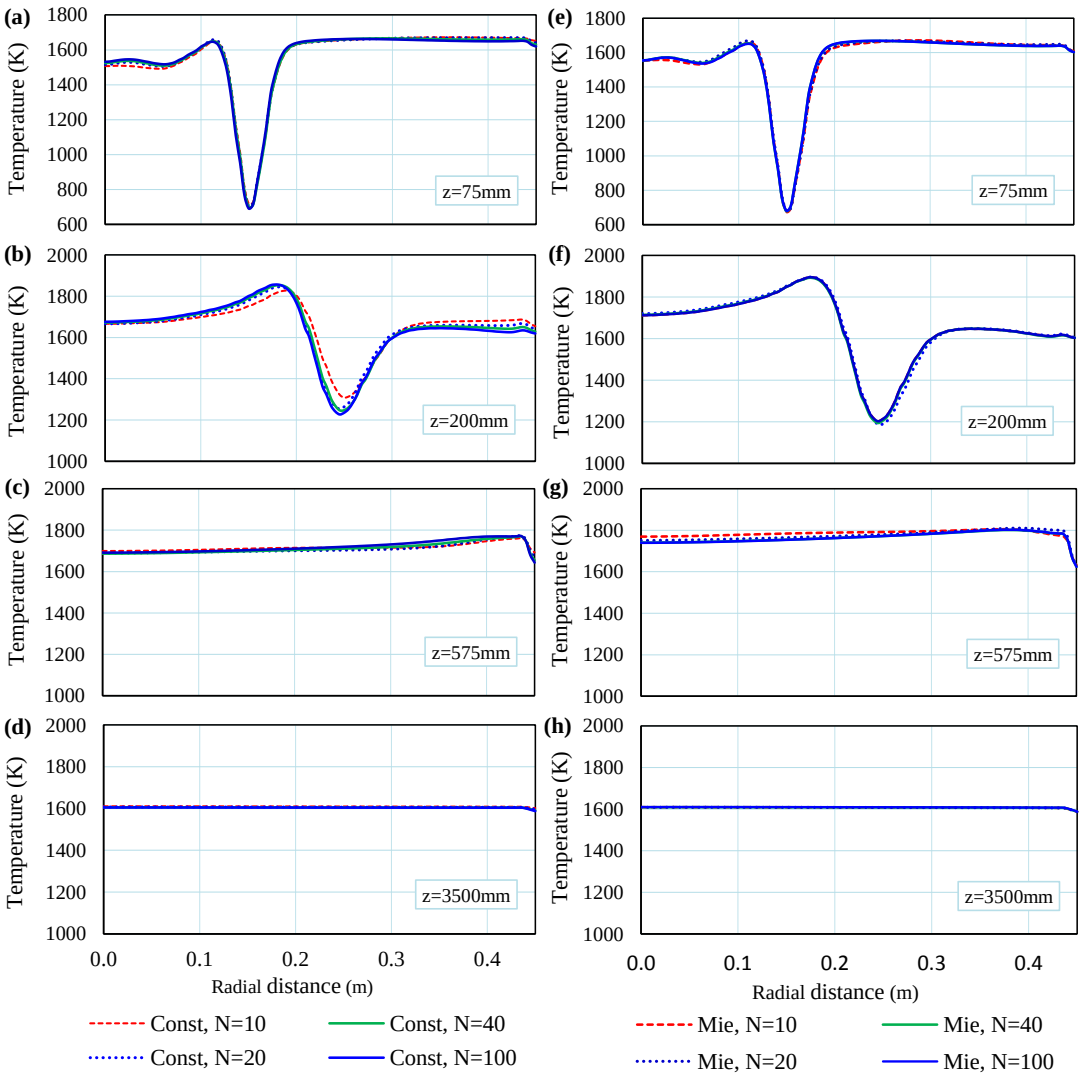

Figure 5.5: Radial temperature distributions with different values of the number of diameters for the air condition, (a-d) NGWSGG-Const, and (e-h) NGWSGG-Mie.

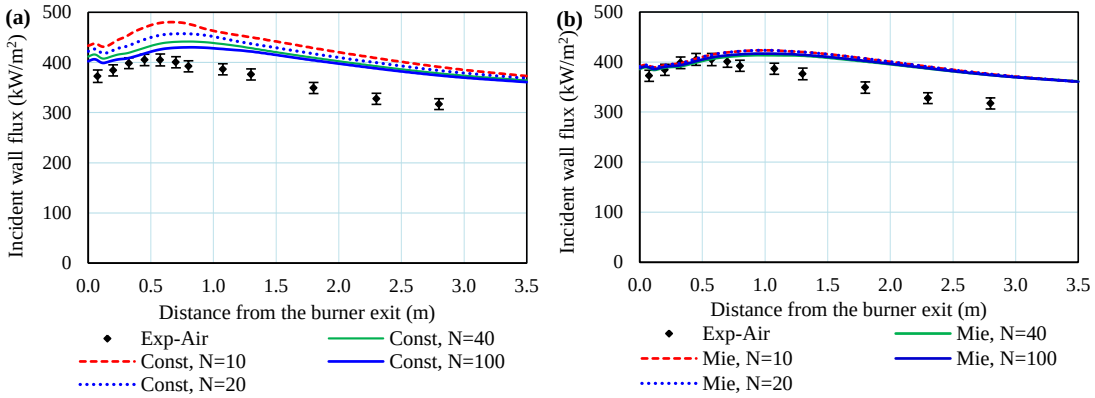

Figure 5.6: Surface incident radiative heat fluxs with different number of diameters for the air condition (a) NGWSGG-Const, and (b) NGWSGG-Mie.

Figs. 5.5 and 5.6 show the sensitivity of the temperature and the wall heat flux to the Rosin-Rammler size distributions for the air-fired conditions, respectively. Different the number of diameters of the particle distribution are employed, namely 10, 20, 40 and 100, in order to examine the two cases corresponding to the constant and Mie-theory properties for particle radiation (NGWSGG-Const, NGWSGG-Mie). The predicted results for the temperature distribution, see Fig. 5.5(a-d), show the influence of the Rosin-Rammler resolution on the in-flame temperature profile for the NGWSGG-Const case. The results show that the temperature profiles are less sensitive to the resolution of the particle distribution, with the sensitivity of the temperature mainly occurring in the high-concentration region of the particles. However, the incident wall heat flux (Fig. 5.6(a)) is significantly dependent on the number of diameters. This can be explained because the lower the number of diameters employed produces more overprediction in the projected surface particle distribution (Fig. 5.7(a)) and consequently a higher extinction coefficient which have dominant equivalent absorption coefficients (Fig. 5.8(a)), and this results in the higher incident wall heat flux. It appears that there is not much change in the incident wall heat flux when the number of diameters is larger than about 40. This is because there is not much decrease in the concentration of the particles when the number of diameters is higher than this value. The less dependence of both the temperature profile and wall heat flux to the Rosin-Rammler resolution was found for the Mie theory case

investigated as shown in Fig. 5.5(e-h) and Fig. 5.6(b). It can be seen that the increase in the number of diameters produces a decrease in the projected surface area concentration of the particles (Fig. 5.7(b)) and this consequently decreases the emission of the particles. However, using the spectral database of Goodwin and Mitchner [247] to describe the radiative properties of the ash particles results in a significantly lower absorption efficiency of the particles, see Fig. 5.8 (c,d). Therefore, the equivalent absorption coefficient becomes less sensitive to the change in the particle concentration, see Equation (5.2). Although the dominant scattering efficiency in this case, the influence of the scattering radiative properties of the particles on the surface radiative heat flux has been found to be negligible in case being optically thin by [338, 346]. From this study, a total of forty particle diameters are employed for cases investigated later in this study.

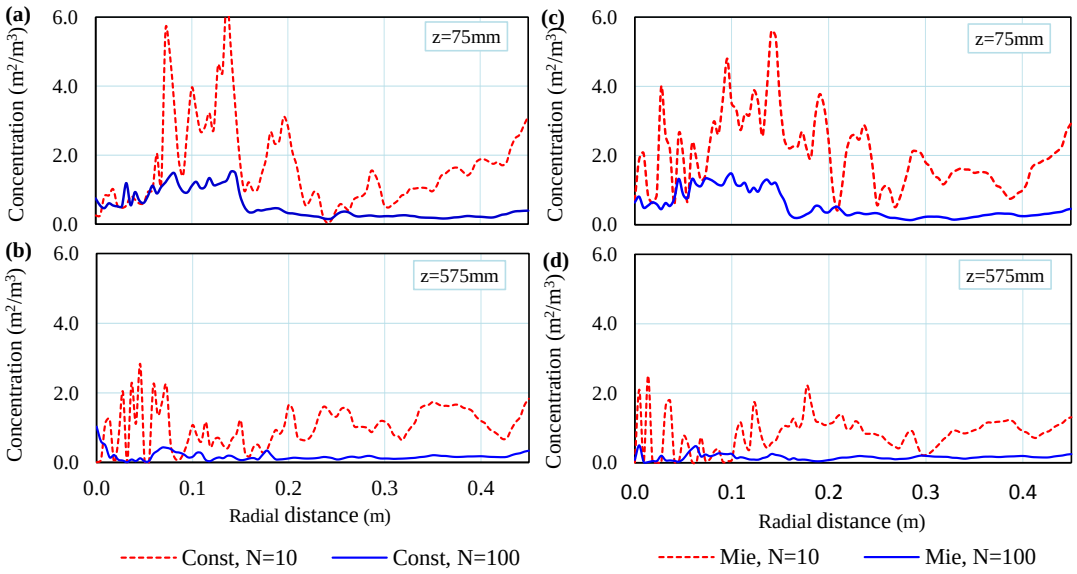

Figure 5.7: Projected surface area distributions of particles at distances 75mm and 575mm from the burner exit for the air condition (a, b) NGWSGG-Const, and (c,d) NGWSGG-Mie.

5.3.2 Particle temperature profile

The presence of the particles in coal-fired combustion has a significant effect on the radiative heat transfer mechanism [72, 327]. The temperature profile of the

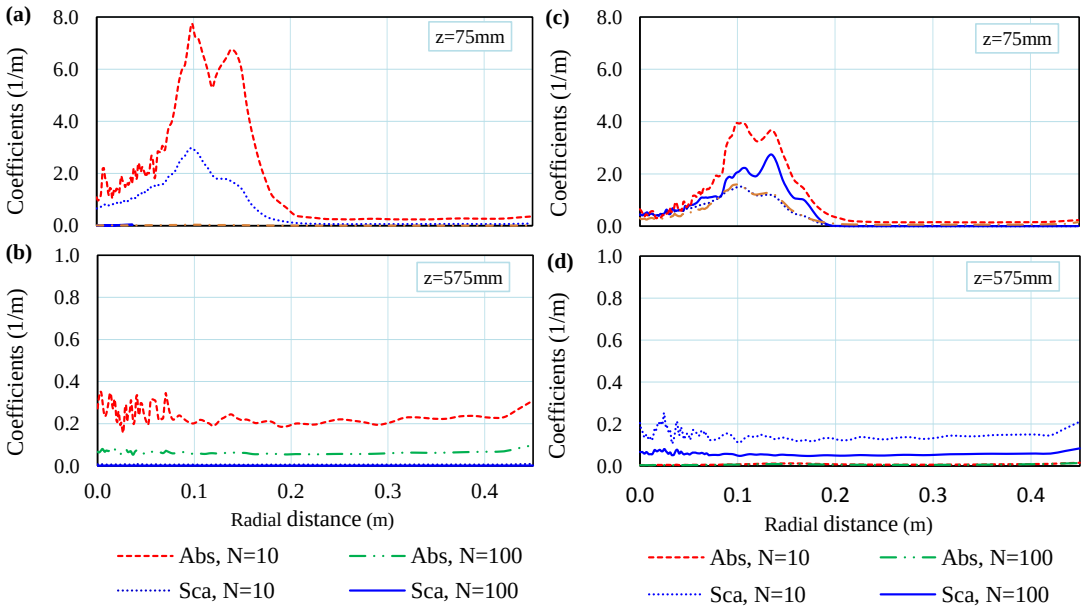

Figure 5.8: Particles radiative properties at distances 75mm from the burner exit for the air condition, (a,b) NGWSGG-Const, and (c,d) NGWSGG-Mie.

particles are different from that of the gas and the difference depends on several parameters, such as coal rank, particle residence time, and the reaction zones [347]. In this section, the temperature profiles of the particles are investigated and compared to that of the gas phase.

Fig. 5.9 shows the averaged particle temperature profiles for the air- and oxy-fired conditions compared to the surrounding gas temperatures, with three types of particles being investigated, namely coal/char, fly ash and a mixture of both the coal/char and the fly ash. While the temperature of the fly ash is close to the gas temperature in the furnace, it is found that the behaviour of the coal/char is quite different. In the inner recirculation region, the temperature of the coal/char is lower compared to the gas temperature and it is higher in the outer recirculation region, where higher concentrations of oxygen are predicted. However, the average temperature of the coal/char and the fly ash are similar to that of the fly ash. This demonstrates that the number of the coal/char particles is much lower than the number of the fly ash particles. The temperature of the coal/char particles under the oxy-fired condition is different from that in the air condition. This may be due to the different effects of the oxy condition on the

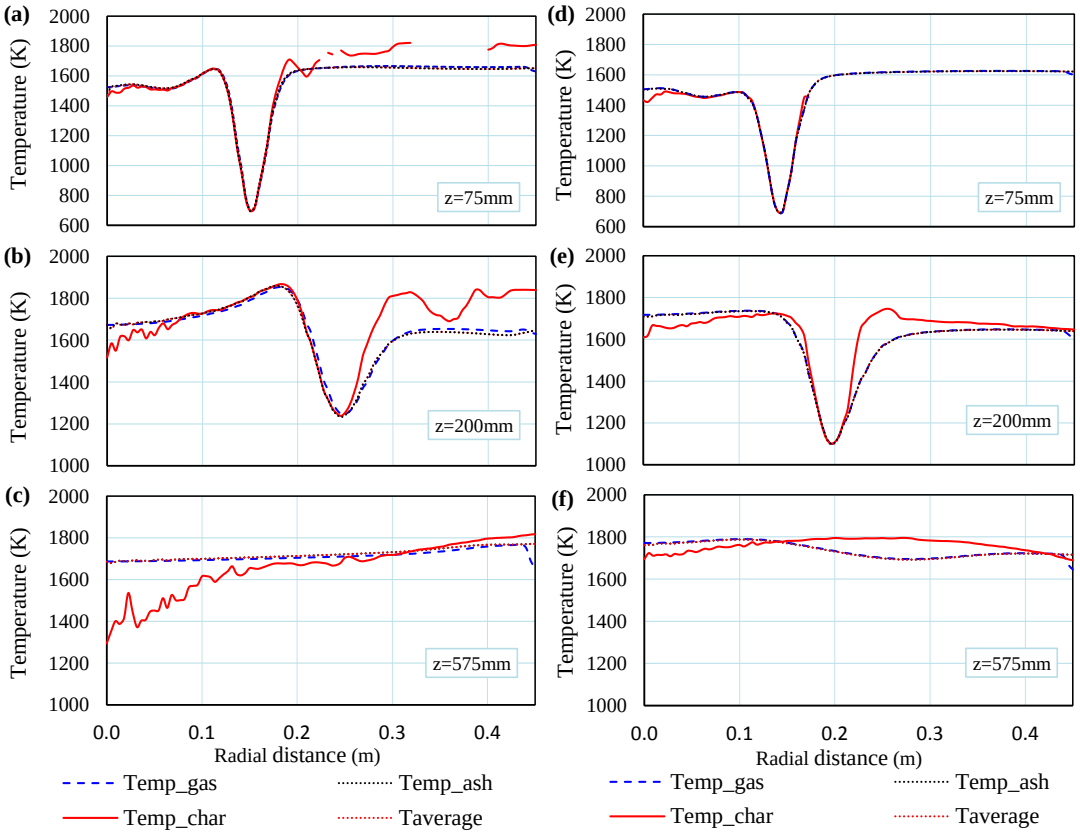

Figure 5.9: Radial distribution of the particle temperature for, (a-c) the air-fired condition, and (d-f) the oxy-fired condition.

burnout and the temperature of the particles. The missing temperature values of the coal/char particles in the outer recirculation region of the furnace at distance 75mm from the burner exit can be explained by there is no presence of these coal/char particles in this region.

5.3.3 Sensitivity of the optical data

The effect of the optical properties of the coal and ash particles on the radiative heat transfer was investigated in Chapter 4. However, the investigation is separated from the other sub-models, such as the turbulence and combustion models and the concentration, temperature of the particle are assumed to be approximately presented by mathematical function while the temperature and concentration of the particles are fluctuate in the different regions of the furnace. In this section, the sensitivity of the radiative heat transfer on the optical proper-

ties is investigated in the combustion process of a pilot-scale facility, namely the 250 kW combustion furnace. The NGWSGG and the grey particles, which are calculated from the Mie theory, are employed to describe the properties of the gas and the particles, respectively. A total of 8 cases, corresponding to 4 optical databases for the coals and 4 databases for the ashes, are investigated.

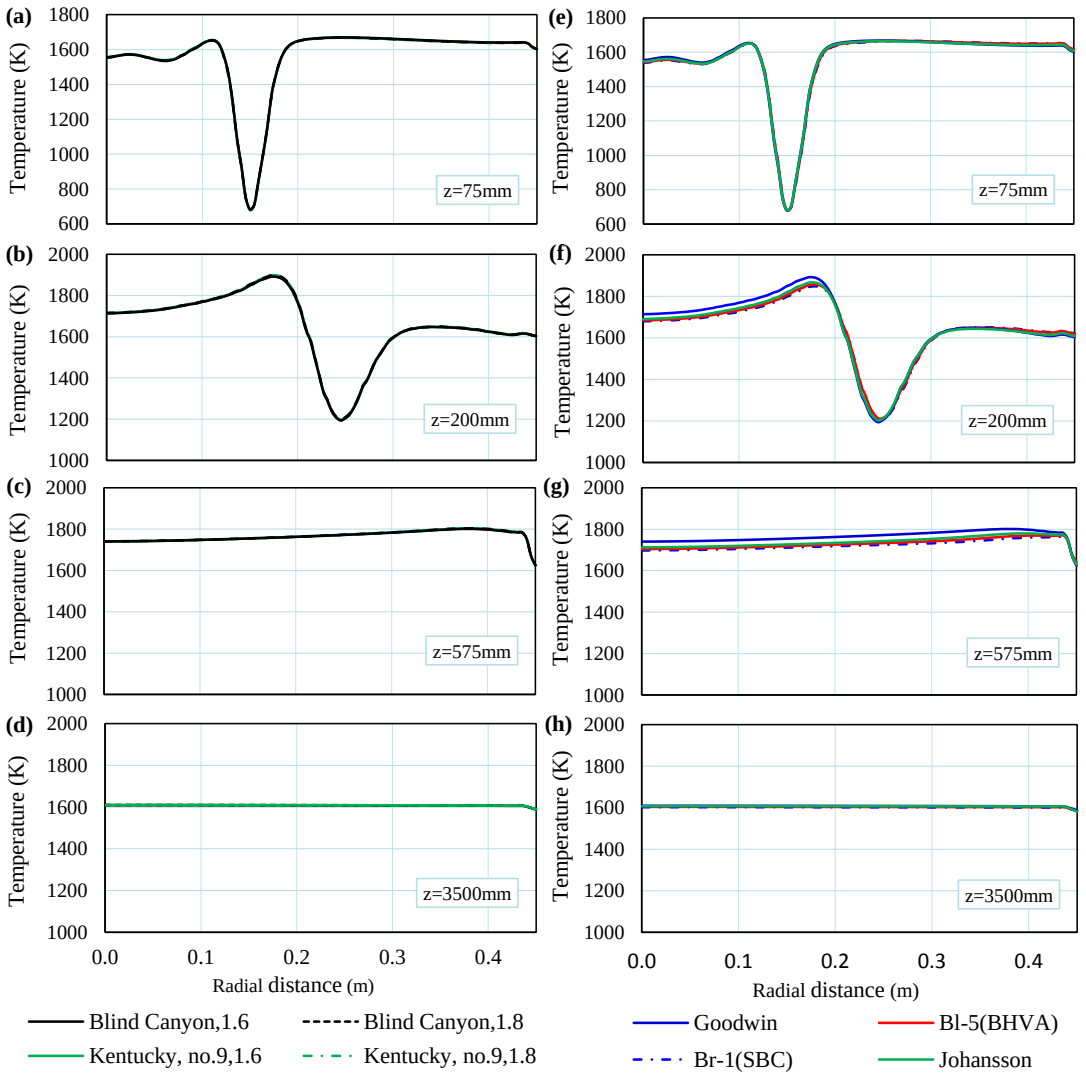

Figure 5.10: Radial temperature distributions for different spectral databases for the air condition, (a-d) coal, and (e-h) ash.

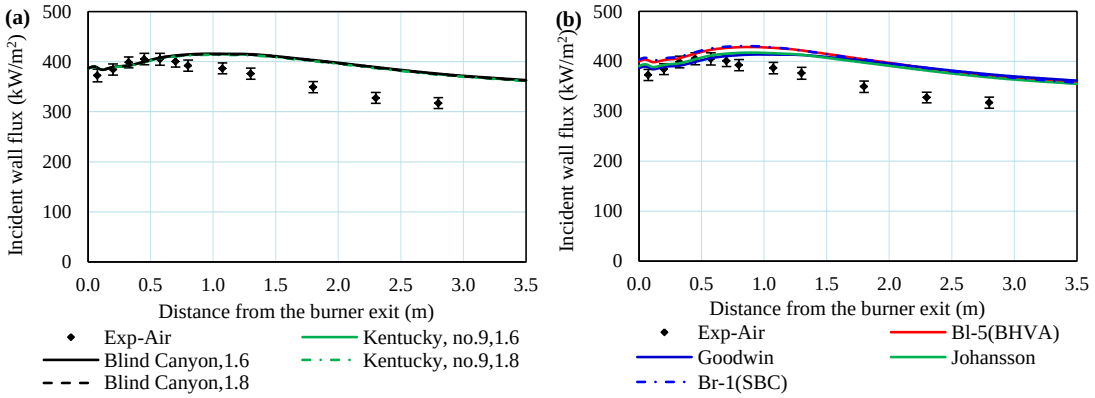

Figure 5.11: Surface incident radiative heat flux for the different spectral databases for the air condition, (a) coal, and (b) ash.

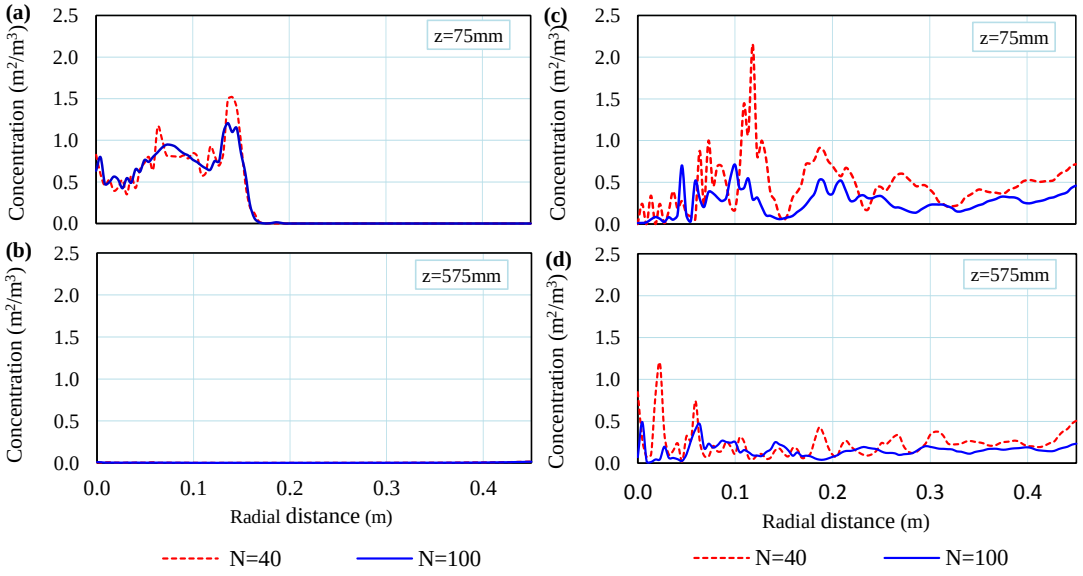

Figure 5.12: Surface incident radiative heat flux for the different spectral databases for the air condition, (a) coal, and (b) ash.

The results for the sensitivity of the radiative heat transfer on the spectral databases that have been selected to describe the properties of the coals and ashes are shown in Figs. 5.10 and 5.11. It can be seen that the temperature and the wall heat flux appear to be less sensitive to the spectral databases of both the ash and coal. For the effect of the coal, it can be seen that the temperature and the heat flux are not sensitive to the spectral database selected, with the largest deviation between the wall heat fluxes from the experimental data being less than 1.0%.

The less sensitivity of the coal, in contrast to the results found in Section 4.3.2 for a small-scale furnace, can be explained by the lower temperature of the coal/char particles compared to that of the gas phase, see Section 5.3.2. This results in the lower influence of the coal particles, although the concentration of the coal is found to be similar, see Fig. 5.12 (a, b). In terms of the sensitivity of fly ashes, there is a significant effect of the spectral databases of the ashes employed on the temperature and the incident wall heat flux, see Fig. 5.10 (e-h) and Fig. 5.11 (b). The high concentration of the ash, see Fig. 5.12 (c, d) results in the high influence of the ash in this case. From these results, the experimental data for fly ash of Goodwin and Mitchner [247], which describes the flyash with a significantly lower absorption efficiency, results in a significantly higher temperature and lower incident wall heat flux compared to the data of Blokh [245]. The large sensitivity of fly ashes to the incident wall heat flux occurs in the flame region, which has a high concentration of particles.

5.3.4 Sensitivity of the approximations for the radiative properties

The effects of the radiation models employed to describe the properties of the gas and particles on the radiative heat transfer are investigated in this section. The non-grey WSGG model is employed to calculate the radiation of the gas phase coupled with the radiation interaction from the particulate phase. The Mie theory, as well as the constant and linear models, are employed to describe the particle radiative properties. The predicted results, calculated from the data for a 250 kW furnace, are compared against the experimental measurements under the air-fired condition and a range of oxyfuel conditions.

Fig. 5.13 shows the radial distribution of the temperature at different positions along the furnace for both the air- and oxy-fired conditions. Different cases are implemented by employing the grey and non-grey gas radiative models coupled with the constant, linear or Planck averaged coefficients for the radiative properties of the particles. In terms of having the same radiative model for the gases

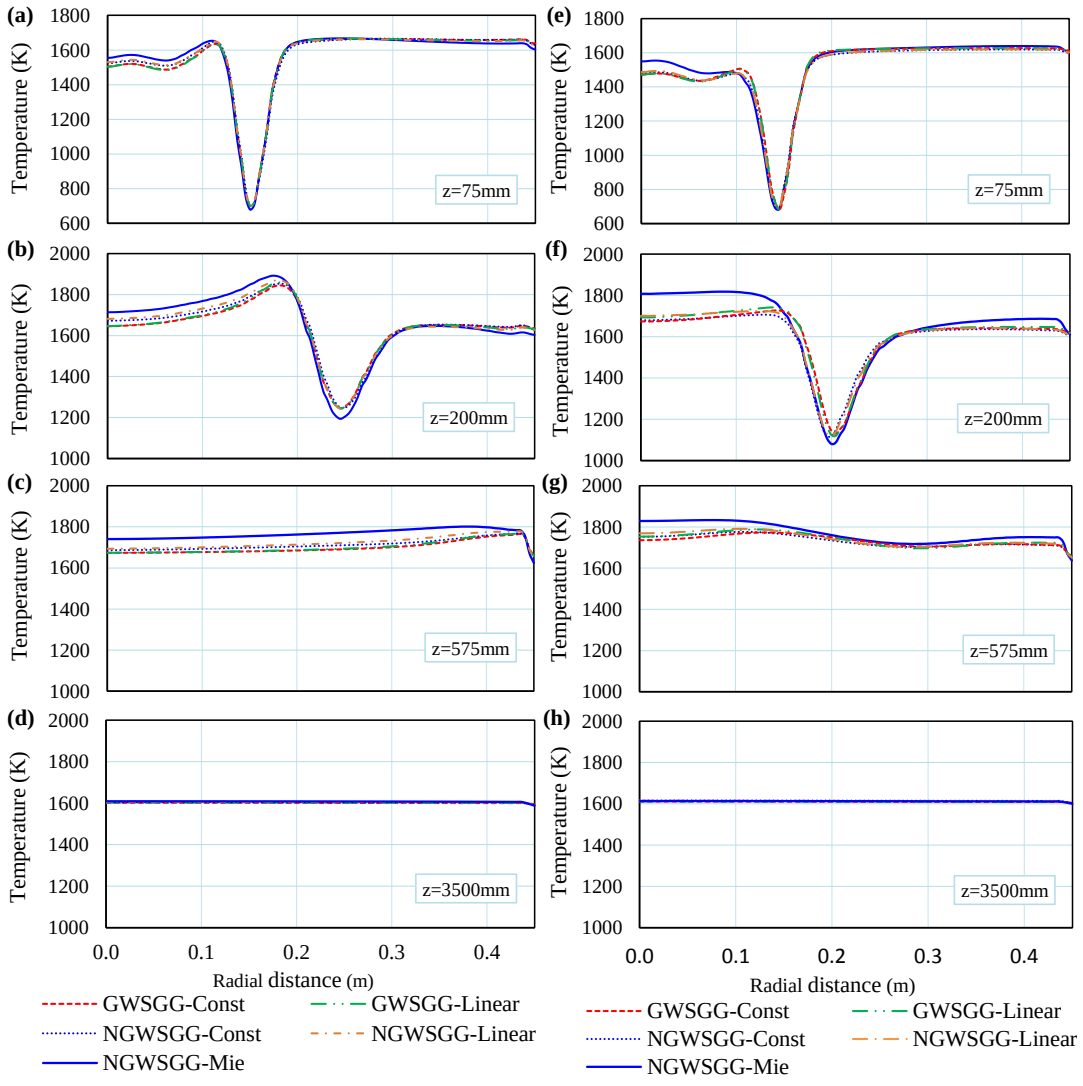

Figure 5.13: Radial temperature distribution at several distances from the burner exit for the air-fired condition (left) and the oxy-27 condition (right).

(grey WSGG or non-grey WSGG), there is only a small difference in the temperature distribution between the cases that have constant and linear radiative properties for the particles. In contrast, being described by the same radiative model for the particles (constant or linear cases), the non-grey gas models show higher temperatures than those situations when employing the grey gas models. This is mainly in regions that contain a higher particle concentration (such as the inner recirculation zone located close to the exit of the burner). The temperatures in the case of the non-grey gas and the Planck mean values for the par-

ticles (NGWSGG-Mie) is more overpredicted in comparison with the cases that have constant or linear radiative coefficients for the particles (NGWSGG-Const, NGWSGG-Linear). This is due to the radiative properties of the particles, that are described by the Mie theory, being the dominant scattering coefficients and having significantly lower absorption coefficients, as shown in Fig. 5.14, and consequently increasing the temperature of the surrounding gas. In the near-burner region, the higher concentration of the particles in the internal recirculation zone also causes a significantly higher in-flame temperature in the non-grey WSGG cases than for the other cases that are described by the grey gas model. In contrast, this is not found to be the situation in the outer recirculation zone, where there is a lower concentration of particles. Further downstream, at an axial distance 575 mm from the exit of the burner, there is a substantial amount of fly ash with an almost constant concentrations in the radial direction and there is no fluctuations in the radial temperature profiles. A similar variation trend can be observed at 3500 mm from the exit of the burner in the burnout region and there is a similar temperature distribution for all cases investigated in this region. The contours of the temperature distribution for both the air-fired and oxy-fired conditions are shown in Fig. 5.15. From this figure, the high-temperature flame of the oxy-fired conditions are closer to the centreline of the furnace compared to that of the air-fired condition. This may be a consequence of the lower volume flow rate of the oxidant flows under the oxy-fired conditions compared to that of the air-fired condition.

The results of this CFD study for the radiative incident wall heat fluxes are shown in Fig. 5.16 for both air and oxy-fired conditions compared to the experimental data from [265]. The experimental data shows that the incident wall heat fluxes increase quickly in the first section of the furnace, reaching their peak values at about 0.5 m and 0.75 m from the burner exit for the air and oxy-fired conditions, respectively. The difference in the positions of the peak values of the incident wall heat flux under the oxy-fired condition, compared to that of the air-fired condition, can be explained by the different flame behaviour under

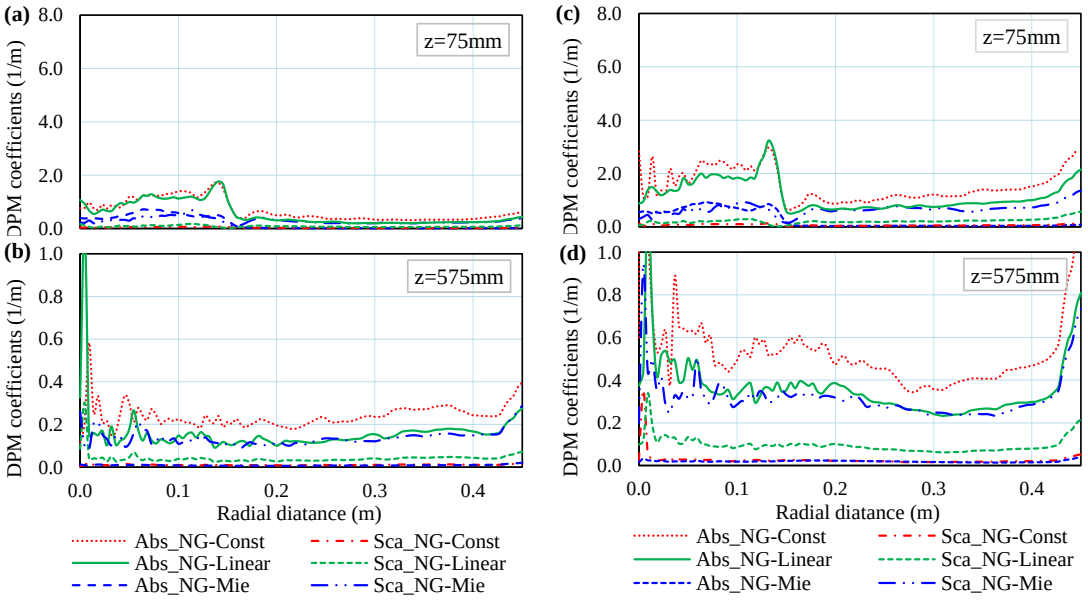

Figure 5.14: Particles radiative properties at distances 75 mm and 575 mm from the burner exit for (a, b) the air-fired condition, and (c, d) the oxy-27 condition.

the conditions investigated in this study and this is caused by the lower volume flow rates of the inlet flows under oxyfuel conditions. The behaviour of the heat fluxes are quite similar for both conditions in the downstream region of the furnace from the axial distance 1 m to the furnace exit. Results from the CFD show the same behaviours for the incident wall heat fluxes compared to the experimental data for both conditions. The different flame behaviours, shown in Fig. 5.15, can be explained by the differences in the peak positions of the heat fluxes for the two conditions.In terms of the effects of the gas and particle models to the incident wall heat fluxes under the CFD study for both the air and oxy-fired conditions, the non-grey gas model shows an improvement in the results in the flame zone compared to that of the grey gas model. The GWSGG-const case and the NGWSGG-Const case show the over-predicted results in comparison with the cases that have linear coefficients for the particle radiation, namely the GWSGG-Linear and the NGWSGG-Linear cases. This is due to reducing the equivalent absorption coefficients of the particles under the linear properties of the particles. The properties of the particles described by the Mie theory have a significantly lower incident wall heat flux but they are in closer agreement with

the experimental data. The lower incident wall radiation is due to the Mie theory cases having a significantly lower equivalent absorption coefficient and a higher scattering efficiency of the particles compared to the constant and linear cases, as shown in Fig. 5.14.

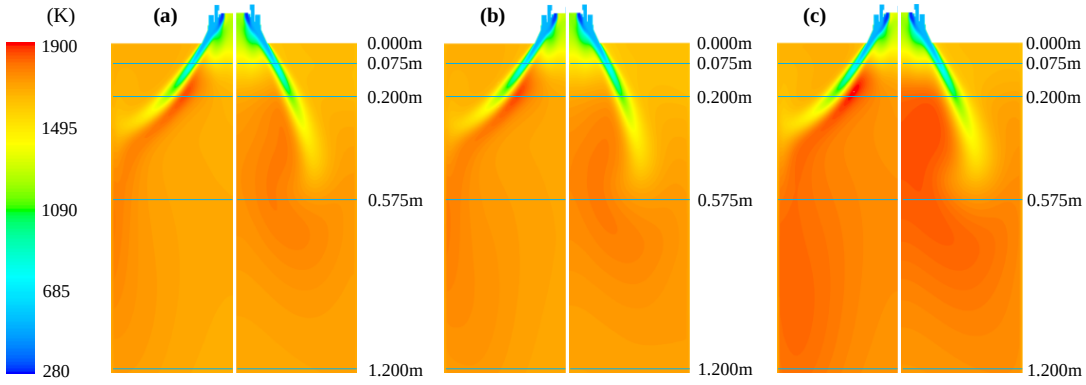

Figure 5.15: Temperature distributions of the air-fired condition (left) and Oxy-27 condition (right) for different radiative properties of the gas and particles. (a)WSGG-Const, (b)NGWSGG-Const, and (c)NGWSGG-Mie.

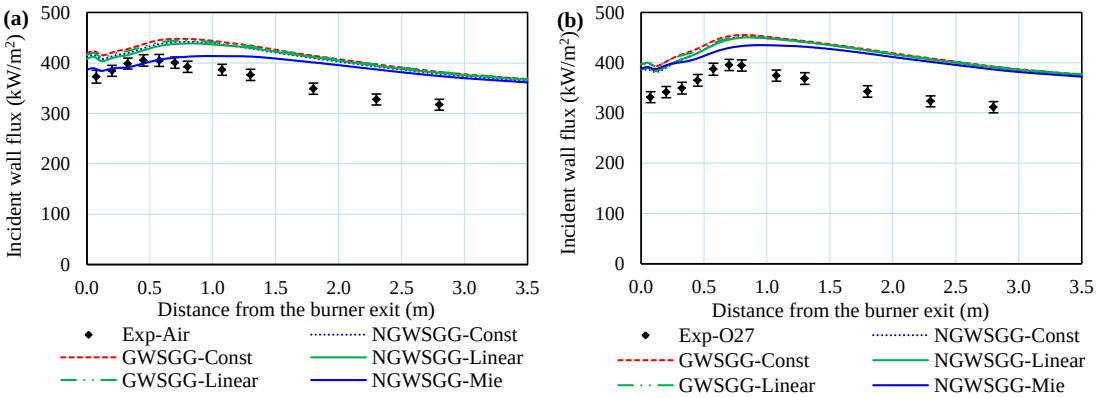

Figure 5.16: The CFD results for the surface incident radiative heat flux for (a) the air-fired condition, and (b) the oxy-27 condition compared to the experimental data [265].

5.4 Effect of the radiation of the particles on the NO emissions

The mechanisms for the NO_x formation and destruction processes in combustion systems are very complicated [297]. As the NO_x species are trace species within the domain, the formation of the pollutant species does not significantly affect the fluid dynamics or heat transfer of the combustion process, and so can be calculated as a post-processing step. This means that the accuracy in the predicting of the flame temperature, volatile release, char burnout and aerodynamics are prerequisites in the NO_x formation predictions [277]. This section determines the sensitivity of the NO_x prediction to the radiation models selected.

In this study, 80% of the coal nitrogen is assumed to be released with the volatiles-N and 20% of the nitrogen is bound with char. The volatile-N converts to HCN and NH_3 as intermediate species at 55% and 10%, respectively, with the rest of the volatile-N forming directly to NO. A similar partition of the intermediate species has been examined on pulverised coal combustion and this showed a good agreement with the experiment data [290]. The char-N is directly converted to NO [348] and the partial equilibrium approach [321] was selected for the reburning solution. Fig. 5.17 illustrates a simple NO formation and destruction pathway that is employed in this section.

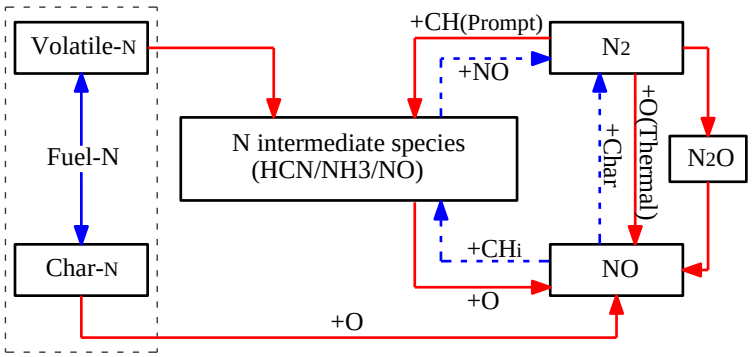

Figure 5.17: Pathway of the NOx formation/destruction employed in the CFD prediction of the NO pollutant.

5.4.1 Sensitivity of equivalent fuels to reburning

The partial equilibrium approach employed for modelling the reburn in this study is a simple procedure compared to a detailed kinetic scheme which is massively computational expensive for coal combustion in order to specify the radical concentrations. In the partial equilibrium approach, the reburn fuel can be selected as an equivalent fuel, such as CH, CH_2, CH_3 or CH_4. The ratio C/H of the fuel can be considered as a way of selecting the equivalent fuel type but this method is still debatable [97]. The sensitivity of the NO concentration to the equivalent fuels, as well as the missing the reburn fuels for both the air and oxyfuel conditions are investigated in this section. The grey WSGG model and constant values are employed to describe the radiative properties of the gas and particles, respectively.

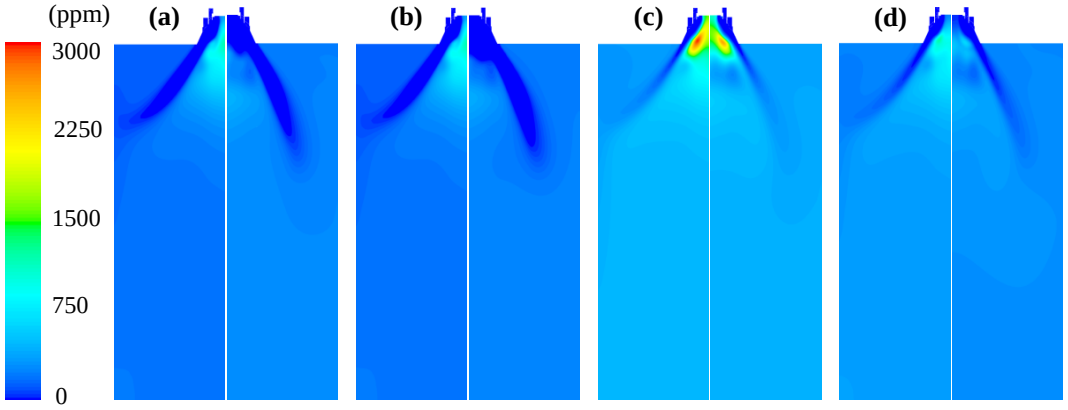

Figure 5.18: The NO distributions of the air-fired condition (left) and the Oxy-27 condition (right) for different equivalent fuels, (a) CH, (b) CH_2, (c) CH_3, and (d) CH_4.

The results for the concentration of NO with the different equivalent fuels employed are shown in Figs. 5.18 to 5.21. The results show that the concentration of NO is significantly sensitive to the equivalent fuel employed. The CH_4 equivalent fuel shows the best agreement with the experimental data for both the air and oxyfuel conditions, being about 10% and 5% higher compared to the experimental data for the air and oxyfuel condition, respectively. The CH_3 appears to fail to predict the concentration of NO for both the air and oxyfuel conditions and

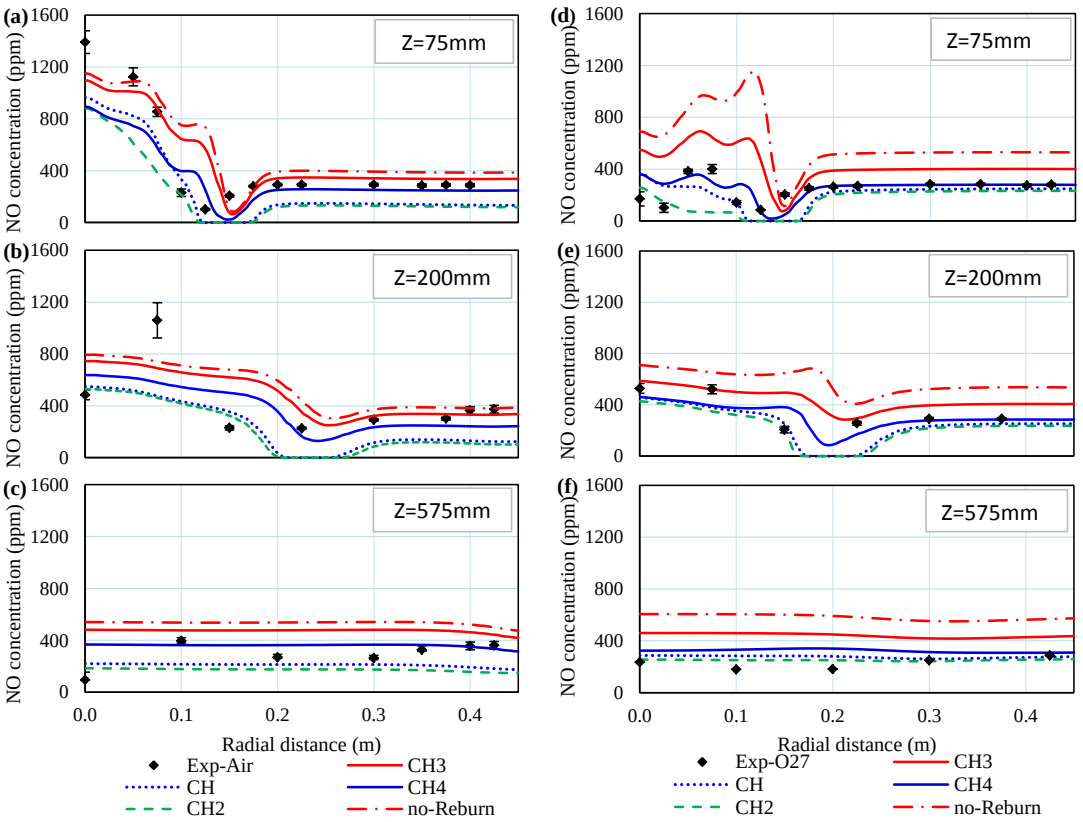

Figure 5.19: Radial NO distribution at 75 mm, 200 mm and 575 mm from the burner exit for different equivalent fuels for (a-c) the air-fired condition and (d-f) the oxy-fired conditions.

the NO prediction result using the CH_3 is close to that of the no-reburn case, which significantly overpredicts the NO results compared to experimental data, being about 43% for the air and 75% for the oxyfuel conditions. The CH, CH_2 show considerably under predicted result for the air case, however, they are in good agreement with the experimental data in the oxyfuel condition. It has been found that the CH_4 can be selected as the best equivalent fuel for the partial equilibrium approach [321] in this study.

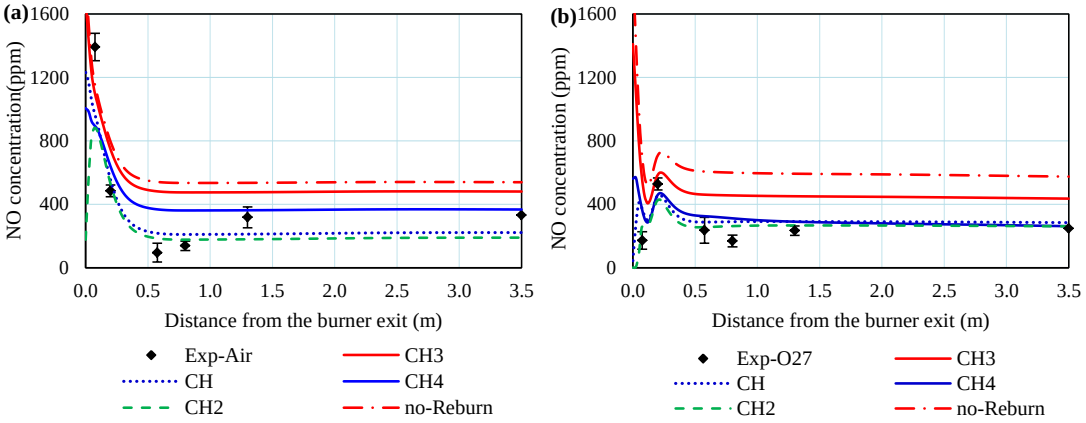

Figure 5.20: Axial NO distribution along the furnace for (a) the air-fired condition, and (b) the oxy-fired conditions.

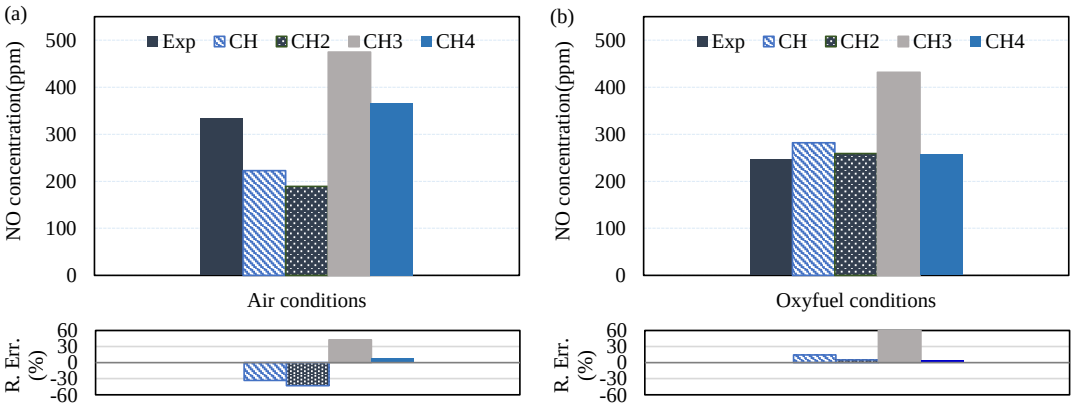

Figure 5.21: The average NO concentration at the exit section of the furnace (a) the air-fired condition, and (b) the oxy-fired conditions.

5.4.2 Effect of the radiative properties on the NOx emission

The effect of the simplified models to the radiation of the gas and particles, the grey WSGG for the radiation of the gas and the constant models for the properties of the particles, and the more exact solutions, the NGWSGG model for the radiation of the gas and the Mie theory the particle radiative properties, on the NO emission are investigated in this section. The modelling results are compared against the experimental measurements for the in-flame NO concentrations, which were obtained under the air-fired and oxy-fired conditions.

The radial and axial profiles of the NO concentration from the measurement

and CFD modelling for both the air- and oxy-fired conditions are shown in Figs. 5.22 and 5.23, respectively. Experimental data for the cases investigated in this study show that the NO concentration in the region close to the burner in the air case is significantly higher than that in the oxy-fired conditions. Under the oxy-fired conditions, the NO concentration at the burner exit, Fig. 5.24, decreases by about 25% for the Oxy-27 and 30% for Oxy-30 cases compared to that of the air case. This is because of the combustion in this study using once-through O_2/CO_2 mixtures, without a recycled flue gas, and the lower NO under the oxy-fuel conditions can be explained by the missing nitrogen and the enhancing of the heterogeneous reburning because of the higher CO concentration [32].

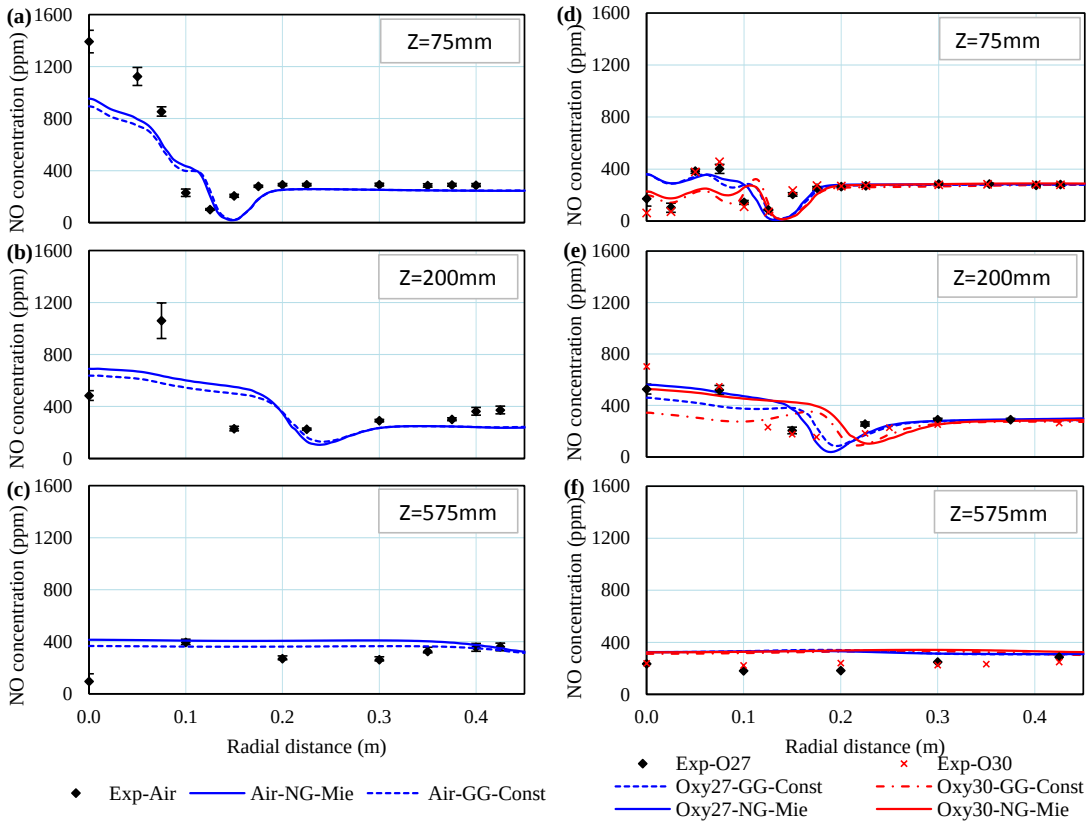

Figure 5.22: Radial NO distribution at 75 mm, 200 mm and 575 mm from the burner exit for (a-c) the air-fired condition and (d-f) the oxy-fired conditions.

The CFD results presented in Figs. 5.22 and 5.23 show a comparison of the predicted NO concentrations under two cases with different radiation properties for the gas and particles, namely, the grey gas coupled with the constant particle

property (GWSGG-Const) and the non-grey gas coupled with the Mie theory (NGWSGG-Mie) for the air-fired and the oxy-fired conditions. Both sets of results show a similar trend and a reasonable agreement with the experimental measurements, except in the inner recirculation zone close to the burner. In this region, the NO distribution under the NGWSGG-Mie case shows a better trend compared to that of the GWSGG-Const case, with a significantly higher NO concentration. This can be due to the higher temperature in the NGWSGG-Mie case subsequent to the other changes in the combustion behaviour in this region, for example the lower volatile concentration as shown in Fig. 5.25. Results from the experiment and simulation, Fig. 5.24, show the same trend and the NO concentration at the exit section of the furnace of the air-fuel condition is higher than that of the oxy-conditions. Under the air conditions, Fig. 5.24(a), the NGWSGG-Mie case results in a significant increase in the exit NO concentration, with a 21% increase compared with the experimental measurement, while the disagreement is only 9.7% for the GWSGG-Const case. These differences are much lower under the oxyfuel conditions as shown in Fig. 5.24(b). However, there is a larger difference in the NO concentration between the NGWSGG-Mie case compared to the GWSGG-Const under the air-fired condition compared to those under the oxy-fired conditions. This can be explained by the NO formation from the thermal mechanism, and this is almost eliminated under the oxy-fired conditions.

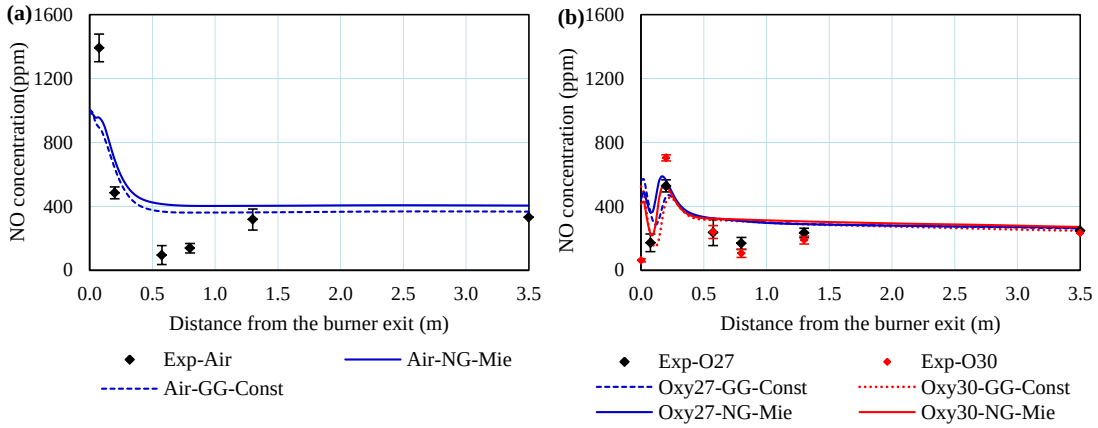

Figure 5.23: Axial NO distribution for (a) the air-fired condition, and (b) the oxy-fired conditions.

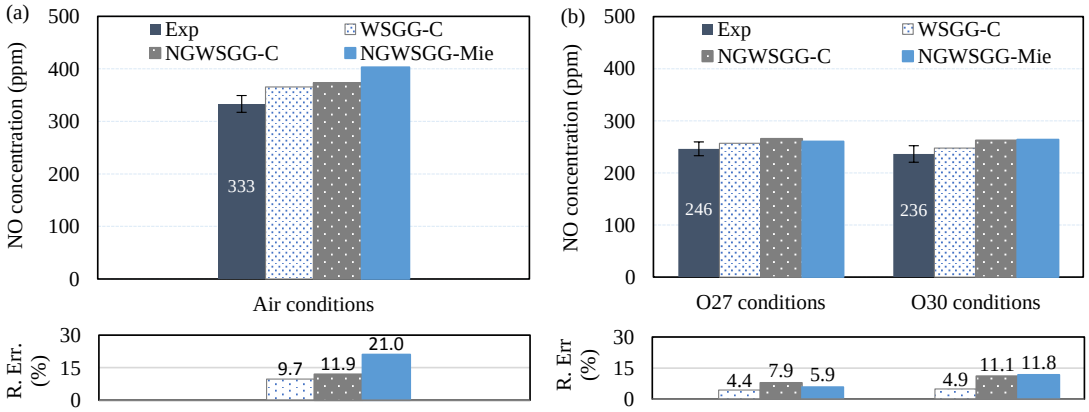

Figure 5.24: The average NO concentration at the exit section of the furnace for (a) the air-fired condition, and (b) the oxy-fired conditions.

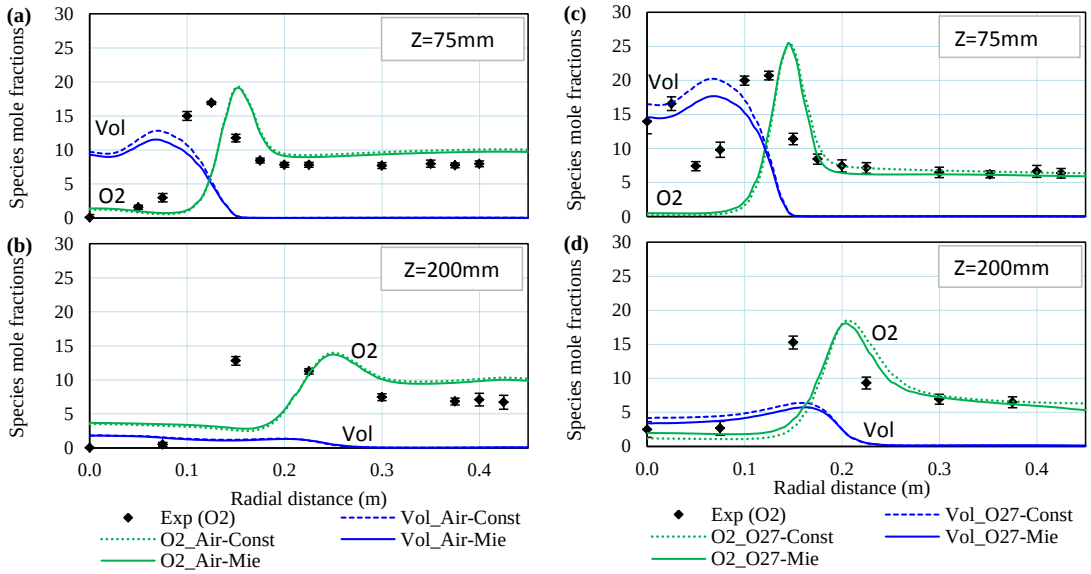

Figure 5.25: The radial oxy and volatile distributions at 75 mm and 200 mm from the burner exit for (a, b) the air-fired condition, and (c, d) the oxy-27 condition compared to the experimental data [265].

5.5 Summary and conclusions

This chapter has focused on the radiative properties of the particles for both air- and oxy-fired coal combustion conditions, and the impact of modelling these properties on the calculated predictions of the NO pollutants on the pilot-scale facility. Different spectral databases and approximation models that were investigated in

Chapters 3 and 4 are employed to investigate the radiative heat transfer and the effects of the radiative models on the NO predictions on the 250 kW combustion. The main conclusions and findings of this chapter are listed as follows:

The sensitivity of the radiative heat transfer to the number of diameters have been investigated. The results show that for the case with the radiative properties of the particles being constant, the number of diameters employed for the Rosin-Rammler distribution has a significant impact on the prediction results of the incident wall heat flux. However, the gas temperature profile in this case is less sensitive to the resolution of the particle distribution. In the case when the particle properties are described by the Mie theory, using the spectral database of Goodwin and Mitchner [247], the influence of the number of diameters on the temperature profile of the gas and the incident wall heat flux are almost eliminated. This is because of the significantly lower absorption properties and the high scattering properties of the particles. However, these effects can be significant when the radiative properties of the particles were described by spectral databases, thus resulting in a significantly high absorption efficiency of the particles.

The UDFs have been developed to calculate the temperature of the particles, coal and flyash, for the 250 kW_{th} under both the air and oxyfuel conditions. The results show that the particle temperature profile of the ash particles is close to that of the gases. However, the temperature profile of the coal/char particles fluctuates through the furnace and this shows a different behavior between the air and oxyfuel conditions. The average temperature of the coal/char and the fly ash is close to the fly ash temperature and this is because of the much lower number of coal/char particles. The results highlight the behaviour of the particles under the air and oxyfuel conditions. The effect of particles on the radiative heat transfer, and also the effect of the air and oxyfuel conditions, on the behaviour of the particles needs to be further studied, especially, the presence of the particles in the burner region where there is a high concentration of the coal/char particles.

Different spectral databases for the particles have been employed to describe

the radiative heat transfer of the 250 kW furnace under the air condition. Similar to the results obtained in Section 4.3.2 for the small-scale furnace, the available spectral databases for the coal/char particles have only a small impact on the temperature and the incident wall heat flux results. The temperature and heat flux are somewhat sensitive to the spectral database of the ash while the sensitivity of the spectral databases for coal for the radiative heat transfer on the pilot-scale furnace are almost eliminated. However, the study was based on currently available spectral databases and for a pilot-scale furnace. This will be different for large scale furnaces, especially, the effect of the flyash, see Chapter 4.

The effect of radiation models employed to describe radiative properties of both the gases and particles on the radiative heat transfer has been investigated. The grey and non-grey gas property models, coupled with the different solutions for the particle properties, are employed to describe the radiation heat transfer and these results are compared with the experimental data. The radiative properties of the particles, that are described by the Mie theory, show a significant improvement in the incident wall heat flux. However, the temperature is much higher compared to the case of having constant properties for the particles in the inner recirculation region where there is a higher coal/char particle concentration.

The effect of the radiation on the NO emissions has been investigated for the pilot-scale furnace for both the air and oxyfuel conditions, with different radiation models for the gases and particles that have been employed. The non-grey WSGG coupled with the Mie theory results in a considerable improvement in the NO prediction in the burner region which contains a high particle concentration of the coal/char particles, compared to those from the simplified models for the gases and the particles. However, these models show an over prediction in the NO concentrations at the exit section of the furnace, especially for the air-fuel case. The NO_x predictions can vary by as much as 10%, depending on the choice of the radiation model. This is due to the sensitivity of the thermal NO_x mechanism, although this is somewhat reduced when considering the oxy-fired conditions.

6 Conclusions and future work

The work presented in this thesis has focused on the radiation simulations for the air and oxyfuel combustions using computational fluid dynamics. The two main objectives of this study are as follows:

- Investigation of the gas and particle radiation in small and large-scale pulverised coal combustion furnaces under air and oxyfuel conditions.

- Effects of the gas and particle models on the radiative heat transfer, as well as the NO pollutants in the 250 kW pilot-scale facility.

The first point of the objectives was addressed in Chapters 3 and 4 and the second point was investigated in Chapter 5. The results from this study are summarised through the main conclusions in Section 6.1, and suggestions for further studies are proposed in Section 6.2.

6.1 Conclusions

A range of global radiation models for the gaseous radiative properties and a range of particle radiative properties have been investigated through several theoretical test cases and against measurement data within a pilot scale furnace. The main conclusions in the study are summarised as follows:

The non-grey property of the particles, which is calculated based on the wavelength-dependent optical constants, should be employed for calculating the radiative properties of the particles. There is a large discrepancy between the radiative property results, which were calculated from the different databases for the wavelength-dependent optical constants. However, the radiative heat transfer appears to be less sensitive to the spectral databases and this depends on the scale

of the furnaces employed. For the small scale boiler furnace, the heat transfer results are much more sensitive to the spectral databases of the coal compared to the ash. In contrast, the radiative heat transfer results show a sensitivity to the ash for large-scale boiler furnaces and a less sensitivity to the coal data. Therefore, the choice of the databases for the CFD calculations of the radiative properties of the ash, which is considered to have a significant influence on the radiative heat transfer in large-scale furnaces, needs to be considered carefully, such as the composition, temperature of the ash and the accuracy of the measurement method.

Employing approximate solutions for calculating the radiative properties of the particles, coal and ash, can reduce the computational time compared to that of the Mie theory. However, applying these solutions can give significant errors when these approximations employ the wavelength-dependent optical constants in the calculations. In terms of the non-grey approximations, the Kim and Loir approximation [259] for the coal and the anomalous approximation [271] for the ash can be used for CFD modelling. However, these solutions can give considerable errors that depend on the scale of the furnace, such as the small-scale furnace for the coal and the large-scale furnace for the ash. In terms of the grey-properties approximations, which are developed using a specific spectral database, may give a large error when they are applied for different spectral databases compared to that of the Mie theory.

The NGWSGG and the SLW models have been validated in the 1D and 3D cases for both the air and oxyfuel conditions. It is demonstrated that the SLW model shows very good agreement with the benchmark, while the NGWSGG model is in reasonable agreement with the benchmark. However, the number of gases required for this model to reach good accuracy may result in a significant computational cost in comparison to the use of the NGWSGG model. Further, the implementation of the SLW model is more complex compared to that of the NGWSGG model. Furthermore, the results obtained in Chapter 4 have shown that particle radiation dominates the total radiation of a mixture of the gas and

the particles. Therefore, the NGWSGG model is recommended for the CFD modelling of a practical combustion furnace.

Results from Chapters 3 and 4, for the presence of gas only, show that the oxyfuel environment can increase the emission of combustion products, which can increase the total wall heat flux. However, this environment can increase the optical pathlength, which decreases the incident heat flux to the wall. Therefore, the heat flux to the wall can increase or decrease depending on the temperature profile. In a combustion furnace, with a high temperature of the gas close to the wall, the effect of the optical thickness is likely to be small. Therefore, the heat flux under the oxyfuel conditions can be higher than that under the air condition. However, when having the presence of particles, it has been found that there is not much difference between the results obtained for the radiative heat fluxes under the air and oxyfuel conditions. This demonstrates the dominant effect of the particles to the radiative heat transfer compared to that of the gas. It should be noted that this will be different for a real furnace, where the oxyfuel condition will change the temperature of the furnace and the concentration of the coal/char particles.

The Planck and constant radiative properties of the particles, which have been widely used in CFD modelling, has been evaluated for both small and large-scale furnaces. It has been found that the effect of the particles on the radiative heat transfer depends on the scale of the furnace, with a higher sensitivity under the small-scale furnace being found. The NGWSGG model for the gas, coupled with the Planck mean properties for the particles, can produce good results in comparison to the benchmark under a large-scale furnace. However, a significant error occurs when applied to a small-scale furnace. In terms of the constant properties of the particles, the total surface heat flux increases with increasing the absorption coefficient of the particles in the small-scale furnace while it decreases in the large-scale furnace and the absorption coefficient of about 0.9 is recommended for CFD modelling for both small and large-scale furnaces.

The sensitivity of the radiative heat transfer to the coal/char particle concentration are investigated in Chapter 4 for different scales of the furnace. The results show that the radiative heat flux is significantly sensitive to the coal/char particle concentration for a small-scale furnace. For the 250 kW combustion, the number of diameters in the Rosin-Rammler distribution, which affects the particle concentration, has a considerable impact on the prediction results of the radiative heat transfer. This is more pronounced for the incident wall heat flux for the case when the constant values of the radiative properties of the particles are employed. However, this influence on the temperature and the incident wall heat flux can be different for the Mie theory calculation, depending on the spectral databases employed.

The NGWSGG, coupled with the Mie theory, results in a considerable improvement in the NO prediction in the burner region where there is a high particle concentration of the coal/char particles, compared to those from the simplified models for the gases and the particles. However, these models show an over prediction in the NO concentrations at the exit section of the furnace, especially for the air-fuel case. The NO_x predictions can vary by as much as 10%, depending on the choice of the radiation model, and this is due to the sensitivity of the thermal NO_x mechanism, although this is somewhat reduced when considering oxy-fired conditions.

Overall, radiation heat transfer plays an important role in pulverised coal combustion, influencing the overall combustion efficiency, pollutant formation and flame ignition and propagation. An accuracy in calculation of the radiative heat transfer is considered to be a priority for the retrofitting of existing units to oxyfuel combustion. The results obtained from this study clearly show that particle radiation in pulverised coal combustion is dominant compared to that of the gas. The sensitivity of the radiative heat transfer to the particle properties and solutions employed to calculate the radiative properties of the particles have been investigated for both small and large-scale furnaces. The results obtained from this study can be employed in CFD calculations for the improvement and

design of air and oxyfuel pulverised coal combustion.

6.2 Future work

Different available spectral databases for the coal and ash have been employed to study the sensitivity of the radiative properties of the particles to the radiative heat transfer. Although many investigations have been performed for the measurements of the optical properties of the coal and ash particles, the number of measurements for the coal and fly ash appear to be not enough to be confident for applying in the modelling of a specific type of coal in combustion. This is because there are still large difference in the reported experimental measurements until now. Therefore, an accurate measurement and a wide range of coal/char and fly ash particles employed for measuring can assist in the reduction of the sensitivity of the radiative properties of the particles in the calculations of the radiative heat transfer.

The temperature of the coal/char and fly ash were investigated in the CFD modelling and presented in Chapter 5 for the pilot-scale facility under the air and oxyfuel conditions. The results show that the temperature of the coal/char are lower than that of the gas in the regions closed to the centreline of the furnace. Those results show the same trend with the measurement results for a 77 kW_{th} furnace [349]. However, these results appear to be different in comparison to some other measurements [117, 347]. In CFD modelling, different temperature profiles for the coal/char particles has been assumed in studies [326, 327, 350]. The results presented in Chapter 4 show that the temperature of the coal/char particles has a significant effect to the total wall heat flux under the small-scale furnaces. Therefore, it is important to have further modelling and experimental studies on the particle parameters, such as the profile, concentration and temperature of the coal/char particles, for different types of furnaces under air and oxyfuel conditions.

The effects of the particles on the radiative heat transfer for the small and large-scale furnaces have been investigated in Chapter 4. The study only fo-

cused on the radiative heat transfer so this study is separated from the other sub-models, such as the turbulence and combustion models. Therefore, it is important to investigate the radiation, including the effect of these sub-models, which significantly influences the gas and particle distributions, and the temperature profiles. The investigation of the radiative heat transfer for a real furnace has been performed in Chapter 5 for pilot-scale furnace. Therefore, a further study needs to be performed for a large-scale furnace which has been shown complex behaviour of the heat transfer to the radiative properties of the particles by the influence of the optical pathlength. It would also important to consider simultaneously the effects of other accurate sub-models, such as the turbulence and chemical reaction models, when investigating the radiative heat transfer.

The anisotropic scattering phase function in this study was simplified to an isotropic scattering one with the scale of the scattering efficiency by asymmetry factor as mentioned in Section 5.2. This solution has been determined to be appropriate for pulverised coal combustion modelling [208, 338], which has a highly forward scattering medium, and can assist in the reduction of the computational time. However, the accuracy of the scattering phase function that has been applied in this study needs to be evaluated at different scales of the combustion furnaces. Furthermore, there are different approximations for the anisotropic scattering phase function and there are still different discussions on the effect of these approximations. Therefore, further studies need to focus on the evaluation of the different approximations for the scattering phase function in a 3D combustion environment as being defined in this thesis.

In this study, the influence of the radiation properties of the particles, as well as the gas property models, on the prediction of the formation of NO_x pollutants have been investigated. The study in Chapter 5 has found that the main sensitivity of the radiation models to the NO_x concentration occur in the flame region, where there is a high concentration of particles and the change in the temperature profile in the flame region results in other changes in the combustion behaviour in this region, for example the lower volatile concentration. One of the more

important future extensions of the work should include the other effects of the radiation on the behaviour of the coal particles, such as the effect of the radiation models on the ignition, and the burnout under both air and oxyfuel conditions.

Accurate radiation modelling needs to consider both gaseous phase and particulate participation in the radiative mechanism. The increase in the concentration of participating species under the oxyfuel combustion, namely CO_2 and H_2O, has been received a special attention over the past decades. Results from this study show that the particles radiation is dominance to the total radiative heat transfer compared to that of the gases in pulverised coal combustion. The effect of the gases composition to the total heat flux under the oxyfuel condition appears to be slightly different compared to that under the air condition when there is the presence of the particles. Therefore, more attention needs to be focused on the effect of particles on the radiative heat transfer under the oxyfuel condition.

References

[1] British Petroleum, "BP Energy Outlook 2018," 2018.

[2] British Petroleum, "BP Statistic Review of World Energy," June 2014.

[3] British Petroleum, "BP Statistic Review of World Energy," June 2017.

[4] International Energy Agency (IEA), "World Energy Outlook," 2016.

[5] D. Clarke, B. Debeljak, V. de Janeiro, G. Göttlicher, D. Graham, N. Kirkegaard, M. Madsen, S. Pasini, B. Stortelder, L. Strömberg, *et al.*, "CO_2 Capture and Storage: A VGB report on the state of the art," *Essen, Germany, VGB PowerTech eV. Retrieved August*, vol. 26, p. 2006, 2004.

[6] I. Energy Agency (IEA), "Energy and air pollution," 2016.

[7] British Petroleum, "BP Energy Outlook 2035," February 2015.

[8] B. Singh, A. H. Strømman, and E. G. Hertwich, "Comparative life cycle environmental assessment of CCS technologies," *International Journal of Greenhouse Gas Control*, vol. 5, no. 4, pp. 911–921, 2011.

[9] International Energy Agency (IEA), "20 years of Carbon Capture and Storage," 2016.

[10] B. Metz, O. Davidson, H. De Coninck, M. Loos, and L. Meyer, "IPCC special report on carbon dioxide capture and storage," tech. rep., Intergovernmental Panel on Climate Change, Geneva (Switzerland). Working Group III, 2005.

[11] J. Pires, F. Martins, M. Alvim-Ferraz, and M. Simões, "Recent developments on carbon capture and storage: an overview," *Chemical Engineering Research and Design*, vol. 89, no. 9, pp. 1446–1460, 2011.

[12] A. A. Olajire, "CO_2 capture and separation technologies for end-of-pipe applications: a review," *Energy*, vol. 35, no. 6, pp. 2610–2628, 2010.

[13] J. Gibbins and H. Chalmers, "Carbon capture and storage," *Energy policy*, vol. 36, no. 12, pp. 4317–4322, 2008.

[14] M. Wang, A. Lawal, P. Stephenson, J. Sidders, and C. Ramshaw, "Post-combustion CO_2 capture with chemical absorption: a state-of-the-art review," *Chemical Engineering Research and Design*, vol. 89, no. 9, pp. 1609–1624, 2011.

[15] T. C. Merkel, H. Lin, X. Wei, and R. Baker, "Power plant post-combustion carbon dioxide capture: an opportunity for membranes," *Journal of Membrane Science*, vol. 359, no. 1, pp. 126–139, 2010.

[16] A. F. Ghoniem, "Needs, resources and climate change: clean and efficient conversion technologies," *Progress in Energy and Combustion Science*, vol. 37, no. 1, pp. 15–51, 2011.

[17] N. Florin and P. Fennell, "Carbon capture technology: future fossil fuel use and mitigating climate change," *Grantham Institute for Climate Change, Briefing Paper*, no. 3, 2010.

[18] International Energy Agency (IEA), "Energy technology perspectives 2012,"

[19] J. Davison and K. Thambimuthu, "An overview of technologies and costs of carbon dioxide capture in power generation," *Proceedings of the Institution of Mechanical Engineers, Part A: Journal of Power and Energy*, vol. 223, no. 3, pp. 201–212, 2009.

[20] F. L. Horn and M. Steinberg, "Control of carbon dioxide emissions from a power plant (and use in enhanced oil recovery)," *Fuel*, vol. 61, no. 5, pp. 415–422, 1982.

[21] A. Abele, G. Kindt, W. Clark, R. Payne, and S. Chen, "An experimental program to test the feasibility of obtaining normal performance from combustors using oxygen and recycled gas instead of air," tech. rep., Argonne National Lab., IL (USA); Energy and Environmental Research Corp., Irvine, CA (USA), 1987.

[22] International Energy Agency (IEA), "Oxyfuel combustion of pulverised coal," 2010.

[23] M. B. Toftegaard, J. Brix, P. A. Jensen, P. Glarborg, and A. D. Jensen, "Oxy-fuel combustion of solid fuels," *Progress in Energy and Combustion Science*, vol. 36, no. 5, pp. 581–625, 2010.

[24] G. Scheffknecht, L. Al-Makhadmeh, U. Schnell, and J. Maier, "Oxy-fuel coal combustion-A review of the current state-of-the-art," *International Journal of Greenhouse Gas Control*, vol. 5, pp. S16–S35, 2011.

[25] L. Chen, S. Z. Yong, and A. F. Ghoniem, "Oxy-fuel combustion of pulverized coal: characterization, fundamentals, stabilization and CFD modeling," *Progress in Energy and Combustion Science*, vol. 38, no. 2, pp. 156–214, 2012.

[26] D. Singh, E. Croiset, P. L. Douglas, and M. A. Douglas, "Techno-economic study of CO_2 capture from an existing coal-fired power plant: MEA scrubbing vs. O_2/CO_2 recycle combustion," *Energy Conversion and Management*, vol. 44, no. 19, pp. 3073–3091, 2003.

[27] D. Zhu, J. P. Eason, and L. T. Biegler, "Energy-efficient CO_2 liquefaction for oxy-combustion power plant with ASU-CPU integration enhanced by cascaded sub-ambient energy utilization and waste heat recovery," *International Journal of Greenhouse Gas Control*, vol. 61, pp. 124–137, 2017.

[28] C. Fu and T. Gundersen, "Exergy analysis and heat integration of a coal-based oxy-combustion power plant," *Energy & Fuels*, vol. 27, no. 11, pp. 7138–7149, 2013.

[29] A. W. Dowling and L. T. Biegler, "A framework for efficient large scale equation-oriented flowsheet optimization," *Computers & Chemical Engineering*, vol. 72, pp. 3–20, 2015.

[30] B. J. Buhre, L. K. Elliott, C. Sheng, R. P. Gupta, and T. F. Wall, "Oxy-fuel combustion technology for coal-fired power generation," *Progress in Energy and Combustion Sscience*, vol. 31, no. 4, pp. 283–307, 2005.

[31] E. Kakaras, A. Koumanakos, A. Doukelis, D. Giannakopoulos, and I. Vorrias, "Oxyfuel boiler design in a lignite-fired power plant," *Fuel*, vol. 86, no. 14, pp. 2144–2150, 2007.

[32] H. Liu, R. Zailani, and B. M. Gibbs, "Comparisons of pulverized coal combustion in air and in mixtures of O_2/CO_2," *Fuel*, vol. 84, no. 7, pp. 833–840, 2005.

[33] Y. Tan, E. Croiset, M. A. Douglas, and K. V. Thambimuthu, "Combustion characteristics of coal in a mixture of oxygen and recycled flue gas," *Fuel*, vol. 85, no. 4, pp. 507–512, 2006.

[34] S. Khare, T. Wall, A. Farida, Y. Liu, B. Moghtaderi, and R. Gupta, "Factors influencing the ignition of flames from air-fired swirl pf burners retrofitted to oxy-fuel," *Fuel*, vol. 87, no. 7, pp. 1042–1049, 2008.

[35] J. Smart, P. O'Nions, and G. Riley, "Radiation and convective heat transfer, and burnout in oxy-coal combustion," *Fuel*, vol. 89, no. 9, pp. 2468–2476, 2010.

[36] W. Zhou and D. Moyeda, "Process evaluation of oxy-fuel combustion with flue gas recycle in a conventional utility boiler," *Energy & Fuels*, vol. 24, no. 3, pp. 2162–2169, 2010.

[37] P. Heil, D. Toporov, H. Stadler, S. Tschunko, M. Förster, and R. Kneer, "Development of an oxycoal swirl burner operating at low O_2 concentrations," *Fuel*, vol. 88, no. 7, pp. 1269–1274, 2009.

[38] M. Habermehl, J. Erfurth, D. Toporov, M. Förster, and R. Kneer, "Experimental and numerical investigations on a swirl oxycoal flame," *Applied Thermal Engineering*, vol. 49, pp. 161–169, 2012.

[39] J. Zhang, B. Dai, Y. Meng, X. Wu, J. Zhang, X. Zhang, Y. Ninomiya, Z. Zhang, and L. Zhang, "Pilot-scale experimental and CFD modeling investigations of oxy-fuel combustion of Victorian brown coal," *Fuel*, vol. 144, pp. 111–120, 2015.

[40] J. Guo, Z. Liu, X. Huang, T. Zhang, W. Luo, F. Hu, P. Li, and C. Zheng, "Experimental and numerical investigations on oxy-coal combustion in a 35MW large pilot boiler," *Fuel*, vol. 187, pp. 315–327, 2017.

[41] Y. Hu, H. Li, and J. Yan, "Numerical investigation of heat transfer characteristics in utility boilers of oxy-coal combustion," *Applied Energy*, vol. 130, pp. 543–551, 2014.

[42] H. Wu, Z. Liu, and H. Liao, "The study on the heat transfer characteristics of oxygen fuel combustion boiler," *Journal of Thermal Science*, vol. 25, no. 5, pp. 470–475, 2016.

[43] P. Edge, M. Gharebaghi, R. Irons, R. Porter, R. Porter, M. Pourkashanian, D. Smith, P. Stephenson, and A. Williams, "Combustion modelling opportunities and challenges for oxy-coal carbon capture technology," *Chemical Engineering Research and Design*, vol. 89, no. 9, pp. 1470–1493, 2011.

[44] N. Kimura, K. Omata, T. Kiga, S. Takano, and S. Shikisima, "The characteristics of pulverized coal combustion in O_2/CO_2 mixtures for CO_2 recovery," *Energy Conversion and Management*, vol. 36, no. 6, pp. 805–808, 1995.

[45] T. Nozaki, S. Takano, T. Kiga, K. Omata, and N. Kimura, "Analysis of the flame formed during oxidation of pulverized coal by an O_2-CO_2 mixture," *Energy*, vol. 22, no. 2-3, pp. 199–205, 1997.

[46] T. Kiga, S. Takano, N. Kimura, K. Omata, M. Okawa, T. Mori, and M. Kato, "Characteristics of pulverized-coal combustion in the system of oxygen/recycled flue gas combustion," *Energy Conversion and Management*, vol. 38, pp. S129–S134, 1997.

[47] K. Okazaki and T. Ando, "NO_x reduction mechanism in coal combustion with recycled CO_2," *Energy*, vol. 22, no. 2-3, pp. 207–215, 1997.

[48] E. Croiset and K. Thambimuthu, "NO_x and SO_2 emissions from O_2/CO_2 recycle coal combustion," *Fuel*, vol. 80, no. 14, pp. 2117–2121, 2001.

[49] Y. Hu, N. Kobayashi, and M. Hasatani, "The reduction of recycled-NO_x in coal combustion with O_2/recycled flue gas under low recycling ratio," *Fuel*, vol. 80, no. 13, pp. 1851–1855, 2001.

[50] H. Liu, R. Zailani, and B. M. Gibbs, "Pulverized coal combustion in air and in O_2/CO_2 mixtures with NO_x recycle," *Fuel*, vol. 84, no. 16, pp. 2109–2115, 2005.

[51] K. Andersson, F. Normann, F. Johnsson, and B. Leckner, "NO emission during oxy-fuel combustion of lignite," *Industrial & Engineering Chemistry Research*, vol. 47, no. 6, pp. 1835–1845, 2008.

[52] T. Wall, Y. Liu, C. Spero, L. Elliott, S. Khare, R. Rathnam, F. Zeenathal, B. Moghtaderi, B. Buhre, C. Sheng, *et al.*, "An overview on oxyfuel coal combustion-state of the art research and technology development," *Chemical Engineering Research and Design*, vol. 87, no. 8, pp. 1003–1016, 2009.

[53] S. Hjärtstam, K. Andersson, F. Johnsson, and B. Leckner, "Combustion characteristics of lignite-fired oxy-fuel flames," *Fuel*, vol. 88, no. 11, pp. 2216–2224, 2009.

[54] R. Yoshiie, N. Hikosaka, Y. Nunome, Y. Ueki, and I. Naruse, "Effects of flue gas re-circulation and nitrogen contents in coal on NO_x emissions under oxy-fuel coal combustion," *Fuel Processing Technology*, vol. 136, pp. 106–111, 2015.

[55] P. F. Nelson, A. N. Buckley, and M. D. Kelly, "Functional forms of nitrogen in coals and the release of coal nitrogen as NO_x precursors (HCN and NH_3)," in *Symposium (International) on combustion*, vol. 24, pp. 1259–1267, Elsevier, 1992.

[56] L. D. Smoot and P. J. Smith, *Coal combustion and gasification*. 2013.

[57] F. Normann, K. Andersson, B. Leckner, and F. Johnsson, "Emission control of nitrogen oxides in the oxy-fuel process," *Progress in Energy and Combustion Science*, vol. 35, no. 5, pp. 385–397, 2009.

[58] H. Cao, S. Sun, Y. Liu, and T. F. Wall, "Computational fluid dynamics modeling of NO_x reduction mechanism in oxy-fuel combustion," *Energy & Fuels*, vol. 24, no. 1, pp. 131–135, 2009.

[59] J. P. Spinti and D. W. Pershing, "The fate of char-N at pulverized coal conditions," *Combustion and Flame*, vol. 135, no. 3, pp. 299–313, 2003.

[60] C. Yin and J. Yan, "Oxy-fuel combustion of pulverized fuels: combustion fundamentals and modeling," *Applied Energy*, vol. 162, pp. 742–762, 2016.

[61] T. Smith, Z. Shen, and J. Friedman, "Evaluation of coefficients for the weighted sum of gray gases model," *Journal of Heat Transfer*, vol. 104, no. 4, pp. 602–608, 1982.

[62] C. Yin, L. C. Johansen, L. A. Rosendahl, and S. K. Kær, "New weighted sum of gray gases model applicable to computational fluid dynamics (CFD) modeling of oxy- fuel combustion: derivation, validation, and implementation," *Energy & Fuels*, vol. 24, no. 12, pp. 6275–6282, 2010.

[63] R. Johansson, B. Leckner, K. Andersson, and F. Johnsson, "Account for variations in the H_2O to CO_2 molar ratio when modelling gaseous radiative heat transfer with the weighted-sum-of-grey-gases model," *Combustion and Flame*, vol. 158, no. 5, pp. 893–901, 2011.

[64] T. Kangwanpongpan, F. H. França, R. C. da Silva, P. S. Schneider, and H. J. Krautz, "New correlations for the weighted-sum-of-gray-gases model in oxy-fuel conditions based on HITEMP 2010 database," *International Journal of Heat and Mass Transfer*, vol. 55, no. 25, pp. 7419–7433, 2012.

[65] G. Krishnamoorthy, "A new weighted-sum-of-gray-gases model for oxy-combustion scenarios," *International Journal of Energy Research*, vol. 37, no. 14, pp. 1752–1763, 2013.

[66] M. H. Bordbar, G. Węcel, and T. Hyppänen, "A line by line based weighted sum of gray gases model for inhomogeneous CO_2–H_2O mixture in oxy-fired combustion," *Combustion and Flame*, vol. 161, no. 9, pp. 2435–2445, 2014.

[67] L. J. Dorigon, G. Duciak, R. Brittes, F. Cassol, M. Galarça, and F. H. França, "WSGG correlations based on HITEMP 2010 for computation of thermal radiation in non-isothermal, non-homogeneous H_2O/CO_2 mixtures," *International Journal of Heat and Mass Transfer*, vol. 64, pp. 863–873, 2013.

[68] B. Dhungel, J. Maier, and G. Scheffknecht, "Emission behaviour during oxy-coal combustion," in *AIchE 2007 Annual Meeting, Salt Lake City, UT*, 2007.

[69] R. Stanger, T. Wall, R. Spoerl, M. Paneru, S. Grathwohl, M. Weidmann, G. Scheffknecht, D. McDonald, K. Myöhänen, J. Ritvanen, *et al.*, "Oxy-fuel combustion for CO_2 capture in power plants," *International Journal of Greenhouse Gas Control*, vol. 40, pp. 55–125, 2015.

[70] A. Sarofim, "Oxy-fuel combustion: progress and remaining issues," in *2nd Workshop of IEAGHG International Oxy-Fuel Combustion Network, Windsor, CT, USA*, 2007.

[71] A. J. Mackrory and D. R. Tree, "Predictions of NO_x in a laboratory pulverized coal combustor operating under air and oxy-fuel conditions," *Combustion Science and Technology*, vol. 181, no. 11, pp. 1413–1430, 2009.

[72] R. Viskanta and M. Mengüç, "Radiation heat transfer in combustion systems," *Progress in Energy and Combustion Science*, vol. 13, no. 2, pp. 97–160, 1987.

[73] J. Colannino, "Modeling of combustion systems: A practical approach," 2006.

[74] R. Backreedy, J. Jones, M. Pourkashanian, D. Waldron, and A. Williams, "Application of coal combustion model to pulverised fuel furnaces," *Journal of the Energy Institute*, vol. 79, no. 2, pp. 101–109, 2006.

[75] B. Böhm, J. Brübach, C. Ertem, and A. Dreizler, "Experiments for combustion-LES validation," *Flow, Turbulence and Combustion*, vol. 80, no. 4, pp. 507–529, 2008.

[76] K. Luo, H. Wang, J. Fan, and F. Yi, "Direct numerical simulation of pulverized coal combustion in a hot vitiated co-flow," *Energy & Fuels*, vol. 26, no. 10, pp. 6128–6136, 2012.

[77] B. E. Launder and D. B. Spalding, "The numerical computation of turbulent flows," *Computer Methods in Applied Mechanics and Engineering*, vol. 3, no. 2, pp. 269–289, 1974.

[78] D. C. Wilcox *et al.*, "Turbulence modeling for CFD," vol. 2, 1998.

[79] S. A. Orszag and V. Yakhot, "Renormalization group analysis of turbulence," in *Proceedins of the International Congress of Mathematicians*, pp. 1395–9, 1986.

[80] T.-H. Shih, W. W. Liou, A. Shabbir, Z. Yang, and J. Zhu, "A new k-ϵ eddy viscosity model for high reynolds number turbulent flows," *Computers & Fluids*, vol. 24, no. 3, pp. 227–238, 1995.

[81] F. R. Menter, "Improved two-equation k-omega turbulence models for aerodynamic flows," 1992.

[82] A. G. Clements, *Modelling mercury oxidation and radiative heat transfer in oxy-coal environments*. PhD thesis, University of Leeds, 2016.

[83] M. Gibson and B. Launder, "Ground effects on pressure fluctuations in the atmospheric boundary layer," *Journal of Fluid Mechanics*, vol. 86, no. 03, pp. 491–511, 1978.

[84] B. Launder, G. J. Reece, and W. Rodi, "Progress in the development of a Reynolds-stress turbulence closure," *Journal of Fluid Mechanics*, vol. 68, no. 03, pp. 537–566, 1975.

[85] R. M. Davidson and S. O. Santos, *Oxyfuel combustion of pulverised coal*. IEA Clean Coal Centre London, UK, 2010.

[86] A. Williams, R. Backreedy, R. Habib, J. Jones, and M. Pourkashanian, "Modelling coal combustion: the current position," *Fuel*, vol. 81, no. 5, pp. 605–618, 2002.

[87] A. Williams, M. Pourkashanian, and J. Jones, "Combustion of pulverised coal and biomass," *Progress in Energy and Combustion Science*, vol. 27, no. 6, pp. 587–610, 2001.

[88] A. M. Carpenter, S. Niksa, SRI International, D. H. Scott, and Z. Wu, "Fundamentals of coal combustion, http://www.coalonline.org," *IEA Clean Coal Centre*, 2007.

[89] P. Solomon and M. Colket, "Coal devolatilization," in *Symposium (International) on combustion*, vol. 17, pp. 131–143, Elsevier, 1979.

[90] I. Smith, "The combustion rates of coal chars: a review," in *Symposium (International) on Combustion*, vol. 19, pp. 1045–1065, Elsevier, 1982.

[91] W. Hutny, G. Lee, and J. Price, "Fundamentals of coal combustion during injection into a blast furnace," *Progress in Energy and Combustion Science*, vol. 17, no. 4, pp. 373–395, 1991.

[92] H. Lu, W. Robert, G. Peirce, B. Ripa, and L. L. Baxter, "Comprehensive study of biomass particle combustion," *Energy & Fuels*, vol. 22, no. 4, pp. 2826–2839, 2008.

[93] Y. B. Yang, V. N. Sharifi, J. Swithenbank, L. Ma, L. I. Darvell, J. M. Jones, M. Pourkashanian, and A. Williams, "Combustion of a single particle of biomass," *Energy & Fuels*, vol. 22, no. 1, pp. 306–316, 2007.

[94] M. Baum and P. Street, "Predicting the combustion behaviour of coal particles," *Combustion Science and Technology*, vol. 3, no. 5, pp. 231–243, 1971.

[95] S. Gubba, L. Ma, M. Pourkashanian, and A. Williams, "Influence of particle shape and internal thermal gradients of biomass particles on pulverised coal/biomass co-fired flames," *Fuel Processing Technology*, vol. 92, no. 11, pp. 2185–2195, 2011.

[96] X. Yu, Weiping Yan, "Unsteady heating of coal particles before ignition," *Heat Transfer Engineering*, vol. 20, no. 4, pp. 45–51, 1999.

[97] ANSYS Inc, "ANSYS Fluent Theory Guide," 2013.

[98] W. E. Ranz, "Evaporation from drops: Part II," *Chem. Engng. Prog.*, vol. 48, pp. 173–180, 1952.

[99] L. Álvarez, C. Yin, J. Riaza, C. Pevida, J. Pis, and F. Rubiera, "Oxy-coal combustion in an entrained flow reactor: Application of specific char and volatile combustion and radiation models for oxy-firing conditions," *Energy*, vol. 62, pp. 255–268, 2013.

[100] J. Yu, J. A. Lucas, and T. F. Wall, "Formation of the structure of chars during devolatilization of pulverized coal and its thermoproperties: A review," *Progress in Energy and Combustion Science*, vol. 33, no. 2, pp. 135–170, 2007.

[101] P. Solomon, T. Fletcher, and R. Pugmire, "Progress in coal pyrolysis," *Fuel*, vol. 72, no. 5, pp. 587–597, 1993.

[102] S. Badzioch and P. G. Hawksley, "Kinetics of thermal decomposition of pulverized coal particles," *Industrial & Engineering Chemistry Process Design and Development*, vol. 9, no. 4, pp. 521–530, 1970.

[103] H. Kobayashi, J. Howard, and A. F. Sarofim, "Coal devolatilization at high temperatures," in *Symposium (International) on Combustion*, vol. 16, pp. 411–425, Elsevier, 1977.

[104] D. B. Anthony and J. B. Howard, "Coal devolatilization and hydrogastification," *AIChE Journal*, vol. 22, no. 4, pp. 625–656, 1976.

[105] P. R. Solomon, D. G. Hamblen, R. Carangelo, M. Serio, and G. Deshpande, "General model of coal devolatilization," *Energy & Fuels*, vol. 2, no. 4, pp. 405–422, 1988.

[106] S. Niksa and A. R. Kerstein, "FLASHCHAIN theory for rapid coal devolatilization kinetics. 1. Formulation," *Energy & Fuels*, vol. 5, no. 5, pp. 647–665, 1991.

[107] D. M. Grant, R. J. Pugmire, T. H. Fletcher, and A. R. Kerstein, "Chemical model of coal devolatilization using percolation lattice statistics," *Energy & Fuels*, vol. 3, no. 2, pp. 175–186, 1989.

[108] T. H. Fletcher, A. R. Kerstein, R. J. Pugmire, and D. M. Grant, "Chemical percolation model for devolatilization. 2. temperature and heating rate effects on product yields," *Energy & Fuels*, vol. 4, no. 1, pp. 54–60, 1990.

[109] T. H. Fletcher, A. R. Kerstein, R. J. Pugmire, M. S. Solum, and D. M. Grant, "Chemical percolation model for devolatilization. 3. Direct use of carbon-13 NMR data to predict effects of coal type," *Energy & Fuels*, vol. 6, no. 4, pp. 414–431, 1992.

[110] A. Williams, M. Pourkashanian, and J. Jones, "The combustion of coal and some other solid fuels," *Proceedings of the Combustion Institute*, vol. 28, no. 2, pp. 2141–2162, 2000.

[111] C. K. Westbrook and F. L. Dryer, "Simplified reaction mechanisms for the oxidation of hydrocarbon fuels in flames," *Combustion Science and Technology*, vol. 27, no. 1-2, pp. 31–43, 1981.

[112] F. L. Dryer, "High temperature oxidation of carbon monoxide and methane in a turbulent flow reactor," tech. rep., Princeton Univ NJ Dept of Aerospace and Mechanical Sciences, 1972.

[113] D. Hautman, F. Dryer, K. Schug, and I. Glassman, "A multiple-step overall kinetic mechanism for the oxidation of hydrocarbons," 1981.

[114] W. Jones and R. Lindstedt, "Global reaction schemes for hydrocarbon combustion," *Combustion and Flame*, vol. 73, no. 3, pp. 233–249, 1988.

[115] A. Brink, P. Kilpinen, M. Hupa, and L. Kjäldman, "Study of alternative descriptions of methane oxidation for CFD modeling of turbulent combustors," *Combustion Science and Technology*, vol. 141, no. 1-6, pp. 59–81, 1999.

[116] A. G. Clements, S. Black, J. Szuhánszki, K. Stęchły, A. Pranzitelli, W. Nimmo, and M. Pourkashanian, "LES and RANS of air and oxy-coal combustion in a pilot-scale facility: predictions of radiative heat transfer," *Fuel*, vol. 151, pp. 146–155, 2015.

[117] D. Toporov, P. Bocian, P. Heil, A. Kellermann, H. Stadler, S. Tschunko, M. Förster, and R. Kneer, "Detailed investigation of a pulverized fuel swirl

flame in CO_2/O_2 atmosphere," *Combustion and Flame*, vol. 155, no. 4, pp. 605–618, 2008.

[118] T. Kangwanpongpan, R. C. da Silva, and H. J. Krautz, "Prediction of oxy-coal combustion through an optimized weighted sum of gray gases model," *Energy*, vol. 41, no. 1, pp. 244–251, 2012.

[119] J. Andersen, C. L. Rasmussen, T. Giselsson, and P. Glarborg, "Global combustion mechanisms for use in CFD modeling under oxy-fuel conditions," *Energy & Fuels*, vol. 23, no. 3, pp. 1379–1389, 2009.

[120] P. Glarborg and L. L. Bentzen, "Chemical effects of a high CO_2 concentration in oxy-fuel combustion of methane," *Energy & Fuels*, vol. 22, no. 1, pp. 291–296, 2007.

[121] C. Yin, L. A. Rosendahl, and S. K. Kær, "Chemistry and radiation in oxy-fuel combustion: a computational fluid dynamics modeling study," *Fuel*, vol. 90, no. 7, pp. 2519–2529, 2011.

[122] L. Chen and A. F. Ghoniem, "Modeling CO_2 chemical effects on CO formation in oxy-fuel diffusion flames using detailed, quasi-global, and global reaction mechanisms," *Combustion Science and Technology*, vol. 186, no. 7, pp. 829–848, 2014.

[123] P. A. Campbell, R. E. Mitchell, and L. Ma, "Characterization of coal char and biomass char reactivities to oxygen," *Proceedings of the Combustion Institute*, vol. 29, no. 1, pp. 519–526, 2002.

[124] M. Sami, K. Annamalai, and M. Wooldridge, "Co-firing of coal and biomass fuel blends," *Progress in Energy and Combustion Science*, vol. 27, no. 2, pp. 171–214, 2001.

[125] M. Field, D. Gill, B. Morgan, and P. Hawksley, "Combustion of Pulverized Coal British Coal Utilization Research Association," *Leatherland, UK*, 1967.

[126] R. Hurt, J.-K. Sun, and M. Lunden, "A kinetic model of carbon burnout in pulverized coal combustion," *Combustion and Flame*, vol. 113, no. 1, pp. 181–197, 1998.

[127] D. Spalding, "Mixing and chemical reaction in steady confined turbulent flames," in *Symposium (International) on Combustion*, vol. 13, pp. 649–657, Elsevier, 1971.

[128] B. F. Magnussen and B. Hjertager, "On the structure of turbulence and a generalized eddy dissipation concept for chemical reaction in turbulent flow," in *19th AIAA aerospace meeting, St.Louis, USA*, vol. 198, 1981.

[129] I. Gran, M. Melaaen, and B. Magnussen, "Numerical simulation of local extinction effects in turbulent combustor flows of methane and air," in *Symposium (International) on Combustion*, vol. 25, pp. 1283–1291, Elsevier, 1994.

[130] H.-C. Magel, U. Schnell, and K. R. Hein, "Simulation of detailed chemistry in a turbulent combustor flow," in *Symposium (International) on Combustion*, vol. 26, pp. 67–74, Elsevier, 1996.

[131] M. F. Modest and G. Pal, "Advanced differential approximation formulation of the pn method for radiative transfer," in *ASME 2009 Heat Transfer Summer Conference collocated with the InterPACK09 and 3rd Energy Sustainability Conferences*, pp. 233–240, American Society of Mechanical Engineers, 2009.

[132] H. Knaus, R. Schneider, X. Han, J. Ströhle, U. Schnell, and K. Hein, *Comparison of different radiative heat transfer models and their applicability in coal-fired utility boiler simulations*. Universität Stuttgart, Fakultät Energietechnik, 1997.

[133] M. F. Modest, *Radiative heat transfer*. Academic press, 2013.

[134] R. Viskanta and M. Menguc, "Radiative transfer in dispersed media," *Applied Mechanics Reviews*, vol. 42, no. 9, pp. 241–259, 1989.

[135] M. Carvalho and T. Farias, "Modelling of heat transfer in radiating and combusting systems," *Chemical Engineering Research and Design*, vol. 76, no. 2, pp. 175–184, 1998.

[136] J. Yang and M. Modest, "High-order PN approximation for radiative transfer in arbitrary geometries," *J. Quant. Spectrosc. Radiat. Transfer*, vol. 104, no. 2, pp. 217–227, 2007.

[137] S.-C. S. Ou and K.-N. Liou, "Generalization of the spherical harmonic method to radiative transfer in multi-dimensional space," *Journal of Quantitative Spectroscopy and Radiative Transfer*, vol. 28, no. 4, pp. 271–288, 1982.

[138] M. F. Modest and J. Yang, "Elliptic PDE formulation and boundary conditions of the spherical harmonics method of arbitrary order for general three-dimensional geometries," *Journal of Quantitative Spectroscopy and Radiative Transfer*, vol. 109, no. 9, pp. 1641–1666, 2008.

[139] G. Pal and M. F. Modest, "Advanced differential approximation formulation of the PN method for radiative transfer," *Journal of Heat Transfer*, vol. 137, no. 7, p. 072701, 2015.

[140] F. Liu, J. Swithenbank, and E. S. Garbett, "The boundary condition of the PN-approximation used to solve the radiative transfer equation," *International Journal of Heat and Mass Transfer*, vol. 35, no. 8, pp. 2043–2052, 1992.

[141] B. Su, "More on boundary conditions for differential approximations," *Journal of Quantitative Spectroscopy and Radiative Transfer*, vol. 64, no. 4, pp. 409–419, 2000.

[142] D. Olfe, "A modification of the differential approximation for radiative transfer," *AIAA J*, vol. 5, no. 4, pp. 638–643, 1967.

[143] M. Modest, "Two-dimensional radiative equilibrium of a gray medium in a plane layer bounded by gray nonisothermal walls," *(American Society of Mechanical Engineers, 1975.) ASME, Transactions, Series C- Journal of Heat Transfer,*, vol. 96, pp. 483–488, 1974.

[144] S. Sazhin, E. Sazhina, O. Faltsi-Saravelou, and P. Wild, "The P-1 model for thermal radiation transfer: advantages and limitations," *Fuel*, vol. 75, no. 3, pp. 289–294, 1996.

[145] R. Prieler, M. Demuth, D. Spoljaric, and C. Hochenauer, "Evaluation of a steady flamelet approach for use in oxy-fuel combustion," *Fuel*, vol. 118, pp. 55–68, 2014.

[146] R. Porter, F. Liu, M. Pourkashanian, A. Williams, and D. Smith, "Evaluation of solution methods for radiative heat transfer in gaseous oxy-fuel combustion environments," *Journal of Quantitative Spectroscopy and Radiative Transfer*, vol. 111, no. 14, pp. 2084–2094, 2010.

[147] R. Holkar and O. D. Hebbal, "CFD anlysis of pulverised-coal combustion of burner used in furnace with different radiation models," *IOSR Journal of Mechanical and Civil Engineering*, vol. 5, pp. 25–34, 2013.

[148] F. Lockwood and N. Shah, "A new radiation solution method for incorporation in general combustion prediction procedures," in *Symposium (International) on Combustion*, vol. 18, pp. 1405–1414, Elsevier, 1981.

[149] F. Liu, Ö. Gülder, G. Smallwood, and Y. Ju, "Non-grey gas radiative transfer analyses using the statistical narrow-band model," *International Journal of Heat and Mass Transfer*, vol. 41, no. 14, pp. 2227–2236, 1998.

[150] F. Liu, G. Smallwood, D. Snelling, and Ö. Gülder, "A ray-tracing method for solving the radiative transfer equation in three-dimensional participating media," *ASME Journal of Heat Transfer*, 1997.

[151] J. C. Henson and W. Malalasekera, "Comparison of the discrete transfer and Monte Carlo methods for radiative heat transfer in three-dimensional nonhomogeneous scattering media," *Numerical Heat Transfer, Part A Applications*, vol. 32, no. 1, pp. 19–36, 1997.

[152] D. Sarma, S. C. Mishra, and P. Mahanta, "Analysis of collimated radiation in participating media using the discrete transfer method," *Journal of Quantitative Spectroscopy and Radiative Transfer*, vol. 96, no. 1, pp. 123–135, 2005.

[153] N. A. Krishna and S. C. Mishra, "Discrete transfer method applied to radiative transfer in a variable refractive index semitransparent medium," *Journal of Quantitative Spectroscopy and Radiative Transfer*, vol. 102, no. 3, pp. 432–440, 2006.

[154] S. C. Mishra, P. Chugh, P. Kumar, and K. Mitra, "Development and comparison of the DTM, the DOM and the FVM formulations for the short-pulse laser transport through a participating medium," *International Journal of Heat and Mass Transfer*, vol. 49, no. 11, pp. 1820–1832, 2006.

[155] S. C. Mishra, P. Talukdar, D. Trimis, and F. Durst, "Effect of angular quadrature schemes on the computational efficiency of the discrete transfer method for solving radiative transport problems with participating medium," *Numerical Heat Transfer, Part B: Fundamentals*, vol. 46, no. 5, pp. 463–478, 2004.

[156] S. A. N. Heugang, H. T. T. Kamdem, and F. B. Pelap, "A discrete transfer method for radiative transfer through anisotropically scattering media," *American Journal of Heat and Mass Transfer*, vol. 3, no. 6, pp. 396–411, 2016.

[157] K. D. Lathrop and B. G. Carlson, "Discrete ordinates angular quadrature of the neutron transport equation," tech. rep., Los Alamos Scientific Lab., N. Mex., 1964.

[158] J. Truelove, "Discrete-ordinate solutions of the radiation transport equation," *Journal of Heat Transfer (Transcations of the ASME (American Society of Mechanical Engineers), Series C);(United States)*, vol. 109, no. 4, 1987.

[159] W. Fiveland, "Discrete ordinate methods for radiative heat transfer in isotropically and anisotropically scattering media," *Journal of Heat Transfer (Transactions of the ASME (American Society of Mechanical Engineers), Series C);(United States)*, vol. 109, no. 3, 1987.

[160] C. Thurgood, A. Pollard, and H. Becker, "The TN quadrature set for the discrete ordinates method," *Transactions-American Society of Mechanical Engineers Journal of Heat Transfer*, vol. 117, pp. 1068–1069, 1995.

[161] R. Koch, W. Krebs, S. Wittig, and R. Viskanta, "Discrete ordinates quadrature schemes for multidimensional radiative transfer," *Journal of Quantitative Spectroscopy and Radiative Transfer*, vol. 53, no. 4, pp. 353–372, 1995.

[162] J. C. Chai, H. S. Lee, and S. V. Patankar, "Ray effect and false scattering in the discrete ordinates method," *Numerical Heat Transfer, Part B Fundamentals*, vol. 24, no. 4, pp. 373–389, 1993.

[163] F. Liu, H. Becker, and A. Pollard, "Spatial differencing schemes of the discrete-ordinates method," *Numerical Heat Transfer*, vol. 30, no. 1, pp. 23–43, 1996.

[164] R. Koch and R. Becker, "Evaluation of quadrature schemes for the discrete ordinates method," *Journal of Quantitative Spectroscopy and Radiative Transfer*, vol. 84, no. 4, pp. 423–435, 2004.

[165] P. J. Coelho, "The role of ray effects and false scattering on the accuracy of the standard and modified discrete ordinates methods," *Journal of Quantitative Spectroscopy and Radiative Transfer*, vol. 73, no. 2, pp. 231–238, 2002.

[166] R. Porter, M. Pourkashanian, A. Williams, and D. Smith, "Modelling radiative heat transfer in oxy-coal combustion," in *2009 ASME Summer Heat Transfer Conference, San Francisco, California, USA*, 2009.

[167] M. F. Modest and V. Singh, "Engineering correlations for full spectrum k-distributions of H_2O from the HITEMP spectroscopic databank," *Journal of Quantitative Spectroscopy and Radiative Transfer*, vol. 93, no. 1-3, pp. 263–271, 2005.

[168] J. Hartmann, R. L. Di Leon, and J. Taine, "Line-by-line and narrow-band statistical model calculations for H_2O," *Journal of Quantitative Spectroscopy and Radiative Transfer*, vol. 32, no. 2, pp. 119–127, 1984.

[169] L. Rothman, I. Gordon, R. Barber, H. Dothe, R. Gamache, A. Goldman, V. Perevalov, S. Tashkun, and J. Tennyson, "HITEMP, the high-temperature molecular spectroscopic database," *Journal of Quantitative Spectroscopy and Radiative Transfer*, vol. 111, no. 15, pp. 2139–2150, 2010.

[170] J. T. Pearson, B. W. Webb, V. P. Solovjov, and J. Ma, "Effect of total pressure on the absorption line blackbody distribution function and radiative transfer in H_2O, CO_2, and CO," *Journal of Quantitative Spectroscopy and Radiative Transfer*, vol. 143, pp. 100–110, 2014.

[171] L. S. Rothman, C. Rinsland, A. Goldman, S. Massie, D. Edwards, J. Flaud, A. Perrin, C. Camy-Peyret, V. Dana, J.-Y. Mandin, *et al.*, "The HITRAN molecular spectroscopic database and HAWKS (HITRAN Atmospheric Workstation): 1996 edition," *Journal of Quantitative Spectroscopy and Radiative Transfer*, vol. 60, no. 5, pp. 665–710, 1998.

[172] F. R. Centeno, R. Brittes, F. H. França, and O. A. Ezekoye, "Evaluation of gas radiation heat transfer in a 2D axisymmetric geometry using the line-by-line integration and WSGG models," *Journal of Quantitative Spectroscopy and Radiative Transfer*, vol. 156, pp. 1–11, 2015.

[173] J. Taine, "A line-by-line calculation of low-resolution radiative properties of CO_2-CO-transparent nonisothermal gases mixtures up to 3000 K," *Journal of Quantitative Spectroscopy and Radiative Transfer*, vol. 30, no. 4, pp. 371–379, 1983.

[174] L. Sparks, "Efficient line-by-line calculation of absorption coefficients to high numerical accuracy," *Journal of Quantitative Spectroscopy and Radiative Transfer*, vol. 57, no. 5, pp. 631–650, 1997.

[175] M. Kuntz and M. Höpfner, "Efficient line-by-line calculation of absorption coefficients," *Journal of Quantitative Spectroscopy and Radiative Transfer*, vol. 63, no. 1, pp. 97–114, 1999.

[176] S. Tashkun and V. Perevalov, "CDSD-4000: High-resolution, high-temperature carbon dioxide spectroscopic databank," *Journal of Quantitative Spectroscopy and Radiative Transfer*, vol. 112, no. 9, pp. 1403–1410, 2011.

[177] S. P. Bharadwaj, M. F. Modest, and R. J. Riazzi, "Medium resolution transmission measurements of water vapor at high temperature," *Journal of Heat Transfer*, vol. 128, no. 4, pp. 374–381, 2006.

[178] S. P. Bharadwaj and M. F. Modest, "Medium resolution transmission measurements of CO_2 at high temperature - an update," *Journal of Quantitative Spectroscopy and Radiative Transfer*, vol. 103, no. 1, pp. 146–155, 2007.

[179] V. Becher, S. Clausen, A. Fateev, and H. Spliethoff, "Validation of spectral gas radiation models under oxyfuel conditions. part A: Gas cell experiments," *International Journal of Greenhouse Gas Control*, vol. 5, pp. S76–S99, 2011.

[180] V. Evseev, A. Fateev, and S. Clausen, "High-resolution transmission measurements of CO_2 at high temperatures for industrial applications," *Journal of Quantitative Spectroscopy and Radiative Transfer*, vol. 113, no. 17, pp. 2222–2233, 2012.

[181] M. Alberti, R. Weber, M. Mancini, A. Fateev, and S. Clausen, "Validation of HITEMP-2010 for carbon dioxide and water vapour at high temperatures and atmospheric pressures in 450–7600cm- 1 spectral range," *Journal of Quantitative Spectroscopy and Radiative Transfer*, vol. 157, pp. 14–33, 2015.

[182] I. Gordon, L. Rothman, C. Hill, R. Kochanov, Y. Tan, P. Bernath, M. Birk, V. Boudon, A. Campargue, K. Chance, *et al.*, "The HITRAN2016 molecular spectroscopic database," *Journal of Quantitative Spectroscopy and Radiative Transfer*, 2017.

[183] M. F. Modest and S. P. Bharadwaj, "Medium resolution transmission measurements of CO_2 at high temperature," *Journal of Quantitative Spectroscopy and Radiative Transfer*, vol. 73, no. 2, pp. 329–338, 2002.

[184] A. Wang and M. F. Modest, "Importance of combined Lorentz-Doppler broadening in high-temperature radiative heat transfer applications," *Transactions-American Society of Mechanical Engineers Journal of Heat Transfer*, vol. 126, pp. 858–861, 2004.

[185] P. Rivière and A. Soufiani, "Updated band model parameters for H_2O, CO_2, CH_4 and CO radiation at high temperature," *International Journal of Heat and Mass Transfer*, vol. 55, no. 13, pp. 3349–3358, 2012.

[186] H. Chu, F. Liu, and H. Zhou, "Calculations of gas thermal radiation transfer in one-dimensional planar enclosure using LBL and SNB models," *International Journal of Heat and Mass Transfer*, vol. 54, no. 21, pp. 4736–4745, 2011.

[187] M. Alberti, R. Weber, M. Mancini, and M. Modest, "Comparison of models for predicting band emissivity of carbon dioxide and water vapour at high temperatures," *International Journal of Heat and Mass Transfer*, vol. 64, pp. 910–925, 2013.

[188] H. Chu, M. Gu, J.-L. Consalvi, F. Liu, and H. Zhou, "Effects of total pressure on non-grey gas radiation transfer in oxy-fuel combustion using the LBL, SNB, SNBCK, WSGG, and FSCK methods," *Journal of Quantitative Spectroscopy and Radiative Transfer*, vol. 172, pp. 24–35, 2016.

[189] A. Soufiani, J. Hartmann, and J. Taine, "Validity of band-model calculations for CO_2 and H_2O applied to radiative properties and conductive-radiative transfer," *Journal of Quantitative Spectroscopy and Radiative Transfer*, vol. 33, no. 3, pp. 243–257, 1985.

[190] R. Goody, "A statistical model for water-vapour absorption," *Quarterly Journal of the Royal Meteorological Society*, vol. 78, no. 336, pp. 165–169, 1952.

[191] W. Malkmus, "Random Lorentz band model with exponential-tailed S- 1 line-intensity distribution function," *JOSA*, vol. 57, no. 3, pp. 323–329, 1967.

[192] A. Soufiani and J. Taine, "Experimental and theoretical studies of combined radiative and convective transfer in CO_2 and H_2O laminar flows," *International Journal of Heat and Mass Transfer*, vol. 32, no. 3, pp. 477–486, 1989.

[193] A. Soufiani and J. Taine, "High temperature gas radiative property parameters of statistical narrow-band model for H_2O, CO_2 and CO, and correlated-K model for H_2O and CO_2," *International Journal of Heat and Mass Transfer*, vol. 40, no. 4, pp. 987–991, 1997.

[194] F. Liu, G. J. Smallwood, and Ö. L. Gülder, "Application of the statistical narrow-band correlated-k method to low-resolution spectral intensity and

radiative heat transfer calculations-effects of the quadrature scheme," *International Journal of Heat and Mass Transfer*, vol. 43, no. 17, pp. 3119–3135, 2000.

[195] J. Meulemans, "An assessment of some non-gray global radiation models in enclosures," in *Journal of Physics: Conference Series*, vol. 676, p. 012017, IOP Publishing, 2016.

[196] R. Goody, R. West, L. Chen, and D. Crisp, "The correlated-k method for radiation calculations in nonhomogeneous atmospheres," *Journal of Quantitative Spectroscopy and Radiative Transfer*, vol. 42, no. 6, pp. 539–550, 1989.

[197] A. A. Lacis and V. Oinas, "A description of the correlated k distribution method for modeling nongray gaseous absorption, thermal emission, and multiple scattering in vertically inhomogeneous atmospheres," *Journal of Geophysical Research: Atmospheres*, vol. 96, no. D5, pp. 9027–9063, 1991.

[198] M. F. Modest, "Narrow-band and full-spectrum k-distributions for radiative heat transfer-correlated-k vs. scaling approximation," *Journal of Quantitative Spectroscopy and Radiative Transfer*, vol. 76, no. 1, pp. 69–83, 2003.

[199] M. F. Modest and R. J. Riazzi, "Assembly of full-spectrum k-distributions from a narrow-band database; effects of mixing gases, gases and nongray absorbing particles, and mixtures with nongray scatterers in nongray enclosures," *Journal of Quantitative Spectroscopy and Radiative Transfer*, vol. 90, no. 2, pp. 169–189, 2005.

[200] M. F. Modest, "The treatment of nongray properties in radiative heat transfer: from past to present," *Journal of Heat Transfer*, vol. 135, no. 6, p. 061801, 2013.

[201] S.-S. Yang and T.-H. Song, "An improved WSGGM-based narrow band model for the CO_2 4.3 μm band," *International Journal of Thermal Sciences*, vol. 38, no. 3, pp. 228–238, 1999.

[202] F. Liu, G. J. Smallwood, and Ö. L. Gülder, "Application of the statistical narrow-band correlated-k method to non-grey gas radiation in CO_2–H_2O mixtures: approximate treatments of overlapping bands," *Journal of Quantitative Spectroscopy and Radiative Transfer*, vol. 68, no. 4, pp. 401–417, 2001.

[203] S. Dembele, J. Zhang, and J. X. Wen, "Evaluation of the correlated-k and other gas radiation models for combustion applications," *Fire Safety Science*, vol. 7, pp. 927–938, 2003.

[204] H. Amiri, K. Lari, and P. J. Coelho, "Comparison of CK model and line by line method using old and updated parameters/databases," *International Journal of Thermal Sciences*, vol. 118, pp. 448–460, 2017.

[205] P. Coelho, "Numerical simulation of radiative heat transfer from non-gray gases in three-dimensional enclosures," *Journal of Quantitative Spectroscopy and Radiative Transfer*, vol. 74, no. 3, pp. 307–328, 2002.

[206] C. Yin, "On gas and particle radiation in pulverized fuel combustion furnaces," *Applied Energy*, vol. 157, pp. 554–561, 2015.

[207] G. Krishnamoorthy, "A comparison of gray and non-gray modeling approaches to radiative transfer in pool fire simulations," *Journal of Hazardous Materials*, vol. 182, no. 1, pp. 570–580, 2010.

[208] M. F. Modest, *Radiative heat transfer*. Academic press, 2003.

[209] H. C. Hottel and A. F. Sarofim, "Radiative Transfer," *McGraw-Hill, New York, 1967*.

[210] M. F. Modest, "The weighted-sum-of-gray-gases model for arbitrary solution methods in radiative transfer," *Journal of Heat Transfer*, vol. 113, no. 3, pp. 650–656, 1991.

[211] C. Yin, "Refined weighted sum of gray gases model for air-fuel combustion and its impacts," *Energy & Fuels*, vol. 27, no. 10, pp. 6287–6294, 2013.

[212] F. Cassol, R. Brittes, F. H. França, and O. A. Ezekoye, "Application of the weighted-sum-of-gray-gases model for media composed of arbitrary concentrations of H_2O, CO_2 and soot," *International Journal of Heat and Mass Transfer*, vol. 79, pp. 796–806, 2014.

[213] V. Kez, J. Consalvi, F. Liu, J. Ströhle, and B. Epple, "Assessment of several gas radiation models for radiative heat transfer calculations in a three-dimensional oxy-fuel furnace under coal-fired conditions," *International Journal of Thermal Sciences*, vol. 120, pp. 289–302, 2017.

[214] M. K. Denison and B. W. Webb, "A spectral line-based weighted-sum-of-gray-gases model for arbitrary RTE solvers," *Transactions-American Society of Mechanical Engineers Journal of Heat Transfer*, vol. 115, pp. 1004–1004, 1993.

[215] M. Denison and B. Webb, "The spectral line-based weighted-sum-of-gray-gases model in nonisothermal nonhomogeneous media," *Journal of Heat Transfer*, vol. 117, no. 2, pp. 359–365, 1995.

[216] V. Solovjov and B. Webb, "Global spectral methods in gas radiation: the exact limit of the SLW model and its relationship to the ADF and FSK methods," *Journal of Heat Transfer*, vol. 133, no. 4, p. 042701, 2011.

[217] M. Denison and B. W. Webb, "An absorption-line blackbody distribution function for efficient calculation of total gas radiative transfer," *Journal of Quantitative Spectroscopy and Radiative Transferr*, vol. 50, no. 5, pp. 499–510, 1993.

[218] M. Denison and B. W. Webb, "Development and application of an absorptionline blackbody distribution function for CO_2," *International Journal of Heat and Mass Transfer*, vol. 38, no. 10, pp. 1813–1821, 1995.

[219] J. T. Pearson, B. W. Webb, V. P. Solovjov, and J. Ma, "Efficient representation of the absorption line blackbody distribution function for H_2O, CO_2,

and CO at variable temperature, mole fraction, and total pressure," *Journal of Quantitative Spectroscopy and Radiative Transfer*, vol. 138, pp. 82–96, 2014.

[220] V. P. Solovjov and B. W. Webb, "SLW modeling of radiative transfer in multicomponent gas mixtures," *Journal of Quantitative Spectroscopy and Radiative Transfer*, vol. 65, no. 4, pp. 655–672, 2000.

[221] V. Goutiere, F. Liu, and A. Charette, "An assessment of real-gas modelling in 2D enclosures," *Journal of Quantitative Spectroscopy and Radiative Transfer*, vol. 64, no. 3, pp. 299–326, 2000.

[222] V. P. Solovjov and B. W. Webb, "The cumulative wavenumber method for modeling radiative transfer in gas mixtures with soot," *Journal of Quantitative Spectroscopy and Radiative Transfer*, vol. 93, no. 1, pp. 273–287, 2005.

[223] V. P. Solovjov and B. W. Webb, "An efficient method for modeling radiative transfer in multicomponent gas mixtures with soot," *Transactions-American Society of Mechanical Engineers Journal of Heat Transfer*, vol. 123, no. 3, pp. 450–457, 2001.

[224] V. Goutière, A. Charette, and L. Kiss, "Comparative performance of nongray gas modeling techniques," *Numerical Heat Transfer: Part B: Fundamentals*, vol. 41, no. 3-4, pp. 361–381, 2002.

[225] N. Doner and N. Selçuk, "An application of spectral line-based weighted sum of grey gases (SLW) model with geometric optics approximation for radiative heat transfer in 3-D participating media," *Applied Thermal Engineering*, vol. 50, no. 1, pp. 89–93, 2013.

[226] G. Ozen and N. Selçuk, "SLW model for computational fluid dynamics modeling of combustion systems: Implementation and validation," *Numerical Heat Transfer, Part B: Fundamentals*, vol. 70, no. 1, pp. 47–55, 2016.

[227] H. Amiri and S. H. Mansouri, "Inverse boundary design problems in enclosures with non-gray media," *Heat Transfer Engineering*, vol. 38, no. 2, pp. 227–243, 2017.

[228] M. Mengüç, S. Manickavasagam, and D. D'sa, "Determination of radiative properties of pulverized coal particles from experiments," *Fuel*, vol. 73, no. 4, pp. 613–625, 1994.

[229] L. G. Henyey and J. L. Greenstein, "Diffuse radiation in the galaxy," *The Astrophysical Journal*, vol. 93, pp. 70–83, 1941.

[230] A. L. Crosbie and G. W. Davidson, "Dirac-delta function approximations to the scattering phase function," *Journal of Quantitative Spectroscopy and Radiative Transfer*, vol. 33, no. 4, pp. 391–409, 1985.

[231] D. Deirmendjian, "Electromagnetic scattering on spherical polydispersions," tech. rep., RAND CORP SANTA MONICA CA, 1969.

[232] L.-S. Fan and C. Zhu, *Principles of gas-solid flows*. Cambridge University Press, 2005.

[233] P. A. Vesilind, "The Rosin-Rammler particle size distribution," *Resource Recovery and Conservation*, vol. 5, no. 3, pp. 275–277, 1980.

[234] P. González-Tello, F. Camacho, J. Vicaria, and P. González, "A modified Nukiyama–Tanasawa distribution function and a Rosin–Rammler model for the particle-size-distribution analysis," *Powder Technology*, vol. 186, no. 3, pp. 278–281, 2008.

[235] D. Goodwin and M. Mitchner, "Flyash radiative properties and effects on radiative heat transfer in coal-fired systems," *International Journal of Heat and Mass Transfer*, vol. 32, no. 4, pp. 627–638, 1989.

[236] S. Manickavasagam and M. Mengüç, "Effective optical properties of pulverized coal particles determined from FT-IR spectrometer experiments," *Energy & Fuels*, vol. 7, no. 6, pp. 860–869, 1993.

[237] S. Self, "Optical properties of fly ash. volume 2, Final report," tech. rep., Stanford Univ., CA (United States). High Temperature Gasdynamics Lab., 1994.

[238] S. Ghosal, J. L. Ebert, and S. A. Self, "Chemical composition and size distributions for fly ashes," *Fuel Processing Technology*, vol. 44, no. 1-3, pp. 81–94, 1995.

[239] S. Ghosal and S. A. Self, "Particle size-density relation and cenosphere content of coal fly ash," *Fuel*, vol. 74, no. 4, pp. 522–529, 1995.

[240] F. E. Volz, "Infrared optical constants of ammonium sulfate, Sahara dust, volcanic pumice, and flyash," *Applied Optics*, vol. 12, no. 3, pp. 564–568, 1973.

[241] C. Willis, "The complex refractive index of particles in a flame," *Journal of Physics D: Applied Physics*, vol. 3, no. 12, p. 1944, 1970.

[242] A. Lowe, I. M. Stewart, and T. Wall, "The measurement and interpretation of radiation from fly ash particles in large pulverized coal flames," in *Symposium (International) on Combustion*, vol. 17, pp. 105–114, Elsevier, 1979.

[243] P. J. Wyatt, "Some chemical, physical, and optical properties of fly ash particles," *Applied Optics*, vol. 19, no. 6, pp. 975–983, 1980.

[244] R. Gupta and T. Wall, "The optical properties of fly ash in coal fired furnaces," *Combustion and Flame*, vol. 61, no. 2, pp. 145–151, 1985.

[245] A. G. Blokh, *Heat transfer in steam boiler furnaces*. 1987.

[246] S. Bhattacharya, "A theoretical investigation of the influence of optical constants and particle size on the radiative properties and heat transfer involving ash clouds and deposits," *Chemical Engineering and Processing: Process Intensification*, vol. 39, no. 5, pp. 471–483, 2000.

[247] D. Goodwin and M. Mitchner, "Measurements of the near infrared optical properties of coal slags," *Chemical Engineering Communications*, vol. 44, no. 1-6, pp. 241–255, 1986.

[248] T. Wall, S. Bhattacharya, D. Zhang, R. Gupta, and X. He, "The properties and thermal effects of ash deposits in coal-fired furnaces," *Progress in Energy and Combustion Science*, vol. 19, no. 6, pp. 487–504, 1993.

[249] M. Mengüç and S. Subramaniam, "Radiative transfer through an in homogeneous fly-ash cloud: Effects of temperature and wavelength dependent optical properties," *Numerical Heat Transfer*, vol. 21, no. 3, pp. 261–273, 1992.

[250] F. Liu and J. Swithenbank, "The effects of particle size distribution and refractive index on fly-ash radiative properties using a simplified approach," *International Journal of Heat and Mass Transfer*, vol. 36, no. 7, pp. 1905–1912, 1993.

[251] R. Johansson, T. Gronarz, and R. Kneer, "Influence of index of refraction and particle size distribution on radiative heat transfer in a pulverized coal combustion furnace," *Journal of Heat Transfer*, vol. 139, no. 4, p. 042702, 2017.

[252] A. Lowe, T. F. Wall, and I. M. Stewart, "Combustion kinetics in the modeling of large, pulverized fuel furnaces: A numerical experiment in sensitivity," *AIChE Journal*, vol. 23, no. 4, pp. 440–448, 1977.

[253] R. Gupta, T. Wall, and J. Truelove, "Radiative scatter by fly ash in pulverized-coal-fired furnaces: application of the Monte Carlo method to anisotropic scatter," *International Journal of Heat and Mass Transfer*, vol. 26, no. 11, pp. 1649–1660, 1983.

[254] P. Foster and C. Howarth, "Optical constants of carbons and coals in the infrared," *Carbon*, vol. 6, no. 5, pp. 719IN23IN24725–724729, 1968.

[255] M. Brewster and T. Kunitomo, "The optical constants of coal, char, and limestone," *Journal of Heat Transfer*, vol. 106, no. 4, pp. 678–683, 1984.

[256] P. R. Solomon, R. M. Carangelo, P. E. Best, J. R. Markham, and D. G. Hamblen, "The spectral emittance of pulverized coal and char," in *Symposium (International) on Combustion*, vol. 21, pp. 437–446, Elsevier, 1988.

[257] M. Menguc and R. Viskanta, "On the radiative properties of polydispersions: a simplified approach," *Combustion Science and Technology*, vol. 44, no. 3-4, pp. 143–159, 1985.

[258] H. Hulst, "Light scattering by small particles," *John Wiley and Sons, Inc., New York*, vol. 1, p. 957, 1981.

[259] C. Kim and N. Lior, "Easily computable good approximations for spectral radiative properties of particle-gas components and mixture in pulverized coal combustors," *Fuel*, vol. 74, no. 12, pp. 1891–1902, 1995.

[260] A. H. Al-Abbas, J. Naser, and D. Dodds, "CFD modelling of air-fired and oxy-fuel combustion of lignite in a 100KW furnace," *Fuel*, vol. 90, no. 5, pp. 1778–1795, 2011.

[261] J. Zhang, W. Prationo, L. Zhang, and Z. Zhang, "Computational fluid dynamics modeling on the air-firing and oxy-fuel combustion of dried victorian brown coal," *Energy & Fuels*, vol. 27, no. 8, pp. 4258–4269, 2013.

[262] R. Backreedy, L. Fletcher, L. Ma, M. Pourkashanian, and A. Williams, "Modelling pulverised coal combustion using a detailed coal combustion model," *Combustion science and technology*, vol. 178, no. 4, pp. 763–787, 2006.

[263] L. Ma, M. Gharebaghi, R. Porter, M. Pourkashanian, J. Jones, and A. Williams, "Modelling methods for co-fired pulverised fuel furnaces," *Fuel*, vol. 88, no. 12, pp. 2448–2454, 2009.

[264] M. N. Borjini, K. Guedri, and R. Saïd, "Modeling of radiative heat transfer in 3D complex boiler with non-gray sooting media," *Journal of Quantitative Spectroscopy and Radiative Transfer*, vol. 105, no. 2, pp. 167–179, 2007.

[265] X. Yang, A. Clements, J. Szuhánszki, X. Huang, O. F. Moguel, J. Li, J. Gibbins, Z. Liu, C. Zheng, D. Ingham, *et al.*, "Prediction of the radiative heat transfer in small and large scale oxy-coal furnaces," *Applied Energy*, vol. 211, pp. 523–537, 2018.

[266] F. Lockwood, S. Rizvi, and N. Shah, "Comparative predictive experience of coal firing," *Proceedings of the Institution of Mechanical Engineers, Part C: Journal of Mechanical Engineering Science*, vol. 200, no. 2, pp. 79–87, 1986.

[267] E. Chui, P. M. HUGHES, and G. Raithby, "Implementation of the finite volume method for calculating radiative transfer in a pulverized fuel flame," *Combustion Science and Technology*, vol. 92, no. 4-6, pp. 225–242, 1993.

[268] D. Hwang, "Radiation Properties for olydispersions: Application to Coal," *Journal of Heat Transfer*, vol. 102, p. 99, 1980.

[269] R. Marquez, M. F. Modest, and J. Cai, "Spectral photon Monte Carlo with energy splitting across phases for gas–particle mixtures," *Journal of Heat Transfer*, vol. 137, no. 12, p. 121012, 2015.

[270] B. Wu, S. P. Roy, X. Zhao, and M. F. Modest, "Effect of multiphase radiation on coal combustion in a pulverized coal jet flame," *Journal of Quantitative Spectroscopy and Radiative Transfer*, 2017.

[271] H. C. van de Hulst, *Light scattering by small particles*. Courier Corporation, 1957.

[272] R. Johansson, "Efficient treatment of non-grey radiative properties of particles and gases in modelling of radiative heat transfer in combustion en-

vironments," *International Journal of Heat and Mass Transfer*, vol. 108, pp. 519–528, 2017.

[273] L. Cox and R. Blaszczak, *Nitrogen oxides (NO_x) why and how they are controlled*. DIANE Publishing, 1999.

[274] R. Boardman, C. Eatough, G. Germane, and L. Smoot, "Comparison of measurements and predictions of flame structure and thermal NO_x, in a swirling, natural gas diffusion flame," *Combustion Science and Technology*, vol. 93, no. 1, pp. 193–210, 1993.

[275] A. Eaton, L. Smoot, S. Hill, and C. Eatough, "Components, formulations, solutions, evaluation, and application of comprehensive combustion models," *Progress in Energy and Combustion Science*, vol. 25, no. 4, pp. 387–436, 1999.

[276] C. T. Bowman, "Control of combustion-generated nitrogen oxide emissions: technology driven by regulation," in *Symposium (International) on Combustion*, vol. 24, pp. 859–878, Elsevier, 1992.

[277] A. Williams, M. Pourkashanian, P. Bysh, and J. Norman, "Modelling of coal combustion in low-NO_x pf flames," *Fuel*, vol. 73, no. 7, pp. 1006–1019, 1994.

[278] P. Coelho and M. Carvalho, "Mathematical modelling of NO formation in a power station boiler," *Combustion Science and Technology*, vol. 108, no. 4-6, pp. 363–382, 1995.

[279] J. A. Miller and C. T. Bowman, "Mechanism and modeling of nitrogen chemistry in combustion," *Progress in Energy and Combustion Science*, vol. 15, no. 4, pp. 287–338, 1989.

[280] R. K. Hanson and S. Salimian, "Survey of rate constants in the N/H/O system," *Combustion Chemistry*, pp. 361–421, 1984.

[281] C. T. Bowman, "Kinetics of pollutant formation and destruction in combustion," *Progress in Energy and Combustion Science*, vol. 1, no. 1, pp. 33–45, 1975.

[282] R. F. Sawyer, "The formation and destruction of pollutants in combustion processes: Clearing the air on the role of combustion research," in *Symposium (International) on Combustion*, vol. 18, pp. 1–22, Elsevier, 1981.

[283] C. Ma, T. Mahmud, E. Hampartsoumian, J. RICHAROSON, and P. Gaskell, "Mathematical modelling of nitric oxide formation in turbulent diffusion flames doped with a nitrogen compound," *Combustion Science and Technology*, vol. 160, no. 1, pp. 345–367, 2000.

[284] M. C. Drake, J. W. Ratcliffe, R. J. Blint, C. D. Carter, and N. M. Laurendeau, "Measurements and modeling of flamefront NO formation and superequilibrium radical concentrations in laminar high-pressure premixed flames," in *Symposium (International) on Combustion*, vol. 23, pp. 387–395, Elsevier, 1991.

[285] W. P. Adamczyk, S. Werle, and A. Ryfa, "Application of the computational method for predicting NO_x reduction within large scale coal-fired boiler," *Applied Thermal Engineering*, vol. 73, no. 1, pp. 343–350, 2014.

[286] A. H. Al-Abbas and J. Naser, "Effect of chemical reaction mechanisms and NO_x modeling on air-fired and oxy-fuel combustion of lignite in a 100-kW furnace," *Energy & Fuels*, vol. 26, no. 6, pp. 3329–3348, 2012.

[287] Q. Fang, H. Wang, H. Zhou, L. Lei, and X. Duan, "Improving the performance of a 300 MW down-fired pulverized-coal utility boiler by inclining downward the F-layer secondary air," *Energy & Fuels*, vol. 24, no. 9, pp. 4857–4865, 2010.

[288] N. Nikolopoulos, A. Nikolopoulos, E. Karampinis, P. Grammelis, and E. Kakaras, "Numerical investigation of the oxy-fuel combustion in large

scale boilers adopting the ECO-Scrub technology," *Fuel*, vol. 90, no. 1, pp. 198–214, 2011.

[289] R. Straka and M. Bene, "Numerical simulation of NO production in air-staged pulverized coal fired furnace," *Open Thermodynamics Journal*, vol. 4, no. 1, pp. 27–35, 2010.

[290] B. Alganash, M. C. Paul, and I. A. Watson, "Numerical investigation of the heterogeneous combustion processes of solid fuels," *Fuel*, vol. 141, pp. 236–249, 2015.

[291] A. H. Al-Abbas, J. Naser, and D. Dodds, "CFD modelling of air-fired and oxy-fuel combustion in a large-scale furnace at Loy Yang a brown coal power station," *Fuel*, vol. 102, pp. 646–665, 2012.

[292] L. Álvarez, M. Gharebaghi, J. Jones, M. Pourkashanian, A. Williams, J. Riaza, C. Pevida, J. Pis, and F. Rubiera, "Numerical investigation of NO emissions from an entrained flow reactor under oxy-coal conditions," *Fuel Processing Technology*, vol. 93, no. 1, pp. 53–64, 2012.

[293] C. Fenimore, "Formation of nitric oxide in premixed hydrocarbon flames," in *Symposium (International) on Combustion*, vol. 13, pp. 373–380, Elsevier, 1971.

[294] J. Blauwens, B. Smets, and J. Peeters, "Mechanism of "prompt" NO formation in hydrocarbon flames," in *Symposium (International) on Combustion*, vol. 16, pp. 1055–1064, Elsevier, 1977.

[295] W. Sanders, C. Lin, and M. Lin, "On the importance of the reaction CH_2+N_2 $\rightarrow$ HCN+ NH as a precursor for Prompt NO formation," *Combustion Science and Technology*, vol. 51, no. 1-3, pp. 103–108, 1987.

[296] B. Stanmore and S. Visona, "Prediction of NO emissions from a number of coal-fired power station boilers," *Fuel Processing Technology*, vol. 64, no. 1, pp. 25–46, 2000.

[297] S. Hill and L. D. Smoot, "Modeling of nitrogen oxides formation and destruction in combustion systems," *Progress in Energy and Combustion Science*, vol. 26, no. 4, pp. 417–458, 2000.

[298] A. Hayhurst and I. Vince, "Nitric oxide formation from N_2 in flames: the importance of "prompt" NO," *Progress in Energy and Combustion Science*, vol. 6, no. 1, pp. 35–51, 1980.

[299] N. Spitz, R. Saveliev, E. Korytnyi, M. Perelman, E. Bar-Ziv, and B. Chudnovsky, *Prediction of performance and pollutant emission from pulverized coal utility boilers.* Nova Science Publishers, Inc., Hauppauge, NY, 2007.

[300] J. H. Pohl and A. F. Sarofim, "Devolatilization and oxidation of coal nitrogen," in *Symposium (International) on Combustion*, vol. 16, pp. 491–501, Elsevier, 1977.

[301] P. Glarborg, A. Jensen, and J. E. Johnsson, "Fuel nitrogen conversion in solid fuel fired systems," *Progress in Energy and Combustion Science*, vol. 29, no. 2, pp. 89–113, 2003.

[302] L. I. Díez, C. Cortés, and J. Pallarés, "Numerical investigation of NO_x emissions from a tangentially-fired utility boiler under conventional and overfire air operation," *Fuel*, vol. 87, no. 7, pp. 1259–1269, 2008.

[303] I. Naruse, Y. Yamamoto, Y. Itoh, and K. Ohtake, "Fundamental study on N_2O formation/decomposition characteristics by means of low-temperature pulverized coal combustion," in *Symposium (International) on Combustion*, vol. 26, pp. 3213–3221, Elsevier, 1996.

[304] J. Leppälahti, "Formation of NH_3 and HCN in slow-heating-rate inert pyrolysis of peat, coal and bark," *Fuel*, vol. 74, no. 9, pp. 1363–1368, 1995.

[305] R. Bassilakis, Y. Zhao, P. Solomon, and M. Serio, "Sulfur and nitrogen evolution in the Argonne coals: Experiment and modeling," *Energy & Fuels*, vol. 7, no. 6, pp. 710–720, 1993.

[306] J. Levy, L. Chan, A. Sarofim, and J. Beer, "NO/char reactions at pulverized coal flame conditions," in *Symposium (International) on Combustion*, vol. 18, pp. 111–120, Elsevier, 1981.

[307] J. Glass and J. Wendt, "Mechanisms governing the destruction of nitrogeneous species during the fuel rich combustion of pulverized coal," in *Symposium (International) on Combustion*, vol. 19, pp. 1243–1251, Elsevier, 1982.

[308] T. Shimizu, Y. Sazawa, T. Adschiri, and T. Furusawa, "Conversion of char-bound nitrogen to nitric oxide during combustion," *Fuel*, vol. 71, no. 4, pp. 361–365, 1992.

[309] F. Guo and W. C. Hecker, "Kinetics of NO reduction by char: Effects of coal rank," in *Symposium (International) on Combustion*, vol. 27, pp. 3085–3092, Elsevier, 1998.

[310] L. Chan, A. Sarofim, and J. Beer, "Kinetics of the NO - carbon reaction at fluidized bed combustor conditions," *Combustion and Flame*, vol. 52, pp. 37–45, 1983.

[311] I. Aarna and E. M. Suuberg, "A review of the kinetics of the nitric oxide-carbon reaction," *Fuel*, vol. 76, no. 6, pp. 475–491, 1997.

[312] I. Aarna and E. M. Suuberg, "The role of carbon monoxide in the NO-carbon reaction," *Energy & Fuels*, vol. 13, no. 6, pp. 1145–1153, 1999.

[313] H.-l. Du, M. Zhang, Y. Zhang, and Y.-h. Luo, "Characteristics of NO reduction by char layer in fixed-bed coal combustion," *Energy Sources, Part A: Recovery, Utilization, and Environmental Effects*, pp. 1–8, 2017.

[314] E. H. Chui and H. Gao, "Estimation of NO_x emissions from coal-fired utility boilers," *Fuel*, vol. 89, no. 10, pp. 2977–2984, 2010.

[315] Y. Hu, N. Kobayashi, and M. Hasatani, "Effects of coal properties on recycled-NO_x reduction in coal combustion with O_2/recycled flue gas," *Energy Conversion and Management*, vol. 44, no. 14, pp. 2331–2340, 2003.

[316] P. Malte and D. Pratt, "Measurement of atomic oxygen and nitrogen oxides in jet-stirred combustion," in *Symposium (International) on Combustion*, vol. 15, pp. 1061–1070, Elsevier, 1975.

[317] L. Muzio, T. Montgomery, G. Samuelsen, J. C. Kramlich, R. Lyon, and A. Kokkinos, "Formation and measurement of N_2O in combustion systems," in *Symposium (International) on Combustion*, vol. 23, pp. 245–250, Elsevier, 1991.

[318] J. L. Wendt, "Mechanisms governing the formation and destruction of NO_x and other nitrogenous species in low NO_x coal combustion systems1," *Combustion Science and Technology*, vol. 108, no. 4-6, pp. 323–344, 1995.

[319] W. Chen, L. Smoot, S. Hill, and T. Fletcher, "Global rate expression for nitric oxide reburning. Part 2," *Energy & Fuels*, vol. 10, no. 5, pp. 1046–1052, 1996.

[320] D. Dimitriou, N. Kandamby, and F. Lockwood, "A mathematical modelling technique for gaseous and solid fuel reburning in pulverised coal combustors," *Fuel*, vol. 82, no. 15, pp. 2107–2114, 2003.

[321] N. Kandamby, G. Lazopoulos, F. Lockwood, A. Perera, and L. Vigevano, "Mathematical modeling of NO_x emission reduction by the use of reburn technology in utility boilers," in *ASME Int. Joint Power Generation Conference and Exhibition, Houston, Texas*, 1996.

[322] A. J. Dean, R. K. Hanson, and C. T. Bowman, "A shock tube study of reactions of carbon atoms and methylidyne with nitric oxide including product channel measurements," *The Journal of Physical Chemistry*, vol. 95, no. 8, pp. 3180–3189, 1991.

[323] B. Atakan, D. Kocis, J. Wolfrum, and P. Nelson, "Direct investigations of the kinetics of the reactions of CN radicals with n atoms and 3 CH_2 radicals with NO," in *Symposium (International) on Combustion*, vol. 24, pp. 691–699, Elsevier, 1992.

[324] K. M. Leung, *Kinetic modelling of hydrocarbon flames using detailed and systematically reduced chemistry.* PhD thesis, Imperial College London (University of London), 1995.

[325] M. Mengüç and R. Viskanta, "A sensitivity analysis for radiative heat transfer in a pulverized coal-fired furnace," *Combustion Science and Technology*, vol. 51, no. 1-3, pp. 51–74, 1987.

[326] T. Gronarz, J. Schulze, M. Laemmerhold, P. Graeser, J. Gorewoda, V. Kez, M. Habermehl, M. Schiemann, J. Ströhle, B. Epple, *et al.*, "Quantification of the influence of parameters determining radiative heat transfer in an oxy-fuel operated boiler," *Fuel Processing Technology*, vol. 157, pp. 76–89, 2017.

[327] R. Johansson, B. Leckner, K. Andersson, and F. Johnsson, "Influence of particle and gas radiation in oxy-fuel combustion," *International Journal of Heat and Mass Transfer*, vol. 65, pp. 143–152, 2013.

[328] C. Bohren and D. Huffman, "Absorbing and scattering of light by small particles," *Wiley Interscience*, vol. 13, no. 2, pp. 123–127, 1983.

[329] D. G. Goodwin, "Infrared optical constants of coal slags," tech. rep., Stanford Univ., CA (USA), 1986.

[330] A. Lohi, J. Wynnyckyj, and E. Rhodes, "Spectral measurement of the complex refractive index of fly ashes of canadian lignite and sub-bituminous coals," *The Canadian Journal of Chemical Engineering*, vol. 70, no. 4, pp. 751–758, 1992.

[331] A. B. De Miranda and J. Sacadura, "An alternative formulation of the sn discrete ordinates for predicting radiative transfer in nongray gases," *Journal of Heat Transfer*, vol. 118, no. 3, pp. 650–653, 1996.

[332] R. Johansson, K. Andersson, B. Leckner, and H. Thunman, "Models for gaseous radiative heat transfer applied to oxy-fuel conditions in boilers," *International Journal of Heat and Mass Transfer*, vol. 53, no. 1, pp. 220–230, 2010.

[333] F. Liu, "Numerical solutions of three-dimensional non-grey gas radiative transfer using the statistical narrow-band model," *Journal of Heat Transfer*, vol. 121, no. 1, pp. 200–203, 1999.

[334] A. G. Clements, R. Porter, A. Pranzitelli, and M. Pourkashanian, "Evaluation of FSK models for radiative heat transfer under oxyfuel conditions," *Journal of Quantitative Spectroscopy and Radiative Transfer*, vol. 151, pp. 67–75, 2015.

[335] J. Zhang, T. Ito, S. Ito, D. Riechelmann, and T. Fujimori, "Numerical investigation of oxy-coal combustion in a large-scale furnace: Non-gray effect of gas and role of particle radiation," *Fuel*, vol. 139, pp. 87–93, 2015.

[336] P. J. Coelho, P. Perez, and M. El Hafi, "Benchmark numerical solutions for radiative heat transfer in two-dimensional axisymmetric enclosures with nongray sooting media," *Numerical Heat Transfer: Part B: Fundamentals*, vol. 43, no. 5, pp. 425–444, 2003.

[337] C. F. Bohren and D. R. Huffman, "Absorption and scattering of light by small particles," Wiley science paperback series. Wiley, 1983.

[338] F. Liu, E. Garbett, and J. Swithenbank, "Effects of anisotropic scattering on radiative heat transfer using the P1-approximation," *International Journal of Heat and Mass Transfer*, vol. 35, no. 10, pp. 2491–2499, 1992.

[339] A. J. Black, *Oxy-fuel combustion for carbon capture using computational fluid dynamics*. PhD thesis, University of Leeds, 2014.

[340] A. German and T. Mahmud, "Modelling of non-premixed swirl burner flows using a Reynolds-stress turbulence closure," *Fuel*, vol. 84, no. 5, pp. 583–594, 2005.

[341] F. Breussin, F. Pigari, and R. Weber, "Predicting the near-burner-one flow field and chemistry of swirl-stabilied low-NO_x flames of pulveried coal using the RNG-k-ε, RSM and k-ε turbulence models," in *Symposium (International) on Combustion*, vol. 26, pp. 211–217, Elsevier, 1996.

[342] A. Pranzitellia, "Development and application of a novel f radiation property model for oxy-coal combustion," in *Oxyfuel Combustion Conference*, vol. 3, 2013.

[343] R. V. Filkoski, I. J. Petrovski, and P. Karas, "Optimization of pulverised coal combustion by means of CFD/CTA modeling," *Thermal Science*, vol. 10, no. 3, pp. 161–179, 2006.

[344] R. V. Filkoski, "Pulverised-coal combustion with staged air introduction: CFD analysis with different thermal radiation methods," *The Open Thermodynamics Journal*, vol. 4, no. 1, 2010.

[345] G. Krishnamoorthy and C. Wolf, "Assessing the role of particles in radiative heat transfer during oxy-combustion of coal and biomass blends," *Journal of Combustion*, vol. 2015, 2015.

[346] T. Wall, A. Lowe, L. J. WIBBERLEY, T. Mai-Viet, and R. Gupta, "Fly ash characteristics and radiative heat transfer in pulverized-coal-fired furnaces," *Combustion Science and Technology*, vol. 26, no. 3-4, pp. 107–121, 1981.

[347] B. Butler, M. Denison, and B. Webb, "Radiation heat transfer in a laboratory-scale, pulverized coal-fired reactor," *Experimental thermal and fluid science*, vol. 9, no. 1, pp. 69–79, 1994.

[348] A. Arenillas, R. Backreedy, J. Jones, J. Pis, M. Pourkashanian, F. Rubiera, and A. Williams, "Modelling of NO formation in the combustion of coal blends," *Fuel*, vol. 81, no. 5, pp. 627–636, 2002.

[349] D. Bäckström, R. Johansson, K. Andersson, F. Johnsson, S. Clausen, and A. Fateev, "Measurement and modeling of particle radiation in coal flames,"

[350] D. Trivic, "3-D radiation modeling of nongray gases–particles mixture by two different numerical methods," *International Journal of Heat and Mass Transfer*, vol. 70, pp. 298–312, 2014.